



**GEOLOGICAL SURVEY OF CANADA  
OPEN FILE 7285**

**Space weather events with ground-based muon observations  
(state-of-the-art)**

**G. Kalugin, L. Trichtchenko, K. Boudjemline, J. Armitage, and D. Waller**

**2013**



Natural Resources  
Canada

Ressources naturelles  
Canada

**Canada**



**GEOLOGICAL SURVEY OF CANADA  
OPEN FILE 7285**

**Space weather events with ground-based muon observations  
(state-of-the-art)**

**G. Kalugin<sup>1</sup>, L. Trichtchenko<sup>1</sup>, K. Boudjemline<sup>2</sup>, J. Armitage<sup>2</sup>, and D. Waller<sup>3</sup>**

<sup>1</sup> Natural Resources Canada (Ottawa), 2617 Anderson Road, Ottawa, ON K1A 0E7

<sup>2</sup> Department of Physics, Carleton University, Ottawa, ON K1S 5B6

<sup>3</sup> Defence Research and Development Canada (Ottawa), 3701 Carling Avenue, Ottawa, ON K1A 0Z4

**2013**

©Her Majesty the Queen in Right of Canada 2013

doi:10.4095/292231

This publication is available for free download through GEOSCAN (<http://geoscan.ess.nrcan.gc.ca/>).

**Recommended citation**

Kalugin, G., Trichtchenko, L., Boudjemline, K., Armitage J., and Waller, D., 2013. Space weather events with ground-based muon observations (state-of-the-art), Geological Survey of Canada, Open File 7285, 158 p.

doi:10.4095/292231

For more information related to this document please contact

German Kalugin  
Visiting Fellow  
Geomagnetic Laboratory  
2617 Anderson Road  
Ottawa ON K1A 0E7

Tel: (613) 837-5134  
Fax: (613) 824-9803  
Email: [German.Kalugin@NRCan-RNCan.gc.ca](mailto:German.Kalugin@NRCan-RNCan.gc.ca)

## Table of contents

1. Introduction and main definitions.....	5
1.1 Cosmic rays and their detection.....	5
1.2 GMDN and LC-anisotropy.....	6
1.3 Classification of geomagnetic storms.....	8
2. Two types of precursors.....	8
3. First-order anisotropy analysis for searching for precursors .....	11
4. CME-driven storm precursors.....	16
5. CIR-driven storm precursors.....	23
6. Asymptotic directions and global coverage by GMDN.....	27
7. Real-time cosmic ray monitoring system for space weather.....	32
8. Muon detector at Carleton University.....	33
9. Conclusions.....	35
Acknowledgements.....	36
References.....	37
Appendices	
Appendix 1. <i>The prototype of database for Global Muon Detector Network (MDDDB) and possibilities of its usage for Space Weather goals</i> (E. Eroshenko et al.).....	44
Appendix 2. <i>Temperature effect of muon component and practical questions of its account in real time for Global Muon Detector Network</i> (V. Yanke, M. Berkova, E. Eroshenko, A. Belov).....	66
Appendix 3. <i>Global Muon Detector Network (GMDN)</i> (K. Munakata et al.).....	82
Appendix 4. <i>Ground-Based Cosmic Ray Detectors for Space Weather Applications</i> (J.W. Bieber).....	114
Appendix 5. <i>FOREWARN Detector Construction</i> (J. Armitage, J. Botte, K. Boudjemline and A. Robichaud).....	130
Appendix 6. <i>GEANT4 Simulation of FOREWARN Detector</i> (K. Boudjemline).....	141
Appendix 7. <i>FOREWARN Detector. Data Analysis.</i> (K. Boudjemline).....	148
Appendix 8. <i>Proposal for future Canadian detector</i> (J. Armitage).....	157



It is important to understand that due to the geometry of the geomagnetic field not all the CR particles can reach Earth. This effect can be described by *rigidity*. By definition, rigidity is the product of magnetic field intensity and Larmor radius (see e.g. Rossi, 1964, p. 55) (i.e. it is inversely proportional to the curvature of the path of a charged particle traversing the geomagnetic field). Therefore the rigidities of primary CR particles responsible for the counting rates registered at ground level should have values larger than the so-called *cut-off rigidity* which describes the magnetic shielding provided by the geomagnetic field against the arrival of charged CR particles (Humble et al., 1985). In addition, owing to the particle motion inside the geomagnetic field, each ground level detector is capable of recording particles produced by primaries originating from a limited set of directions in space, which is called the *asymptotic cone of viewing* (Plainaki et al., 2009); the directions themselves are called *asymptotic directions* (Duldig, 2001) (for details, see Section 6).

One of the noticeable results of the interaction of CRs with solar disturbances is a *Forbush Decrease* (FD) which is characterized by reductions of near-earth flux up to 25-30% over a few days. Interactions of CRs with solar disturbances, including FD effect, can produce signatures in the CRs registered by detectors on the ground. Such signatures were found before the beginning of strong geomagnetic storms and large FD effects (Asipenka et al., 2009). They are called *precursors*. In this report we review the literature in order to determine the feasibility of using ground-based muon detectors for early warning of extreme space weather conditions in terms of searching for precursors for geomagnetic storms.

## 1.2 GMDN and LC-anisotropy

Muon detectors have some advantages compared to neutron monitors because of a number of useful properties muons possess. Particularly, energy of muons is higher than energy of other particles, therefore when muons penetrate through a thick absorber it stops other particles allowing muons to be easily detected. In addition, muons have minor energy losses and small angular displacement allowing to determine their incident directions. Thus, muons are detected with high accuracy and low noise. Today the Global Muon Detector Network (GMDN) has been established. GMDN includes four muon stations in Nagoya, Hobart, São Martinho and Kuwait, as listed in Table 1 (Braga et al., 2010).

Muon detectors record secondary CRs created by primary CRs with energies greater than 1 GeV. The CRs with energies up to  $\sim 100$  GeV experience significant variations in response to passing solar wind disturbances such as ICMEs (Kuwabara et al., 2009). The ICMEs generate IP shocks. These shocks and ICME itself propagate through IP space and may reach the Earth. Behind such a shock there is a region of suppressed CRs density (by 1% - 10%) which is called a *depleted region* (Munakata et al., 2000). Some particles from the depleted region leak into the upstream region and, traveling nearly at the speed of light, enter the magnetosphere before the shock arrives there (Fig. 2). They are typically visible 4-8 hours before the shock arrives at the Earth to cause a geomagnetic storm. Specifically, these particles are observable as precursory *loss-cone (LC) anisotropy* and characterized by intensity deficits confined to a small pitch-angle region around the sunward direction along the *interplanetary magnetic field (IMF)*. The *pitch angle* of each direction of viewing is defined as the angle between the sunward IMF direction and the viewing direction; IMF

(along with other solar wind parameters) is observed in near real-time by the Advanced Composition Explorer (ACE) spacecraft. The muon intensity for each viewing direction is usually computed relative to the omnidirectional intensity using pressure corrected one-hour count rate data and the results are often depicted in one ‘time - pitch angle’ plane (see sections 3 and 4).

Table 1. Information on GMDN detectors<sup>1</sup>

Station	Detection area, m <sup>2</sup>	Number of viewing directions	Geographic Latitude	Geographic Longitude	Altitude, m
Nagoya (Japan)	36	17	35.1° N	137.0° E	77
Hobart (Australia)	9 / 16	25	42.9° S	147.4° E	65
São Martinho (Brazil)	28	21 x 21	29.4° S	308.2° E	488
Kuwait (Kuwait)	9	23 x 23	29.4° N	48.0° E	50

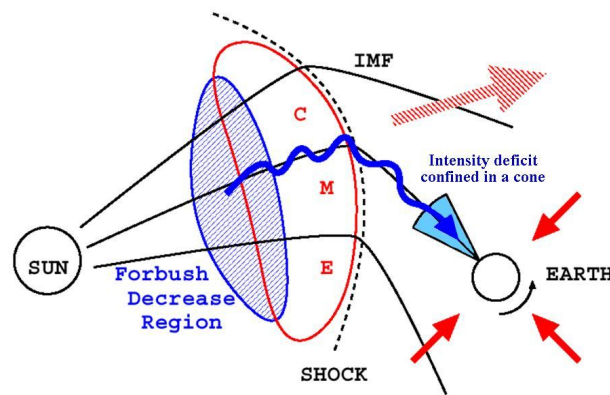


Fig. 2 The effects of a shock driven by ICME (Asipenka et al., 2009).

Most of modern muon detectors employed in space research, including GMDN, are used to find early identification of precursors of geomagnetic storms by measuring cosmic-rays produced-muon intensity. Two main types of precursors, one of which is the above mentioned LC precursor, are considered in Section 2. It is also found that the GMDN is

<sup>1</sup> The table shows two values for detection area in Hobart, which was enlarged from 9 m<sup>2</sup> to 16 m<sup>2</sup> in December 2010.

capable of being used for observation of geomagnetic storms caused not only by ICME but also by the so-called *Corotating Interaction Regions (CIRs)* considered in Section 5. The CIRs are mostly responsible for small storms which, however, pose the same dangerous situations for space-based assets as in the case of CME-driven storms. In this manuscript we review the main results obtained for both types of storms with using muon detectors during different periods of solar activity.

### 1.3 Classification of geomagnetic storms

There are different ways to classify geomagnetic storms. We briefly explain only two of them, which are used in this review. Table 2 shows a classification given in Gonzalez et al., [1994], Gonzalez et al., [1999] and Rockenbach et al., [2009] in terms of the peak of *the Disturbance storm-time (Dst) index* that expresses disturbance of mid-latitude geomagnetic field parallel to geomagnetic dipole axis. For example, in this classification, CIR-driven geomagnetic storms are classified as small (Hutchinson et al., 2011; Wanliss and Showalter, 2006). Another way to classify geomagnetic activity is to compute *the Kp index* that quantifies disturbed magnetic-field activity derived from magnetic observatory measurements around the world by assigning a 3-hour range of the horizontal component of the geomagnetic field to a quasi-logarithmic scale: 0 for the most quiet to 9 for the most disturbed (Rangarajan & Iyemori, 1997).

Table 2. Classification of geomagnetic storms by the Dst peak

Super Storms (SS)	more negative than -250 nT
Intense Storms (IS)	between -250 nT and -100 nT
Moderate Storms (MS)	between -100 nT and -50 nT
Small storms	between -50 nT and -30 nT
Negligible storm activity	less negative than -30 nT

## 2. Two types of precursors

Along with LC intensity deficits there also occurs intensity excess due to a reflection of galactic CRs by IP shock approaching the Earth (Appendix 3). Thus LC precursors apparently result from a LC effect, in which a muon detector is magnetically connected to the CR-depleted region downstream of the shock, and the precursory increases apparently result



from particles reflecting from the approaching shock (Leerunnavarat et al., 2003). These two effects result in two types of precursors of geomagnetic storms observed by ground-level stations. They are a LC precursor, which is characterized by intensity deficits localized near the zero pitch angle, and an enhanced variance (EV) precursor which is characterized by an increase or decrease of intensity that can not be described as a systematic function of pitch angle (Munakata et al., 2000). Several possible explanations for the EV-type precursors are given in Munakata et al., [2000] and Leerunnavarat et al., [2003]. Thus, measurements of cosmic-ray produced muons (and neutrons), depending on the solar wind-magnetosphere coupling, can have signatures of LC precursors and EV precursors for the impending geomagnetic storms.

Figure 3 (taken from Leerunnavarat et al., [2003]) displays results from two surveys of CR precursors. In particular, the histogram on the left is given for 22 “large” storms surveyed with surface muon telescopes in Munakata et al., [2000] and the right histogram is for 14 “major” geomagnetic storms surveyed with a network of neutron monitors in Belov et al., [2001]. The histograms display the lead time of the precursor relative to the SSC associated with the shock driven by ICME. The typical primary CR energy producing the secondary particles modulated by FD is taken as  $\sim 30$  GeV for muon detectors and  $\sim 10$  GeV for neutron monitors.

It follows from Fig. 3 that the muon detectors observed precursors in 15 of 22 large storms and that the lead time of precursors relative to the SSC is typically 8 hours and can be as long as 12 hours. This is more than the lead time of precursors for neutron monitors and sufficient to be useful for space weather forecasting as it provides substantially longer advance warning than 0.5-1 hr lead time provided by direct shock detection at a spacecraft stationed at the upstream Sun-Earth Lagrangian point (Leerunnavarat et al., 2003).

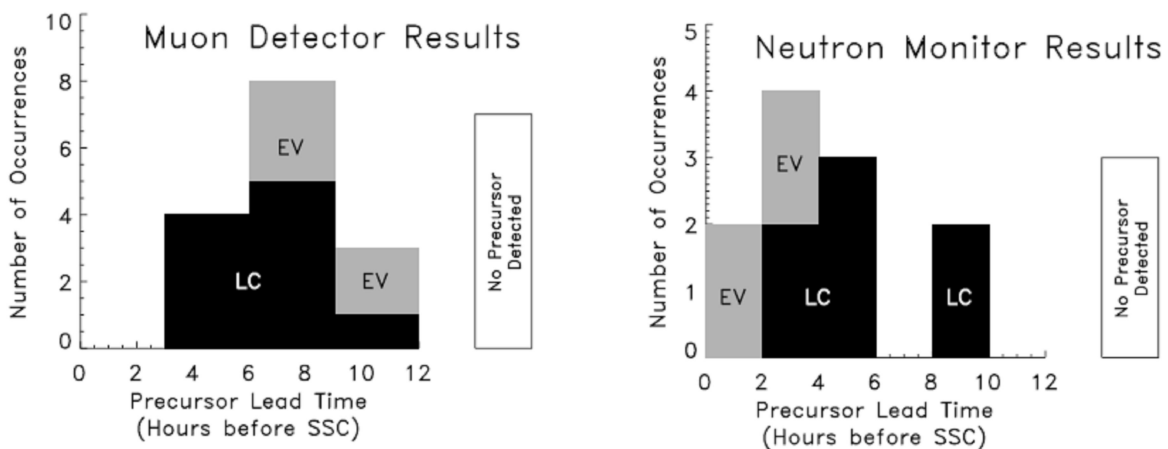


Fig. 3 Histograms of the earliest observation of precursors by muon detectors (on the left) and neutron monitors (on the right) before SSC (Leerunnavarat et al., 2003).

The difference in the lead time for muon detectors and neutron monitors is rather surprising because the FD following a shock is typically more depressed at the lower energies measured

by neutron monitors. Therefore it would be natural to expect LC particles escaping into the upstream region from the depleted region downstream of the shock to be more readily detected at the lower energies, the opposite of what is observed. Leerunnavarat et al. (2003) found an explanation for this in terms of a power-law index  $q$  of the reduced power spectrum as a function of wavenumber which affects the transport of CRs (Jokipii, 1966). Specifically, it was found that CRs of  $\sim 30\text{GeV}$ , to which a muon detector is sensitive, experience a substantially lower  $q$ -value than CRs at  $\sim 10\text{ GeV}$ , as measured by neutron monitors ( $q = 0.5$  and  $q = 1.1$  respectively). As a result the parallel mean free path for IP scattering and a decay length for the former are larger than for the latter and as a consequence, the lead time provided by muon detectors is larger than by neutron monitors.

In addition, a comparison between LC and EV precursors in each histogram in Fig. 3 shows that the former can serve as a signature of a precursor of geomagnetic storms more frequently than the latter. In other words, the LC effect is more easily recognized in the data and thus more useful as an indicator of impending space weather disturbances.

The same conclusions can be made from Fig. 4 which shows the results from an analysis of 133 geomagnetic storms between March 2001 and December 2007 with good data coverage by GMDN (Rockenbach et al., 2009). The abbreviations MS, IS and SS are explained in Table 2, ‘NP’ means a non-precursor case. One can see on the left panel that 86% of the SS, 30% of the IS and 15% of the MS had precursors observed by the GMDN with the number of NP events decreasing with the magnetic storm intensity. The right panel illustrates a prediction capability of GMDN and shows that LC precursors were observed more frequently between 9 and 12 hours before the SSC. Remarkably, the LC precursor of a super storm was observed as early as 18 hours prior to the SSC. It is worth mentioning that since strong geomagnetic storms are rare, the statistics should be viewed with caution.

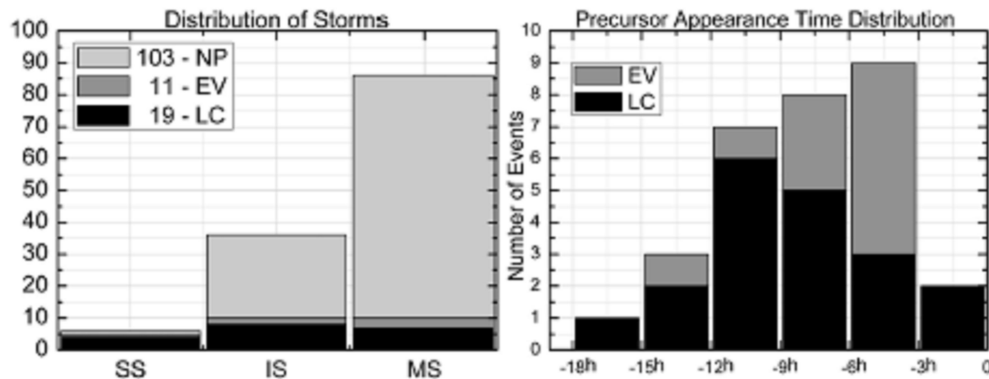


Fig. 4 Histograms of magnetic storms intensity and the appearance time of LC and EV precursors; ‘NP’ represents no-precursor cases (Rockenbach et al., 2009).

We note that the LC anisotropy has a small angular scale structure  $\sim 30^\circ$ . Therefore, observations require a relatively good angular resolution and high statistical accuracy (Nonaka et al., 2005b). Recent success in two-dimensional observation of LC effects is mainly due to observations by muon telescopes with angular resolution smaller than  $\sim 10^\circ$

(Nonaka et al., 2003; Fujimoto et. al., 2003; Munakata et al., 2005). Accumulation of LC events allows extraction of average and typical properties and features of LC effects as well as their correlations with the FD.

### 3. First-order anisotropy analysis for searching for precursors

We describe a methodology used to analyze LC precursors following Rockenbach et al. (2011). Let us consider a count rate of CR muons corrected for the atmospheric pressure variation, called intensity. The LC precursor is observed as a deficit of intensity when the sunward IMF direction is monitored by the muon detector. To provide an accurate analysis of LC events and improve the precursor observations, it is necessary to properly remove the contribution from the diurnal anisotropy (DA), which always exists in space with an amplitude comparable to the intensity deficit because of the LC anisotropy (Fushishita et al., 2010). The DA, when observed by a detector on the Earth, produces a diurnal variation which is generally different in different directional channels. We derive the anisotropy by fitting the following function

$$\begin{aligned}
I_{i,j}^{fit}(t) = & I_{i,j}^0(t) + \xi_x^{GEO}(t) \left( c_{1i,j}^1 \cos(\omega t_i) - s_{1i,j}^1 \sin(\omega t_i) \right) \\
& + \xi_y^{GEO}(t) \left( s_{1i,j}^1 \cos(\omega t_i) + c_{1i,j}^1 \sin(\omega t_i) \right) \\
& + \xi_z^{GEO}(t) c_{1i,j}^0
\end{aligned} \tag{1}$$

to the observed hourly count rate  $I_{i,j}^{obs}(t)$  of muons at universal time  $t$  in the  $j$ -th directional channel of the  $i$ -th muon detector (Okazaki et al., 2008; Kuwabara et al., 2004). In this equation  $t_i$  is the local time at the location of the  $i$ -th detector and  $\omega = \pi/12$ . The coupling coefficients  $c_{1i,j}^1$ ,  $s_{1i,j}^1$  and  $c_{1i,j}^0$  relate the observed muon intensity to the primary CR intensity in free space (Kuwabara et al., 2004); they are calculated by assuming a rigidity independent anisotropy.

The best-fit parameters  $\xi_x^{GEO}(t)$ ,  $\xi_y^{GEO}(t)$  and  $\xi_z^{GEO}(t)$  denote three components of the anisotropy which are defined in a local geographical coordinate system (GEO), in which the  $z$ -axis is directed toward geographic north, the  $x$ -axis is in the equatorial plane and directed to the zenith of a point on the Earth equator at 00:00 local time, and the  $y$ -axis completes the right-handed coordinate set. Thus, for example,  $\xi_z^{GEO}(t)$  represents the north-south anisotropy (Okazaki et al., 2008). These best-fit parameters along with  $I_{i,j}^0(t)$  are determined by minimizing  $S$  defined, for example, in the case of one detector with two viewing directions, as

$$S = \sqrt{\frac{1}{M} \sum_{m=1}^M s^2(t_m)} = \sqrt{\frac{1}{2M} \sum_{m=1}^M \left[ \frac{\left( I_{1,1}^{obs}(t_m) - I_{1,1}^{fit}(t_m) \right)^2}{\sigma_{1,1}^2} + \frac{\left( I_{1,2}^{obs}(t_m) - I_{1,2}^{fit}(t_m) \right)^2}{\sigma_{1,2}^2} \right]},$$

where  $s(t_m)$  is hourly residual of the best fitting at the time  $t = t_m$ ,  $M$  is the total number of hours used for the best fit calculations and  $\sigma_{i,j}$  is the count rate error for the  $(i,j)$  directional channel.

Now we define a part of  $I_{i,j}^{obs}(t)$ , associated with the DA, as follows (Rockenbach et al., 2011)

$$\begin{aligned}
I_{i,j}^{DA}(t) = & \bar{I}_{i,j}^0(t) + \bar{\xi}_x^{GEO}(t) \left( c_{1i,j}^1 \cos(\omega t_i) - s_{1i,j}^1 \sin(\omega t_i) \right) \\
& + \bar{\xi}_y^{GEO}(t) \left( s_{1i,j}^1 \cos(\omega t_i) + c_{1i,j}^1 \sin(\omega t_i) \right) \\
& + \bar{\xi}_z^{GEO}(t) c_{1i,j}^0
\end{aligned} \tag{2}$$

The best-fit parameters in (2) are defined as the 12-hours Trailing Moving Averages (TMAs), i.e.

$$\begin{aligned}
\bar{I}_{i,j}^0(t) &= \frac{1}{12} \sum_{t-11}^t I_{i,j}^0(t), \\
\bar{\xi}_x^{GEO}(t) &= \frac{1}{12} \sum_{t-11}^t \xi_x^{GEO}(t), \\
\bar{\xi}_y^{GEO}(t) &= \frac{1}{12} \sum_{t-11}^t \xi_y^{GEO}(t), \\
\bar{\xi}_z^{GEO}(t) &= \frac{1}{12} \sum_{t-11}^t \xi_z^{GEO}(t).
\end{aligned} \tag{3}$$

Comparing between the 12-hours and the 24-hours TMAs of the best-fit parameters shows that the former are better than the latter in terms of observation of the LC effect (Rockenbach et al., 2011).

To remove the contribution of the DA from the data for precise analysis of the LC precursor, we subtract  $I_{i,j}^{DA}(t)$ , defined by Eq. (2), from the observed intensity  $I_{i,j}^{obs}(t)$

$$\Delta I_{i,j}^{cal}(t) = I_{i,j}^{obs}(t) - I_{i,j}^{DA}(t). \tag{4}$$

As a result we obtain the directional intensity distribution free from the DA. Moreover, to visualize the precursor signatures more clearly, we suppress the statistical fluctuations which are larger in the inclined channels. For this purpose, instead of  $\Delta I_{i,j}^{cal}(t)$ , we use the ‘‘significance’’ defined as (Rockenbach et al., 2011)

$$s_{i,j}^{cal}(t) = \frac{\Delta I_{i,j}^{cal}(t)}{\sigma_{i,j}} = \frac{I_{i,j}^{obs}(t) - I_{i,j}^{DA}(t)}{\sigma_{i,j}}.$$

*Remark 1.* Since the difference  $\Delta I_{i,j}^{cal}(t)$  is calculated using TMAs, it is not affected by the variation occurring after time  $t$  (Fushishita et al., 2010). This is important for real time predictions in space weather forecasting (Rockenbach et al., 2011).

*Remark 2.* In some works, to avoid spurious diurnal variation, instead of  $I_{i,j}^{obs}(t)$ , the following is used

$$\tilde{I}_{i,j}^{obs}(t) = I_{i,j}^{obs}(t) \frac{\bar{I}_{1,1}^{obs}(t)}{\bar{I}_{i,j}^{obs}(t)}$$

with the 24hr TMAs (Okazaki et al., 2008; Kuwabara et al., 2004).

For analysis of muon intensity distribution, the calculated values of  $\Delta I_{i,j}^{cal}(t)$  can be represented in two ways. One of them is to show the results for all of the directional channels in the form of a two-dimensional color contour map where the latitude of incident direction spanning from the north (upper) and south (lower) directions in the field of view is scaled along the vertical axis, while the longitude from the east (right) and west (left) directions is on the horizontal axis. Additionally, in the map there are contour lines of pitch angle measured from the observed IMF direction; the pitch angle is calculated for CRs incident to each directional channel with the median primary energy appropriate to that channel (Munakata et al., 2005). As an example, intensity distributions observed in 121 directional channels with a muon hodoscope at Mt. Noricura (Japan) over 6 hours preceding the SSC are shown in Fig. 5 (Munakata et al., 2005) where the LC precursor can be identified by a region of the deficit intensity (displayed by blue color) localized around small pitch angle. Similar intensity distributions were analyzed by Nonaka et al. (2003). See also (Fushishita et al., 2010) and Appendices 1 and 3.

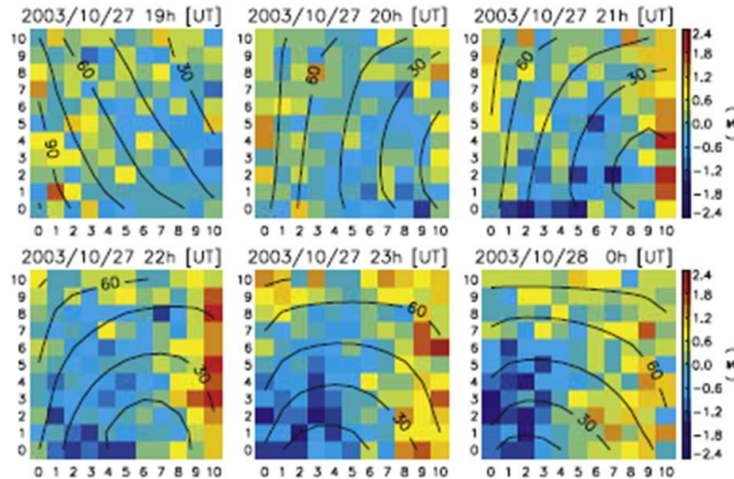


Fig. 5 The intensity distributions observed with a muon hodoscope at Mt. Noricura (Japan) over 6 hours preceding SSC. In the panels the LC precursor relates to the region of deficit intensity displayed by blue color (Munakata et al., 2005).

Another way to represent muon intensity relative to the omnidirectional intensity is to use a two-dimensional map with measurements along two coordinate axes of time and pitch angle. An implementation of this technique is illustrated in Fig. 6 which shows the pitch angle distribution of CR intensity vs. time observed by São Martinho da Serra's muon telescope during the geomagnetic storm on April 28, 2003 (Rockenbach et al., 2009) and on December 14, 2006 (Schuch et al., 2009; Rockenbach et al., 2011) at the top and the bottom respectively. The pitch angle of each direction of viewing is defined as the angle between the sunward IMF direction and the viewing direction of  $j$ -th directional telescope in  $i$ -th muon detector of the GMDN (Munakata et al., 2000). The open and solid circles represent, respectively, an excess and deficit of CR intensity relative to the DA intensity in accordance with formula (4), and the diameter of each circle is proportional to the magnitude of deficit or excess. In the top figure, the LC effect can be seen clearly approximately 7 hours before the SSC shown by the vertical line and can serve as a precursor of the storm. At the bottom, additionally, is shown the intensity recorded with five single channels. One can see that LC has 3hr duration implying about  $45^\circ$  width and onsets first in the eastward viewing channel, then in the vertical and westward channels, as expected for an anisotropic depression of the CR intensity (Schuch et al., 2009).

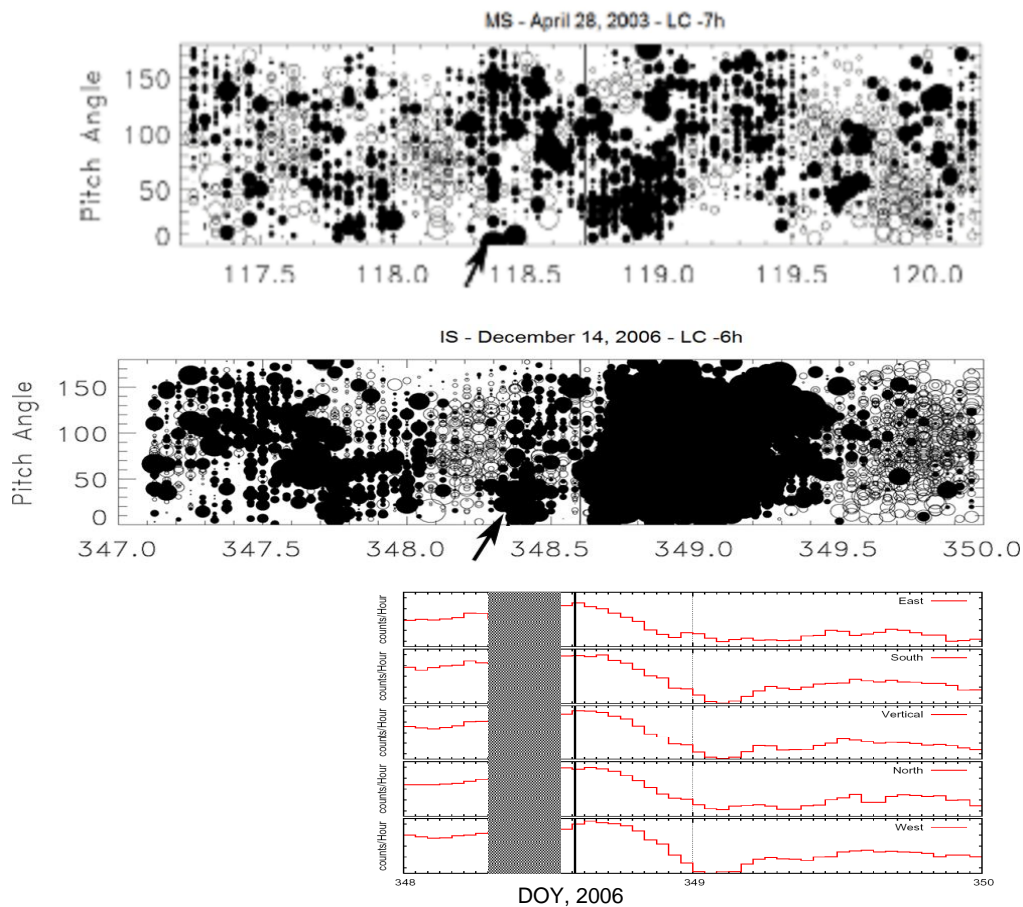


Fig. 6 Examples of LC precursors observed by São Martinho da Serra's muon telescope on April 28, 2003 (Rockenbach et al., 2009) and on December 14, 2006 (Schuch et al., 2009; Rockenbach et al., 2011) at the top and the bottom respectively.

A distribution of particle intensity using a similar approach is shown in Fig. 7 (Asipenka et al., 2009; Appendix 1). The red circles show intensity deficit and yellow circles indicate intensity increase on different longitudes before and after the occurrence of the geomagnetic storm that happened on September 9th, 1992. One can see on the top panel that first, the closer the shock arrival time at Earth (vertical line), the more the red circles. Secondly, on September 7th one can clearly observe an increase in the number of red circles. As in the case of the aforementioned events, an intensity deficit can serve as a precursor of the storm. The lower panels illustrate the same effect but with measurements taken from a few stations only. As a result, at a fixed time we do not have information about the particle intensity on all latitudes and so it is hard to analyse such data. Thus the sky coverage in the asymptotic directions of the stations should be as full as possible.

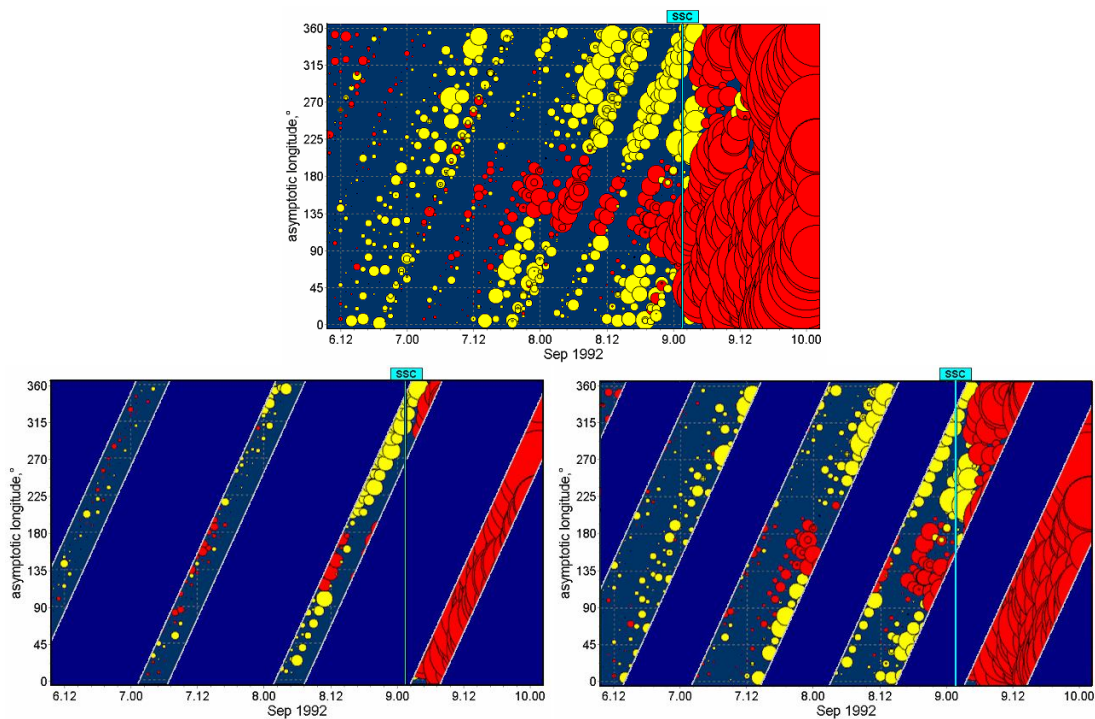


Fig. 7 Precursors in real time observations (Appendix 1).

For further study and better understanding of precursor anisotropy, different physical models are currently being developed. For example, Ruffolo et al. (1999) and Petukhov (2009) try to build models to describe the dynamics of CR intensity. Another approach is to use anisotropy to derive the CR density gradient associated with the drift of CR (Bieber & Evenson, 1998; Okazaki et al., 2008). The density gradient in turn is used to deduce ICME geometry and orientation (Kuwabara et al., 2009), which is important to predict the effect of ICME on Earth's magnetosphere. One of the difficulties of such an approach is that the commonly used diffusive approximation becomes invalid at some limiting rigidity while the transition between diffusive and nondiffusive behaviours is not yet well understood (Okazaki et al., 2008).

We also note that generally the pattern of daily variations of muons with energies higher than 5 GeV is more complicated than for neutrons. For example, based on data related to the storm in December, 2006 and measured by Aragats Multichannel Muon Monitor, Mailyan & Chilingarian (2010) described both solar and sidereal periodicities using a fitting function with two cosines with 24- and 12-hr periods (Fig. 8) while for neutron data it was sufficient to use one cosine function following the approach by Kudela et al. (2008).

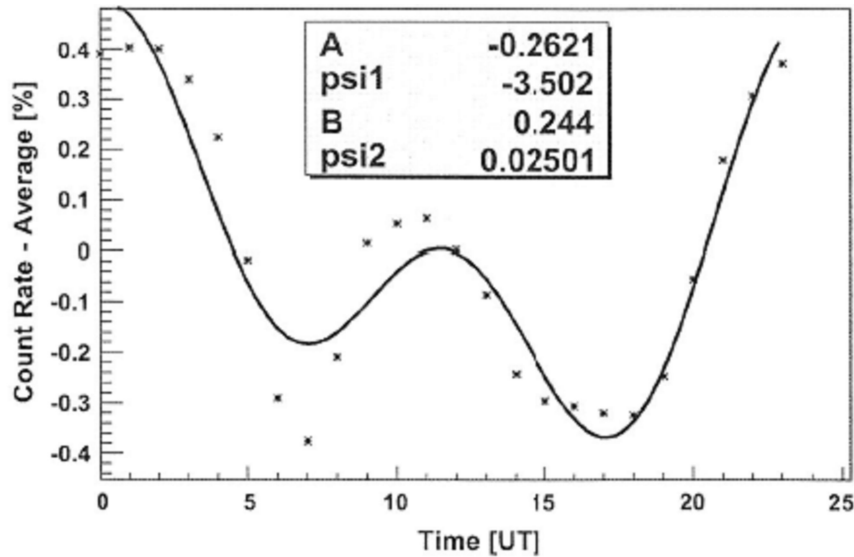


Fig. 8 Daily variations of muon data in December, 2006 without pressure and temperature corrections fitted by sum of harmonic functions  
 $f(t) = A \cos(2\pi t/24 + \psi_1) + B \cos(2\pi t/12 + \psi_2)$  (Mailyan & Chilingarian, 2010).

#### 4. CME-driven storm precursors

Munakata, et al. (2005) observed galactic CR intensity during an LC precursor period related to an IP shock arrival on October 28, 2003. They used a large single muon hodoscope on the top of Mt. Norikura (Japan) and analyzed 121 directional channels which cover  $360^\circ$  of the azimuth angle and  $0^\circ$  to  $55^\circ$  of the zenith angle. The estimated median energy of CR is in the range from 48 GeV (for the vertical channel) to 80 GeV (for the most inclined channel). In the lower panel in Fig. 9 is shown the intensity relative to the average muon intensity in each hour as a function of the pitch angle of the incident direction where the pitch angle is calculated using one-hour averages of the ACE IMF data (level 2), lagged by 1 hour as a rough correction for the solar wind transit time between the ACE satellite and the Earth. The hourly data of the IMF magnitude and the solar wind velocity ( $V_{sw}$ ) are shown in the top two plots of Fig. 9. One can see a signature of LC precursor (solid circles) localized around  $0^\circ$  pitch angle during  $\sim 7$  hours prior to the SSC indicated by a vertical line when IMF and  $V_{sw}$  experience a sharp increase. Note that by analyzing a 2D map of the intensity Munakata, et al. reported a lead time of 4.9 hr for the LC precursor. However, they had difficulties in establishing the direction in which the shock was propagating.



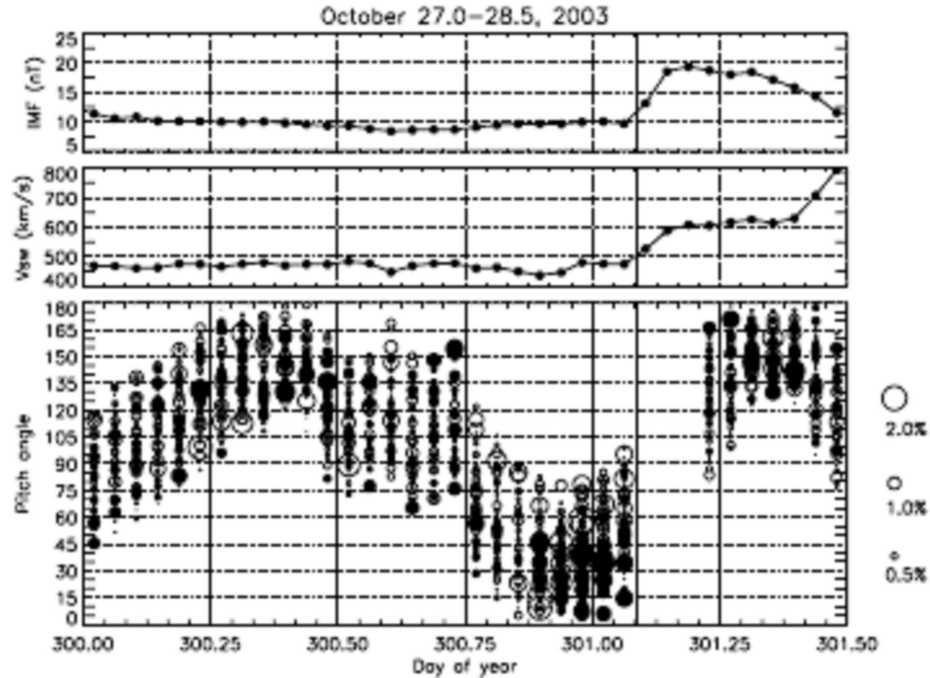


Fig. 9 The top two plots show the hourly data (Level 2) of the IMF magnitude and the solar wind velocity ( $V_{sw}$ ) observed by the ACE on October 27-28, 2003. In the bottom panel, each circle represents an intensity of muons in a single directional channel relative to the omnidirectional intensity as a function of time (abscissa) and a pitch angle corresponding to the viewing direction (ordinate). Open and solid circles represent, respectively, an excess and deficit of the intensity, the diameter of a circle is proportional to the magnitude of the excess or deficit (Munakata, et al., 2005).

Fushishita et al. (2010) analyzed a precursor of FD related to an intense geomagnetic storm on December 14, 2006. The data were obtained using the GMDN by monitoring the directional intensity of CR with median energies ranging from  $\sim 50\text{GeV}$  to  $\sim 110\text{GeV}$ . To analyze the data they improved the method of Munakata, et al. (2005) by eliminating the influence of the diurnal anisotropy (DA) and by a better visualization of the signatures of CR precursors. As a result a significant LC signature was recorded by the Hobart detector at  $\sim 20$  hr before SSC and then by the São Martinho detector with a larger amplitude at  $\sim 6$ hr. A weak LC signature was first recorded more than a day prior to the SSC onset. This suggests that the LC precursor appeared only 7 hr after the CME eruption from the Sun, when the IP shock driven by the CME was located at 0.4 AU from the Sun (i.e. the average shock speed was about 2381 km/s).

Figures 10 and 11 relate to the event on December 14, 2006. At the time of the SSC the amplitude ( $-6.45\%$ ) of the LC anisotropy was more than twice the FD size (cf. Fig. 10 (b) and Fig. 11). The peak  $K_p$  index was 8+. The long lead time of the LC precursor was 15.6 hr. Fushishita et al. also found excess intensity from sunward IMF direction clearly observed during  $\sim 10$  hr preceding the SSC. This was the first detailed observation with muon detectors of the precursor due to the shock reflected particles.

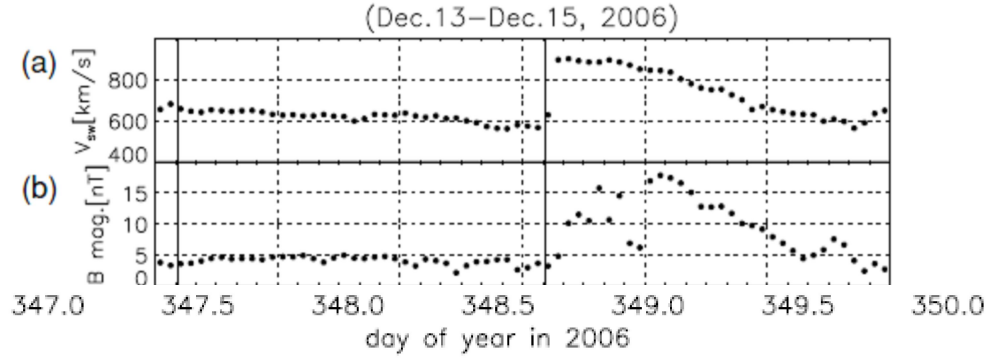


Fig. 10 The hourly data (Level 2) of the solar wind velocity (a) and the IMF magnitude (b) measured by the ACE over a three-day period between 2006 December 13 and 15 (Fushishita et al., 2010).

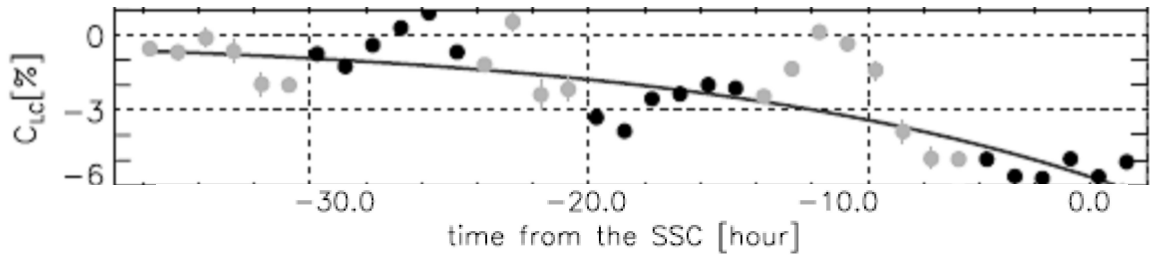


Fig. 11 The amplitude of the LC anisotropy ( $C_{LC}(t)$ ) with black and grey circles displaying the parameters obtained when the sunward IMF direction is monitored by the GMDN and is out of the Field of View (FOV) of the GMDN respectively. The solid line is an exponential function of the time as the best fitting to the black circles (Fushishita et al., 2010).

Rockenbach et al. (2009) analyzed 133 geomagnetic storms monitored by the GMDN from 2001 to 2007 to identify their precursors (see Section 2) and found CR precursors to be observed on average 7.2 hours in advance of the SSC. Rockenbach et al. (2011) sorted these storms by their intensity using the Dst index and found a dependence of a presence of storm precursors on the storm intensity as shown in the top of Table 3. The rest of the table shows, as an example, a particular storm from each class and an advanced time for LC precursor's observations by an indicated station prior to the SSC for the storm. It follows from Table 3 that the stronger the storm the longer the precursor time. However, this conclusion should be regarded as preliminary as the number of strong storms considered is not sufficient for a statistical treatment (on the other hand, the occurrences of strong storms are infrequent).

Figure 12 shows the pitch angle distributions of muon intensity in time calculated by formula (4) for the storms listed in Table 3 (Rockenbach et al., 2011). (The event on December 14, 2006 is also considered in Fushishita et al., [2010] and described above.) A pitch angle  $0^\circ$  corresponds to the sunward IMF direction. SSC occurrence is shown by a vertical line. Open and solid circles represent, respectively, an excess and deficit of CR intensity relative to the average, and the diameter of each circle is proportional to the magnitude of deficit or excess.

Figure 13 shows the pitch angle distribution of the CR intensity on November 9, 2004 ten hours prior to the SSC at  $t = 314.583$  indicated by arrow in the top panel of Fig. 12.

Table 3. Distribution of storms accompanied by LC precursors

Types of storms by their intensity (number of storms)	Moderate Storms (89)	Intense Storms (37)	Super Storms (7)
Example of a storm	October 24, 2003	December 14, 2006	November 9, 2004
Advanced LC observations (by station)	5 hrs (Hobart)	8 hrs (São Martinho)	10 hrs (Hobart)

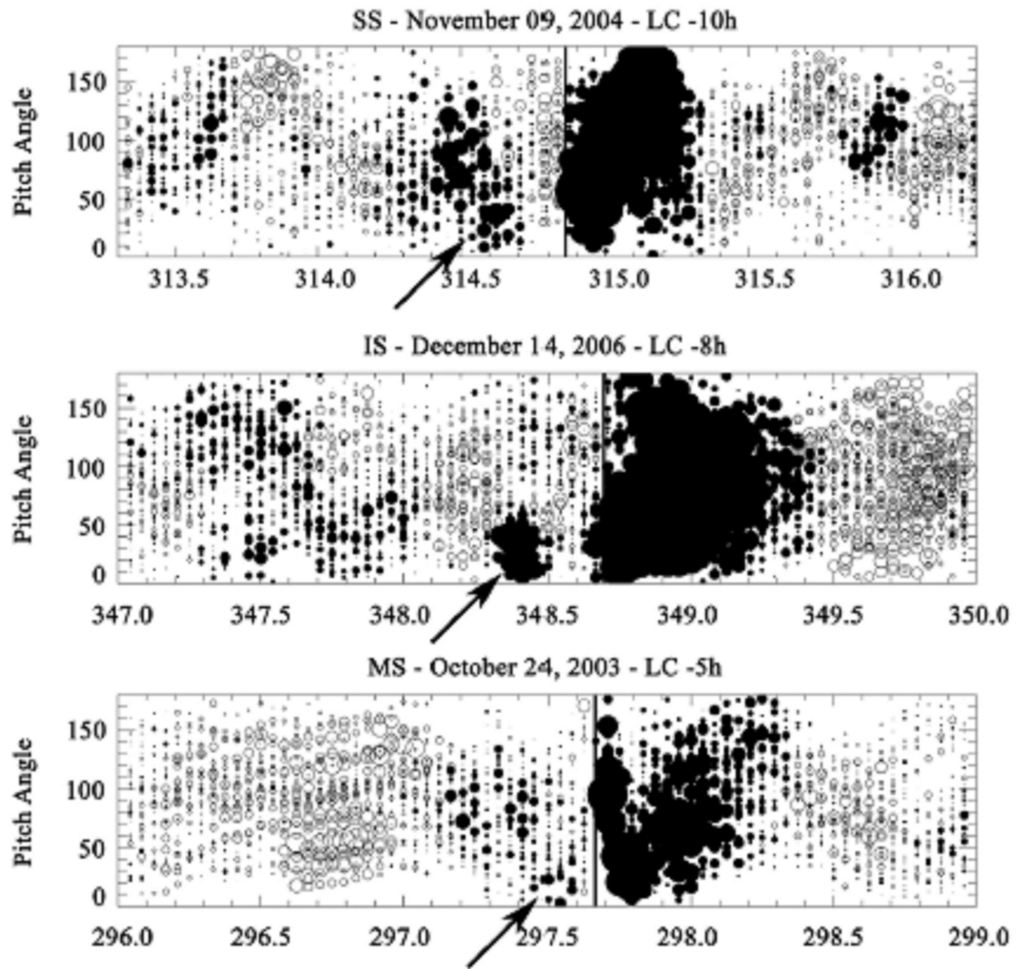


Fig. 12 Pitch angle distributions of CR intensity for storms of different intensity before and after the SSC occurrence shown by vertical lines (Rockenbach et al., 2011).

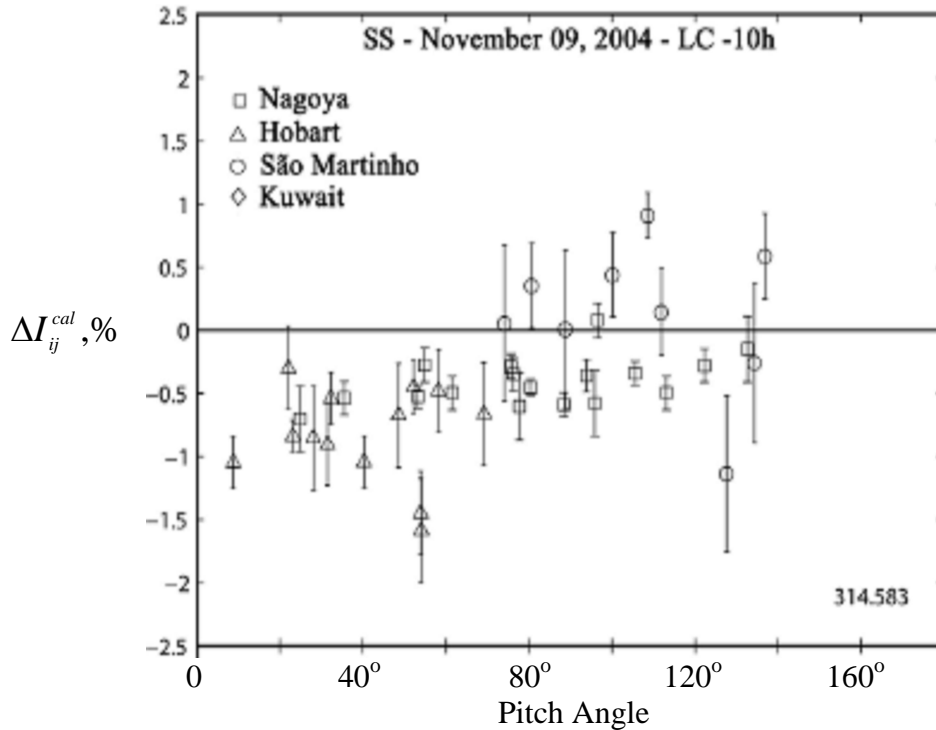


Fig. 13 Cut of the top distribution in Fig. 12 at  $t = 314.583$  indicated by arrow there (Rockenbach et al., 2011).

A similar analysis was applied to 22 storms observed with good coverage by Munakata et al. (2000) who concluded that the lead time of observed precursors relative to the SSC is typically 8 hours and can be as much as 12 hours (see Section 2). Moreover, the authors believe that LC precursors may often be observable in muon data earlier because the appearance time of LC precursors is often determined by the changing network coverage, i.e. the precursor seems to be already present when network viewing direction moves into the sunward IMF direction. In other words, with more stations for observations of precursors the lead time can be found to be larger than the values mentioned above.

Figure 14 shows observations for the period covering SSC of the storm on September 9, 1992, one of the 22 storms mentioned above. The anisotropy measured by the muon telescopes appears as the third plot from the top. The open and solid circles represent an excess and a deficit of CR intensity relative to the average and the diameter of each circle is proportional to the magnitude of deficit or excess (see 1% scale to the right of the plot). There is evidence for a loss cone 25 hours prior the SSC (Munakata et al., 2000) but due to poor network coverage from -23 hours to -10 hours the statistical significance is not sufficient to be certain and the appearance time is conservatively stated as about 10 hours before the SSC (Jansen et al., 2001). McMurdo neutron monitor observations (on the second plot from the top) show the long lasting nature of the event. A similar remark can be made about events occurred September 5, 1982, February 20, 1992, March 23, 1993 and September 24, 1998 (Munakata et al., 2000).

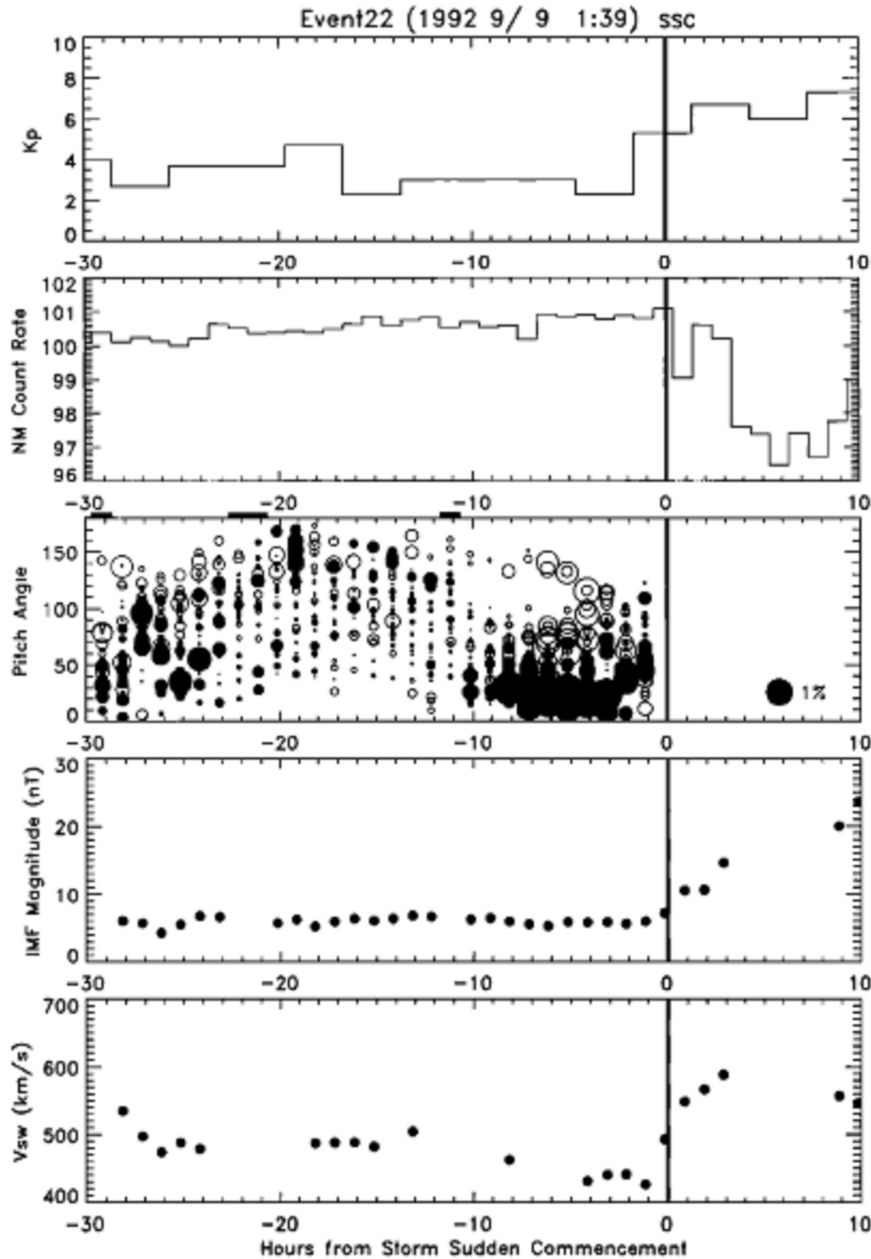


Fig. 14 Observations for the period covering the geomagnetic storm on September 9, 1992 (from top to bottom): Kp index, McMurdo neutron monitor relative count rate, anisotropy derived from the muon telescopes, IMF magnitude and solar wind velocity (Munakata et al., 2000).

Muon data with FD effect were obtained not only from GMDN telescopes but also from other ones. For example, in Fig. 15 it is shown a local anisotropy associated with a large FD which started at around UT 0h on 27 July 2004 and observed with muon telescopes in Akeno and Ooty (GRAPES-3) with the median rigidity of 63.5 GV and 65.5 GV respectively (Nonaka et al., 2005a).

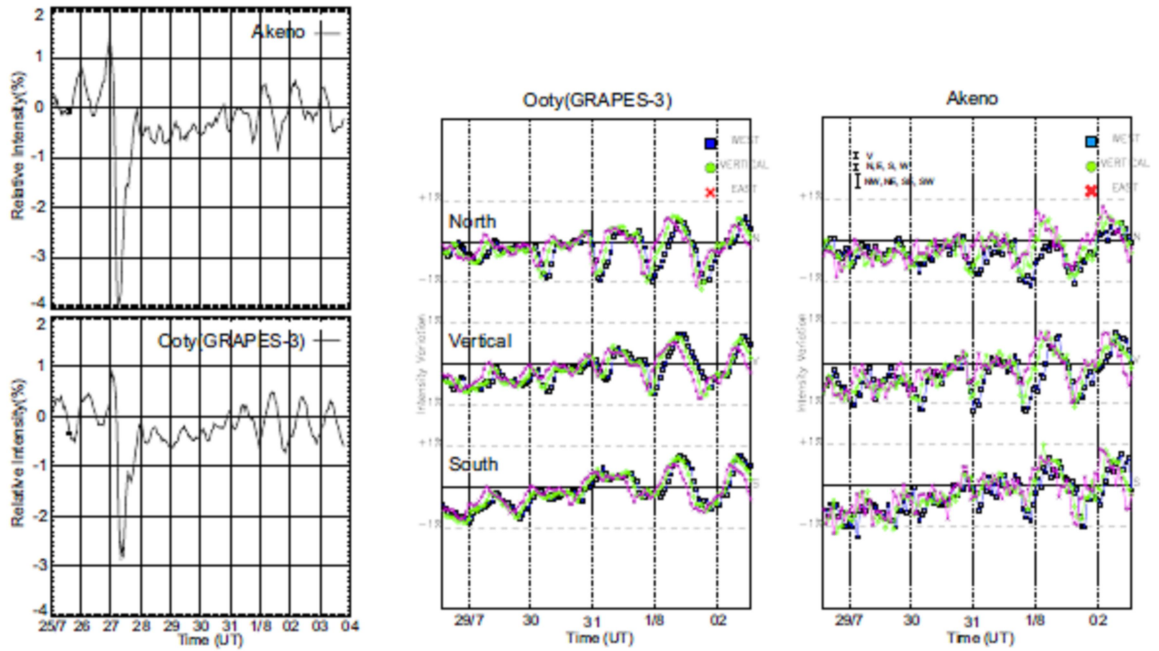


Fig. 15 Relative muon intensity (on left) and intensity variations (at centre and on right) during Forbush decrease on 27 July 2004 observed by muon telescopes in Akeno and Ooty (Nonaka et al., 2005a).

Munakata et al., [2000] and Nonaka et al., [2005b] discussed a correlation between LC-precursor depth and FD amplitude. Although the incidence of precursors increases with storm size, the correlations are far from perfect because the LC effect is determined not only by the FD amplitude but also other factors such as the upstream mean free path and the magnetic field angle at the shock. A trend found in Nonaka et al., [2005b] on the basis of analysis of storm events observed with GRAPES-3 during period 2001-2002 confirms these considerations in Fig. 16 where two categories of data associated with the start of the FD are shown.

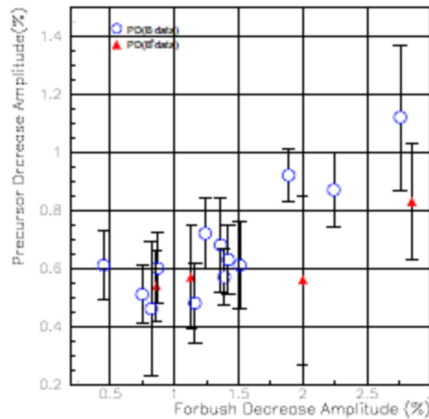


Fig. 16 A trend between LC-precursor depth and FD amplitude (Nonaka et al., 2005b).

## 5. CIR-driven storm precursors

Corotating Interaction Regions (CIRs) constitute an important set of large scale structures in the heliosphere observed in the declining and minimum phases of the solar activity cycle (Balogh et al., 1999). CIRs are associated with a co-existence of fast solar wind (typically ~800 km/s) and slow solar wind (around 400 km/s). When fast solar wind emitting from the coronal holes rams into a slower flowing wind ahead an interaction region is formed so that regions of fast and slow solar wind are separated by sharp boundaries (Fig. 17). If the structure is stable for several rotations the interaction region is repeatedly observed in space and for this reason called CIR (Heber et al., 1999). Thus CIRs are stream-interaction regions which are formed as a result of interaction of slow solar-wind streams with high-speed streams emanating from solar coronal holes and persistent over several solar rotations (Echer et al., 2011). CIR produce changes in CR particles observed at the earth surface prior to the transient arrival observed at the ACE location. A comparison between the properties of CME-driven storms and CIR-driven storms is summarized by Borovsky and Denton (2006). In particular, CIR-driven storms are of longer duration, have hotter plasmas and stronger spacecraft charging than CME-driven storms and while CME-driven storms pose more of a problem for Earth-based electrical systems CIR-driven storms pose more of a problem for space-based assets.

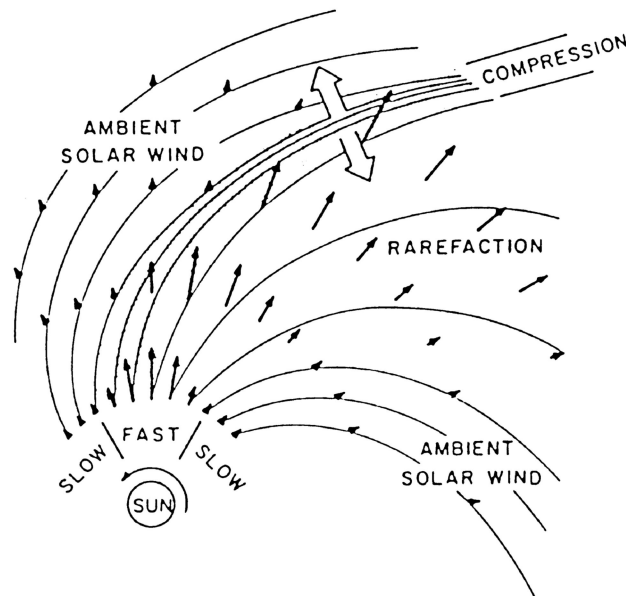


Fig. 17 Schematic illustration of CIR in the solar equatorial plane in the inner heliosphere (Pizzo, 1978).

Braga et al. (2010) studied CR precursors of small and moderate geomagnetic storms caused by CIR in a period of minimum solar activity from June 26, 2008 to December 31, 2008. The criteria for selecting events was the presence at least one SSC (rather than a criteria of maximum Kp index). They used hourly count rates for 60 directional channels of all the four

stations of the GMDN. The data were corrected for both the atmospheric pressure and temperature effects, the latter being based on the twice-a-day 100hPa altitude measurements. The difference between corrected and uncorrected data is 1% - 2%. Temperature effect correction in an hourly perspective is still an open question, although some progress in methodology has been made by Berkova et al. (2011) (see also Appendix 2). Also, Okazaki et al. (2008) developed an approach which is free from temperature effects.

For visualizing possible precursors, the pitch angle distributions of two quantities were used in Braga et al., [2010]. One of them is based on calculation of a deviation of muon count rate with respect to the mean value and called MPA; another one is associated with the time-derivative of muon deviations and called VPA. The panels of Fig. 18, from the top to the bottom, show the MPA and VPA distributions, the magnitude and z-component of IMF in GSM coordinates, the proton temperature, speed and density as well as the Dst index during the geomagnetic storm on July 12, 2008. Since the Dst index peak is between -50 nT and -30 nT, the geomagnetic storm is classified as small. A rapid increase in the proton density followed by rarefaction as well as an increase in proton temperature and speed followed by slow decreasing point to the presence of a CIR.

In the top two panels, a range with magnitude up to 3% and 30% is represented in yellow color for MPA and VPA distributions respectively. The increases and decreases with larger amplitude are represented, respectively, in blue and red colors. The white rectangles are 10°-pitch angle ranges that relate to the absence of data and satisfy one of the following conditions:

- they do not have coverage in a given hour;
- they have gap on muon data in a given station;
- they have gaps on IMF data so that it is impossible to calculate the pitch angle for any directional channel of the GMDN.

Both MPA and VPA satisfy the criterion for classification of precursors of geomagnetic storms. As VPA is the approximate derivative of the deviations, negative values mean an inflection in the deviation curve. This could be due to CR particles deflected in their path in the interplanetary medium because of a positive gradient of magnetic field related to an interplanetary transient which was observed after the SSC with a maximum of more than 10 nT. As CR particles have almost the speed of light and the CIR has speed of hundreds of km/s, CR particles are observed at the earth surface prior to the transient arrival observation at the Lagrangian point, where satellite ACE is located. MPA shows also a signature between days 8 and 9, i.e. 3 days in advance the SSC.

The results of some events analyzed in Braga et al., [2010] are summarized in Table 4. The last event that occurred on November 24, 2008 is of special interest. Muon data and IMF together with plasma data, similar to Fig. 18, are shown in Fig. 19. One can see that although the Dst index being positive does not indicate any geomagnetic storm, a clear transient in IP medium is observed, and magnetic field and the proton speed have sudden increases in magnitude. The fact is that although the ejecta was not detected because it was not directed towards the Earth, the associated IP shock having a greater longitudinal extent was. More



than 24 hours in advance of the shock detection a possible precursor can be seen in MPA. After the shock MPA show systematic decreases that are Forbush decreases. Braga et al. (2010) showed that possible precursors were seen in 4 of the 7 events registered in the selected period from June 26, 2008 to December 31, 2008. Some systematic increases or decreases in the daily period before the SSC were observed with intensity higher than 3% (30%) for VPA (MPA). However, some false precursors were also present in the analysis. The MPA methodology showed precursors more frequently than the VPA methodology. Possible precursors can be associated both to CIR and IP shocks. Since the more intense the geomagnetic storms, the higher the chance of visualization of precursors one can expect more intense geomagnetic activity and/or transient with higher magnetic field to be detected by the GMDN during the next solar maximum.

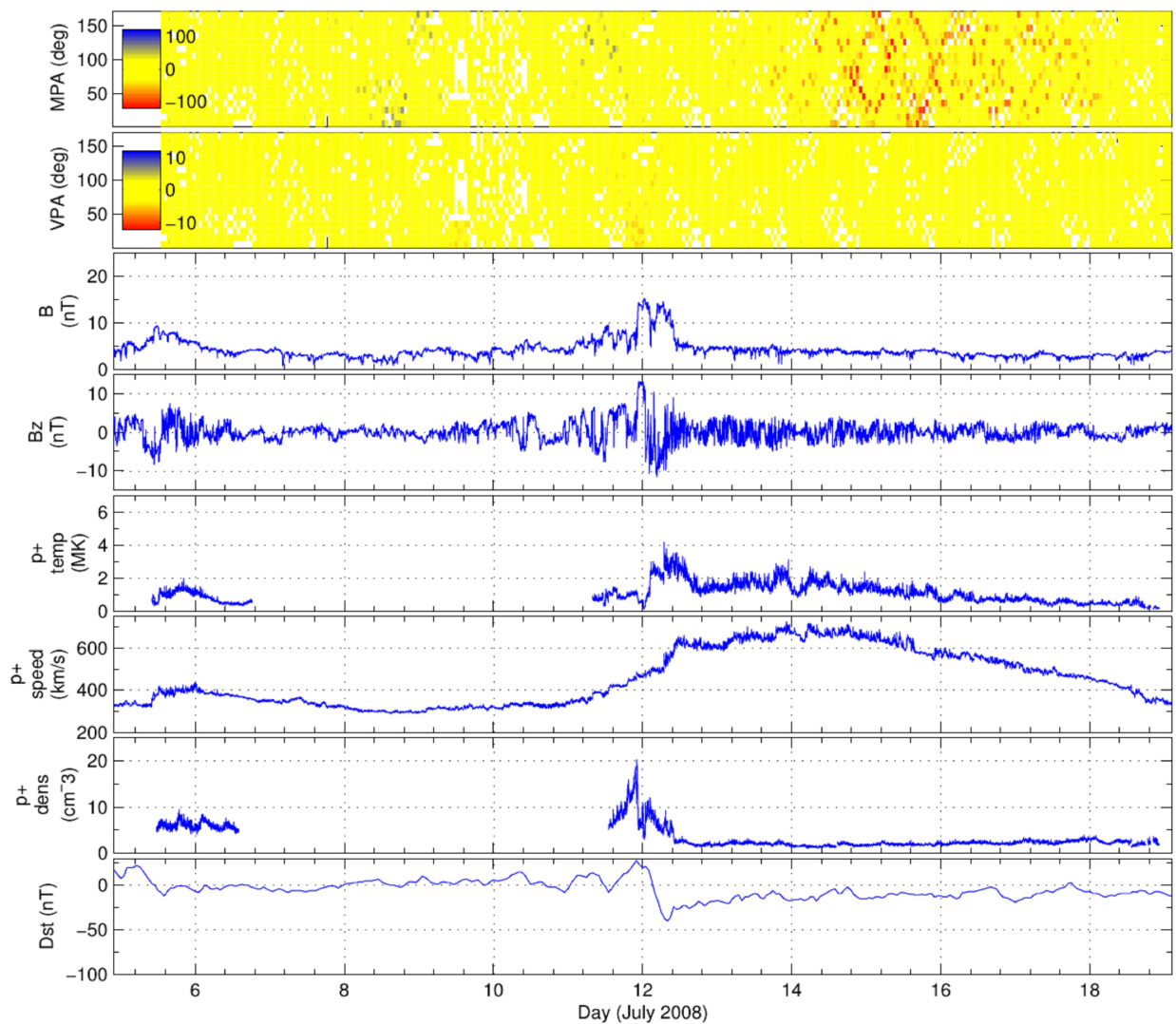


Fig. 18 Muon data and IMF during small a geomagnetic storm on July 12, 2008 (Braga et al., 2010).

Table 4. Summary of events analyzed in (Braga et al., 2010).

#	Date	Time	Kp peak	Precursor	Transient
1	2008/07/12	00:38	4+	MPA, MPA	CIR
2	2008/08/08	23:44	5+	MPA	CIR
3	2008/09/03	06:40 15:42	6	none	CIR
4	2008/09/14	19:13	4-	Data not clear	CIR
5	2008/11/07	03:53	4+	MPA, VPA	CIR
6	2008/11/15	16:25	4-	Data not clear	CIR
7	2008/11/24	23:51	4-	MPA	SHOCK

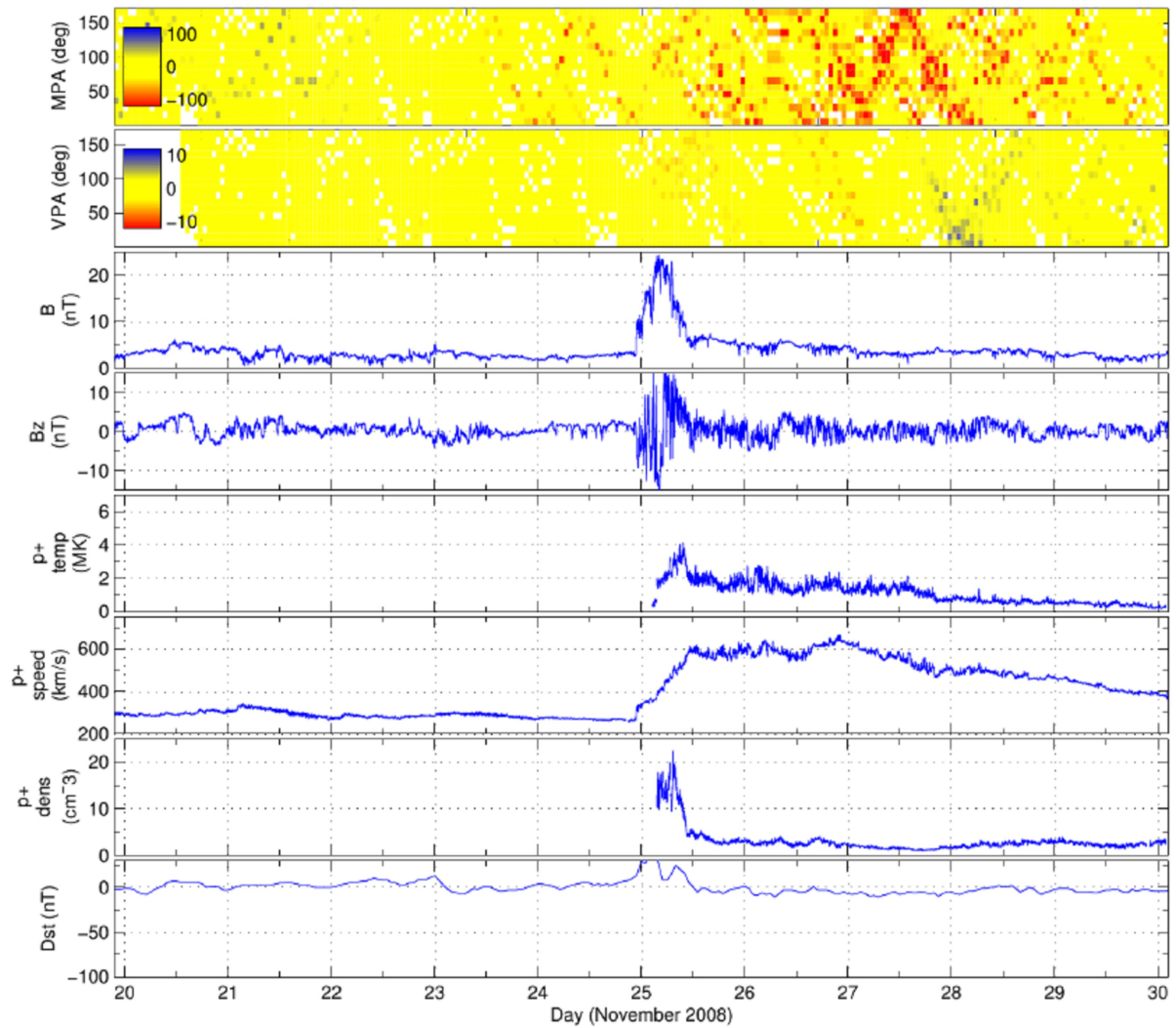


Fig. 19 Muon data and IMF during a geomagnetic storm on November 24, 2008 (Braga et al., 2010).

## 6. Asymptotic directions and global coverage by GMDN

The CR particles approaching the Earth encounter the geomagnetic field and are deflected by it so that the highest energy of particles experience the least amount of deflection in the geomagnetic field. Therefore, if the particles are sufficiently energetic, they can propagate inside the magnetosphere and enter the Earth's atmosphere. In principle it should be possible to trace the path of such a particle until it reaches the ground as long as we have a sufficiently accurate mathematical description of the field. Such an approach would require particles from all space directions to be traced to the ground to determine the response. It is more practical to trace particles of opposite charge but with the same rigidity (which is momentum per unit charge) from the location of the detector station through the field to free space because they will follow the same path as particles arriving from the Sun (Dulig, 2001). When calculated in this way it is found that for a given rigidity there may be some trajectories that remain forever within the geomagnetic field or intersect the Earth's surface. These trajectories are termed "forbidden" as they indicate that the site is not accessible from space for that rigidity and arrival direction at the station. The particle trajectories that escape to free space are called "allowed" and associated with the accessible directions which are known as asymptotic directions of approach (McCracken et al., 1962, 1968; Shea et al., 1965; Smart et al., 2000). The set of accessible directions, dependent on rigidity, defines the asymptotic cone of view (or the asymptotic cone of acceptance) for a given station. On the other hand, for a given arrival direction at the station there is a minimum rigidity below which particles cannot gain access. This is termed the geomagnetic cutoff for that direction at that location and time (Dulig, 2001). Above the minimum cutoff rigidity for a given arrival direction there may be a series of accessible and inaccessible rigidity windows known as the penumbral region (Cooke et al. 1991). The penumbral region ends at the rigidity above which all particles gain access for that arrival direction. It is worth noting that cutoff rigidity of CRs being dependent on geomagnetic field decreases with increasing geomagnetic disturbance level (Danilova et al., 1999).

A conceptual illustration of an asymptotic cone of acceptance is presented in Fig. 20 (Shea & Smart, 1982). The tracing of the allowed CR particles trajectories from the station through the Earth's magnetic field to IP space results in a family of trajectories that define an asymptotic cone of acceptance. The increased geomagnetic bending that lower rigidity particles undergo is illustrated by increased bending of the trajectories curving to the right. The direction of the trajectory at a distant surface, such as the magnetopause boundary, is the asymptotic direction of approach. The locus of points formed by the individual trajectory asymptotic directions depicted by the dotted line is used to illustrate the asymptotic cone acceptance (Shea & Smart, 1982). As the Earth rotates, CR incident on a given location must pass through different regions of the magnetosphere. Therefore the asymptotic directions are functions of the time of day (Bieber et al., 1992). For the same reason the cutoff rigidity also depends on the local time. As an example, Fig. 21 shows the daily variation of proton cutoff rigidities along the 260°E meridian (Smart et al., 1969).

Thus the asymptotic direction of a CR particle represents its direction of motion before entering into the magnetosphere. In particular, the asymptotic directions of the CR particles can be considered as the particle coordinates on the sphere with a large enough radius where

the geomagnetic field effects on the trajectory become negligible, for example, 25 earth radii (Danilova et al., 1999) or 30 earth radii (Lin et al., 1993). They are computed by means of numerical back-tracing of the particle trajectories in the geomagnetic field which is usually represented as a sum of magnetic fields from internal and external sources (Danilova et al., 1999; Bieber et al., 1992; Smart et al., 1969). The magnetic field of internal sources is described by International Geomagnetic Reference Field (IGRF) models and represents the main geomagnetic field and its secular variation through a spherical harmonics expansion of the scalar potential in the geocentric coordinates. The magnetic field of external sources is represented by the models developed by Tsyganenko (see N.A. Tsyganenko's site) which take into account the main magnetospheric current systems such as ring currents, magnetopause currents and the magnetosphere tail currents (Danilova et al., 1999). We note that at mid-latitudes and near the polar cap boundary both IGRF and Tsyganenko's methods may not be very accurate during geomagnetic storms and a global magnetohydrodynamic simulation of the Earth's magnetosphere should be employed (Weygand & Raeder, 2005). Also, Smart and Shea (1981) found that for precise calculations of trajectories involving exact locations on the earth the initial directions must be specified in geodetic coordinates rather than in geocentric coordinates which, however, should be used for spacecraft (Smart and Shea, 1997).

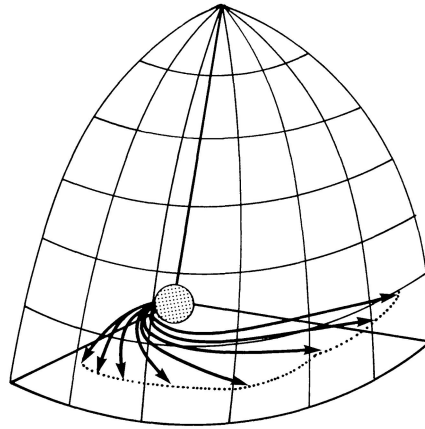


Fig. 20 Conceptual illustration of an asymptotic cone of acceptance (Shea & Smart, 1982).

Usually the asymptotic directions are calculated under some assumptions listed in Lin et al., [1995]. In particular, in integrating a motion equation for a given model of magnetic field (e.g. an IGRF model) the time step size is adaptively chosen so that to make the field variation along the particle trajectory to be a small fraction of the total field. Then the motion of a particle within such a time step is considered as the helical motion of the same particle in a uniform magnetic field. In addition, effects of electric fields are neglected. For instance, if the total potential drop across the magnetosphere is 200 kV then the average electric field is  $\sim 1$  mV/m at 10 earth radii. If the magnetic field at the same location is  $\sim 20$  nT then the ratio of electric to magnetic forces acting on a relativistic particle is  $\sim 2 \times 10^{-4}$ . However, such electric forces may be potentially important because systematic changes in even a small electric field that originally appears second order might well provide a small perturbation to convert some forbidden trajectories to allowed ones.

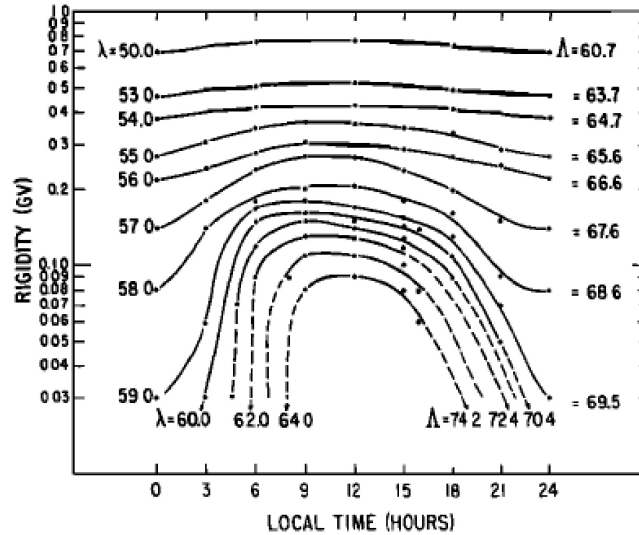


Fig. 21 The daily variation of proton cutoff rigidities along the  $260^\circ$  E meridian. The data points represent the calculated values and the dashed lines indicate extrapolated values.  $\lambda$  indicates the geographic latitude along the  $260^\circ$  E meridian and  $\Lambda$  denotes the invariant latitude (Smart et al., 1969).

For polar or even mid-latitude muon detectors that only respond to high-energy particles, the asymptotic cones of acceptance are restricted to specific regions of the celestial sphere. Thus if multiple stations simultaneously observe an anisotropic solar CR flux, it is possible to deconvolve the flux direction in space and the anisotropy (Cramp *et al.*, 1995). If these stations are located at different geomagnetic cutoffs, it is possible to deduce the solar particle spectra (Smart & Shea, 2000). Similarly, if a number of CR stations, each having asymptotic cones of acceptance viewing a different portion of the celestial sphere, rotate through a slowly evolving CR anisotropy, then it is possible to deconvolve the spatial anisotropy as in Nagashima et al., [1994].

When the directions of approach in IP space beyond the magnetopause are mapped on a projection of extended geocentric coordinates, the set of accessible directions in space for each CR particle detectable at a specific location is uniquely defined in terms of geocentric coordinates. For conceptual purposes these asymptotic directions of approach are plotted on an extended Earth projection in order to help visualize the spatial region of cosmic-ray anisotropy with respect to the geocentric coordinate system (Shea & Smart, 1982). Figure 22 shows the world map projection of the asymptotic directions of approach computed for the GMDN stations at the median rigidity while figures 23 and 24 show the same projection with addition of the proposed Canadian muon detector in Ottawa and Vancouver respectively (Appendix 3). The calculations are performed for each telescope of  $5\text{m} \times 5\text{m}$  proportional counter array with  $11 \times 11 = 121$  directions using the muon response function derived by Murakami et al. (1979). The values for cut-off rigidity are 1.7 GV and 2.6 GV for Ottawa and Vancouver respectively, the median rigidity is 52.4 GV and 52.5 GV in the same order (Appendix 3). In addition, Fig. 25 shows asymptotic directions for a suggested station in Inuvik, Canada.

Muon Detector Network

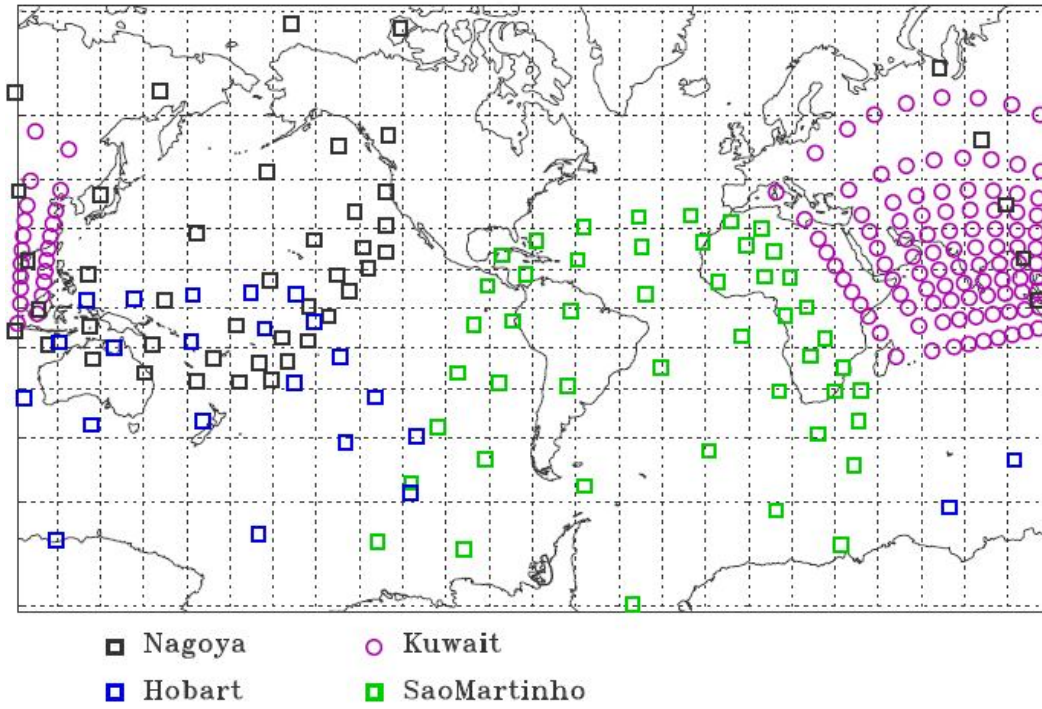


Fig. 22 Current sky coverage by GMDN (Appendix 3).

Muon Detector Network

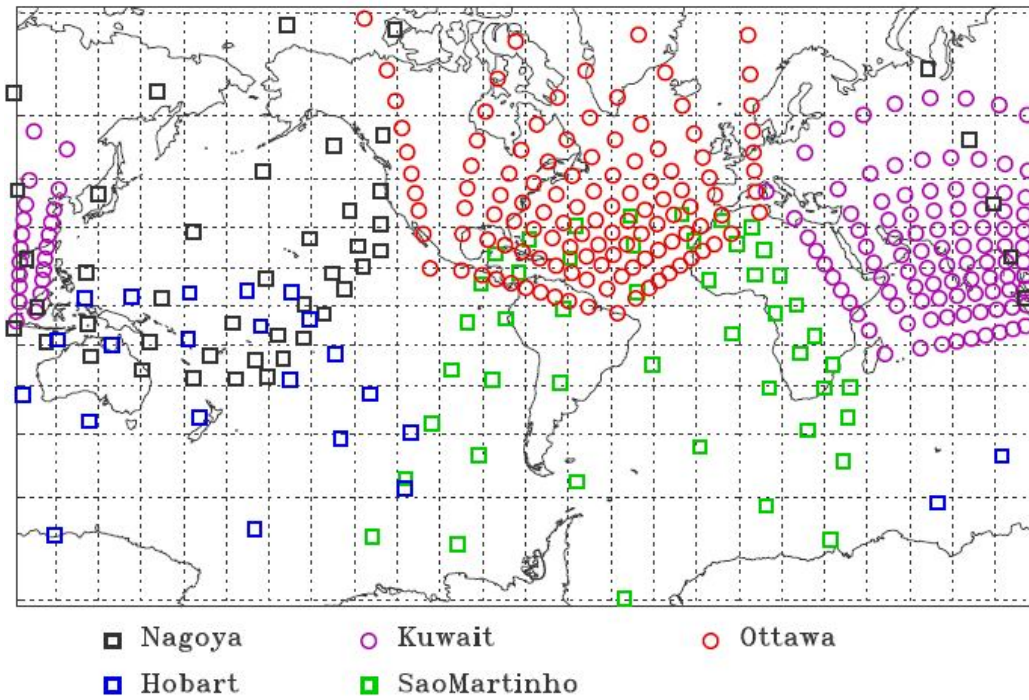


Fig. 23 GMDN sky coverage extended by adding a proposed detector in Ottawa (Appendix 3).

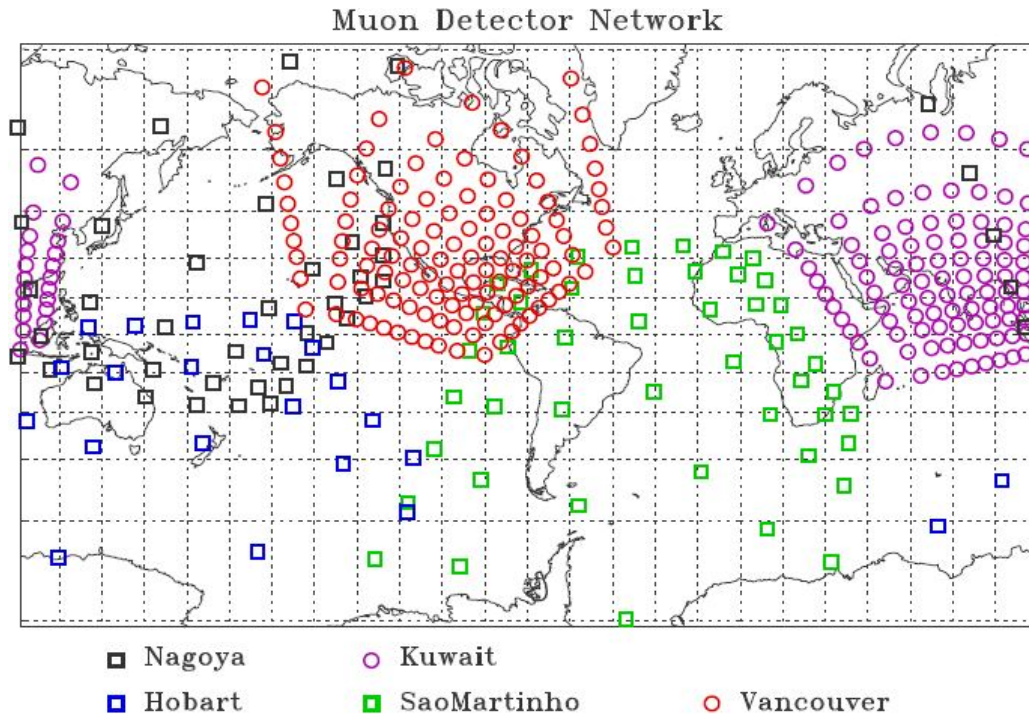


Fig. 24 GMDN sky coverage extended by adding a proposed detector in Vancouver (Appendix 3).

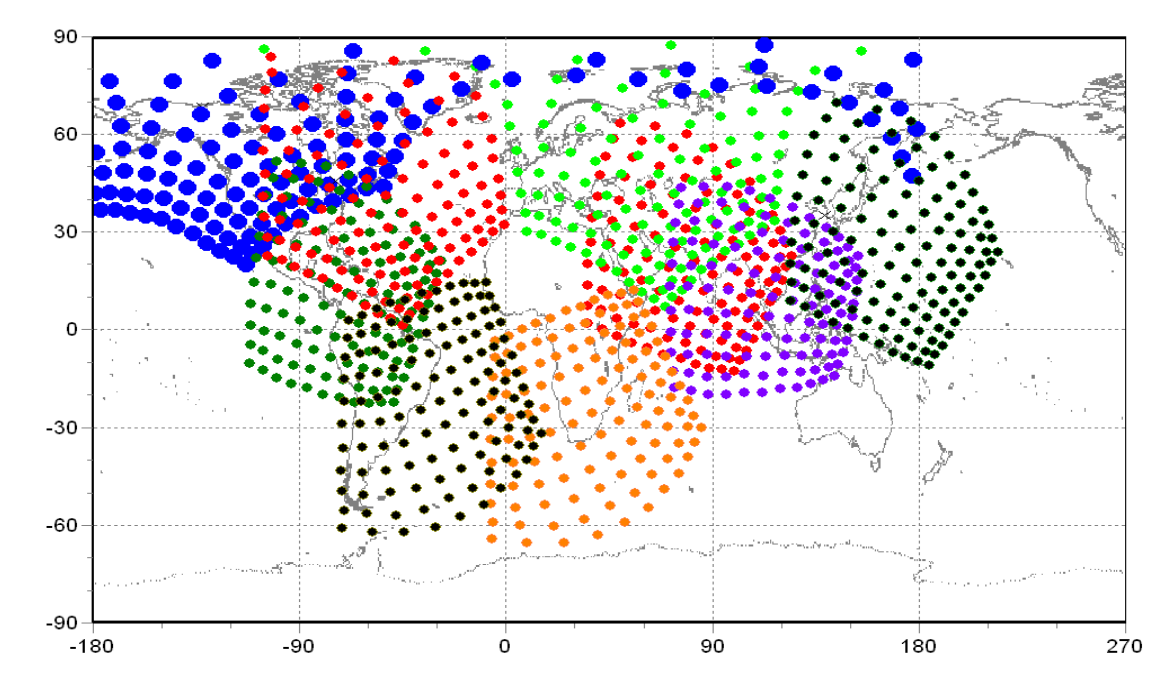


Fig. 25 Maps of asymptotic directions with stations in Inuvik (big blue circles) and Ottawa (red circles overlapped with blue ones) (Appendix 1).

One can see that in Fig. 22, the region above North America and Atlantic are not covered but in figures 23 and 24 a presence of a muon detector in Ottawa and/or Vancouver would apparently eliminate the deficiency of GMDN. A station in Inuvik would be also interesting because Inuvik has a very rare (unique) distribution of the asymptotic directions, especially in polar zone (Appendix 1). The overlapped areas in the figures can be used to provide more accurate data in the network. The viewing directions for some neutron stations are given in Appendix 4.

We emphasize that filling the mentioned gap by the presence of a proposed muon telescope in Ottawa would be of great importance as the interpretation of most cosmic ray modulation phenomena requires good latitude coverage. Today a team in Carleton University is developing muon detector FOREWARN described in Section 7 and Appendices 5-7.

The GMDN is planning to be developed further not only to provide full sky coverage but also for the following reason. High angular resolution systems will play a significant role in advancing our understanding of transient phenomena. In particular, they may help unravel the detailed structure of LC anisotropy (Duldig, 2000). Therefore large area narrow-angle telescope systems within GMDN could be important in such studies. Appendix 8 describes a future Canadian muon telescope with a large detection area proposed by Dr. John Armitage.

## **7. Real-time cosmic ray monitoring system for space weather**

Today there exists an informal tight collaboration between different teams working at muon stations all over the world, which we conditionally call International Muon Detector Network. The network is constantly being developed, extending and including different organizations and institutes from different countries, namely, Japan, Brazil, USA, Australia, Kuwait, Armenia, Germany (Schuch, 2006). In Germany, particularly, the MuSTAnG space weather muon telescope is currently being developed in The University of Greifswald to contribute to the development of European space weather technologies and services (Jansen et al., 2001; Jansen & Behrens, 2008).

An extension of the International Muon Detector Network and recent achievements in data analysis have allowed the development of a real-time monitoring system of high-energy CRs for space weather using muon detectors located all over the world. A LC display and bidirectional streaming display show the pitch angle distribution of the CR intensity variation. They can detect the precursor anisotropy prior to the arrival of the ICME and particle bidirectional streaming inside the ICME. See Fig. 26 with details explained in the figure caption.

The first-order anisotropy analysis shows the particle flow direction and its magnitude. Individual station count rates tell us the time and scale of the Forbush decrease and ground-level-enhancement event at a single location. These displays are made by real time data processing and are updated to a World Wide Web server. It provides a new tool for space weather forecasting and for specifying conditions in the near-Earth space environment. This tool will become even more useful and reliable in the future, as more stations of the



worldwide muon detector network together with neutron monitor network become available in real time (Kuwabara et al., 2006).

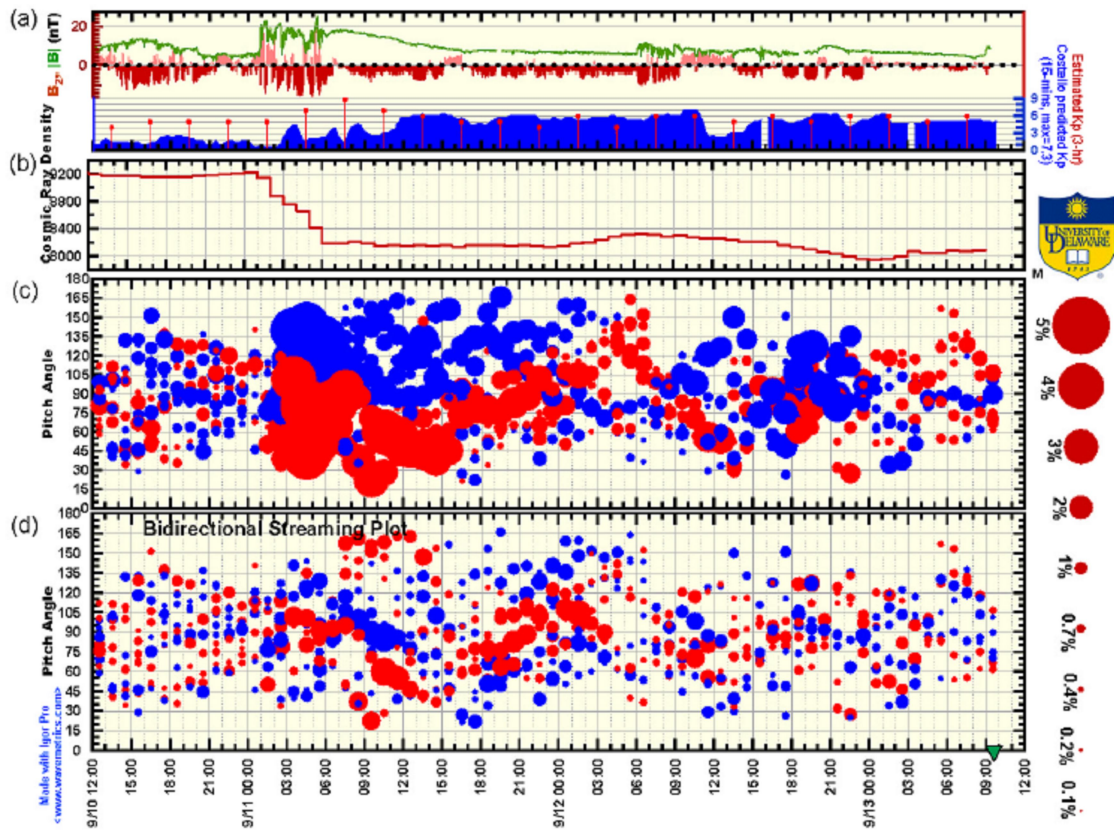


Fig. 26 Sample LC display and bidirectional streaming display in September 2005. (a) Plotted are 1-min ACE magnetic field magnitude  $|B|$  (green) and north-south component  $B_z$  (north, pink; south, red) in GSE coordinates. Also plotted are 3-hour estimated Kp index (red) and the 15-min predicted Costello Kp index (blue). (b) CR density. (c) CR intensity (circles) measured by a single Spaceship Earth station relative to the CR density. Red and blue circles indicate the deficit and excess intensity, respectively, and the radius of the circle scales with the magnitude of the deficit or excess; see right side of plot for scale. (d) Residual deviation after subtracting the fitted first-order anisotropy from each station. Red and blue circles represent deficit and excess relative to first-order anisotropy. In Figures 5c and 5d, vertical axes indicate the pitch angle (Kuwabara et al., 2006).

## 8. Muon detector at Carleton University

A practical (experimental) part of the project relates to a muon detector FOREWARN in Carleton University built by Dr. John Armitage and Dr. Khalil Boudjemline (Physics Department) and described in Appendices 5-7. In Appendix 8 a future Canadian muon telescope with a large detection area of  $25 \text{ m}^2$  proposed by Dr. John Armitage is described.

Operating FOREWARN will allow us to understand whether the muon tracking system would be sufficient to provide early space weather warning. The answer to this question is positive based on the results of the following activities:

- Discussions with world-class experts in Canadian Muon Workshop in St-Émile-de-Suffolk, Québec, Canada, 17-19 October 2011; some presentations from there are collected in Appendices;
- Study of results obtained in using the Global Muon Detector Network (Appendix 3);
- Simulations of the muon detector in Carleton University (Appendices 5-7).

Specifically, the muon detector in Carleton University was simulated using software package GEAN4. In Fig. 2 in Appendix 6 are shown muon trajectories (by red curves in the top panel). Muons interact with different materials of the multi-layer detector but most of them are able to traverse the whole system. Thus, the tracking system allows us to measure the muon intensity and then use the obtained data to look for precursors for geomagnetic storms.

Today a small scale muon telescope has been built at Carleton and it is currently collecting data. To take into account the effect of the atmospheric pressure on the muon count rate a linear regression method is used as follows (Dorman, 1972):

$$I_c = I - \bar{I} \beta_p (P - \bar{P}) , \quad (1)$$

where  $I$ ,  $I_c$  and  $\bar{I}$  are measured, corrected and average muon counts respectively,  $P$  is the atmospheric pressure,  $\bar{P}$  is an average atmospheric pressure (taken as 1000.0 hPa),  $\beta_p$  is the pressure coefficient in %/hPa. Each correction is usually performed separately for a given directional channel. Due to the effect of the absorption in the atmosphere, the pressure coefficient is negative indicating an anti-correlation between observed flux and the atmospheric pressure (Famoso et al., 2005). The pressure coefficient  $\beta_p$  is obtained using the correlation factor  $CF$  from formula

$$\bar{I} \cdot \beta_p = CF \cdot \sigma_I / \sigma_P ,$$

where

$$CF = \frac{\frac{1}{N} \cdot \sum_{i=1}^N (I_i - \bar{I})(P_i - \bar{P})}{\sigma_I \sigma_P} , \quad \sigma_I = \sqrt{\frac{1}{N} \sum_{i=1}^N (I_i - \bar{I})^2} , \quad \sigma_P = \sqrt{\frac{1}{N} \sum_{i=1}^N (P_i - \bar{P})^2} ,$$

$I_i$  and  $P_i$  are measured muon count and atmospheric pressure for a time bin  $i$ . The temperature correction could be made by a formula similar to (1) where the pressure coefficient  $\beta_p$  should be replaced by the temperature coefficient  $\beta_T$  and the pressure variation  $(P - \bar{P})$  by the deviation of the altitude of 100 hPa to its annual average (Blackett,

1938; Okazaki et al., 2008; Braga et al., 2010). However, this approach has not been used because of the absence of information; instead the surface temperature is used for comparison.

Some results on pressure and temperature correction are presented on slides 9-13 in Appendix 7. Specifically, slide 9 shows a comparison between the muon count rate, pressure and temperature where the atmospheric parameters have been taken at the airport, few kilometers from Carleton University. A different way to do a comparison is to plot  $100 \cdot \text{Log}(X / X_0)$  as shown in slide 10, with  $X$  as the count rate, pressure or temperature per time bin and  $X_0$  as the mean value. It follows from both plots that the count rate is anti-correlated to the pressure and correlated to the temperature. Slide 11 shows the correlation before and after correction. It is found that pressure has more effect on the count rate than temperature, and for this data set, particularly, the coefficient factor for pressure changes from -0.85 to -0.02. Slide 12 shows the raw count rate and the corrected one by the pressure and temperature. The remaining effect on the count rate from the pressure and temperature is shown on slide 13. We also note that a muon detector system similar to the current version of FOREWARN was studied and tested by Ankney et al. (2010).

## 9. Conclusions

Coronal mass ejections and associated IP shocks, where IMF and solar wind velocity experience a sharp increase, are typically accompanied by strong enhancements of the CR anisotropy. Such anisotropies represent a key mechanism by which information about the presence of a disturbance can be transmitted to remote locations, including upstream of the shock. Since CRs are fast and have large scattering mean free paths ( $\sim 1$  AU) in the solar wind, this information travels rapidly and may prove useful for space weather forecasting (Ruffolo et al., 1999). Muons being high energy particles and easy to be detected with high accuracy and low noise are more preferable than other particles to provide space weather forecast.

The International Muon Detector Network is constantly extending so that today it allows us to perform a real-time monitoring system of high-energy CRs for space weather forecasting. Energetic CR intensities observed with ground-level muon detectors are subject to modulation effects due to IP disturbances, particularly, associated with ICMEs which are capable to cause geomagnetic storms. Such changes in CR intensity can be interpreted as precursory anisotropy and may result in LC effect. An analysis of LC precursors during different events shows that muon observations can be quite useful for space weather forecasting. Although the lead time of observed precursors relative to the SSC is typically about 10 hours, this can be significantly improved by providing full-sky coverage. For example, an analysis of muon data for one of the storms shows a possibility of observing LC precursor 25 hours in advance the SSC. Moreover, the Global Muon Detector Network provides us with a new tool for investigation of CR transport in the IMF and can be used to observe not only CME-driven storms but also CIR-driven storms which are less intensive and therefore more difficult to be detected than the former but, being the main source of problems for space-based assets, remain important to be studied.

Based on the above analysis of the state-of-the-art of using muon detectors for extreme space weather forecasting and progress made in this research area one can make the following main conclusions.

1. Today there have been developed a methodology to use muon detectors for space weather forecasting. These methods should be further developed for operational use and Canadian researchers could contribute to solving this global problem of high importance.
2. The muon detector in Carleton University, in principle, enables monitoring the muon flux for warning of extreme space weather conditions.
3. To make accurate analysis of muon data one needs to provide full sky coverage which can be done by adding in a muon detector located in Ottawa and participating in the International Muon Detector Network including the GMDN.

Thus a development of experimental techniques for ground-based measurements of cosmic-ray-produced muons and methods for analysis of muon data could allow us to use muon observations in combination with other tools for space weather forecasting in order to obtain timely warning of extreme space weather conditions and improve the protection of Canadian critical infrastructure from large solar disturbances.

**Acknowledgments.** We would like to express our gratitude to David Boteler and Hing-Lan Lam for review of the text. We also thank the authors of presentations given in the Canadian muon workshop on October 17-19, 2011 (St-Émile-de-Suffolk, Québec, Canada) and included in the section ‘Appendices’.

## References

- A.S. Ankney, T.J. Berguson, J.D. Borgardt, and R.T. Kouzes (2010) *Muon Fluence Measurements for Homeland Security Applications*, Report PNNL- 19632, Pacific Northwest National Laboratory, US Department of Energy, 29 pp.
- A. Asipenka, A. Belov, E. Eroshenko, H. Mavromichalaki, M. Papailiou, A. Papaioannou, V. Oleneva, and V. Yanke (2009) *Asymptotic longitudinal distribution of cosmic ray variations in real time as the method of interplanetary space diagnostic*, Proceedings of the 31st ICRC, Lodz, 4 pp.
- A. Balogh, V. Bothmer, N.U. Crooker, R.J. Forsyth, G. Gloeckler, A. Hewish, M. Hilchenbach, R. Kallenbach, B. Klecker, J.A. Linker, E. Lucek, G. Mann, E. Marsch, A. Posner, I.G. Richardson, J.M. Schmidt, M. Scholer, Y.M. Wang, R.F. Wimmer-Schweingruber, M.R. Aellig, P. Bochsler, S. Hefti, and Z. Mikic (1999) *The solar origin of corotating interaction regions and their formation in the inner heliosphere*, Report of Working Group 1, Space Sci. Rev., 89, pp.141-178.
- A.V. Belov, J.W. Bieber, E.A. Eroshenko, P. Evenson, R. Pyle, and V. Yanke (2001) *Pitch-angle features in cosmic rays in advance of severe magnetic storms: Neutron monitor observations*, Proc. 27th Int. Cosmic-Ray Conf., Hamburg, Germany, Vol. 9, pp. 3507–3510.
- M.D. Berkova, A.V. Belov, E.A. Eroshenko, and V.G. Yanke (2011) *Temperature Effect of the Muon Component and Practical Questions for Considering It in Real Time*, Bulletin of the Russian Academy of Sciences. Physics, 2011, Vol. 75, No. 6, pp. 820–824.
- J.W. Bieber, P. Evenson, and Z. M. Lin (1992) *Cosmic ray trajectories in the Tsyganenko magnetosphere*, Antarctic Journal, 27, No. 5 (1992 Review), pp. 318-319.
- J.W. Bieber and P. Evenson (1998) *CME Geometry in Relation to Cosmic Ray Anisotropy*, Geophys. Res. Lett., Vol. 25, No. 15, pp. 2955-2958.
- P.M.S. Blackett (1938) *On the Instability of the Barytron and the Temperature Effect of Cosmic Rays*, Phys. Rev. (Letters to the editor), 54, pp. 973-974.
- J. E. Borovsky and M. H. Denton (2006) *Differences between CME-driven storms and CIR-driven storms*, J. Geoph. Res., Vol. 111, A07S08, doi:10.1029/2005JA011447, 17 pp.
- C.R. Braga, A.D. Lago, W.D. Gonzalez, N.J. Schuch, M.R. Silva, T. Kuwabara, J.W. Bieber, P.A. Evenson, K. Munakata, C. Kato, M. Tokumaru, M.L. Duldig, J. Humble, I.S. Sabbah, H.K.Al Jassar, and M.M. Sharma (2010) *Cosmic ray modulation associated to small and moderate geomagnetic storms during minimum solar activity*, Proceedings of Science, 4th School on Cosmic Rays and Astrophysics, Aug 25 - Sep 4, 2010, São Paulo, Brazil, 14 pp.

D.J. Cooke, J.E. Humble, M.A. Shea, D.F. Smart, N. Lund, I.L. Rasmussen, B.P. Byrnak, P. Goret, and N. Petrou (1991) *On Cosmic-Ray Cutoff Terminology*, *Il Nuovo Cimento*, 14C, pp. 213-234.

J.L. Cramp, M.L. Duldig, and J.E. Humble (1995) *Neutron Monitor Response to Highly Anisotropic Ground Level Enhancements*, *Proc. 24th Int. Cosmic Ray Conf.*, 4, pp. 248-251.

O. Danilova, M. Tyasto, H. Kananen, and P. Tanskanen (1999) *The Cosmic Ray Asymptotic Directions for Station Oulu in the Magnetic Field of the Tsyganenko 1989 Model*, *Geophysica*, 35(1-2), pp. 101-109.

L.I. Dorman (1972) *The meteorological effects of cosmic rays*, 'Nauka' Press, Moscow (English translation in Series NASA TTF-755, Washington, DC, 1973).

M.L. Duldig (2000) *Muon observations*, *Space Science Reviews*, Vol. 93, No.1-2, pp. 207-226.

M.L. Duldig (2001) *Australian Cosmic Ray Modulation Research*, *Publications of The Astronomical Society of Australia*, 18, pp.12-40 (DOI: 10.1071/AS01003, arXiv:astro-ph/0010147v1).

E. Echer, B.T. Tsurutani, W.D. Gonzalez, and J.U. Kozyra (2011) *High Speed Stream Properties and Related Geomagnetic Activity During the Whole Heliosphere Interval (WHI): 20 March to 16 April 2008*, *Sol. Phys.*, doi: 10.1007/s11207-011-9739-0.

B. Famoso, P. Rocca, and F. Riggi (2005) *An educational study of the barometric effect of cosmic rays with a Geiger counter*, *Physics Education* 40(5), pp.461-467.

K. Fujimoto, A. Okada, T. Aoki, Y. Ohashi, K. Mitsui, H. Kojima, K. Munakata, S. Yasue, C. Kato, T. Kuwabara, M. Mori, and K. Takizawa (2003) *Observation of precursory decrease by the narrow angle muon telescope at MT. Norikura*, *Proc.28th Int. Cosmic Ray Conf.*, July 31- August 7, 2003, Tsukuba, Japan, v6, pp. 3565-3568.

A. Fushishita, T. Kuwabara, C. Kato, S. Yasue, J.W. Bieber, P. Evenson, M.R. Da Silva, A. Dal Lago, N.J. Schuch, M. Tokumaru, M.L. Duldig, J.E. Humble, I. Sabbah, H.K. Al Jassar, M.M. Sharma, and K. Munakata (2010) *Precursors of the Forbush decrease on 2006 December 14 observed with the global muon detector network (GMDN)*, *The Astrophysical Journal*, 715, pp. 1239–1247, doi:10.1088/0004-637X/715/2/1239.

W.D. Gonzalez, J.A. Joselyn, Y. Kamide, H.W. Kroehl, G. Rostoker, B.T. Tsurutani, and V.M. Vasyliunas (1994) *What is a magnetic storm?*, *J. Geophys. Res.*, V. 99, No. A4, pp. 5771-5792.

W.D. Gonzalez, B.T. Tsurutani, and A.L.C. Gonzalez (1999) *Interplanetary origin of geomagnetic storms*, *Space Science Review*, 88, pp. 529–562.

B. Heber, T.R. Sanderson, and M. Zhang (1999) *Corotating Interaction Regions*, Adv. in Spac. Res., 23(3), pp. 567-579.

J.E. Humble, M.A. Shea, and D.F. Smart (1985) *Sensitivity of cosmic ray trajectory calculations to geomagnetic field model representations*, Phys. Earth Planet. Inter., 37, pp. 12-19.

J.A. Hutchinson, D.M. Wright, S.E. Milan, and A. Grocott (2011) *A superposed epoch analysis of geomagnetic storms over a solar cycle*, 42nd Lunar and Planetary Science Conference, March 7–11, 2011, Woodlands, Texas, LPI Contribution No. 1608, 2051pdf.

F. Jansen and J. Behrens (2008) *Cosmic rays and space situational awareness in Europe*, IEEE Transactions on Magnetics, 21st European Cosmic Ray Symposium, Košice, Slovakia, 9-12 September 2008, <http://ecrs2008.saske.sk/dvd/s9.07.pdf>, 6 pp.

F. Jansen, K. Munakata, M.L. Duldig, and R. Hippler (2001) *Muon Detectors – the real-time, ground based forecast of geomagnetic storms in Europe*, ESA Space Weather Workshop: Looking towards a European Space Weather Programme, 2001, ESA WPP-144, 6 pp.

J.R. Jokipii (1966) *Cosmic-Ray Propagation. I. Charged Particles in a Random Magnetic Field*, Astrophysical Journal, Vol. 146, pp. 480-487.

K. Kudela, K.A. Firoz, R. Langer, and V. Kollár (2008) *On diurnal variation of cosmic rays: statistical study of neutron monitor data including Lomnický Štít*, Proc. 21st European Cosmic Ray Symposium, pp. 374 – 378.

T. Kuwabara, K. Munakata, S. Yasue, C. Kato, S. Akahane, M. Koyama, J.W. Bieber, P. Evenson, R. Pyle, Z. Fujii, M. Tokumaru, M. Kojima, K. Marubashi, M.L. Duldig, J.E. Humble, M.R. Silva, N.B. Trivedi, W.D. Gonzalez, and N.J. Schuch (2004) *Geometry of an interplanetary CME on October 29, 2003 deduced from cosmic rays*, Geophysical Research Letters 31 (19) L19803, 5 pp.

T. Kuwabara, J.W. Bieber, J. Clem, P. Evenson, R. Pyle, K. Munakata, S. Yasue, C. Kato, S. Akahane, M. Koyama, Z. Fujii, M.L. Duldig, J.E. Humble, M.R. Silva, N.B. Trivedi, W.D. Gonzalez, and N.J. Schuch (2006) *Real-time cosmic ray monitoring system for space weather*, Space weather, Vol. 4, S08001, doi:10.1029/2005SW000204, 10 pp.

T. Kuwabara, J.W. Bieber, P. Evenson, K. Munakata, S. Yasue, C. Kato, A. Fushishita, M. Tokumaru, M.L. Duldig, J.E. Humble, M.R. Silva, A. Dal Lago, and N.J. Schuch (2009) *Determination of interplanetary coronal mass ejection geometry and orientation from ground-based observations of galactic cosmic rays*, J. Geophys. Res., Vol. 114, A05109, doi:10.1029/2008JA013717, 10 pp.

K. Leerunnavarat, D. Ruffolo, and J.W. Bieber (2003), *Loss cone precursors to Forbush decreases and advance warning of space weather effects*, Astrophys. J., 593, pp. 587–596.

Z. Lin, J.W. Bieber, and P. Evenson (1993) *Cosmic Ray Trajectories over Prince Albert: Albedo Electron Measurements and Model Calculations*, Proc. 23rd Int. Cosmic Ray Conf. (Calgary), 3, pp. 777-780.

Z. Lin, J.W. Bieber, and P. Evenson (1995) *Electron trajectories in a model magnetosphere: Simulation and observation under active conditions*, J. Geophys. Res., Vol. 100, No. A12, pp. 23,543-23,549.

J. Luhmann (2000) *Space weather: physics and forecasts*, Physics World (July 2000), pp. 31-36.

B. Mailyan and A. Chilingarian (2010) *Investigation of diurnal variations of cosmic ray fluxes measured with using ASEC and NMDB monitors*, Adv. Space Res., 45, pp. 1380-1387.

K.G. McCracken, U.R. Rao, and M.A. Shea (1962) *The Trajectories of Cosmic Rays in a High Degree Simulation of the Geomagnetic Field*, Technical Report 77, Massachusetts Institute of Technology, Laboratory for Nuclear Science, MIT Press, Cambridge.

K.G. McCracken, U.R. Rao, B.C. Fowler, M.A. Shea, and D.F. Smart (1968) *Cosmic Ray Tables (Asymptotic Directions, etc.)*, Annals of the IQSY, 1, Ch. 14, pp. 198-214, MIT Press, Cambridge.

K. Munakata, J.W. Bieber, S. Yasue, C. Kato, M. Koyama, S. Akahane, K. Fujimoto, Z. Fujii, J.E. Humble, and M.L. Duldig (2000) *Precursors of geomagnetic storms observed by the muon detector network*, J. Geophys. Res., 105, pp. 27,457–27,468.

K. Munakata, T. Kuwabara, S. Yasue, C. Kato, S. Akahane, M. Koyama, Y. Ohashi, A. Okada, T. Aoki, K. Mitsui, H. Kojima, and J.W. Bieber (2005) *A “lose cone” precursor of an approaching shock observed by a cosmic ray muon hodoscope on October 28, 2003*, Geophys. Res. Lett., 32, L03S04, 4 pp.

K. Murakami, K. Nagashima, S. Sagisaka, Y. Mishima, and A. Inoue (1979) *Response Functions for Cosmic-Ray Muons at Various Depths Underground*, IL Nuovo Cimento, Vol. 2C, N. 5, 635-650.

K. Nagashima, K. Fujimoto, and I. Morishita (1994) *Interplanetary Magnetic Field Collimated Cosmic Ray Flow Across Magnetic Shock from Inside of Forbush Decrease, Observed as Local-Time-Dependant Precursory Decrease on the Ground*, J. Geophys. Res., 99, No. A11, pp. 21,419-21,427.

T. Nonaka, Y. Hayashi, Y. Ishida, N. Ito, S. Kawakami, A. Oshima, S. Tamaki, H. Tanaka, T. Yoshikoshi, K. Fujimoto, H. Kojima, S.K. Gupta, Atul Jain, A.V. John, D.K. Mohanty, P.K. Mohanty, S.D. Morris, K.C. Ravindran, K. Sivaprasad, B.V. Sreekantan, S.C. Tonwar, and K. Viswanathan (2003) *Study of Cosmic Ray Short Term Variations Using GRAPES-3 Muon Telescopes*, Proc. 28th Int. Cosmic Ray Conf., July 31- August 7, 2003, Tsukuba, Japan, v6, pp. 3569-3572.



T. Nonaka, S.K. Gupta, Y. Hayashi, N. Hayashida, K. Honda, N. Ito, A. Jain, A.V. John, S. Karthikeyan, S. Kawakami, H. Kojima, K. Matsumoto, Y. Matsumoto, T. Matsuyama, D.K. Mohanty, P.K. Mohanty, S.D. Morris, K. Munakata, T. Okuda, A. Oshima, B.S. Rao, K.C. Ravindran, K. Sivaprasad, B.V. Sreekantan, K. Takizawa, H. Tanaka, S.C. Tonwar, K. Viswanathan, and T. Yoshikoshi (2005a) *Simultaneous detection of the loss-cone anisotropy with Ooty and Akeno muon telescopes*, 29th Int. Cosmic Ray Conf., August 3 - 10, 2005, Pune, India, SH 2.6, poster, 4 pp.

T. Nonaka, S.K. Gupta, Y. Hayashi, N. Ito, A. Jain, A.V. John, S. Karthikeyan, S. Kawakami, H. Kojima, K. Matsumoto, Y. Matsumoto, T. Matsuyama, D.K. Mohanty, P.K. Mohanty, S.D. Morris, T. Okuda, A. Oshima, B.S. Rao, K.C. Ravindran, M. Sasano, K. Sivaprasad, B.V. Sreekantan, H. Tanaka, S.C. Tonwar, K. Viswanathan, and T. Yoshiyoshi (2005b) *Short Term Variations of Galactic Cosmic Rays Observed with GRAPES-3 Muon Telescopes*, 29th Int. Cosmic Ray Conf., August 3 - 10, 2005, Pune, India, SH 2.6, pp. 359-362.

Y. Okazaki, A. Fushishita, T. Narumi, C. Kato, S. Yasue, T. Kuwabara, J.W. Bieber, P. Evenson, M.R. Da Silva, A. Dal Lago, N.J. Schuch, Z. Fujii, M.L. Duldig, J.E. Humble, I. Sabbah, J. Kóta, and K. Munakata (2008) *Drift Effects and the Cosmic Ray Density Gradient in a Solar Rotation Period: First Observation with the Global Muon Detector Network (GMDN)*, The Astrophysical Journal, 681, pp. 693–707.

I. Petukhov and S. Petukhov (2009) *The method of particle trajectories for description of a cosmic ray*, Proc. 31st Int. Cosmic Ray Conf., Łódź, Poland, July 7-15, 2009, 4 pp.

V. Pizzo (1978). *A three-dimensional model of corotating streams in the solar wind I. Theoretical foundations*. Journal of Geophysical Research 83(A12), doi: 10.1029/OJGREA 000083000A12005563000001, ISSN: 0148-0227.

C. Plainaki, H. Mavromichalaki, A. Belov, E. Eroshenko, and V. Yanke (2009) *Neutron monitor asymptotic directions of viewing during the event of 13 December 2006*, Advances in Space Research 43, pp. 518-522.

G.K. Rangarajan and T. Iyemori (1997) *Time variations of geomagnetic activity indices Kp and Ap: an update*, Ann. Geophysicae, 15, pp. 1271-1290.

M. Rockenbach, A. Dal Lago, W.D. Gonzalez, K. Munakata, A. Fushishita, T. Kuwabara, J. Bieber, N.J. Schuch, M.L. Duldig, J.E. Humble, and I. Sabbah (2009) *Global Muon Detector Network Observing Geomagnetic Storm's Precursor Since March 2001*, Proc. 31st Int. Cosmic Ray Conf., Łódź, Poland, July 7-15, 2009, 4 pp.

M. Rockenbach, A. Dal Lago, W.D. Gonzalez, K. Munakata, C. Kato, T. Kuwabara, J. Bieber, N.J. Schuch, M.L. Duldig, J.E. Humble, H.K. Al Jassar, M.M. Sharma, and I. Sabbah (2011) *Geomagnetic storm's precursors observed from 2001 to 2007 with the Global Muon Detector Network (GMDN)*, Geophysical Research Letters, 38, L16108, 4 pp., doi:10.1029/2011GL048556.

B. Rossi, *Cosmic Rays*, New York, McGraw-Hill, 1964.

D. Ruffolo, J.W. Bieber, P. Evenson, and R. Pyle (1999) *Precursors to Forbush Decreases and Space Weather Prediction*, Proc. 26th Int. Cosmic Ray Conf., Vol. 6, Salt Lake City, Utah, USA, August 17-25, 1999, pp.440-443.

N.J. Schuch (2006) *Space and atmospheric sciences at South of Brazil*, SCOSTEP -11th Quadrennial Solar Terrestrial Physics Symposium, Sun, Space Physics and Climate, March 6-10, 2006, Rio de Janeiro, Brazil.

N.J. Schuch, A. Dal Lago, M. Rockenbach, E. Echer, W.D. Gonzalez, C.R. Braga, M. Silveira, R.C. Stekel, N. Kemmerich, L.R. Vieira, D.K. Pinheiro, K. Munakata, C. Kato, A. Fushishita, Z. Fujii, J.W. Bieber, P. Evenson, T. Kuwabara, M.L. Duldig, J.E. Humble, A. Chilingarian, and I. Sabbah (2009) Proposal for a solar heliosphere 3-D visualization with accurate space weather forecasting combining the observations NASA's Stereo Mission and the Global Muon Detector Network-GMDN, XXVII IAU General Assembly – JD16 – IHY Global Campaign – Whole Heliosphere Interval, August 3-14, 2009, Rio de Janeiro, Brazil.

M.A. Shea and D.F. Smart (1982) *Possible evidence for a rigidity-dependent release of relativistic protons from the solar corona*, Space Sci. Rev., 32, pp. 251-271.

D.F. Smart and M.A. Shea (1997) *Calculated Cosmic Ray Cutoff Rigidities at 450 km for Epoch 1990.0*, Proc. Int. Cosmic Ray Conf. 25<sup>th</sup>, 2, pp. 397-400.

D.F. Smart and M.A. Shea (2000) *Geomagnetic Cutoff Rigidity. Computer Program. Theory, Software Description and Example*. Final Report, Grant NAG5-8009, Center for Space Plasmas and Aeronomic Research, The University of Alabama in Huntsville, Huntsville, Alabama 35889, 198 pp.

D.F. Smart, M.A. Shea, and E.O. Flückiger (2000) *Magnetospheric Models and Trajectories Calculations*, Space Science Rev., 93, pp. 281-308.

D.F. Smart, M.A. Shea, and R. Gall (1969) *The Daily Variation of Trajectory-Derived High-Latitude Cutoff Rigidities in a Model Magnetosphere*, J. Geophys. Res., 74(19), pp.4731–4738.

M.A. Shea, D.F. Smart, and K.G. McCracken (1965) *A Study of Vertical Cutoff Rigidities Using Sixth Degree Simulations of the Geomagnetic Field*, J. Geophys. Res., 70, pp. 4117-4130.

N.A. Tsyganenko's site: *Magnetic Field Model and GEOPACK s/w*, <http://modelweb.gsfc.nasa.gov/magnetos/tsygan.html>.

S. Yasue, K. Munakata, C. Kato, T. Kuwabara, S. Akahane, M. Koyama, Z. Fujii, P. Evenson, and J.W. Bieber (2003) *Design of a Recording System for a Muon Telescope Using FPGA and VHDL*, Proc. 28th Int. Cosmic Ray Conf., Universal Academy Press, pp. 3461-3464.

J.A. Wanliss and K.M. Showalter (2006) *High-resolution global storm index: Dst versus SYM\_H*, Journal of Geophysical Research, Vol. 111, A02202, doi:10.1029/2005JA011034, 10 pp.

J.M. Weygand and J. Raeder (2005) *Cosmic ray cutoff prediction using magnetic field from global magnetosphere MHD simulations*, Annales Geophysicae, 23, pp. 1-13.

# Appendix 1

## The prototype of database for Global Muon Detector Network (Mddb) and possibilities of its usage for Space Weather goals

<http://cr20.izmiran.ru/phpMyAdmin>.

*E. Eroshenko et al.*

17-19 October 2011 Quebec, Canada

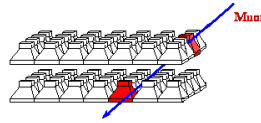
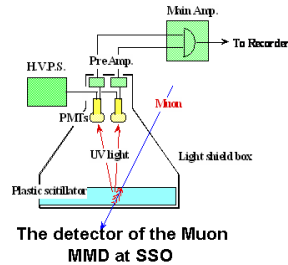
1

### A little history

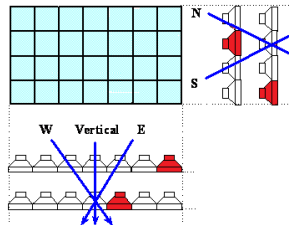
- Bothe, Kolhorster, 1929 – the idea of method of coincidents;
- Rossi (1930) – special scheme of the coincidents;
- Kolhorster, (1941, Berlin) and Alfvén, 1943, (Stockholm)- the first registration;
- Malmfors, 1948; 1949; Elliot, 1949 – the idea to use crossed telescopes;
- IGY-telescopes on Giger counters. Low statistical accuracy. Appeared telescopes on plastic scintillators.
- Drief ~1% per year. Big contribution of the occasional coincidents;
- Big proportional counters. Projects. Really operates in Yakutsk at four levels (0, 7, 20 and 40m w.e.);
- Mt. Norikura (Ohashi, 1997, hodoscope) and giant telescope by Indian-Japanese project in Ooty (Kawakami, 1999);
- *Bercovitch M.- use lead of NM as a filter. Novosibirsk, Yerevan, Mexico, YangBajing.*

2

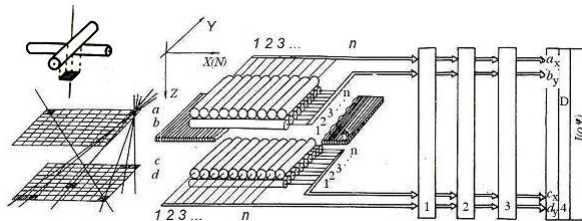
## Geometry of muon detectors



Simple telescope  
on the example of  
San Martinho



Hodoscope at  
Novosibirsk,  
6m<sup>2</sup>, 64 directions



## MT advantages

- **The CR anisotropy**- the MT are adapted better than NM because of:
  - their narrower directional diagram;
  - concentrating of the several multidirectional detectors in one point.
- Using the crossed telescopes allows to avoid the problem of large temperature effect of muon component in some cases.
- It allows also using these data in the global survey method together with the neutron monitor data.
- Because of large temperature effect these detectors were unfairly forced out for some time.

By this moment operate:

6 muon superdetectors of the square  $S \geq 9 \text{ m}^2$ :

Telescopes Nagoya, Sao Martinho, Hobart;

Hodoscopes Kuwait, Mephi-URAGAN , GRAPES-III (Ooty, 560 m<sup>2</sup>).

10 telescopes of the square  $S \sim 2\div 6 \text{ m}^2$ :

Greifswald, YangBaJing, Novosibirsk, Yakutsk CT at 0, 7, 20 и 40 mwe,  
Guangzhou, Moscow CT Cube, Yerevan, Mawson (?)

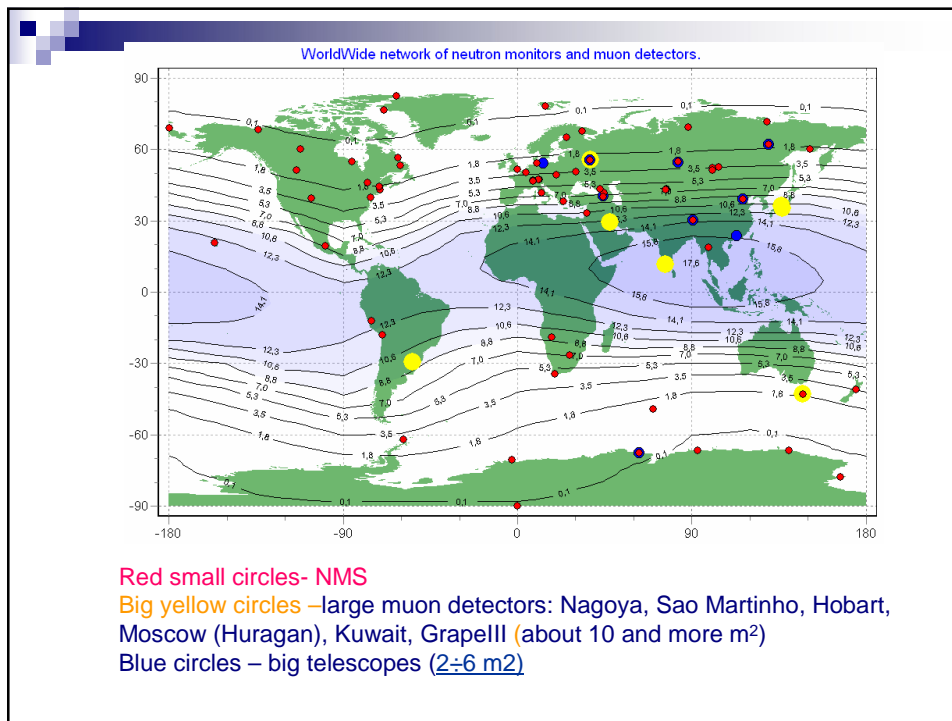
More than 10 telescopes with  $S \sim 1 \text{ m}^2$ .

These are mainly school devices:

Santiago, Putre , Adelaide, Leonsito, Musala, Blagoevgrad, Belgrad, Hafelekar,  
Lodz (?), University Rochester (USA).

Red color- publish or can publish data in real time.

5



## Data from other muon detectors

**Ionization chambers of Yakutsk and Beijing operate tens years since 1953.**

**Underground detectors operated long time:** Sakashita, Misato.

**Continue to work the unique Hodoscope Norikura**  
Ottawa

**Detectors of  $2\pi$  geometry (CARPET)** – Telescopes and separate devices – may be used in a set of applied tasks. These are IceTop, Baksan.

**Underground detectors (EHE –Extra High Energy)** may be used for study of meteorological effects: IceCube, Gran Sacco, MINOS, Baksan BUST.

7

## Other detectors

**GRAPE III – Indian-Japanese collaboration**

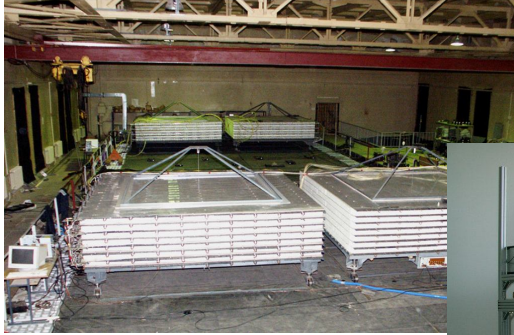


36x16= 560 m<sup>2</sup>  
For comparison: S super  
Telescope 10-40 m<sup>2</sup>



8

## And other detectors



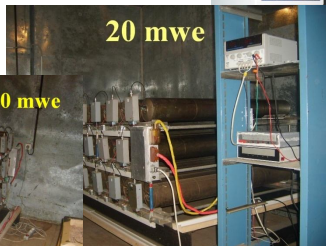
Mephi-URAGAN, 4x11 m<sup>2</sup>, since 1999?



Greifswald, 4 m<sup>2</sup>, since 2006

9

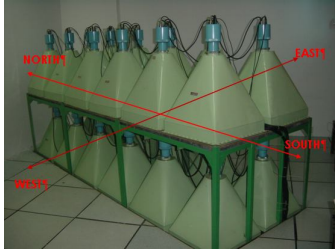
## Yakutsk, 3.5 m<sup>2</sup>, since 1973



10



## And other detectors



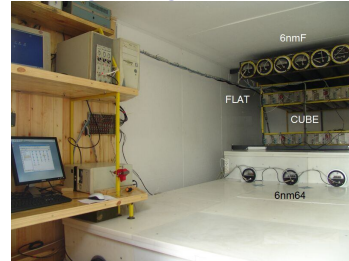
Guangzhou, 3 m<sup>2</sup>, since 1989



YangBaJing, 6m<sup>2</sup>, since 2007



Novosibirsk, 6 m<sup>2</sup>, since 2004?



MoscCube, 2m<sup>2</sup>, since 2006

11



## Global Muon Detector Network

Muon Telescopes, Ionization cameras,  
Muon Hodoscopes, Carpets



<http://cr0.izmiran.ru/gmdnet>

- Home
- History
- Actual Task
- What Are Cosmic Rays
- Looking to the Future
- References

### TELESCOPE

- Nagoya
- Sao Martinho
- Hobart
- Yakutsk
- Greifswald
- YangBaJing
- Moscow
- Novosibirsk
- Yerevan
- Mawson
- Bulgaria
- Belgrade
- Santiago
- Patte
- Hafsløkkar
- Adelaide
- Loft
- Sakashita
- 80 mwe
- Misato\_34 mwe
- Baksan BUST
- MINDS

Station	$\lambda, 0$	$\phi, 0$	$h_0$ (mb)
Nagoya	35.12	136.97	1000
Hobart	-42.88	147.32	1013
Sao Martinho	-28.16	-48.98	1000
Kuwait	29.24	47.97	1013
Greifswald	54.08	13.38	1013
YangbaJing	30.11	90.53	607
Yakutsk	62.01	129.43	1000
Mawson	-67.60	62.87	990
Novosibirsk	54.48	83.00	995
Moscow	55.47	37.32	1000
El LeonCito 2552	-31.8	-69.30	700
Yerevan 2000	40.50	44.17	815
Yerevan 3000	40.50	44.17	700
Vostok 3488	-78.47	106.87	620
Belgrad 78	44.85	20.38	1013
Baksan 1700	43.28	42.69	820
South Pole 2835	-90.00	0.00	680
Gran Sasso 963	42.27	13.34	970

## Description of Detectors and Database of muon detectors

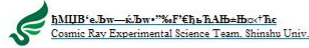
Data collected from muon telescopes since 1976. Volume ~ 50 Gb.

12

## Cosmic Ray Muon Database (Shinshu University).

<http://center.stelab.nagoya-u.ac.jp/cawses/dataact/dataact21.html>

<http://cosray.shinshu-u.ac.jp/crest/DB/Public/main.php>



you are not logging in / [login](#)

search: < CR\_Data >

### Simple Monitor of Cosmic Ray muon data

Output style: Plot data

Station:

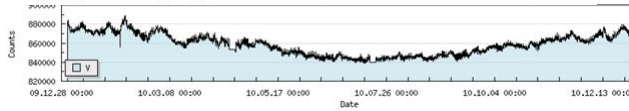
Components:  V  N  S  E  W  NE  NW  SE  SW  
 2N  2S  2E  2W  3N  3S  3E  3W

Time: from: Year 2011 Month 08 Day 27  
 till: Year 2011 Month 09 Day 27

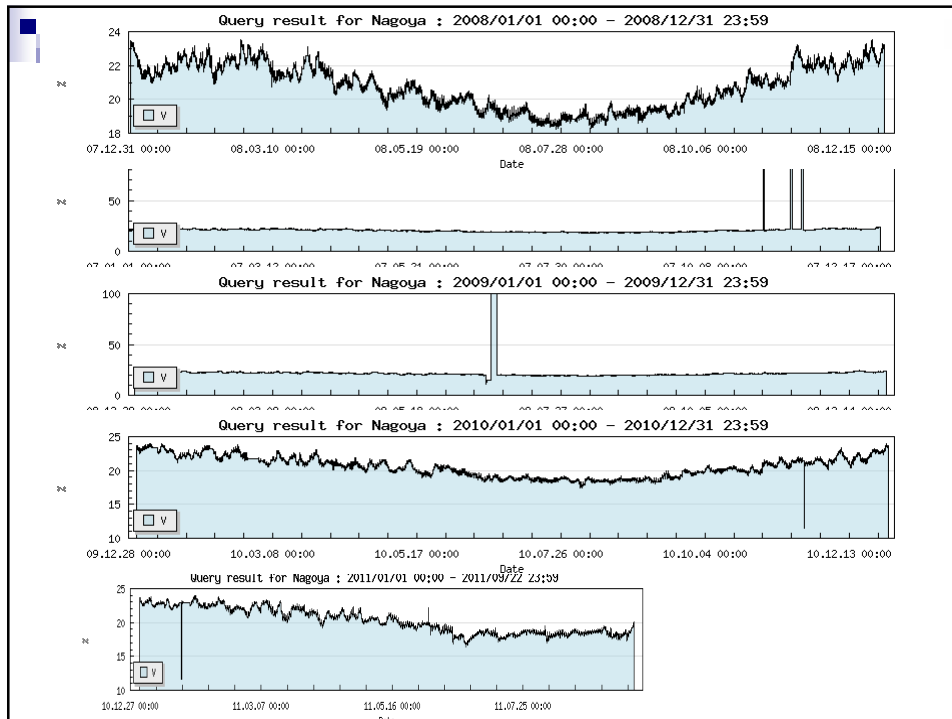
- Kuwait
- surface
- Kuwait
- Nagoya
- SaoMartinho
- underground
- Liapootah
- Misato
- Zohzan

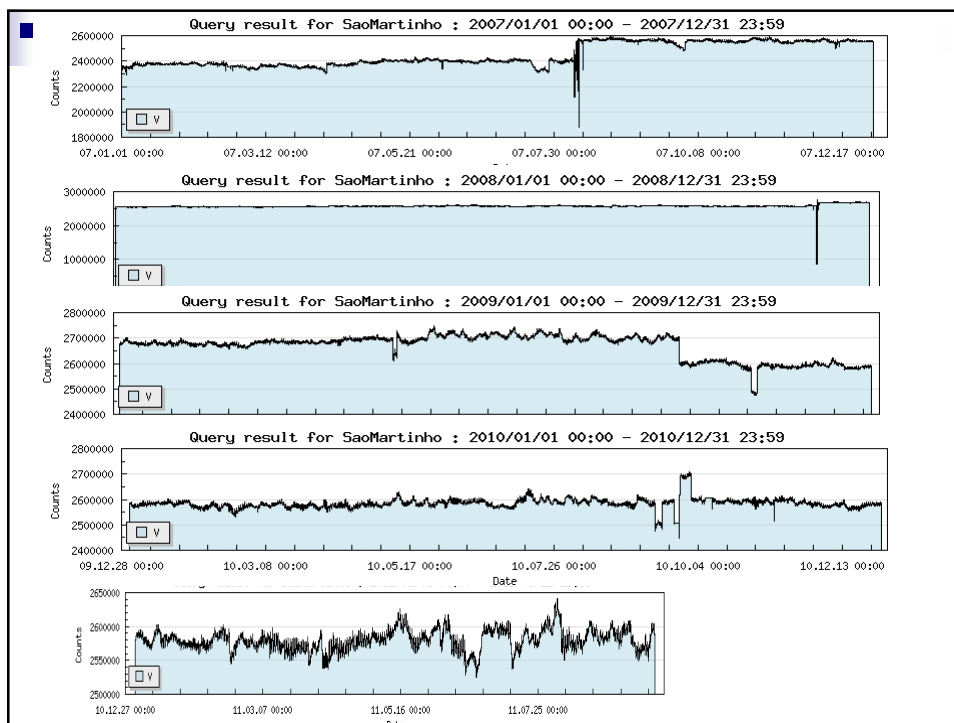
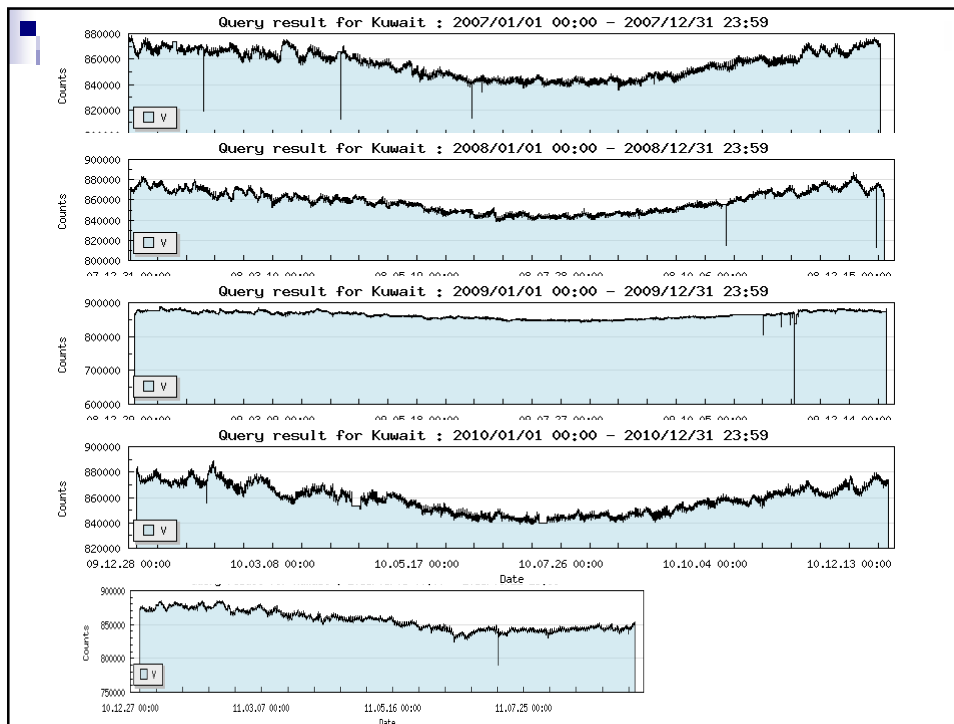
DB in pseudo real time on some muon detectors. Plots of absolute counting rates. No digital data.

Copyright (C) Shinshu University, All rights reserved.



13



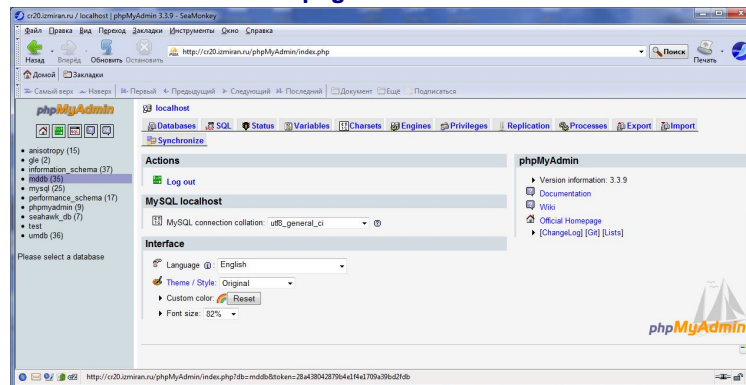


- <http://cosray.shinshu-u.ac.jp/crest/DB/Public/main.php>
- This database is only for detectors Kuwait, Nagoya, Sao Martinho . In the open access is only graphic information. Perhaps, for digital information the PSW is needed. Updated in quasi-real time (once per day).
- **At present the Prototype of database is developed in IZMIRAN on the basis of MySQL. Administrative control is carried by means WEB-application phpMyAdmin**
- **This prototype- on the example of Real Time Data Base for NMN (NMDB) which collects 1-minute and hourly data from >20 stations at present.**

## The prototype of Muon Detectors DataBase Mddb.

<http://cr20.izmiran.ru/phpMyAdmin>

### WEB page of Mddb



The prototype of new database mddb might include the data from world wide network of muon detectors: ground and underground telescopes, ionization chambers, detectors of  $2\pi$  geometry (carpets), hodoscopes.

# mddb — Database of muon detectors

<http://cr20.izmiran.ru/phpMyAdmin>

Three tables are in the basis for the station description: Location, Detectors and Directions, in each case the individual number id is attributed. This accelerates essentially the process of query the information in the tables of detector data and meteorological parameters.

id	name	lat	lon	enable
1	Nagoya	35.12	136.97	1
2	Sao Martinho	-29.44	-53.81	1
3	Kuwait	29.24	47.97	1
4	Hobart	-42.9	147.33	1
5	Ooty	11.38	76.67	1
6	Moscow	55.65	37.67	1
7	Nonkura	36.1	136.6	1
8	Greifswald	54.08	13.38	1
9	NewMoscow	55.47	37.32	1
10	Yakutsk	62.02	129.72	1
11	Novosibirsk	54.48	83	1
12	YangBajing	30.11	90.53	1

**Location**

id	Name	ShortName	FullName	Lat	Lon	Alt
1	NGYA	Nagoya	NAGOYA Muon Multi-Directional SuperTelescope	35.12	136.97	NULL
2	HBRH	Hobart	Hobart Muon Multi-Directional SuperTelescope	-42.9	147.33	193.56
3	SMRN	SaoMartinho	Sao Martinho Muon Multi-Directional SuperTelescope	-29.44	-53.81	192.11
4	YKTO	Yakutsk, O mwe	Yakutsk, Muon Telescope	62.02	129.72	156.16
5	GFLD	Greifswald	Greifswald Muon Multi-Directional	54.08	13.38	206.55

**Detectors**

id	name	detector_id	description	longitude	longitude	latitude	latitude
1	N0w	1	NULL	167.32	167.32	28.37	28.37
2	N1ee	1	NULL	193.56	193.56	10.54	10.54
3	N1fm	1	NULL	192.11	192.11	47.58	47.58
4	N1fs	1	NULL	156.16	156.16	2.99	2.99
5	N1we	1	NULL	132.53	132.53	40.19	40.19
6	N2sw	1	NULL	208.74	208.74	25.46	25.46
7	N2zw	1	NULL	151.4	151.4	65.17	65.17
8	N2sw	1	NULL	181.57	181.57	-6.27	-6.27
9	N2sw	1	NULL	129.34	129.34	12.56	12.56
10	N2ee	1	NULL	206.55	206.55	1.68	1.68
11	N3nn	1	NULL	216.51	216.51	57.12	57.12
12	N3as	1	NULL	151.01	151.01	-14.22	-14.22
13	N3zw	1	NULL	102.74	102.74	39.52	39.52
14	N4se	1	NULL	217.09	217.09	-5.27	-5.27
15	N4em	1	NULL	242.92	242.92	58.32	58.32
16	N4sa	1	NULL	149.17	149.17	-28.56	-28.56
17	N4we	1	NULL	82.07	82.07	33.78	33.78

**Directions**

19

# mddb — Database of muon detectors

<http://cr20.izmiran.ru/phpMyAdmin>

Data are kept in three Tables: Hourly Detector Data, Atmospheric Pressure (P) and Temperature distribution (T).

The main Table of DB for each detector consists of 5 Fields: DateTime, UnCorrected, Pressure, CorrectedForP, Corrected For P&T.

StartDateTime	Direction_id	UnCor_Hz	CorP_Hz	CorPT_Hz
2009-01-01 00:00:00	1	0.00	832.68	813.91
2009-01-01 01:00:00	1	0.00	831.77	812.60
2009-01-01 02:00:00	1	0.00	832.18	812.85
2009-01-01 03:00:00	1	0.00	831.93	812.44
2009-01-01 04:00:00	1	0.00	833.85	814.32
2009-01-01 05:00:00	1	0.00	834.27	814.81
2009-01-01 06:00:00	1	0.00	832.77	814.07
2009-01-01 07:00:00	1	0.00	832.68	814.24
2009-01-01 08:00:00	1	0.00	832.05	814.32
2009-01-01 09:00:00	1	0.00	833.43	814.97
2009-01-01 10:00:00	1	0.00	832.35	813.83
2009-01-01 11:00:00	1	0.00	832.10	813.42
2009-01-01 12:00:00	1	0.00	833.10	814.15
2009-01-01 13:00:00	1	0.00	832.10	813.01
2009-01-01 14:00:00	1	0.00	834.24	814.32
2009-01-01 15:00:00	1	0.00	832.77	814.07
2009-01-01 16:00:00	1	0.00	832.68	814.24
2009-01-01 17:00:00	1	0.00	832.05	814.32
2009-01-01 18:00:00	1	0.00	833.43	814.97
2009-01-01 19:00:00	1	0.00	832.35	813.83
2009-01-01 20:00:00	1	0.00	832.10	813.42
2009-01-01 21:00:00	1	0.00	833.10	814.15
2009-01-01 22:00:00	1	0.00	832.10	813.01
2009-01-01 23:00:00	1	0.00	834.24	814.32

**Hourly Data**

StartDateTime	Location_id	Pressure_mb
1970-09-30 00:00:00	1	1003.91
1970-09-30 01:00:00	1	1002.60
1970-09-30 02:00:00	1	1002.85
1970-09-30 03:00:00	1	1002.44
1970-09-30 04:00:00	1	1004.32
1970-09-30 05:00:00	1	1004.81
1970-09-30 06:00:00	1	1004.40
1970-09-30 07:00:00	1	1005.54
1970-09-30 08:00:00	1	1004.32
1970-09-30 09:00:00	1	1004.07
1970-09-30 10:00:00	1	1004.32
1970-09-30 11:00:00	1	1004.24

**Pressure Data**

**Temperature (P) Data**

Additional Table contains hourly data on vertical profiles of temperature at 17 standard isobaric levels.

20

## *mddb* — Database of muon detectors

<http://cr20.izmiran.ru/phpMyAdmin>

Also four tables are supported in actual stage: Daily means, monthly means yearly means data and table of data for base period 2009. These tables are upgraded automatically or handle.

StartDateTime	Direction_id	UnCor_Hz	CorP_Hz	CorPT_Hz
1996-12-01 00:00:00	9	0.00	177.98	174.17
1996-12-01 00:00:00	10	0.00	134.80	132.17
2001-03-01 00:00:00	11	0.00	143.24	140.46
2001-03-01 00:00:00	12	0.00	140.70	137.96
2001-03-01 00:00:00	13	0.00	143.24	140.56
2001-03-01 00:00:00	14	0.00	137.76	134.50
1970-01-01 00:00:00	15	0.00	40.80	40.25
1970-01-01 00:00:00	16	0.00	41.03	40.34
1970-01-01 00:00:00	17	0.00	43.55	42.83
1970-01-01 00:00:00	1	0.00	811.34	791.30
1970-01-01 00:00:00	2	0.00	352.66	342.97
1970-01-01 00:00:00	3	0.00	386.83	380.89
1970-01-01 00:00:00	4	0.00	343.33	340.89
1970-01-01 00:00:00	5	0.00	357.28	354.73
1970-01-01 00:00:00	6	0.00	189.21	187.42
1970-01-01 00:00:00	7	0.00	178.64	176.96
1970-01-01 00:00:00	8	0.00	187.52	185.75
1970-01-01 00:00:00	9	0.00	137.40	136.18
1970-01-01 00:00:00	10	0.00	144.67	143.38
2009-01-01 00:00:00	1	0.00	815.95	815.79
2009-01-01 00:00:00	2	0.00	353.40	353.32
2009-01-01 00:00:00	3	0.00	368.68	368.60
2009-01-01 00:00:00	4	0.00	362.03	361.96
2009-01-01 00:00:00	5	0.00	371.80	371.72
2009-01-01 00:00:00	6	0.00	171.43	171.40
2009-01-01 00:00:00	7	0.00	183.41	183.37
2009-01-01 00:00:00	8	0.00	171.17	171.14
2009-01-01 00:00:00	9	0.00	178.22	178.18
2009-01-01 00:00:00	10	0.00	134.48	134.45
2009-01-01 00:00:00	11	0.00	143.06	143.04

21

## *mddb* — Database of muon detectors

<http://cr20.izmiran.ru/phpMyAdmin>

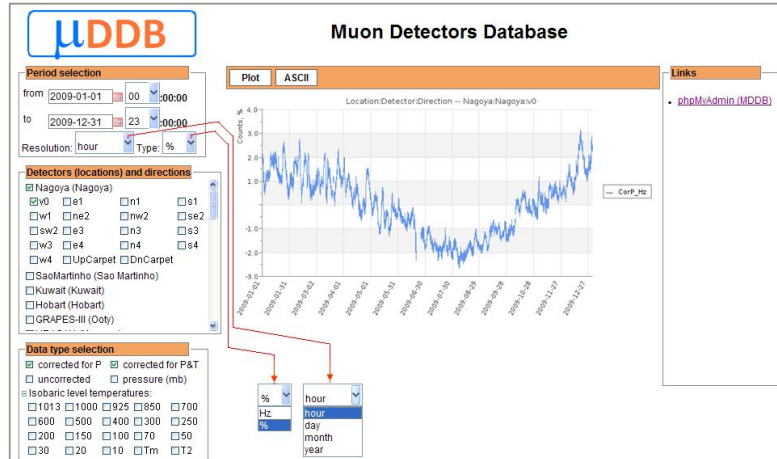
Viewing of the data from *mddb* is carried by means of the tables **VIEW**, for all the directions of each detector. Complete number **VIEW** tables is 360.

StartDateTime	Direction_id	UnCor_Hz	CorP_Hz	CorPT_Hz
2009-01-01 00:00:00	1	0.00	832.68	813.91
2009-01-01 01:00:00	1	0.00	831.77	812.60
2009-01-01 02:00:00	1	0.00	832.18	812.85
2009-01-01 03:00:00	1	0.00	831.93	812.44
2009-01-01 04:00:00	1	0.00	833.85	814.32
2009-01-01 05:00:00	1	0.00	834.27	814.81
2009-01-01 06:00:00	1	0.00	833.77	814.40
2009-01-01 07:00:00	1	0.00	834.68	815.54
2009-01-01 08:00:00	1	0.00	833.27	814.32
2009-01-01 09:00:00	1	0.00	832.77	814.07
2009-01-01 10:00:00	1	0.00	832.85	814.32

22

## The prototype of Muon Detector DataBase MDDb.

<http://cr20.izmiran.ru/mddb>



To view data from mddb in graphic and digital presentation the special program VIEWER MEST is elaborated (Muon Events Search Tool)

23

## The prototype of Muon Detector DataBase MDDb.

<http://cr20.izmiran.ru/mddb>

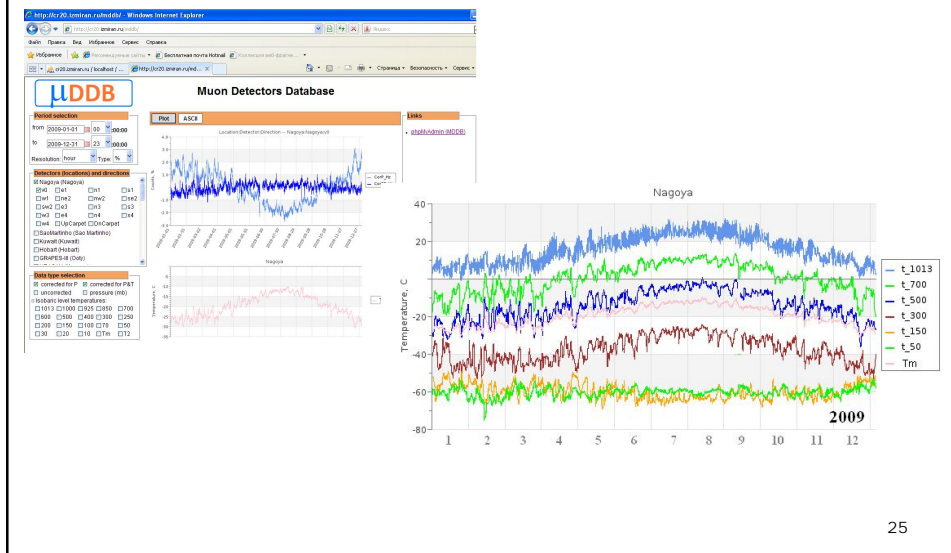
**VIEWER** allows:

- √ Get **Plot** or **ASCII** data for all directions of the detectors.
- √ Get **Plot** or **ASCII** data with hourly, daily, monthly and early resolution.
- √ Get **Plot** or **ASCII** data for temperature at all isobaric levels.
- √ **Compare** counting rates of different detectors.
- √ Compare counting rate, pressure and temperature on the selected levels.
- √ Compare counting rates uncorrected and corrected for temperature effect.
- √ Compare counting rate variations of different directions and detectors relatively to the base level on 2009, or arbitrary selected base values.
- √ Control the work of detectors which data are going in real time.

24

## The prototype of Muon Detector DataBase MDDb.

<http://cr20.izmiran.ru/mddb>



25

## The prototype of Muon Detector DataBase MDDb.

<http://cr20.izmiran.ru/mddb>

Counts for Nagoya:Nagoya.v0

StartDateTime	CorP_Hz, Hz	CorPT_Hz, Hz
2009-01-01 00:00:00	832.68	813.91
2009-01-01 01:00:00	831.77	812.60
2009-01-01 02:00:00	832.18	812.85
2009-01-01 03:00:00	831.93	812.44
2009-01-01 04:00:00	833.85	814.32
2009-01-01 05:00:00	834.27	814.81
2009-01-01 06:00:00	833.77	814.40
2009-01-01 07:00:00	834.68	815.54
2009-01-01 08:00:00	833.27	814.32
2009-01-01 09:00:00	832.77	814.07
2009-01-01 10:00:00	832.85	814.32
2009-01-01 11:00:00	832.68	814.24
2009-01-01 12:00:00	833.10	814.73
...		

Data on temperature on 17 levels are prepared. We hope to include in mddb data from the following detectors: Nagoya, Sao Marthino (Brasil), Moscow-Uragan, Kuwait, Hobart, Greifswald (Germany), YangbaJing (China), Yerevan 2000, four levels at Yakutsk, Novosibirsk, Moscow-Cube.

Temperature for Nagoya

StartDateTime	Tm
2009-01-01 00:00:00	-27.9
2009-01-01 01:00:00	-28.0
2009-01-01 02:00:00	-28.1
2009-01-01 03:00:00	-28.2
2009-01-01 04:00:00	-28.2
2009-01-01 05:00:00	-28.2
2009-01-01 06:00:00	-28.1
2009-01-01 07:00:00	-28.0
2009-01-01 08:00:00	-27.9
2009-01-01 09:00:00	-27.9
2009-01-01 10:00:00	-27.8
2009-01-01 11:00:00	-27.7
2009-01-01 12:00:00	-27.7
...	

26

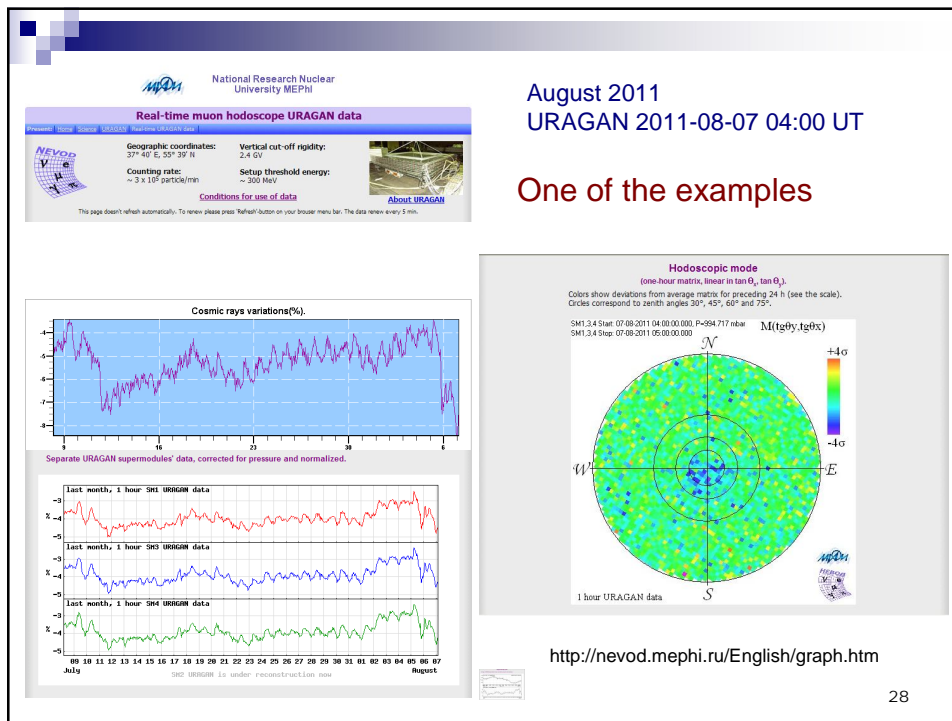


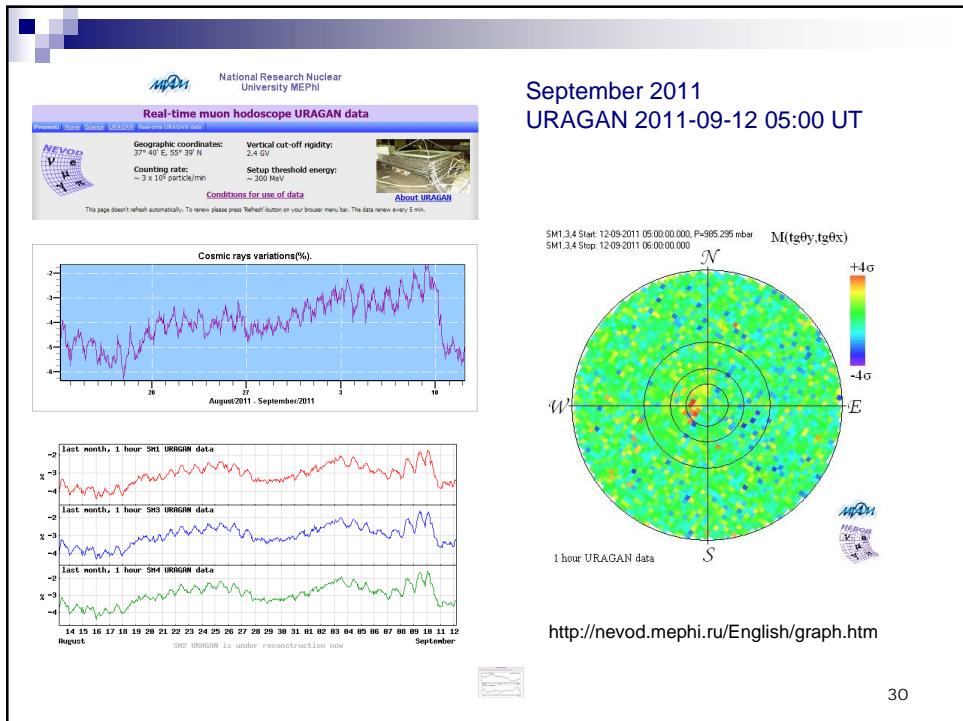
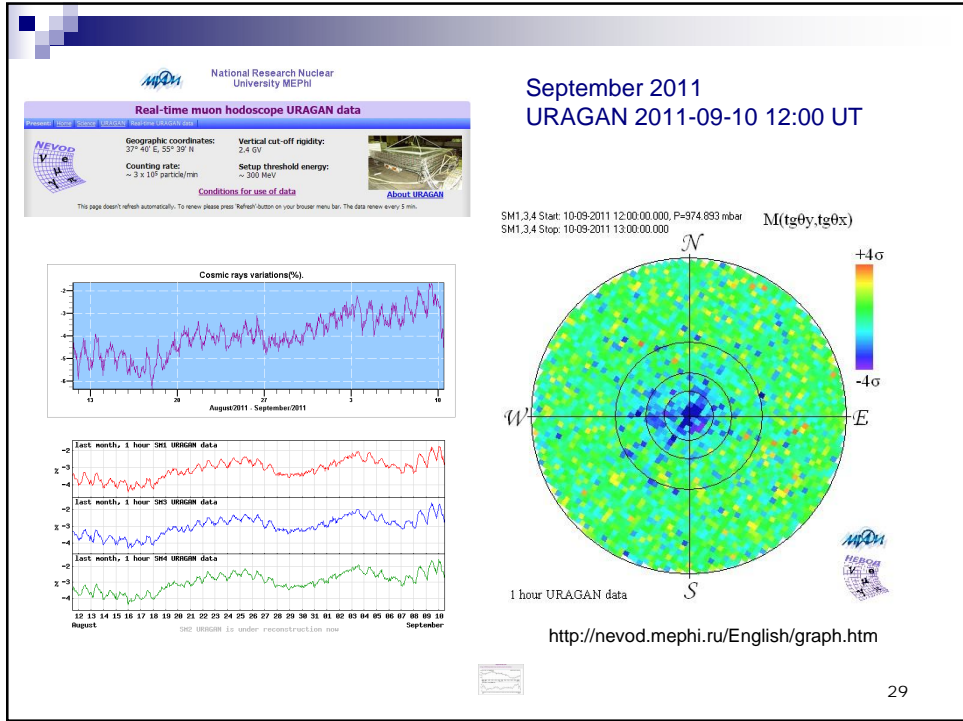
## Applications

For practical use of created DB and training of possible users the following applications are planned to be elaborated

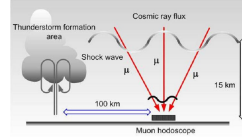
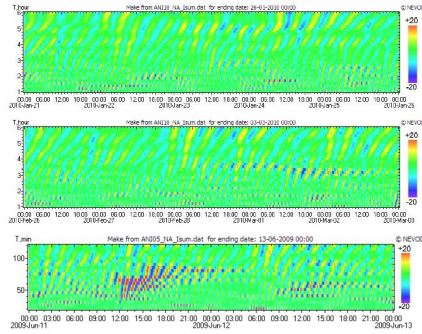
- Estimation of the spectra of isotropic CR variations by the data of one (or several) multidirected detectors.
- Getting of CR anisotropy by the data from one (or several) multidirected detectors (global survey) and precursor estimation.
- Variations of the energy spectrum of Forbush decreases.
- Obtaining of temperature distribution in the atmosphere by means of the cosmic rays.
- Correction data for the temperature effect by the vertical distribution of temperature at 17 standard isobaric levels in the atmosphere.
- Example of calculation of the detector barometric coefficients, correction data for the barometric effect
- Data quality estimation by means of Editors of the data from multi channel detectors: MedianEditor or, SuperEditor.

27





## Other possibility. Muon diagnostics of the Earth's atmosphere.



Modulations of cosmic ray muon flux in upper layers of the atmosphere.

Results of wavelet-analysis of various events:  
upper – quiet period; middle – warm front; below – local thunderstorm.

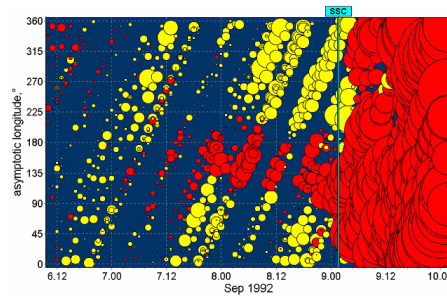
A.A.Petrukhin et al., "Muon diagnostics of the Earth's atmosphere", CD Proc. 32<sup>nd</sup> ICRC, id0310, Beijing, 2011

Dmitrieva A.N., "Modeling of muon flux variations during dynamic atmospheric processes", CD Proc. 32<sup>nd</sup> ICRC, id0165, Beijing, 2011

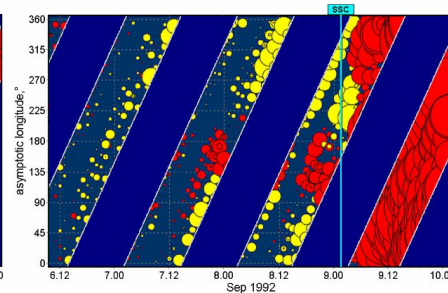
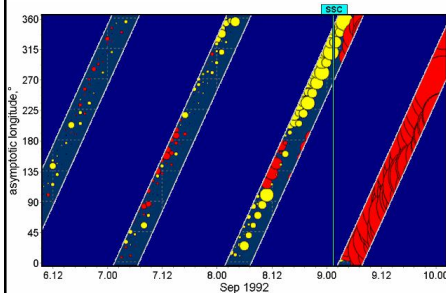
Astapov I.I. et al., "Study of correlations between thunderstorm phenomena and muon flux variations", CD Proc. 32<sup>nd</sup> ICRC, id0319, Beijing, 2011

31

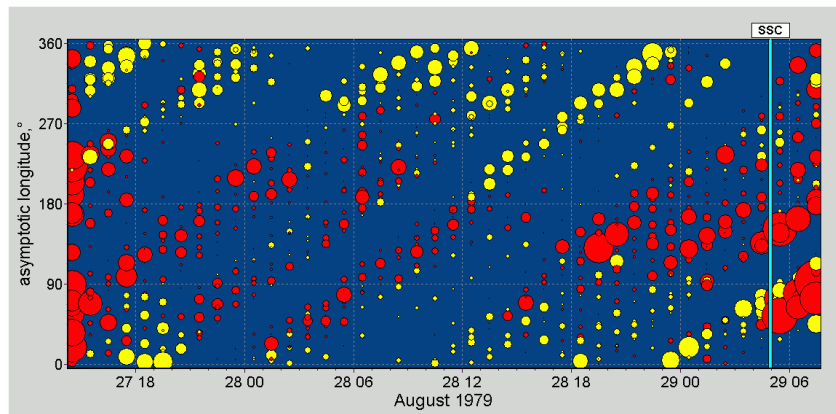
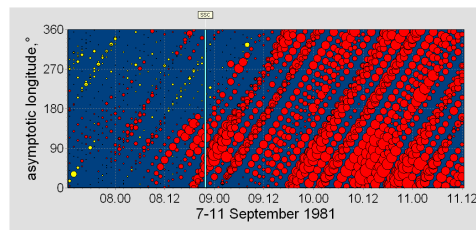
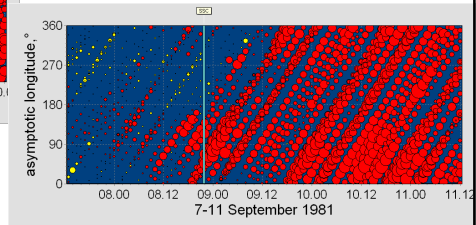
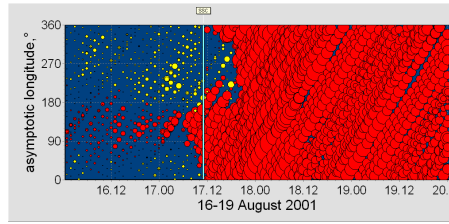
## Observation of precursor by the full network of NMs, by European stations only, and European+Russian stations.

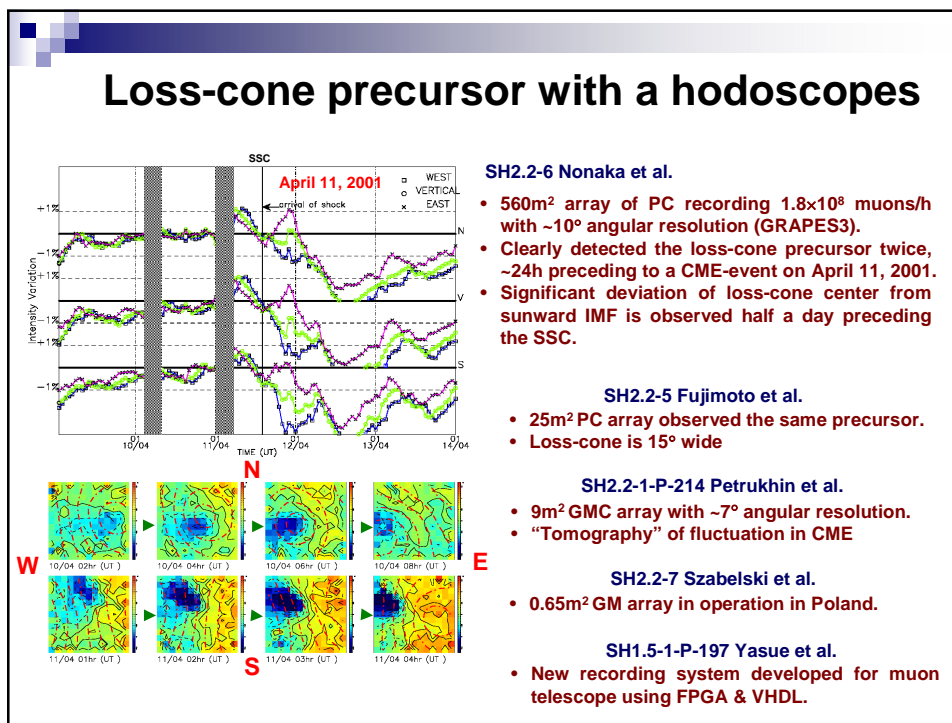
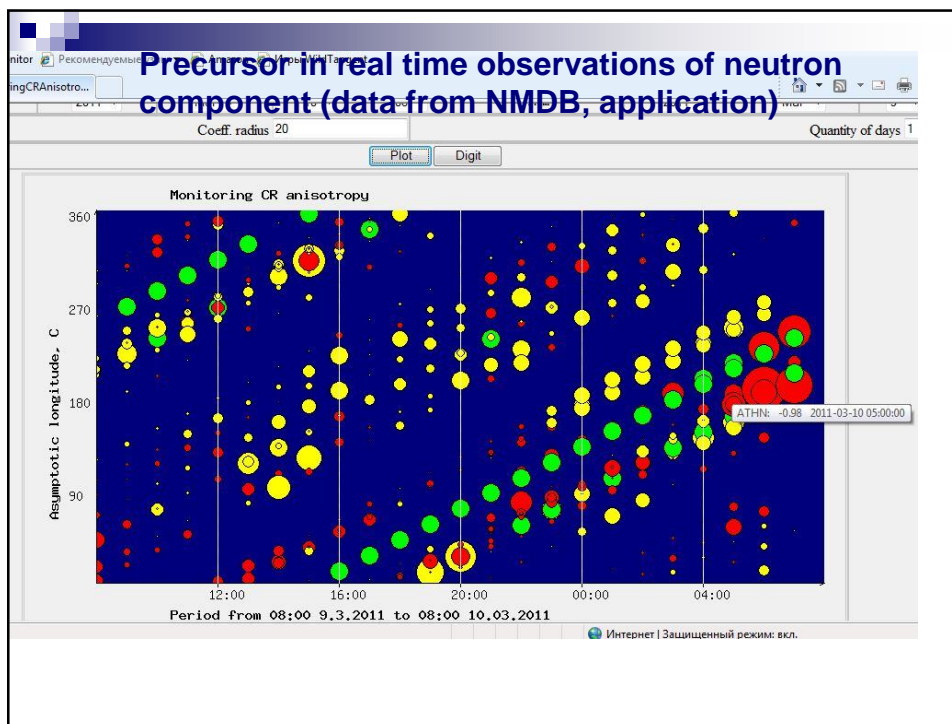


Nagashima et al, 1992  
Belov et al., 1995  
Munakata et al., 2002  
Belov et al., 2003  
.....

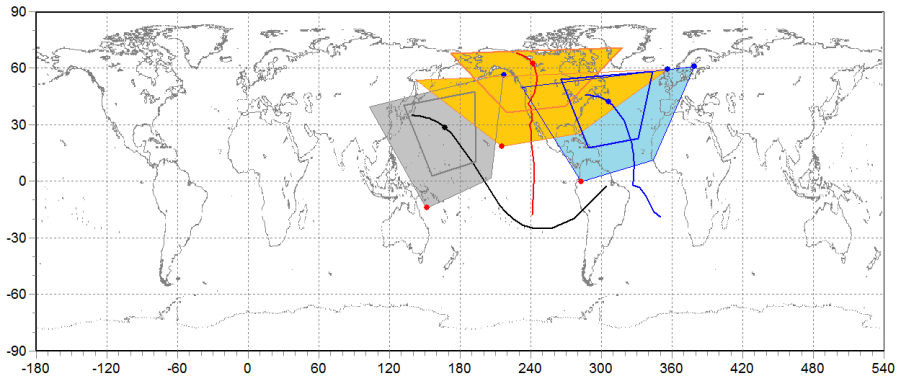


## Examples of precursors





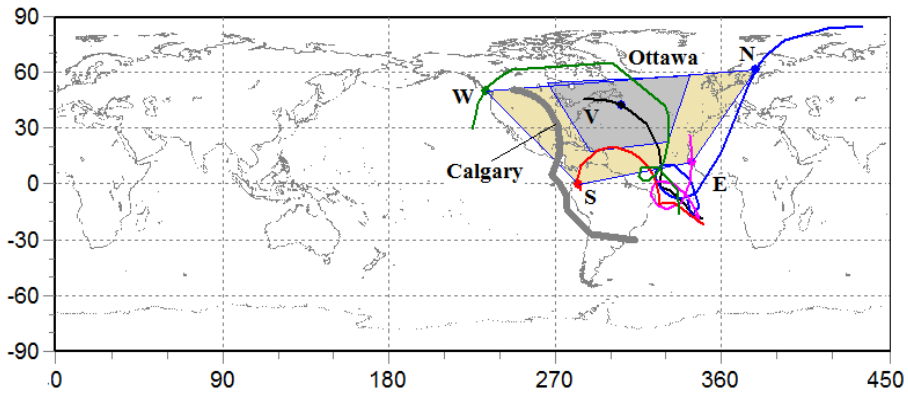
### Asymptotic directions for the muon telescopes located at the east and west of Canada.



Curves – vertical muon telescopes, points correspond to the median energies  
 Smaller figures- inclined muon telescopes with zenith angle 30 deg, bigger figures- telescopes with ~50 deg inclination. Grey-Nagoya, Yellow –Inuvik, Blue –Ottawa.

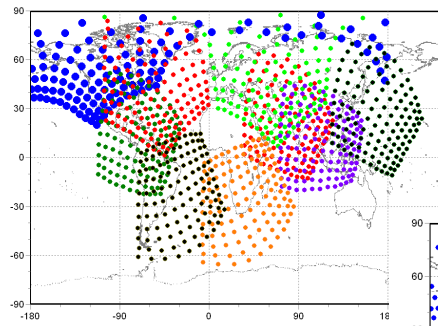
37

### Asymptotic directions for the muon telescopes would be located at Calgary and Ottawa

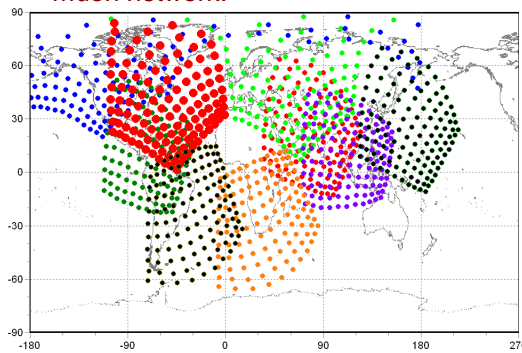


Gray curve-asymptotic directions for Calgary MT telescope, Vertical;  
 Other curves correspond to standard muon telescope at Ottawa: Vertical and four azimuthally directions inclined by  $47^\circ$

## Maps of asymptotic directions. Inuvik (blue) and Ottawa (red).

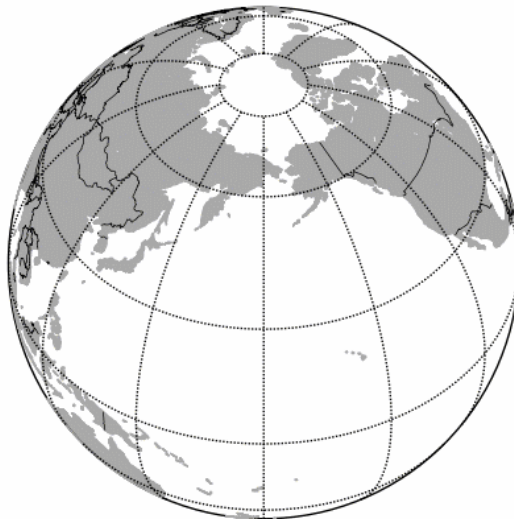


Inuvik has very rare (unique) distribution of the asymptotic directions, especially in polar zone.  
Ottawa has more or less standard distribution, but both of them fill in a big gap of empty directions in the existed muon network.



## Asymptotic directions for hodoscopes at different points

- Inuvik - blue
- SierreNegra - Yellow
- Ottawa - red
- SaoMartinho - violet
- Hermanus - dark blue
- Moscow - dark green
- Kuwait - green
- GRAPES-III - orange
- Nagoya - purple



### **For possible Canadian project on the glance of collecting, processing data and their publication.**

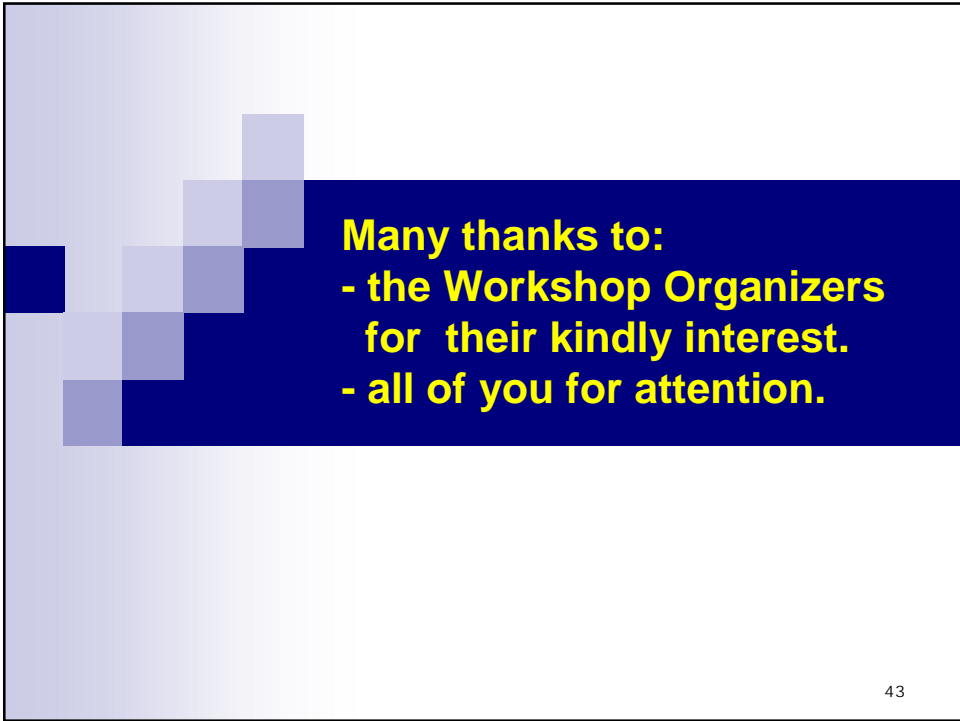
- 1) Hourly data. Store in the local archive in the txt files. It is necessary to organize a high-grade database, for example MySQL. The variant of direct data recording in DB is possible. To organize the graphic both digital publication and data exchange.
  - 2) Hourly or minute data? In case of muon detectors the statistics of the separate channels including the coincidences is sufficient to analyze the minute data, and then to form hourly. In case of a muon telescope it is possible to analyze channels of coincidence, or at least detectors of the top and bottom planes.
  - 3) To adapt for data processing of muon detector SuperEditor which "reasonably" throws out "the bad" data.
  - 4) In a case of hodoscope, because of the small statistics of elementary telescopes, most likely to use the single gages (scintillation lines or counters).
- This should be accounted under projecting.

41

## **Conclusions**

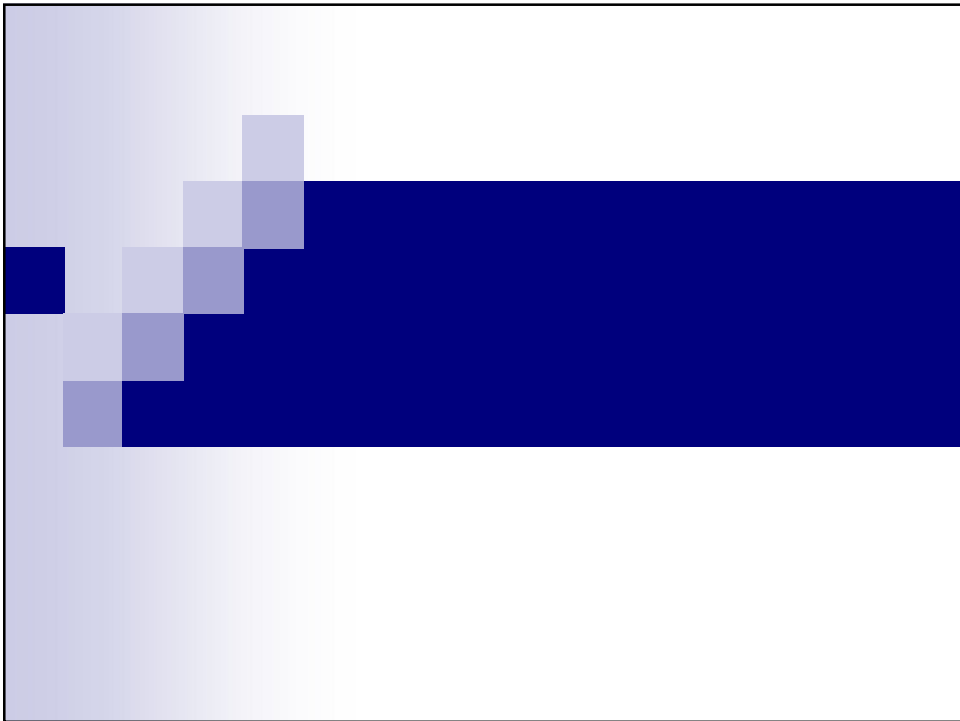
- At present about two tens of super telescopes, hodoscopes and telescopes of mid size operate, data of which are stored in the local and closed databases.
- In database offered, data from russian muon detectors and from other as well, giving and agreement, will be collected with real time updating and provided for comfortable access.
- Except of data on direct measurements of muon component, the meteorological data (atmospheric pressure and vertical distribution of temperature) will be also placed, with updating in real time.
- Special Application (Viewer mddb) for interactive graphics and digital data presentation will be elaborated as well.





**Many thanks to:**  
- the Workshop Organizers  
for their kindly interest.  
- all of you for attention.

43



## Appendix 2

### Temperature effect of muon component and practical questions of its account in real time for Global muon detector Network

Yanke, V., Berkova, M., Eroshenko, E., Belov, A (IZMIRAN)

17-19 October 2011 Ottawa

1

Observations of the CR secondary components

Anisotropy - one of the most important Space Weather parameters.

Muon telescopes are adjusted to the CR anisotropy observation much better than NM because of their narrow direction and specific construction (location at one point several detectors of different directions). In some cases such a telescope may substitute a group of detectors (for example, NMS) located in different points at the globe.

But use of muon detector data very often restrains presence at this data of the big temperature effect inherent muonic component of secondary CR.

**What is the nature of temperature effect?**

**Layer of the muon generation in the atmosphere**

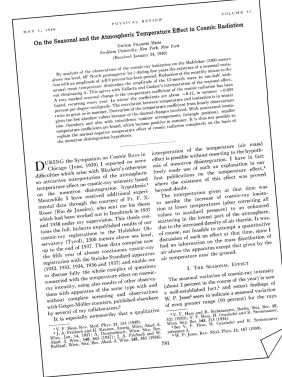
2

## Main stages.

Meteorological effects were discovered just with the beginning of systematic study of the variations of secondary CR. The nature of barometric effect was determined relatively quickly (in 1926!), but an estimation of temperature effect took several tens. In 1932 **P.Blacket**, basing on the hypotetic muon (which was experimentally discovered in 1936), explained successfully the **negative** temperature effect.

**M.Forro** found also **positive** temperature effect in 1947, which he was happened to explain with two-meson model (in 1947 the existence of peon was experimentally confirmed).

Temperature effect was also investigated by **V.Hess**, 100years Anniversary of whom is coming, but in 1940 he could not explain the experimental results obtained.



V. Hess,  
"On the Seasonal and the Atmospheric Temperature Effect in Cosmic Radiation",  
Phys. Rev., V. 57, May 1, 1940.

3

## Method of crossed telescopes [Elliot, 1950] .

It allows to get rid of variations of an atmospheric origin, having kept almost completely anisotropic variations.

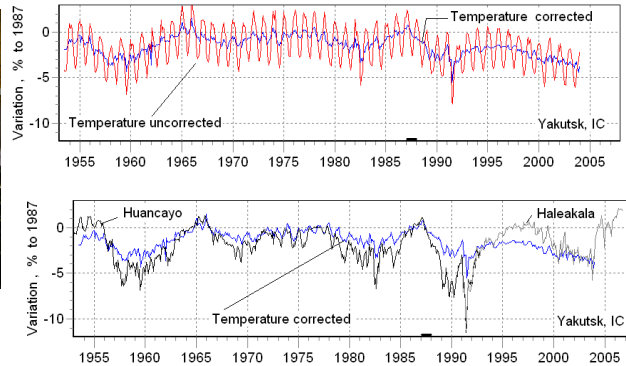
However, we cannot define the CR density in this case, or estimate spectrum of the CR variations. The seasonal temperature effect (~5%) is comparable with the CR variations of non terrestrial origin (for example, 11-year variations), and it is impossible to use muon data in a full volume if it uncorrected for temperature effect.

4

**Temperature effect and long term variations. Ionisation chamber in Yakutsk (wide directed detector with lead screen to cut off the soft component of the CR).**

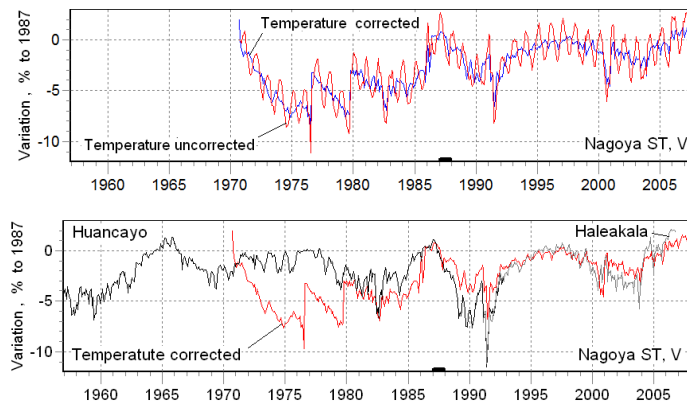


**Ionization chamber In Yakutsk**



**Upper panel – uncorrected and corrected for temperature counting rates. Comparison with the data from NMs Huancayo и Haleakala. From 1995-drief.**

**Temperature effect and long term variations. Muon telescope NAGOYA, vertical**



**Upper panel – uncorrected and corrected for temperature counting rates. Comparison with the data from NMs Huancayo и Haleakala.**

## Methods of the Temperature Effect exclusion.

- 1) **Method Duperier** (A. Duperier, 1949) (empirical)

$$\left. \frac{\delta N}{N} \right|_T = \alpha_H \delta H_{100} + \alpha_T \delta T_{100}$$

Where  $\alpha_H$  decay coefficient (%/km) – negative effect,  $\alpha_T$  positive temperature coefficient (%/C) (empirical)

- 2) **The integral method** (L. Dorman, 1954; Maeda & Wada, 1954; Olbert, 1953)

$$\left. \frac{\delta N}{N} \right|_T = \int_0^{h_0} W_T(h) \cdot \delta T(h) \cdot dh \quad \text{Where } \delta T(h) = T_B - T \text{ and } W_T(h) - \text{density of temperature coefficient.}$$

- 3) **The method of the effective temperature** (P. Barrett et. al., 1952)

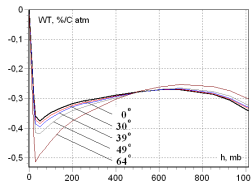
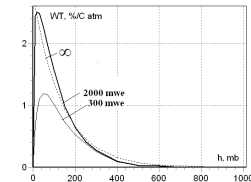
$$\left. \frac{\delta N}{N} \right|_T = \int_0^{h_0} W_T(h) \cdot \delta T(h) \cdot dh = \frac{\int_0^{h_0} W_T(h) \cdot \delta T(h) dh}{\int_0^{h_0} W_T(h) dh} = \alpha_T \delta T_{eff}$$

- 4) **The method of mean-mass temperature** (Yu. Krestyannikov, 1976)

$$\left. \frac{\delta N}{N} \right|_T = \int_0^{h_0} W_T(h) \delta T(h) dh = \bar{\alpha}_T \int_0^{h_0} \delta T(h) \cdot dh = \bar{\alpha}_T \cdot \delta T_m$$

7

## Density of temperature coefficient



We see

$$\frac{\delta N}{N} \Big|_{\mu \text{ Temp}} = \int_0^{h_0} W_T^\mu(h) \delta T(h) dh = \alpha_T \cdot \delta T_{eff} \cong \alpha_m \delta T_m$$

here

$$\alpha_T = \frac{\int_0^{h_0} W_T^\mu(h) dh, [\%/^{\circ}K]}{\int_0^{h_0} W_T^\mu(h) T(h) dh} \quad \hat{\alpha}_T = \alpha_T \cdot \delta T_{eff}, [\%]$$

Mean-mass temperature

$$T_m = \int_0^{\infty} \rho(z) \cdot T(z) dz \Big/ \int_0^{\infty} \rho(z) dz = \frac{1}{h_0} \sum_{n=1}^{L_{skin}} \int_{z_{n-1}}^{z_n} \rho(z) \cdot T(z) dz = \frac{1}{h_0} \sum_{n=1}^{L_{skin}} T_n \int_{z_{n-1}}^{z_n} \rho(z) dz = \sum_{n=1}^{L_{skin}} \frac{\Delta h_n}{h_0} \cdot \bar{T}_n$$

For extra high energies

$$W_T(h) = c \frac{\Lambda}{h} (e^{-h/\Lambda_\pi} - e^{-h/\Lambda_N})$$

P.H.Barrett et. al., Rev. Mod. Phys., 24: 133, 1952.

L.V.Volkova, Nucl. Phys., 12 (2): 347-359, 1970.

L.Dorman, Meteorological Effects of Cosmic Rays, Nauka, 1972.; Dorman & Yanke, 1971.

A.Dmitrieva, Astroparticle Physics 34, 401-411, 2011.

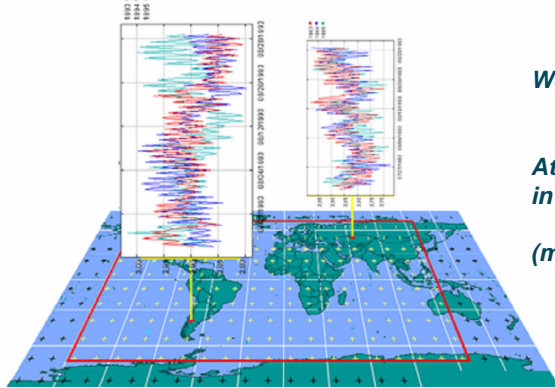
Gaisser, T., Cosmic Rays and Particle Physics, Cambridge University Press, Cambridge, Chapter 6, 1990.

Maeda & Wada, 1954.

8

## Where do we take Temperature data ?

We use the result of the Global Forecast System (GFS) temperature model representing by the National Centers for Environmental Prediction — NCEP (USA).  
On the basis of GFS the system GEFS (Global Ensemble Forecast System) submits temperature data and prognosis at 28 vertical levels every 6 hours (at 00, 06, 12, and 18 UT).  
Data are interpolated on the grid with resolution  $1^{\circ} \times 1^{\circ}$  with 6-hour interval).  
Getting data of GEFS model is going in real time by means of distributed system of access to the geophysical data bases (<http://www.ngdc.noaa.gov/wdc/wdcmain.html>).

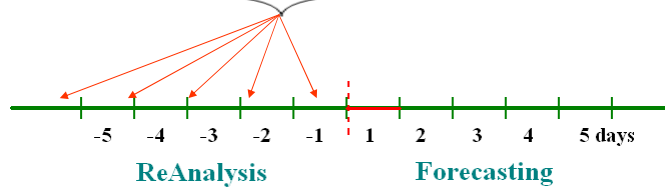
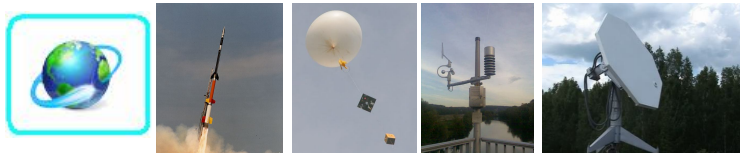


*Weather server*  
<http://esse.wdcb.ru>;

*Atmosphere temperature profile  
in real time*  
<http://phoenix.wdcb.ru>,  
(mirror <http://dimm.wdcb.ru>)

9

## Temperature Data in Real Time



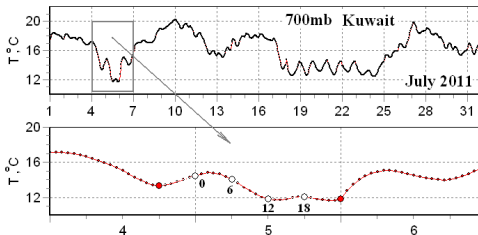
Updating of database for reanalysis is carried up to 5 days.  
Simultaneously the prognosis is performed for the next 5 days. Its data on the current day T(h) is used for calculation and exclusion of temperature effect in real time.

10

## Temperature Data

2011-08-03 00:00+00

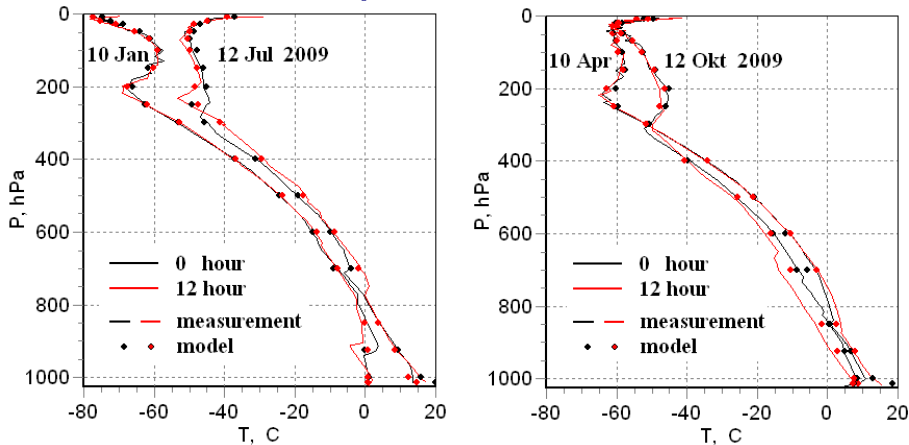
	0	1	2	3	4	5	6	7	8	9	10	11	12	13	14	15	16	17	18	19	20	21	22	23
1013	14.95	12.06	9.50	7.25	5.31	3.68	2.35	1.32	0.62	0.26	0.26	0.65	1.45	2.66	4.18	5.93	7.77	9.62	11.35	12.87	14.10	14.97	15.42	15.37
1000	17.15	16.07	15.06	14.13	13.28	12.52	11.85	11.27	10.80	10.41	10.13	9.94	9.85	9.86	9.99	10.27	10.70	11.32	12.15	13.17	14.27	15.30	16.11	16.54
925	12.15	11.24	10.46	9.79	9.24	8.80	8.45	8.19	8.00	7.85	7.73	7.60	7.45	7.27	7.09	6.98	6.98	7.15	7.55	8.20	9.00	9.82	10.54	11.03
850	5.75	5.41	5.14	4.92	4.76	4.64	4.55	4.49	4.44	4.38	4.27	4.10	3.85	3.50	3.11	2.72	2.41	2.23	2.25	2.49	2.90	3.38	3.84	4.20
700	4.25	4.59	4.84	5.01	5.10	5.11	5.05	4.91	4.71	4.45	4.13	3.76	3.35	2.90	2.40	1.84	1.21	0.48	-0.35	-1.29	-2.28	-3.29	-4.26	-5.13
600	-3.75	-3.91	-4.09	-4.29	-4.49	-4.71	-4.95	-5.20	-5.46	-5.73	-6.00	-6.28	-6.55	-6.82	-7.10	-7.40	-7.73	-8.11	-8.55	-9.06	-9.62	-10.23	-10.84	-11.46
500	-15.25	-14.99	-14.88	-14.90	-15.03	-15.26	-15.55	-15.89	-16.26	-16.62	-16.94	-17.20	-17.35	-17.39	-17.32	-17.16	-16.95	-16.71	-16.45	-16.20	-15.99	-15.85	-15.79	-15.85
400	-27.25	-26.95	-26.82	-26.83	-26.98	-27.22	-27.55	-27.93	-28.34	-28.73	-29.07	-29.32	-29.45	-29.43	-29.27	-29.04	-28.74	-28.44	-28.15	-27.91	-27.73	-27.59	-27.48	-27.41
300	-38.45	-38.55	-38.59	-38.58	-38.51	-38.40	-38.25	-38.06	-37.84	-37.57	-37.27	-36.93	-36.55	-36.13	-35.70	-35.29	-34.92	-34.63	-34.45	-34.39	-34.45	-34.58	-34.78	-35.01
250	-42.85	-42.92	-42.93	-42.89	-42.81	-42.69	-42.55	-42.39	-42.23	-42.09	-41.98	-41.93	-41.95	-42.05	-42.22	-42.41	-42.60	-42.76	-42.85	-42.86	-42.81	-42.73	-42.66	-42.62
200	-48.65	-48.98	-49.22	-49.36	-49.42	-49.41	-49.35	-49.25	-49.13	-49.01	-48.93	-48.90	-48.95	-49.09	-49.31	-49.55	-49.77	-49.96	-50.05	-50.03	-49.94	-49.81	-49.68	-49.62
150	-57.25	-57.69	-58.04	-58.33	-58.56	-58.73	-58.85	-58.93	-58.99	-59.02	-59.03	-59.04	-59.05	-59.07	-59.10	-59.16	-59.25	-59.38	-59.55	-59.77	-60.01	-60.24	-60.45	-60.59
100	-64.35	-64.12	-64.00	-63.98	-64.06	-64.22	-64.45	-64.74	-65.06	-65.39	-65.72	-66.01	-66.25	-66.42	-66.55	-66.67	-66.80	-66.98	-67.25	-67.61	-68.03	-68.45	-68.79	-69.01
70	-68.35	-68.08	-67.82	-67.54	-67.27	-67.01	-66.75	-66.50	-66.27	-66.06	-65.88	-65.74	-65.65	-65.60	-65.60	-65.61	-65.64	-65.65	-65.65	-65.61	-65.49	-65.24	-64.84	-64.22
50	-60.25	-60.73	-61.06	-61.27	-61.36	-61.35	-61.25	-61.08	-60.87	-60.64	-60.41	-60.20	-60.05	-59.97	-59.93	-59.92	-59.91	-59.86	-59.75	-59.56	-59.32	-59.04	-58.75	-58.48
30	-52.85	-53.11	-53.34	-53.54	-53.70	-53.84	-53.95	-54.03	-54.10	-54.16	-54.21	-54.27	-54.35	-54.44	-54.53	-54.59	-54.60	-54.53	-54.35	-54.06	-53.69	-53.29	-52.94	-52.67
20	-50.35	-50.53	-50.67	-50.78	-50.86	-50.92	-50.95	-50.96	-50.96	-50.94	-50.91	-50.88	-50.85	-50.82	-50.80	-50.76	-50.71	-50.64	-50.55	-50.42	-50.27	-50.08	-49.86	-49.62
10	-47.45	-47.91	-48.28	-48.54	-48.72	-48.82	-48.85	-48.81	-48.72	-48.58	-48.39	-48.18	-47.95	-47.70	-47.44	-47.18	-46.91	-46.63	-46.35	-46.08	-45.83	-45.64	-45.52	-45.52
Tm	-19.23	-19.35	-19.48	-19.61	-19.74	-19.88	-20.02	-20.17	-20.31	-20.45	-20.59	-20.72	-20.85	-20.97	-21.09	-21.19	-21.27	-21.33	-21.37	-21.38	-21.39	-21.40	-21.43	-21.51



To obtain temperature values between 0, 6, 12, 18 hrs the spline approximation is used.

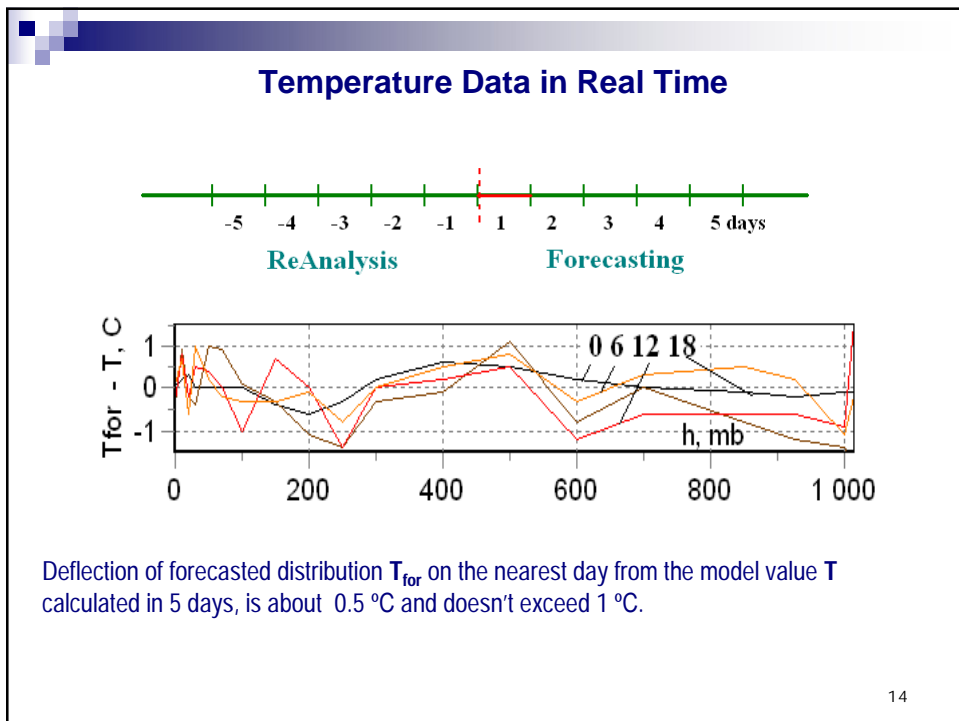
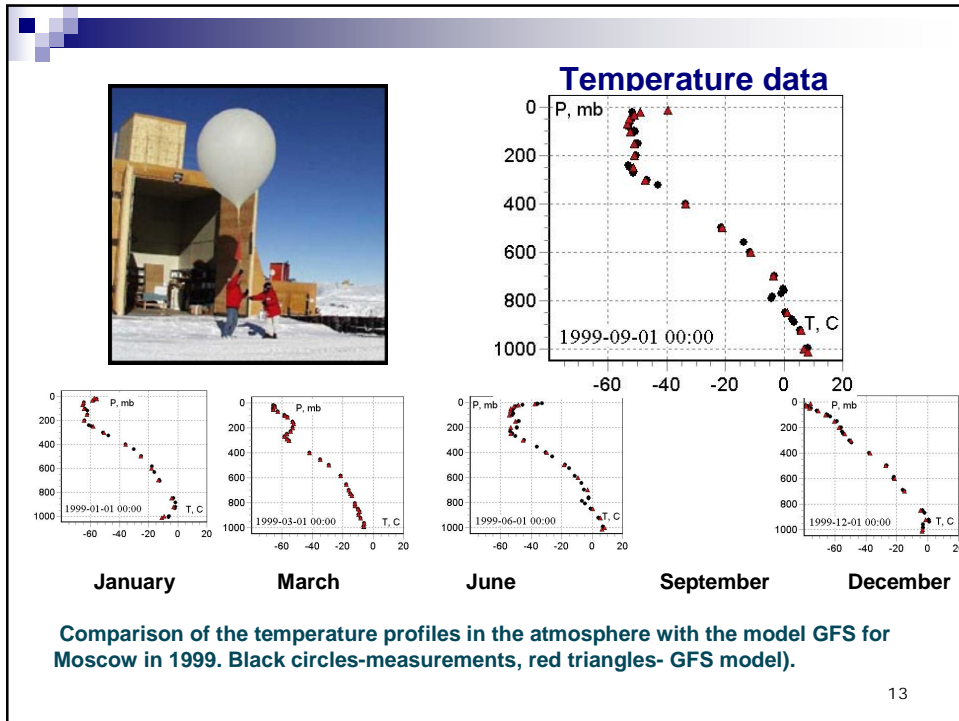
11

## Temperature Data



Comparison of the temperature profiles in the atmosphere with the model GFS for Greifswald point in 2009 (data accuracy).

12





Points where on the basis of GFS (Global Forecast System) model the hourly vertical profiles of temperature at 17 standard isobaric levels of the atmosphere are obtained.

name	Short	$\lambda$	$\phi$	$P_0$ , mb	Z, m
Nagoya	ngya	35.12	136.97	1000	0
Sao Martinho	smm	-28.16	-48.98	1000	488
Hobart	hbrt	-42.88	147.32	1013	18
Kuwait	kuwt	29.24	47.97	1013	50
Grapes-III	grap	12.00	77.00	800	2200
Moscow	mosc	55.47	37.32	1000	200
Yakutsk	ytkk	62.01	129.43	1000	105
Greifswald	grid	54.08	13.38	1013	100
YangBaJing	ybjn	30.11	90.53	607	4300
Novosibirsk	nvbk	54.48	83.00	995	163
Yerevan	erv2	40.50	44.17	815	2000
Mawson	mwsn	-67.60	62.87	990	30
Putre	put	-18.18	-69.55	665	3589
Santiago	sntg	-33.48	-70.71	960	560
El LeonCito	leon	-31.80	-69.30	700	2552
Vostok	vstk	-78.47	106.87	620	3488
Blagoevgrad	swub	42.01	23.10	1000	383
Musala	musl	42.18	23.59	730	2925
Belgrade	bigd	44.85	20.38	1013	78
Baksan	bksn	43.28	42.69	820	1700
South Pole	sopo	-90.00	0.00	680	2835
Gran Sasso	gsas	42.27	13.34	970	963

15

Map of points where on the basis of GFS (Global Forecast System) model the hourly vertical profiles of temperature at 17 standard isobaric levels of the atmosphere are obtained.



16

# μddb — muon detector data base

<http://cr20.izmiran.ru/phpMyAdmin>

Data are kept in three tables: muon data, atmospheric pressure and temperature distribution.

The screenshot shows a phpMyAdmin interface with several tables. A table named 'PressureData' is highlighted, showing columns: StartDateTime, Location\_id, Pressure\_mb, and CorP\_Hz. The data includes entries for various dates in 1970 and 2009, with pressure values ranging from 1002.24 to 1003.91 mb. Another table, 'Temperature (P) Data', is also visible, showing columns for StartDateTime, Location\_id, and Temperature. The interface includes search and navigation tools.

Grey-hourly data, red-daily)

### Example for Greifswald, 2009

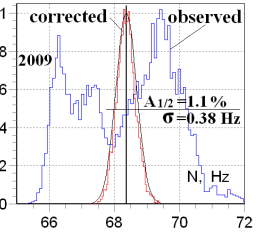
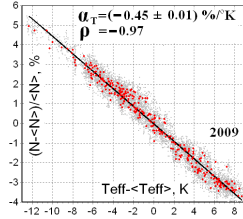
The top plot shows a scatter plot of daily muon count rate  $\langle N \rangle$  versus the difference between daily and hourly rates  $T_{eff} - \langle T_{eff} \rangle$ . The data points are red, and a black line represents a linear fit. The fit parameters are  $\alpha_T = (-0.45 \pm 0.01) \% / K$  and  $\rho = -0.97$ .

The middle plot shows a histogram of the corrected muon count rate  $N_c$  in Hz. The observed data (grey) shows two distinct peaks, while the corrected data (red) shows a single Gaussian distribution. The fit parameters are  $\Delta_{1/2} = 1.1 \%$  and  $\sigma = 0.38 \text{ Hz}$ .

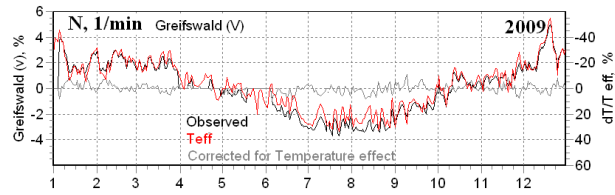
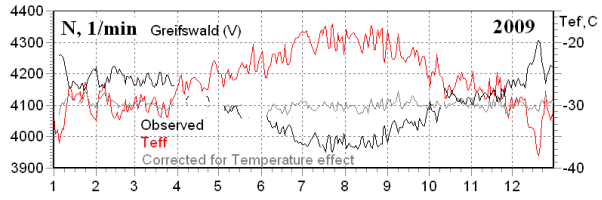
The bottom plot shows time-series data for Greifswald in 2009. The left y-axis is muon count rate  $N$  in 1/min, and the right y-axis is temperature  $T_{eff}$  in K. The observed data (grey) and corrected data (red) are shown, along with the temperature  $T_{eff}$  (black).

$$\frac{\delta N_\mu}{N_\mu}_{Temp} = \int_0^{h_0} W_T^\mu(h) \delta T(h) dh = \alpha_T \cdot \delta T_{eff} = (\alpha_T T_{eff}) \frac{\delta T_{eff}}{T_{eff}} = \bar{\alpha}_T \frac{\delta T_{eff}}{T_{eff}}$$

## Example for Greifswald, 2009



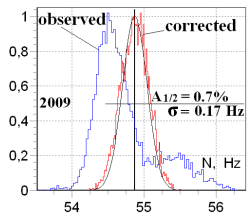
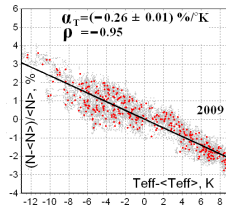
2009!  
Gaussian distribution  
Uncorrected data –  
Two peaks!



$$\frac{\delta N_{\mu}}{N_{\mu}} = \int_0^{h_0} W_T^{\mu}(h) \delta T(h) dh = \alpha_T \cdot \delta T_{eff} = (\alpha_T T_{eff}) \frac{\delta T_{eff}}{T_{eff}} = \hat{\alpha}_T \frac{\delta T_{eff}}{T_{eff}}$$

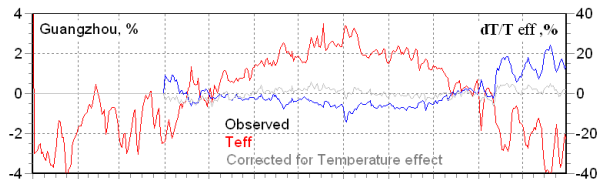
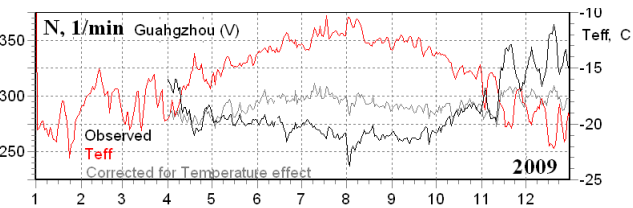
19

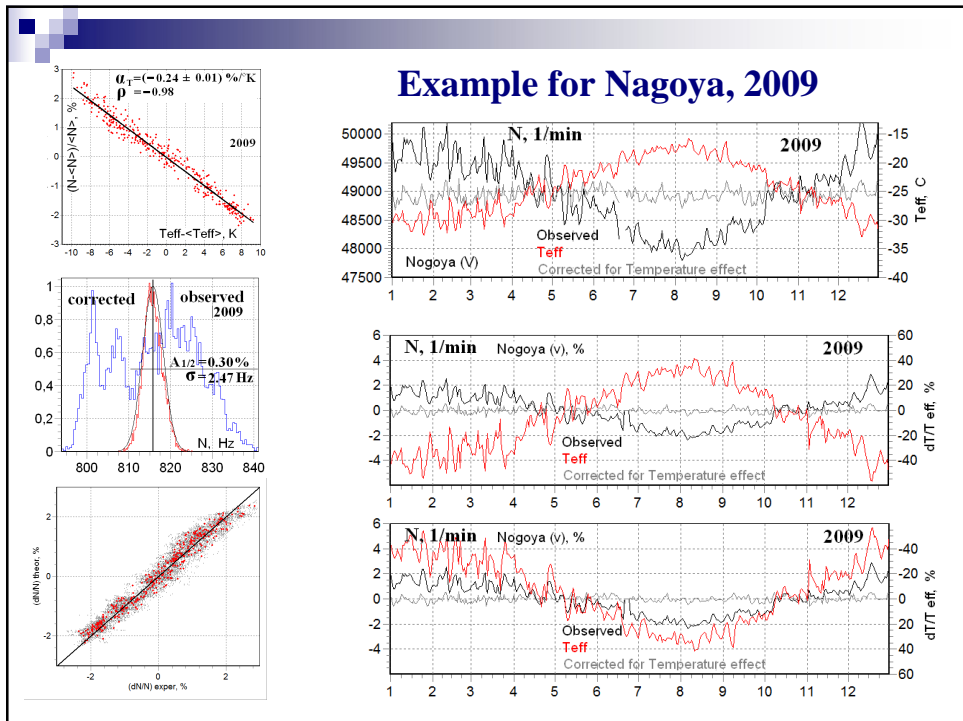
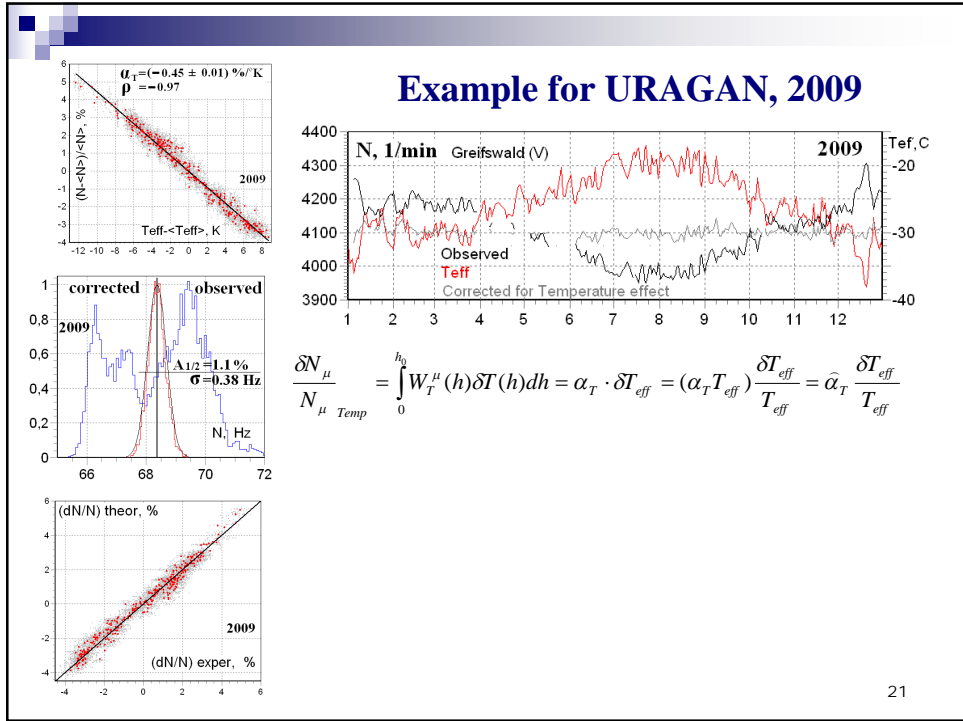
## Example for Guangzhou, 2009



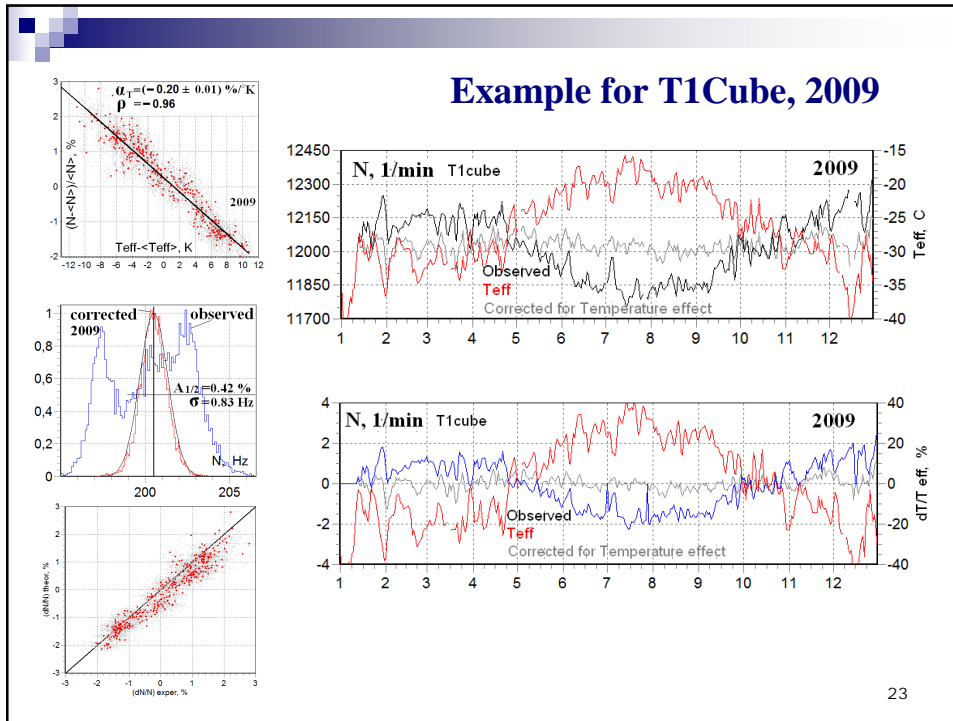
$$\frac{\delta N_{\mu}}{N_{\mu}} = \int_0^{h_0} W_T^{\mu}(h) \delta T(h) dh = \alpha_T \cdot \delta T_{eff} = (\alpha_T T_{eff}) \frac{\delta T_{eff}}{T_{eff}} = \hat{\alpha}_T \frac{\delta T_{eff}}{T_{eff}}$$

20



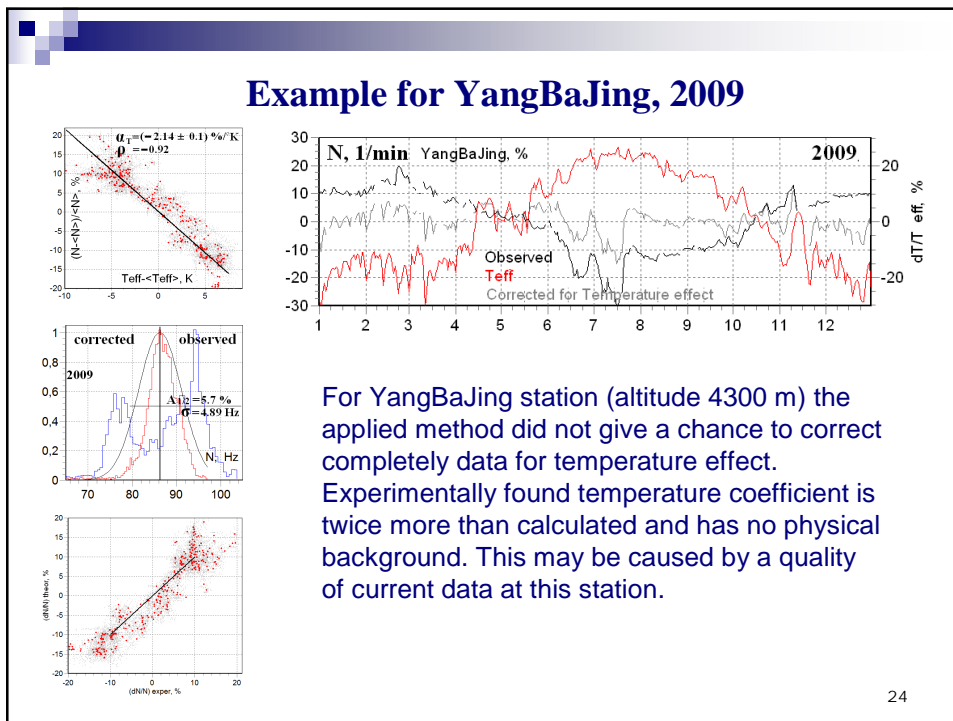


## Example for T1Cube, 2009



23

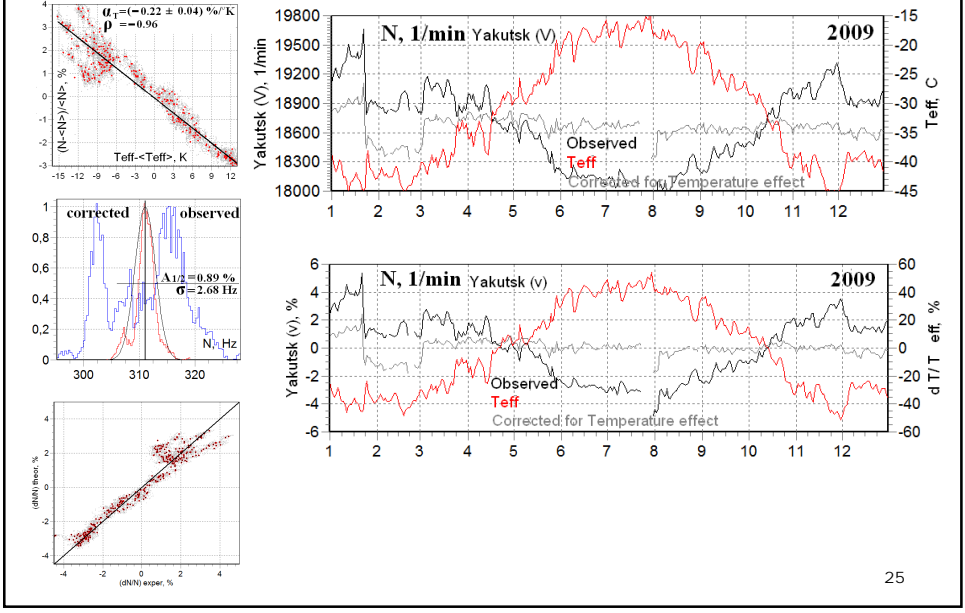
## Example for YangBaJing, 2009



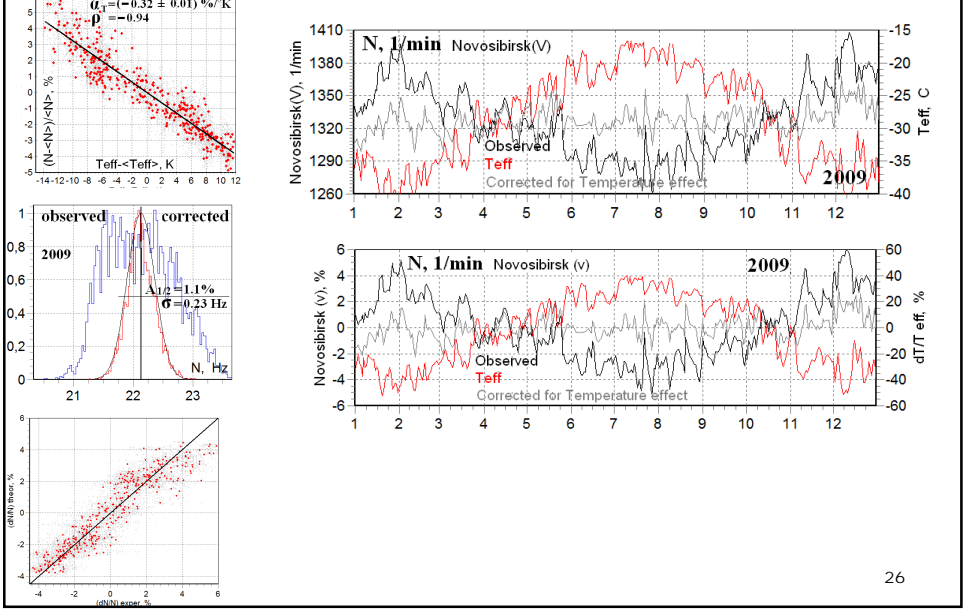
For YangBaJing station (altitude 4300 m) the applied method did not give a chance to correct completely data for temperature effect. Experimentally found temperature coefficient is twice more than calculated and has no physical background. This may be caused by a quality of current data at this station.

24

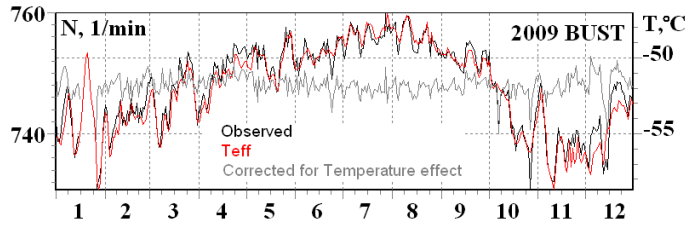
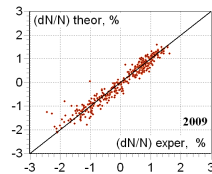
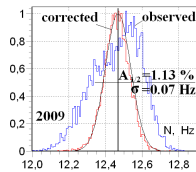
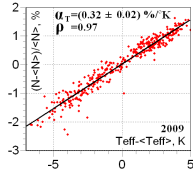
### Example for Yakutsk, 2009



### Example for Novosibirsk, 2009



## Example for Baksan, 2009



For demonstration of the method ability the pictures for the underground detector Baksan are presented (energy threshold is 220 GeV). The usual CR variations should be negligible small at this detector, so, the observed variations reflect only local fluctuations and temperature effect.

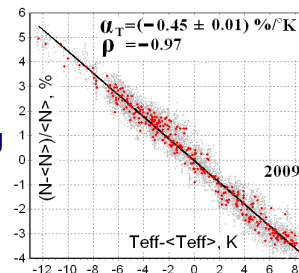
Temperature effect can be estimated on this station for any other year, not only for the quiet period.

In this case (underground detector) the temperature effect is positive in contrast with above demonstrated stations.

27

## Conclusions

- 1) Altitudinal distribution of temperature in the atmosphere, by GFS model obtained, is sufficient for correction for temperature effect the observable muon data in real time.
- 2) For all the points with muon detectors the collection of hourly data on the altitudinal distribution of temperature in the atmosphere is carried out.
- 3) Calculations of the density of temperature coefficient are necessary to perform for all the directions of existed detectors accounting its real geometry.
- 4) It is more preferable to find the temperature coefficients experimentally, using method of effective temperature.



28

**Many thanks to:**  
**- the Workshop Organizers**  
**for their kindly interest.**  
**- all of you for attentions.**

29

Для возможного канадского проекта с точки зрения методики исключения метеорологических эффектов необходимо:

- 1) **Минутные данные.** Прецизионный ДД (точность несколько десятых mb и такая же долговременная стабильность). Необходимость минутных данных обсудить, может достаточно часовых.
- 2) **Часовые данные.** Формирование вертикального температурного распределения по данным модели атмосферы для 17 стандартных изобарических уровней. Измерение локальной приземной температуры T2 (точность несколько десятых градусов и такая же долговременная стабильность).

30

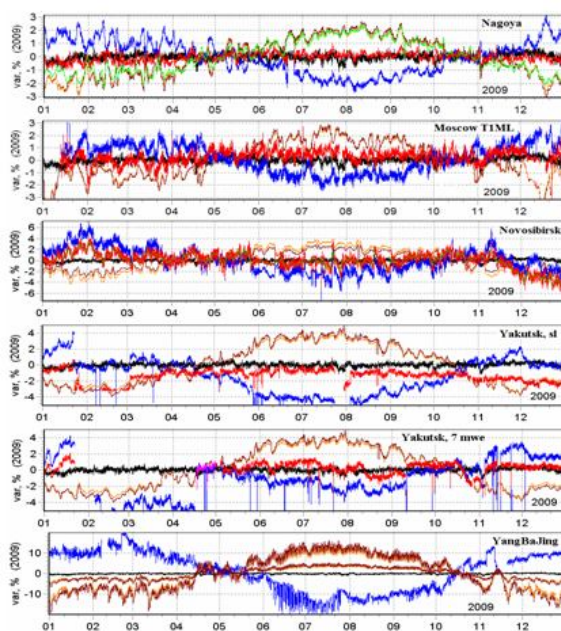


## Выводы

name	$N, \text{Hz}$	$\sigma, \text{Hz}$	$\rho$	$\alpha_T, \% / ^\circ\text{K}$	$T_m, ^\circ\text{K}$	$T_{\text{eff}}, ^\circ\text{K}$	$\alpha_T$
Nagoya 0v	815.8	2.47	-0.24±0.01	-0.24±0.01	253.5	252.4	-0.61±0.03
Nagoya 1v	368.6	1.10	-0.98	-0.25		252.0	-0.64
Nagoya 3v	143.0	0.40	-0.98	-0.28		250.9	-0.69
Nagoya 4v	40.9	0.17	-0.96	-0.27		248.8	-0.68
Greifswald	68.4	0.30	-0.99	-0.44±0.01	248.8	248.1	-1.10±0.04
Novosibirsk	22.1	0.23	-0.94	-0.32±0.02	245.4	244.6	-0.79±0.05
Mephi-URAGAN	281.4	1.04	-0.92	-0.23±0.01	246.8	247.6	-0.58±0.02
Moscow-CUBE s+h	200.5	0.75	-0.96	-0.20±0.02		246.2	-0.49±0.05
Yakutsk, s+h	311.0	1.04	-0.96	-0.22±0.02	242.1	241.5	-0.53±0.05
YangBaJing	86.3	1.04	-0.92	-2.14±0.10	239.1	244.4	-5.23±0.20
Guangzhou	54.9	0.17	-0.95	-0.26±0.02	258.6	257.2	-0.67±0.05
LeonSito, s+h	63.0	0.60	-0.87	-0.32±0.04		241.6	-0.77±0.09
BUST	12.5	0.07	0.97	0.32±0.02		221.1	0.71±0.04

31

## RESULTS on correction for temperature effect



На рисунке приведены:  
 Uncorrected data (blue),  
 Corrected for temperature effect|  
 by integral method (red);  
 Mean-mass T method-black;  
 Temperature variations  
 Computed by integral method-  
 brown,  
 Median method (orange);  
 Duperje method- green

32

# Appendix 3

Muon Detector Workshop (17 October, 2011@La Petite Rouge)

## Global Muon Detector Network (GMDN)

Kaz. Munakata<sup>1</sup>, C. Kato<sup>1</sup>, S. Yasue<sup>1</sup>, J. W. Bieber<sup>2</sup>, P. Evenson<sup>2</sup>, T. Kuwabara<sup>2</sup>,  
M. R. DaSilva<sup>3</sup>, A. Dal Lago<sup>3</sup>, N. J. Schuch<sup>4</sup>, M. Tokumaru<sup>5</sup>, M. L. Duldig<sup>6</sup>, J. E. Humble<sup>6</sup>,  
I. Sabbah<sup>7,8</sup>, H. K. Al Jassar<sup>9</sup>, M. M. Sharma<sup>9</sup>

### GMDN collaboration

<sup>1</sup> Shinshu University, **JAPAN**

<sup>2</sup> Bartol Research Institute, **USA**

<sup>3</sup> INPE, **BRAZIL**

<sup>4</sup> CRS/INPE, **BRAZIL**

<sup>5</sup> STE Laboratory, **JAPAN**

<sup>6</sup> University of Tasmania, **AUSTRALIA**

<sup>7</sup> College of Health Science, **KUWAIT**

<sup>8</sup> Alexandria University, **EGYPT**

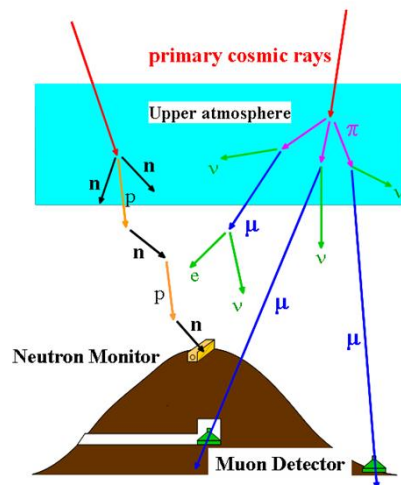
<sup>9</sup> Kuwait University, **KUWAIT**

15 people from 9 institutes in 6 countries  
working with 4 muon detectors in operation at...

**Nagoya**, **Hobart**, **São Martinho**, **Kuwait**  
(36 m<sup>2</sup>) (16 m<sup>2</sup>) (28 m<sup>2</sup>) (9 m<sup>2</sup>)

## Ground-based detectors

use atmosphere as an active component



➤ Ground-based detectors measure byproducts of the interaction of primary **Galactic Cosmic Rays (GCRs)**: predominantly protons and helium nuclei) with Earth's atmosphere.

➤ Two types of observation:

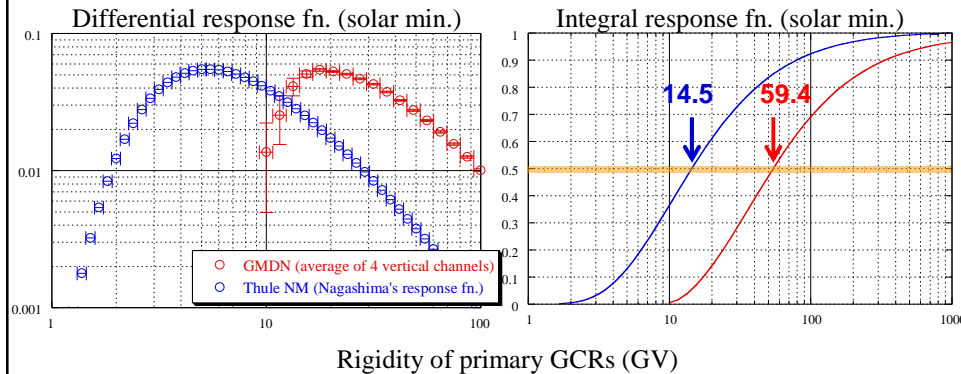
➤ **Neutron Monitors**

Typical energy of primary:  
~1 GeV for solar CRs (GLEs),  
~10 GeV for GCRs  
**omnidirectional**

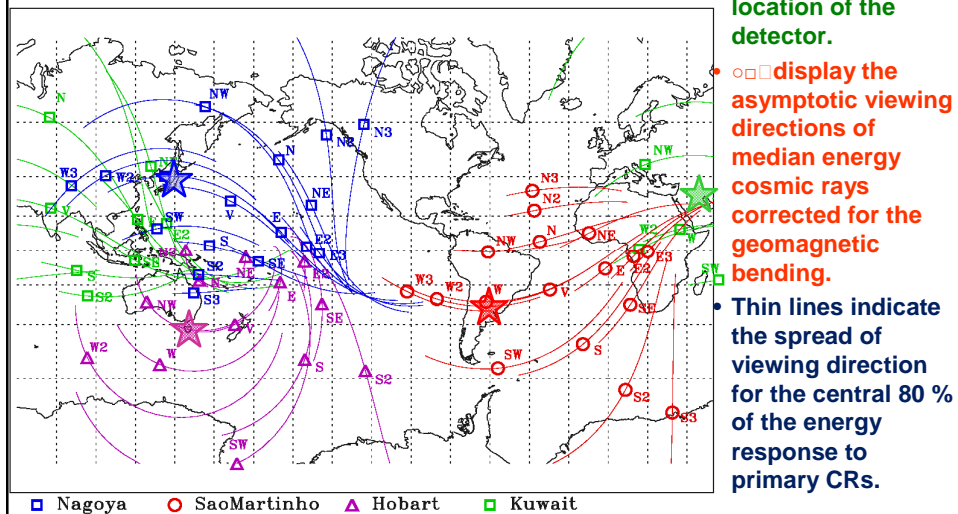
➤ **Muon Detectors**

Typical energy of primary:  
~50 GeV for GCRs  
(surface muon detector)  
**multi-directional**

## Energy responses of NM and GMDN to primary GCRs



## Viewing directions in the Global Muon Detector Network (GMDN)



## Deriving anisotropy vector

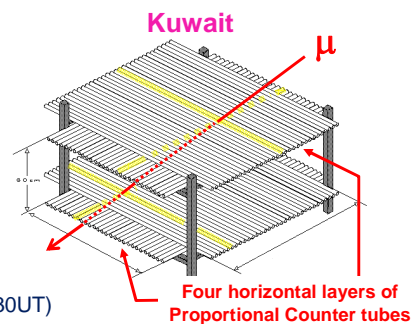
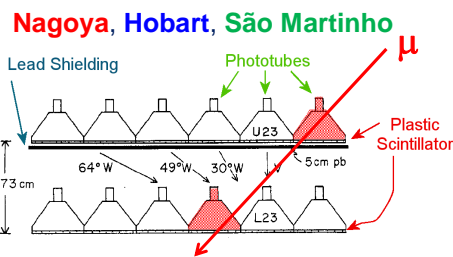
$I_{i,j}^{obs}(t)$  : pressure corrected count rate in the  $j$  th directional channel of the  $i$  th detector

$$I_{i,j}^{cal}(t) = I_{i,j}^0(t) + \xi_x^{GEO}(t) (c_{1,i,j}^1 \cos \omega t_i - s_{1,i,j}^1 \sin \omega t_i) + \xi_y^{GEO}(t) (s_{1,i,j}^1 \cos \omega t_i + c_{1,i,j}^1 \sin \omega t_i) + \xi_z^{GEO}(t) c_{1,i,j}^0$$

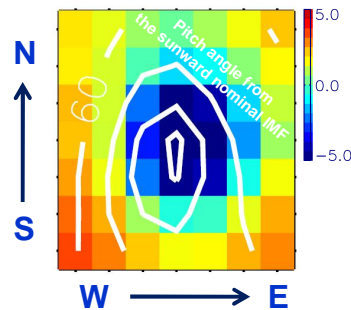
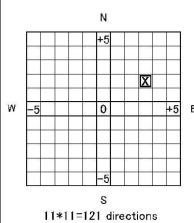
We derive  $\xi_x^{GEO}(t)$ ,  $\xi_y^{GEO}(t)$ ,  $\xi_z^{GEO}(t)$  which minimize ....

$$\sum_{i,j} |I_{i,j}^{obs}(t) - I_{i,j}^{cal}(t)|^2 / \sigma_{i,j}^2$$

## 2D map analysis



1 hour data (2006 12/14 09:30UT)



- Useful when analyzing local-structure like the “loss-cone”.
- Applied to the GMDN data (Fushishita et al., ApJ, 715, 2010).

## GCR transport equation (Parker 1965)

$$U(\mathbf{r}, p, t) dp = 4\pi p^2 f_0(\mathbf{r}, p, t) dp \quad : \text{GCR density (omnidirectional intensity)}$$

$$\frac{\partial U}{\partial t} + \underbrace{\nabla \cdot \left( \frac{2+\gamma}{3} UV_{\text{SW}} - \kappa \cdot \nabla U \right)}_{\text{SW convection diffusion}} = - \underbrace{\frac{\partial}{\partial p} \left( \frac{1}{3} p \mathbf{V}_{\text{SW}} \cdot \nabla U \right)}_{\text{Adiabatic cooling}}$$

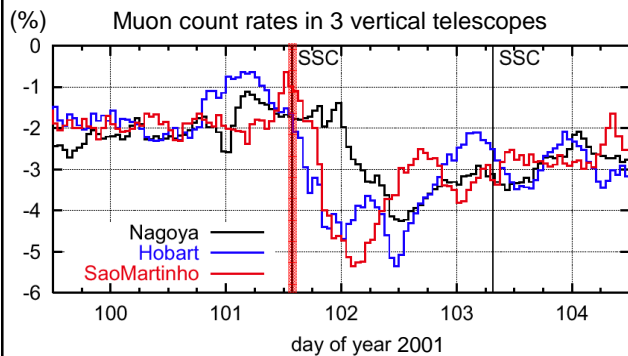
$$\mathbf{S}(\mathbf{r}, p, t) \quad : \text{streaming}$$

$$\xi(\mathbf{r}, p, t) = -\mathbf{S} / \left( \frac{1}{3} v U \right) \quad : \text{anisotropy}$$

$$\mathbf{G} \equiv \nabla U / U = \frac{v}{3} \kappa^{-1} \cdot \left\{ \frac{2+\gamma}{v} (\mathbf{V}_{\text{SW}} - \mathbf{v}_E) + \xi \right\}$$

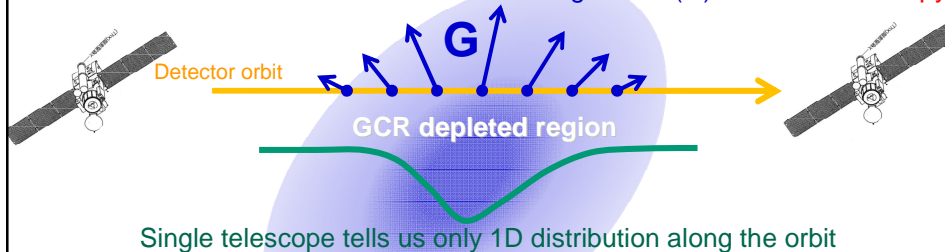
$\therefore$  **Anisotropy** ( $\xi$ ) tells us the **spatial gradient** ( $\mathbf{G}$ ) which **reflects the magnetic field geometry**

## What the anisotropy tells us?

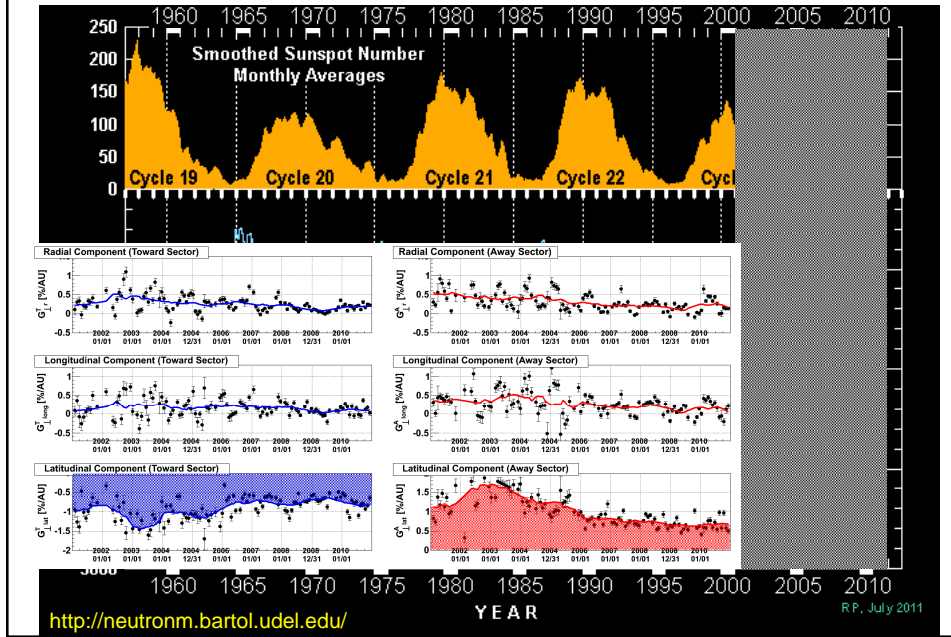


- **GCR density decrease (Forbush Decrease).**
- **Strong GCR streaming (wind) is associated.**
- **Need to measure density & streaming separately.**
- **Only global network can make such a precise measurement.**

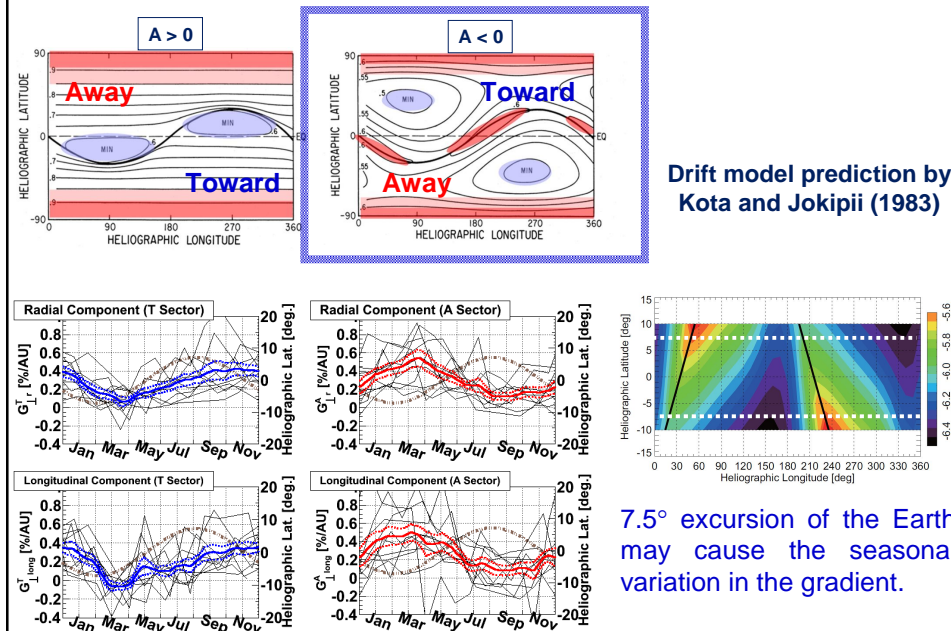
Can deduce 3D distribution from the GCR gradient ( $\mathbf{G}$ ) from the anisotropy



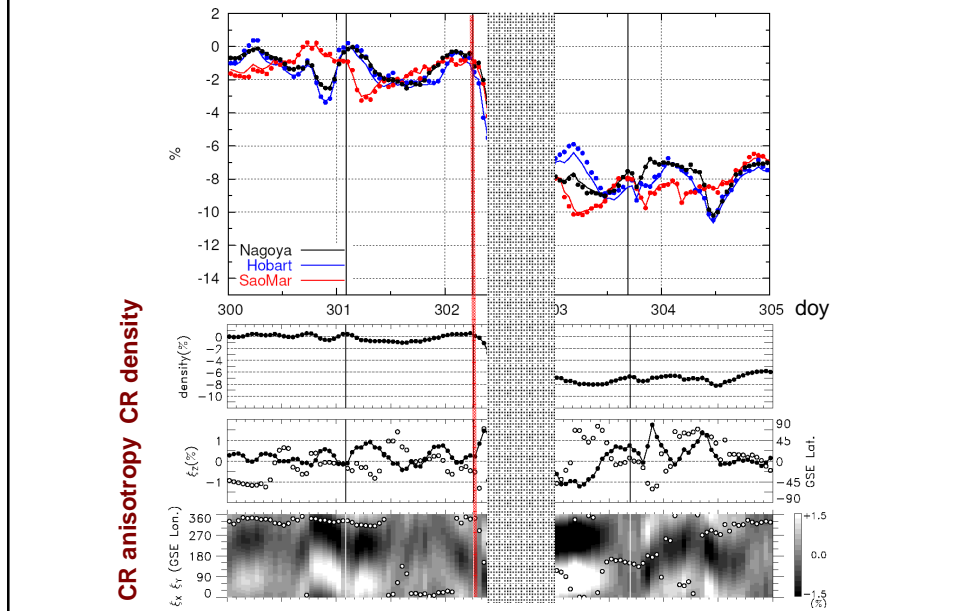
# What does GMDN tell us?



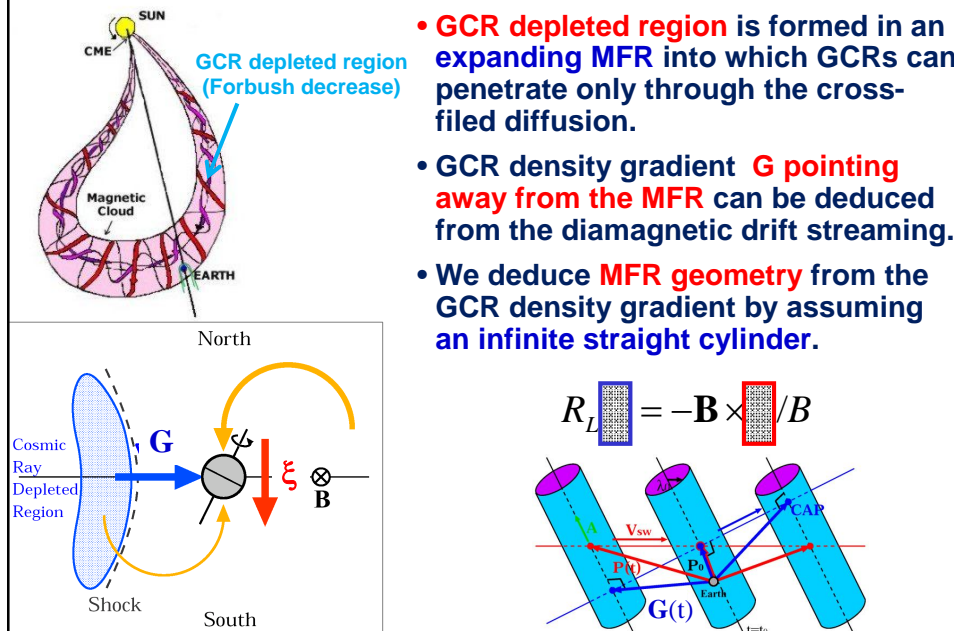
# Testing the drift model



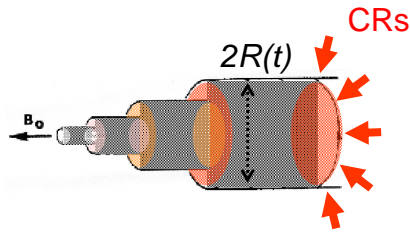
## FD & CME on Oct. 29, 2003



## GCRs in the Magnetic Flux Rope



# CR diffusion into MFR



CRs can penetrate into MFR only by the cross-field diffusion



$\kappa_{\perp}$  can be evaluated from CR data during MFR

Self-similar expansion of MFR

$$R(t) = R_0(t/t_0), \quad v(r,t) = v_0(r/R_0)/(t/t_0)$$

$$\kappa_{\perp}(t) = \kappa_0 v_0 R(t),$$

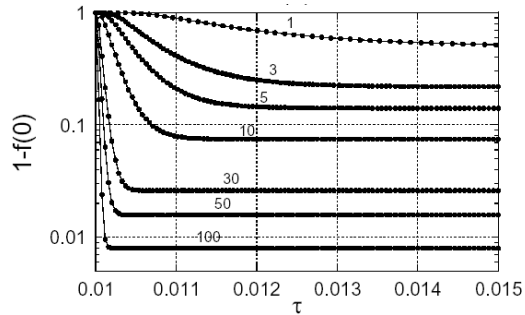
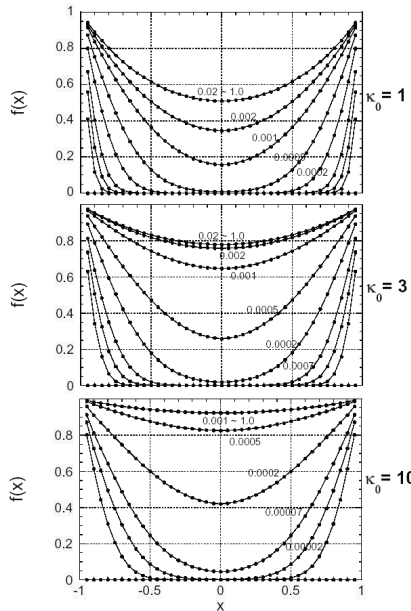
$$f \propto p^{-(2+\gamma)}$$

$$\frac{\partial f}{\partial s} = \kappa_0 \left( \frac{\partial^2 f}{\partial x^2} + \frac{1}{x} \frac{\partial f}{\partial x} \right) - \frac{2(2+\gamma)}{3} f \quad \begin{matrix} x = r/R_0 \quad (0 \leq x \leq 1) \\ s = \log \tau, \quad \tau = t/(R_0^2/\kappa_0) \quad (\tau \geq 0) \end{matrix}$$

Cross-field diffusion      Adiabatic cooling

Dimensionless parameter  $\kappa_0$  determines  $\kappa_{\perp}$

# Numerical solutions



- $\kappa_0$  appropriate to the observed FD is 10 ~ 50.
- $f(x)$  rapidly becomes stationary, much earlier than the 1<sup>st</sup> contact of Earth with MFR at  $t=1$ .

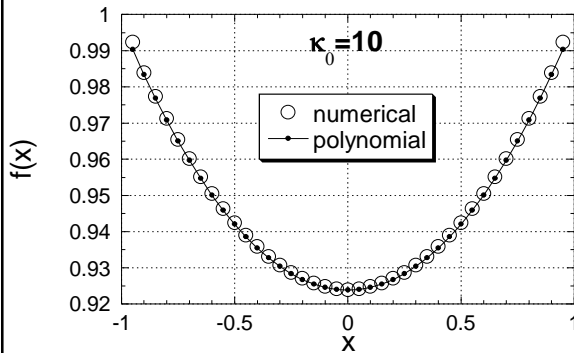


## Stationary solution

$$\frac{\partial^2 f}{\partial x^2} + \frac{1}{x} \frac{\partial f}{\partial x} = \Gamma f \quad : \quad \Gamma = \frac{2(2+\gamma)}{3\kappa_0}$$

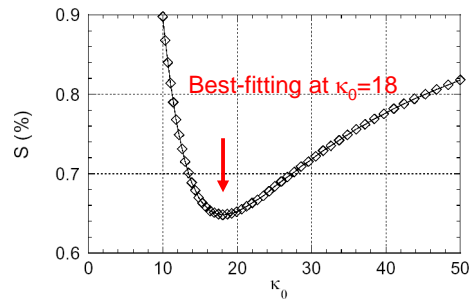
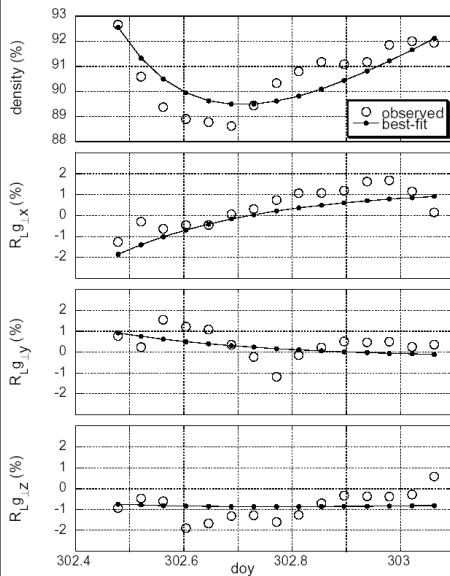
$f(x)$  is given by a polynomial expression....

$$f(x) = \sum_{n=0}^{\infty} a_n x^n \quad \begin{aligned} a_n &= \frac{\Gamma}{n^2} a_{n-2} & : n=0, 2, 4, \dots \\ &= 0 & : n=1, 3, 5, \dots \end{aligned}$$



*Use polynomial  $f(x)$  (  $n \leq 6$  )  
for best-fitting to the data*

## Best-fitting to the data (with MFR geometry)



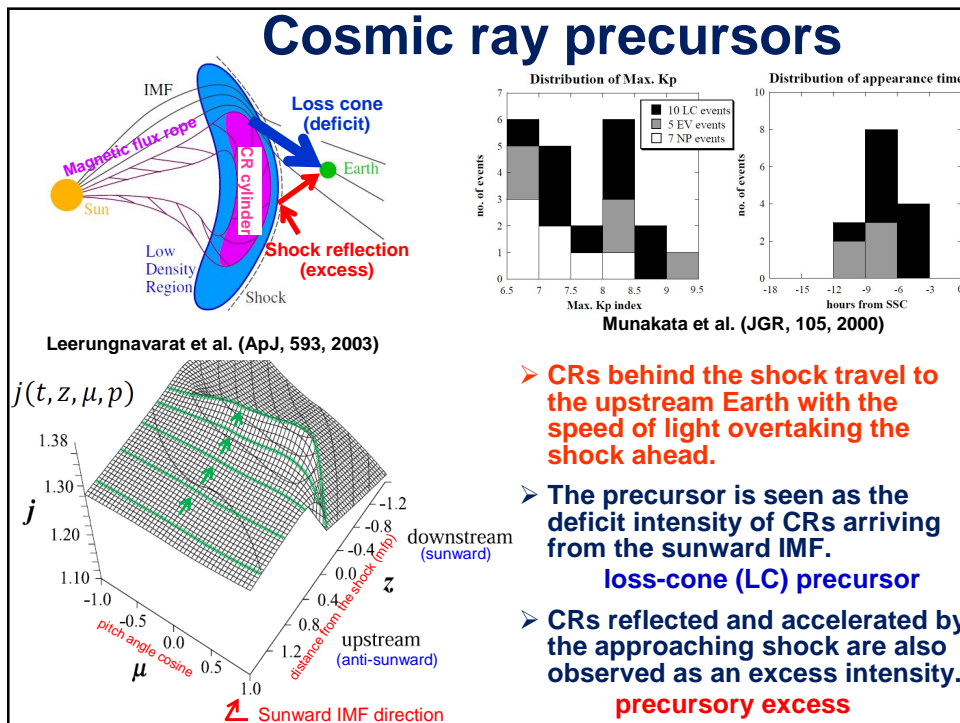
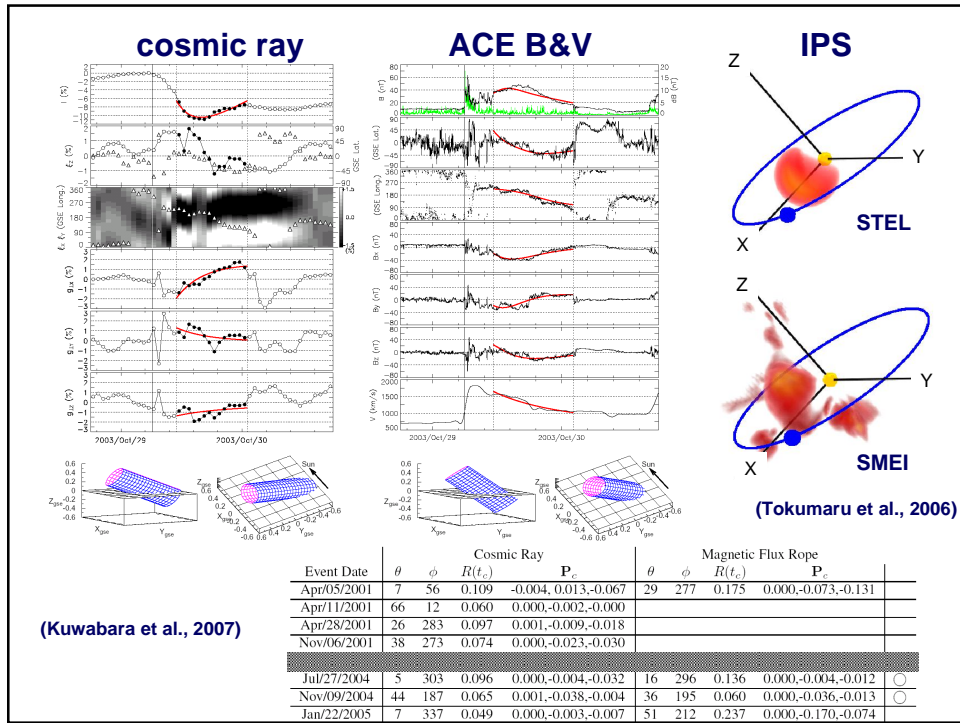
$$\kappa_{\perp} = \kappa_0 v_0 R_0 = 1.6 \times 10^{21} \text{ (cm}^2/\text{s)}$$

$(v_0 = 0.21 \text{ AU/day, } R_0 = 0.17 \text{ AU})$

$$\kappa_{\parallel} \sim 3.0 \times 10^{23} \text{ (cm}^2/\text{s) for muon}$$

(Munakata et al., 2002)

$$\therefore \kappa_{\perp} / \kappa_{\parallel} \sim 0.005 \text{ for muon}$$



# CME event in December 2006

X3.4 flare onset 02:38UT on 12/13

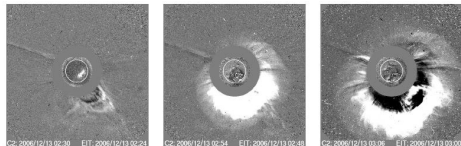


FIG. 1.—Difference images of the CME and the source region at different times. ET difference images at 195 Å are shown within the white circles. A transition layer is visible around the CME front, indicating the existence of a shock (middle and right). Adapted from the LASCO/CME website at <http://cdm.gsfc.nasa.gov>. [This figure is available as an image animation in the electronic edition of the Journal.]

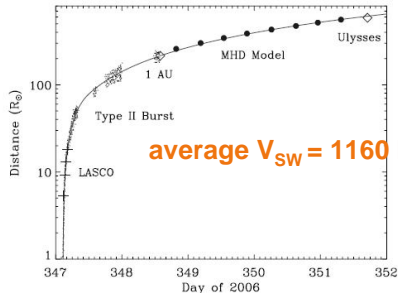
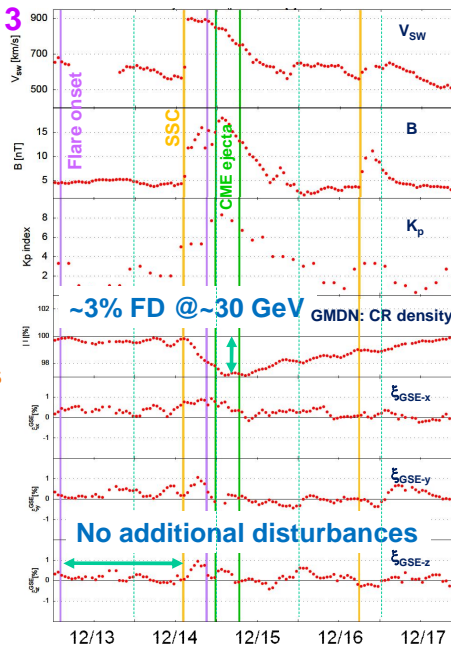


FIG. 10.—Height-time profile (solid line) of shock propagation determined from the frequency drift of the type II bands (dots) and shock parameters measured at 1 AU (where  $R_s$  is the solar radius). Plus signs denote the LASCO data. Diamonds indicate the shock arrival times at 1 AU and Ulysses. Between 1 AU and Ulysses are the shock arrival times (filled circles) at 1.2, 1.4, 1.6, 1.8, 2.0, 2.2, 2.4, and 2.6 AU predicted by the MHD model. [See the electronic edition of the Journal for a color version of this figure.]

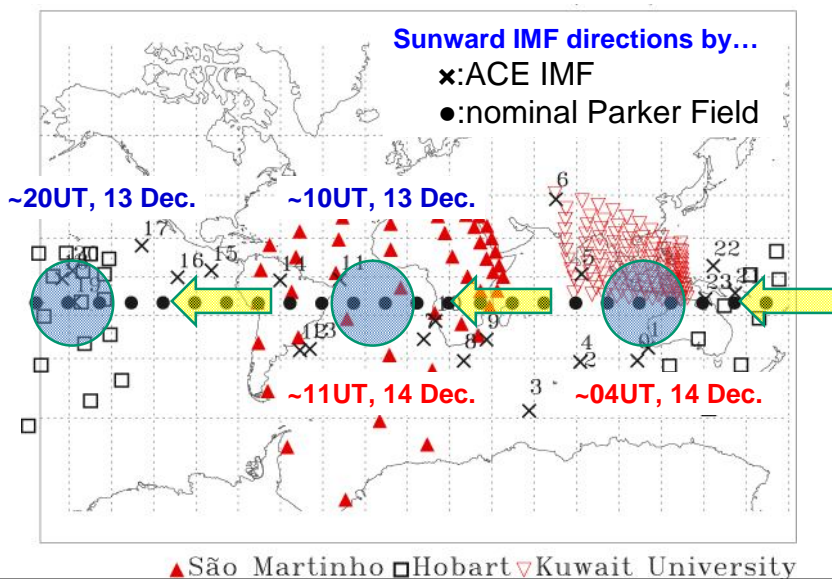
Liu et al., ApJ 689, 2008



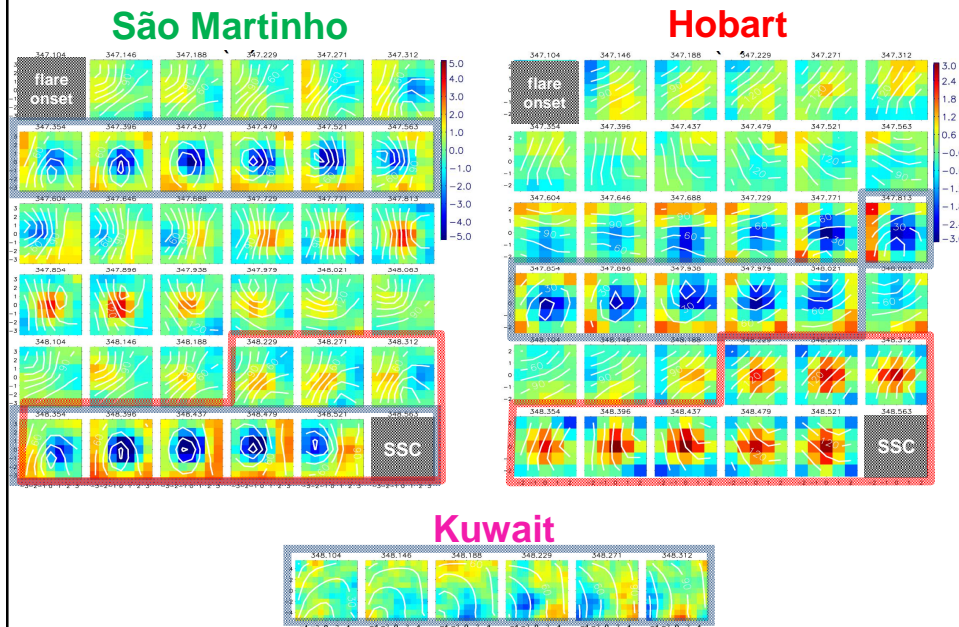
~3% FD @ ~30 GeV GMDN: CR density

No additional disturbances

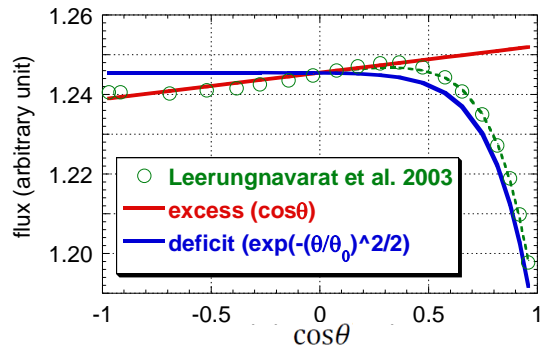
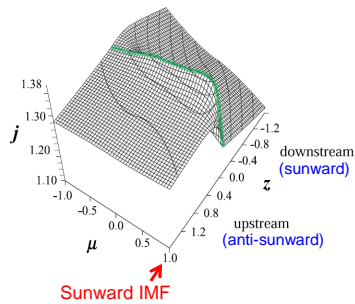
# Sunward IMF directions & FOV



# Observed 2D maps



# Model for the best-fit analysis



$$j(z(t), \mu, p) =$$

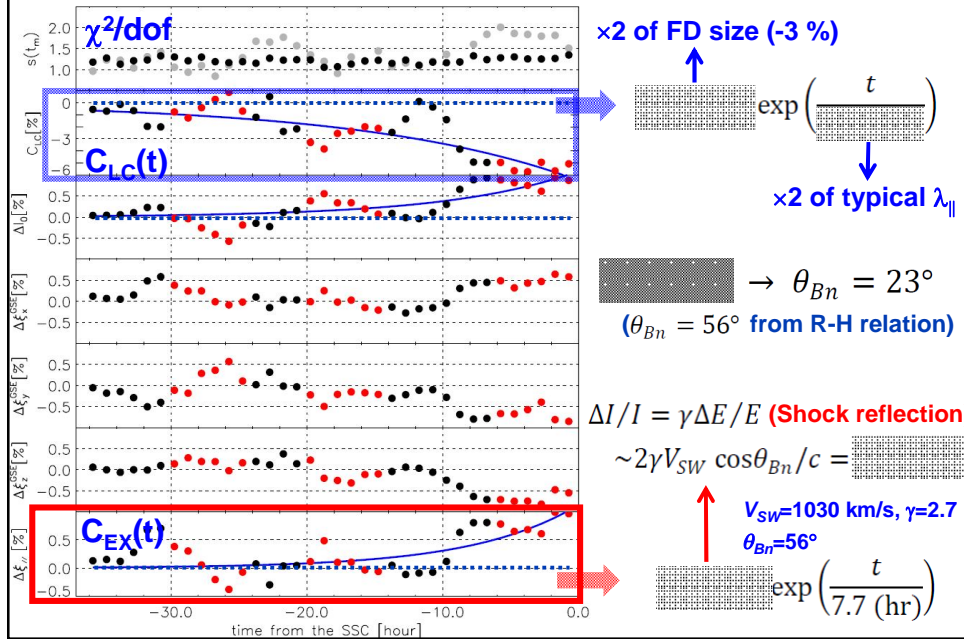
( $\theta$  : pitch angle measured from the sunward IMF direction)

$$\boxed{C_{LC}(z(t))} \left(\frac{p}{30}\right)^{-1} \exp\left(-\frac{\theta^2}{2}\right) + \boxed{C_{EX}(z(t))} (1 + \cos\theta)/2$$

**Loss-cone (deficit)**      **Shock reflection (excess)**

Loss-cone width (constant)  
Related to shock normal

## Best-fit parameters



## Summary

- Muon detectors measure **muons** produced by the interaction of high-energy ( $E > 1 \text{ GeV}$ ) primary cosmic rays (CRs) with the atmospheric nuclei.
- Due to the high longitudinal momentum transfer to muons, their incident directions well preserve the incident direction of primary CRs  $\square$  the **multidirectional muon detector**.
- GMDN is a network of four muon detectors in **Japan, Brazil, Australia, Kuwait**, and capable for measuring CR intensities from many directions simultaneously.
- We measure the **CR streaming** and **CR precursors** accurately with the GMDN and deduce the large-scale magnetic structure in the Space Weather.

GMDN has its root on the international collaboration.

**Anybody willing to join us would be welcome!**

Contact: kmuna00@shinshu-u.ac.jp

## possible Canadian muon detectors

Parameters set for calculations

	Ottawa	Vancouver
Latitude	45.4N	45.2N
Longitude	75.7W	123.0W
Altitude	70m	60m

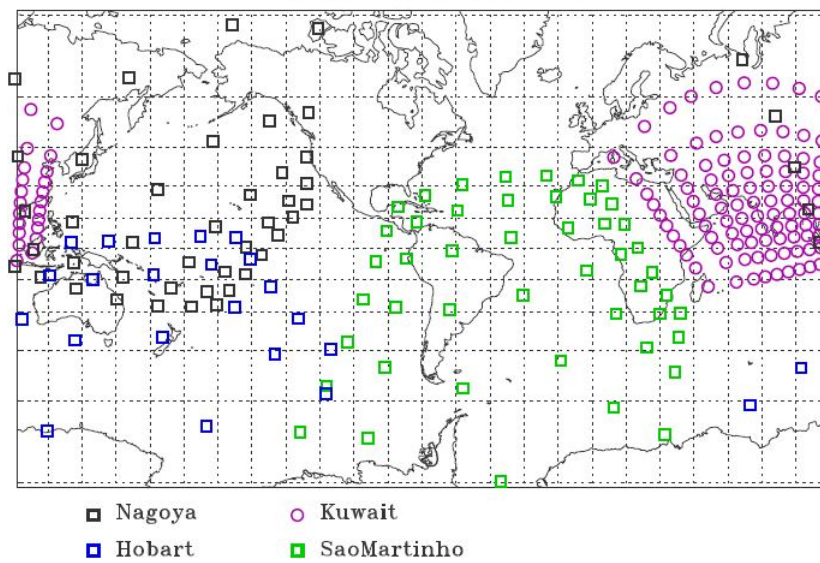
Obtained detector response (5m $\times$ 5m PRC detector)

	Ottawa	Vancouver
Cut-off rigidity	1.7GV	2.6GV
Median rigidity	52.4GV	52.5GV
Hourly trigger rate	6,315,000	6,304,000

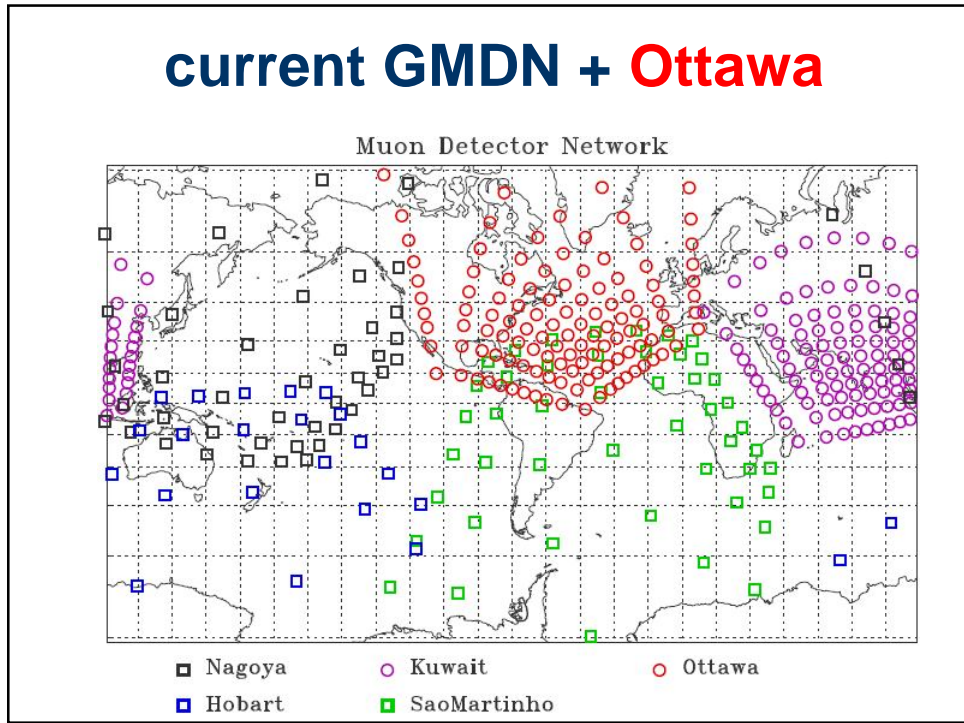
Notes: Using Nagashima's muon response function + IGRF-11 geomagnetic field model (2010). Cut-off and median rigidities are the values at vertical direction

## current GMDN

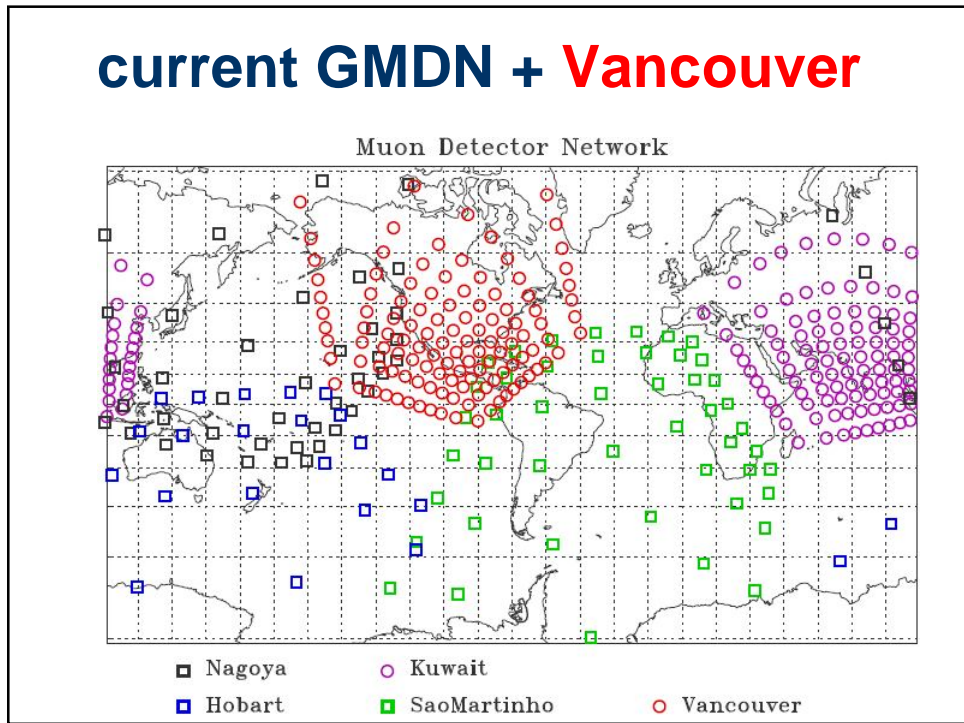
Muon Detector Network

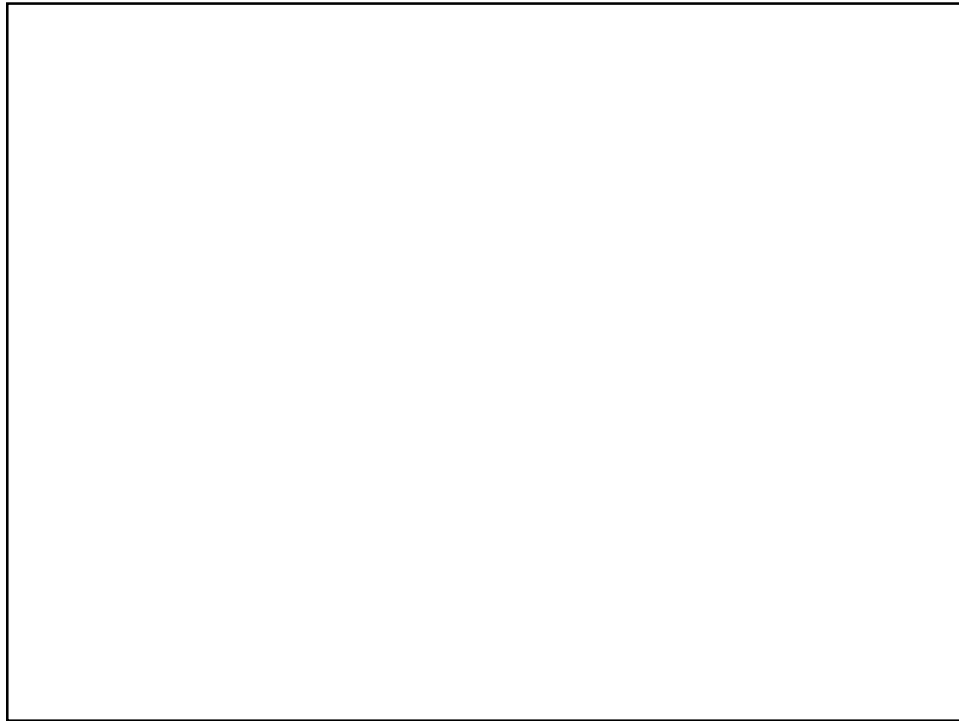


## current GMDN + Ottawa



## current GMDN + Vancouver

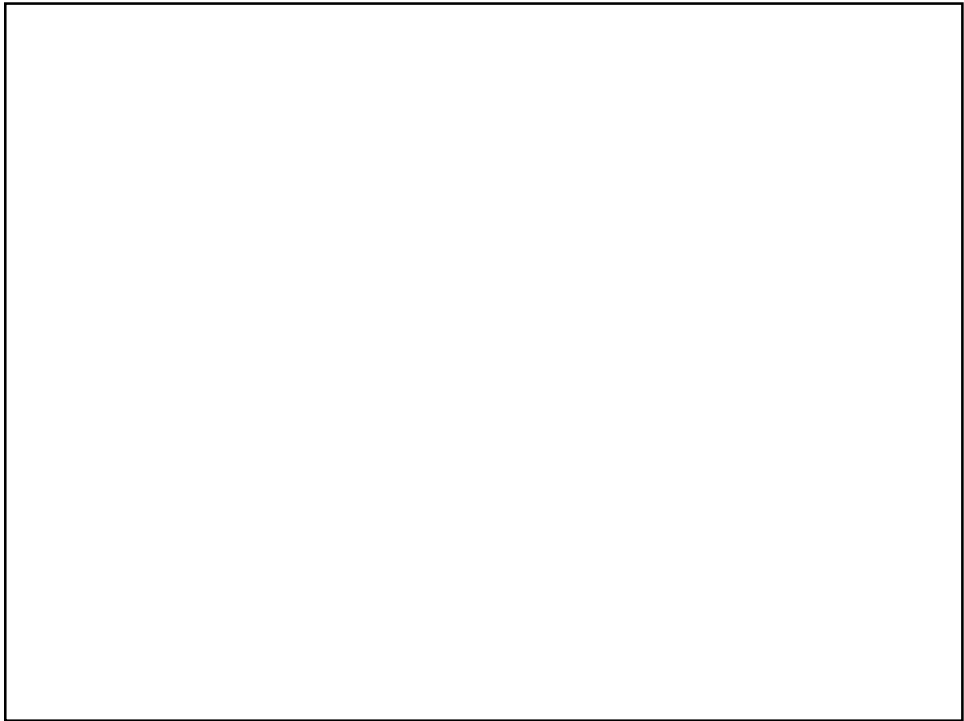




## Cost of each component

item	Spec.	producer	Cost (USD/100)
Plastic scintillator	0.5x0.5x0.1(0.05) m <sup>3</sup>	CI industry Co.	1,000
Photomultiplier tube	5" (R877)	Hamamatsu photonics	1,500
Proportional counter tube	5 m long, 0.1 m $\phi$	CI industry Co.	450
Amplifier board		CI industry Co.	3,240
Cables (EHT + signal)			300
EHT distributor		CI industry Co.	6,500
Steel frame		CI industry Co.	14,500
Lead brick	0.2x0.1x0.5 m <sup>3</sup>	Mitsui Metal Co.	32
FPGA recorder unit		Shinshu	6,000
Barometer	Digi-quartz	Paroscientific Co.	7,000
PC , GPS, DC_PS... etc.			3,000



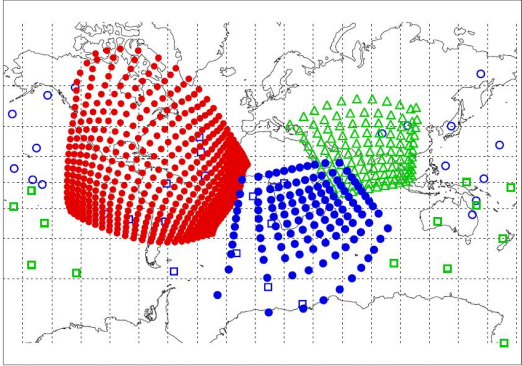


## Possible future expansions of **GMDN**

- We plan to **expand detection areas** of two small detectors.

Hobart: 9 m<sup>2</sup> □ 16 m<sup>2</sup>, Kuwait : 9 m<sup>2</sup> □ 25 m<sup>2</sup>

- We also plan to install new detectors in **Mexico** and **South Africa**.



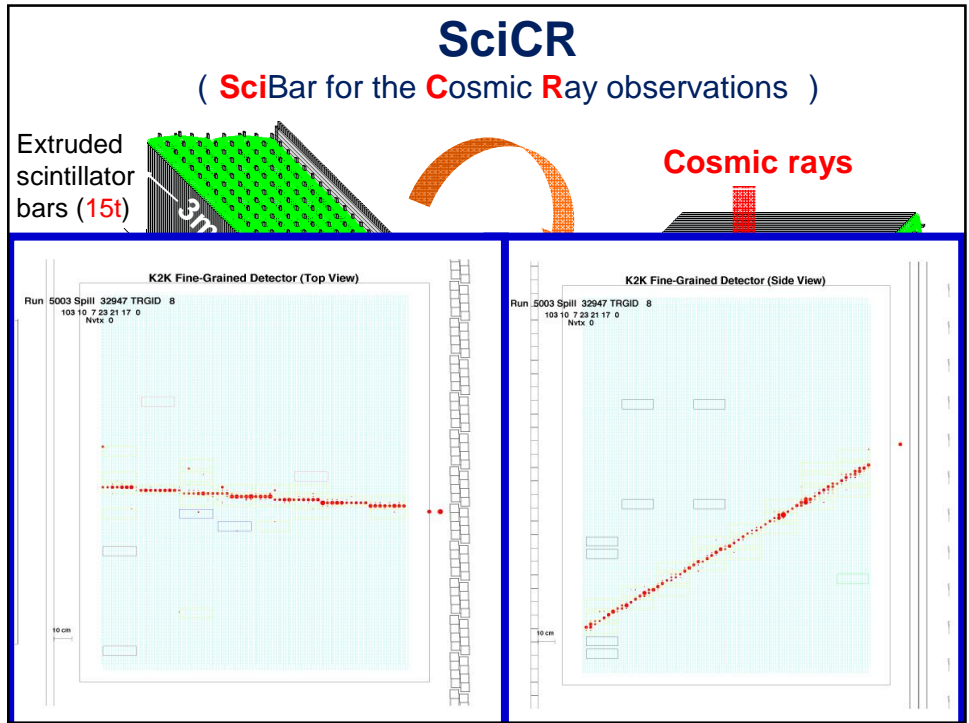
○ Nagoya □ Sao Martinho □ Hobart ▲ Kuwait University  
● Sierra Negra ● Hermanus

### Sierra Negra (Mexico)

- 4600 m a.s.l.
- 14k SciBars viewed by 220 multi-anode PMTs.
- Primarily for the solar neutron detection, but can be used for muon measurement.

### Hermanus (South Africa)

- 200 PRC tubes in four horizontal layers will form a 25 m<sup>2</sup> muon detector.



## Observation site

**Mt. Sierra Negra in Mexico**

**Observation hut**

**mini-SciCR** prototype detector in operation at Mt. Sierra Negra since Oct. 2010

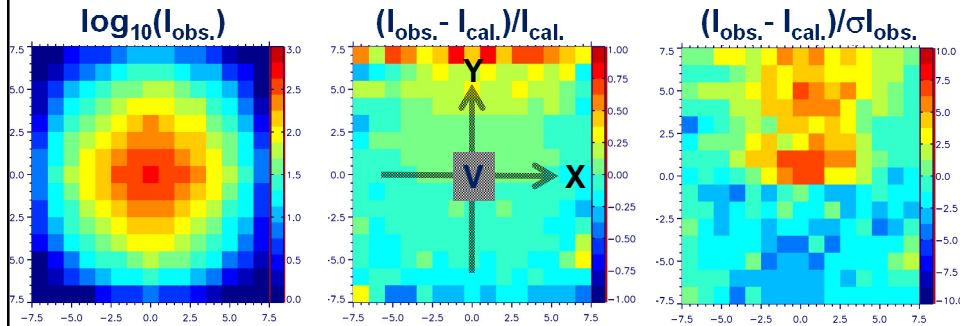
➤ We put a 5 cm lead layer to absorb the soft-component radiation in the air.

➤ We use only two pairs of x-y layers for muon measurement.

## Preliminary results with mini-SciCR

We trigger the muon measurement by 4-fold coincidence between the top & bottom x-y layers.

### Observed 2D-maps of hourly count rate



Vertical count rate: **473 cph**

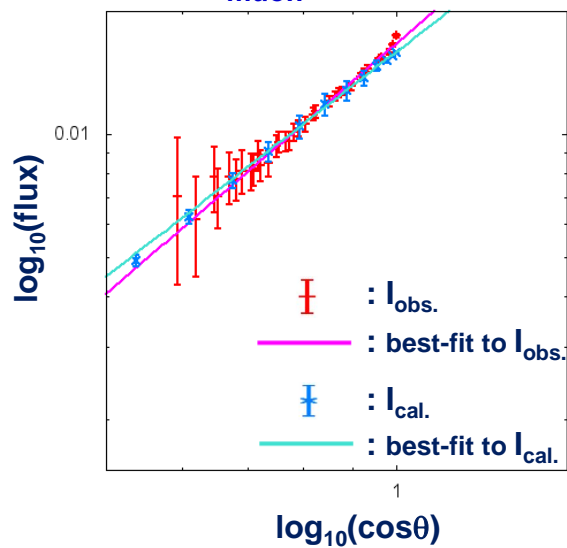
(**363 cph** for SciCR with much higher angular resolution)

Geomagnetic cut-off rigidity (vertical incident): **7.9 GV**

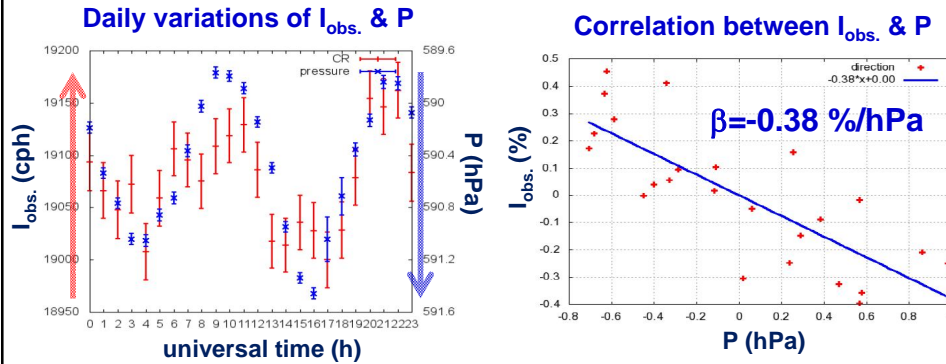
Median primary rigidity: **34 GV**

## Zenith angle distribution

$$I_{\text{muon}} \propto \cos^2 \theta$$

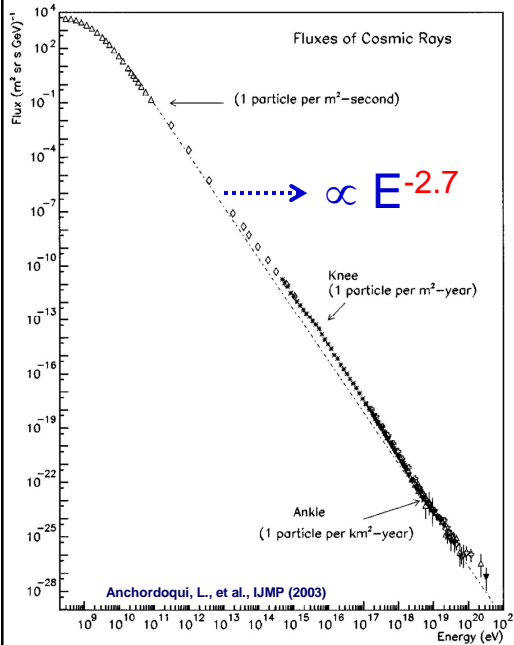


# Atmospheric pressure (barometer) effect (results from ~1 month measurement **without lead layer**)



$\beta$  is larger than the typical  $\sim -0.1 \text{ \%/hPa}$  for muons probably due to  $\sim 30 \text{ \%}$  contamination of AS particles.

# Galactic Cosmic Rays (GCRs)



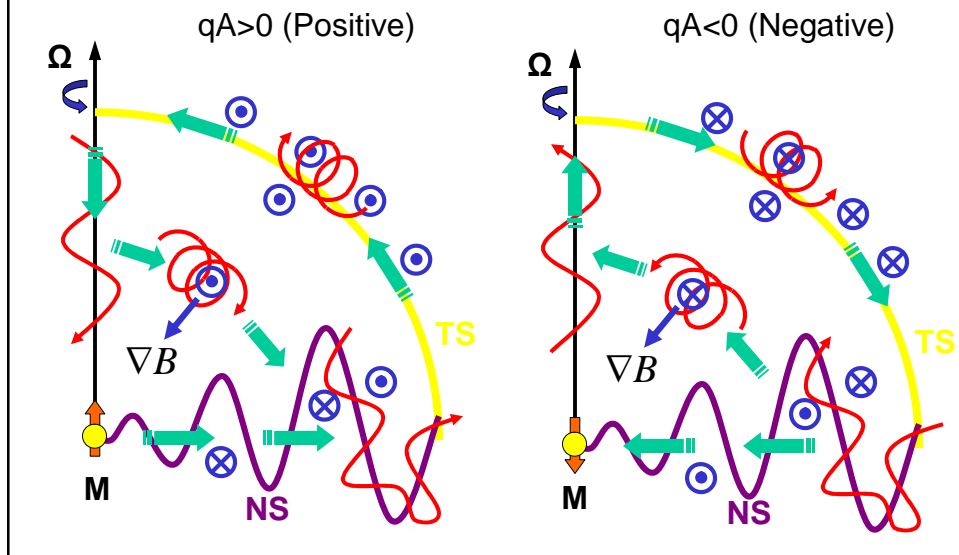
- $\sim 85 \text{ \%}$  **protons**
- $\sim 10 \text{ \%}$  **helium nuclei**
- a few % **heavier nuclei**
- $\sim 1 \text{ \%}$  **electrons**

## Observables

- Energy spectrum
- Elementary & isotopic compositions
- **Isotropic intensity**  
(GCR density)
- **Anisotropy**  
(GCR streaming)

# Drift model (Jokipii et al., ApJ, 213, 1977)

$$qA \equiv q\Omega \cdot \mathbf{M}$$



We first correct the observed  $\xi^{GSE}$ , as ....

$$\xi^{GSE} + (2 + \gamma)(\mathbf{V}_{SW} - \mathbf{v}_E) \equiv \xi_{\parallel} + \xi_{\perp}$$

anisotropy

density gradient

$$\xi_{\perp}(t) = R_L(t)(\alpha_{\perp} \mathbf{G}_{\perp}(t) - \mathbf{b}(t) \times \mathbf{G}_{\perp}(t)),$$

$$\alpha_{\perp} = \lambda_{\perp}(t)/R_L(t) = 3\kappa_{\perp}(t)/R_L(t)/c,$$

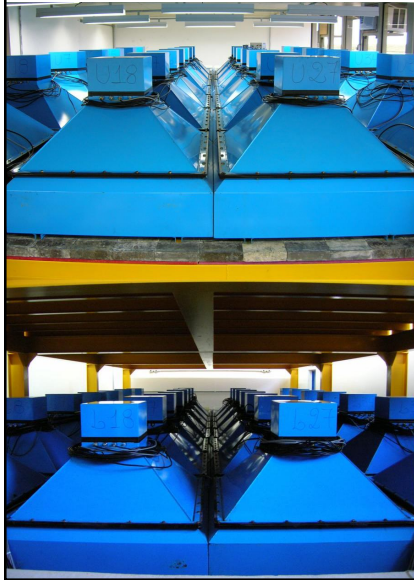
$\mathbf{b}(t)$ : unit vector along the IMF

$$\mathbf{G}_{\perp}(t) = \begin{pmatrix} \alpha_{\perp} & b_z(t) & -b_y(t) \\ -b_z(t) & \alpha_{\perp} & b_x(t) \\ b_y(t) & -b_x(t) & \alpha_{\perp} \end{pmatrix}^{-1} \xi_{\perp}(t)/R_L(t).$$

density gradient                      anisotropy

We haven't looked at  $\xi_{\parallel}$  yet...

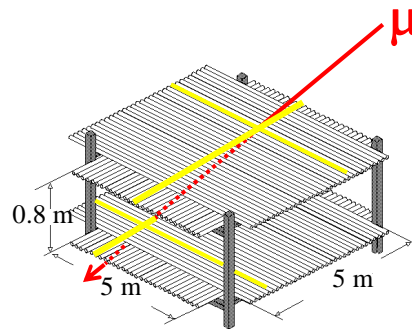
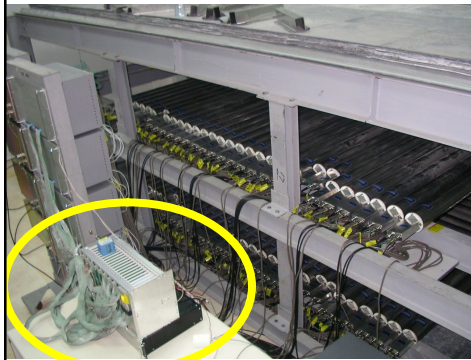
## São Martinho muon detector enlarged in December 2005



Two old (useless?) guys in between  
**excellent young people!**



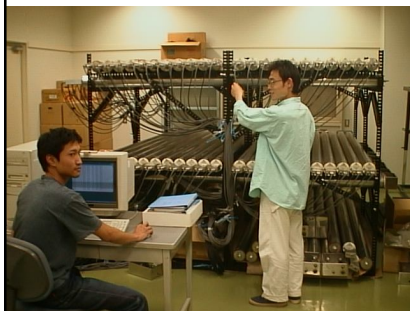
## Muon detector in Kuwait-City



### FPGA ( Xilinx XC2S200 )

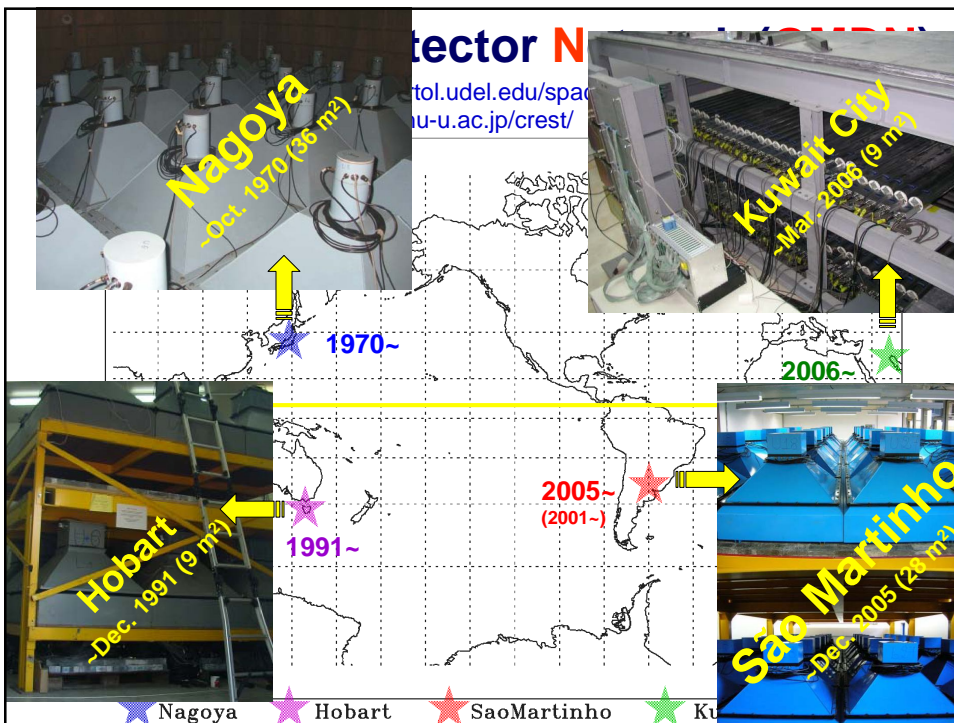
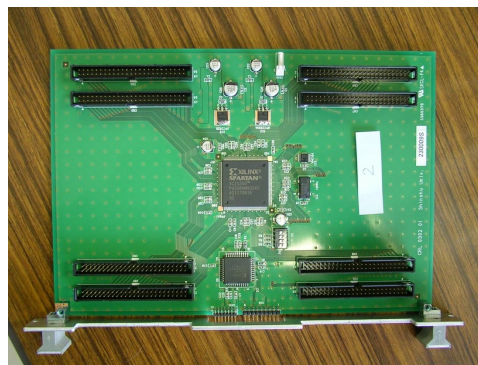
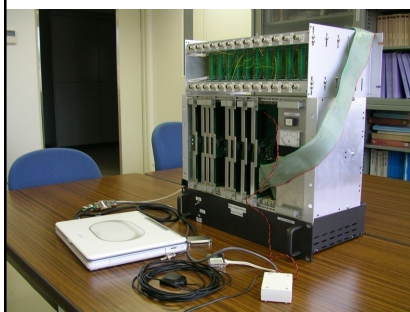
- **Fast** identification of incident direction
- Count rate in **529** (23×23) directions can be stored in **5** FPGAs
- **Flexible** system can be realized
- **Low power consumption**

# New data recording system



## FPGA ( Xilinx XC2S200 )

- Fast identification of incident direction
- Count rate in 441 (21×21) directions can be stored in 3 FPGAs
- Flexible system can be realized
- Low power consumption



## 大気ミューオンの伝播方程式系

$N(E, y)$  : 核子 ( p, n )

$$\frac{dN(E, y)}{dy} = -\frac{1}{\lambda_N(E)} N(E, y) + \int_E^{E_0} \frac{F_{NN}(E, E')}{\lambda_{NN}(E') \cdot E} N(E', y) dE' \quad : y = x \sec\theta$$

$N \rightarrow N, X$ 
 $N \rightarrow N$

$\pi(E, y)$  : パイオン

$$\frac{d\pi(E, y)}{dy} = -\left( \frac{1}{\lambda_\pi(E)} + \frac{\varepsilon_\pi(y)}{E \cdot y} \right) \pi(E, y)$$

$\pi \rightarrow \pi, X$   $\pi \rightarrow \mu$  decayによる $\pi$ の減少

$\mu(E, y)$  : ミューオン

$$\frac{d\mu(E, y)}{dy} = \int_E^{E_0} \frac{F_{N\pi}(E, E')}{\lambda_N(E') \cdot E} N(E', y) dE' + \int_E^{E_0} \frac{F_{\pi\pi}(E, E')}{\lambda_\pi(E') \cdot E} \pi(E', y) dE'$$

$N \rightarrow \pi$ 
 $\pi \rightarrow \pi$

$$\frac{d\mu(E, y)}{dy} = \int_E^{E(m_\pi/m_\mu)^2} \frac{\varepsilon_\pi}{y} \cdot \pi(E', y) \frac{dE'}{p'^2} \left\{ 1 - \left( \frac{m_\mu}{m_\pi} \right)^2 \right\}^{-1}$$

$\pi \rightarrow \mu$  decayによる $\mu$ の増加

$$\frac{dP_\mu(E, y)}{dy} = -\frac{\varepsilon_\mu}{E \cdot y} \cdot P_\mu(E, y) \quad E = E_f + \beta(y_f - y)$$

$\mu \rightarrow e$  decayによる $\mu$ の減少       $\mu$  エネルギーの電離損失

Response function:  $R(p, x, \theta, p_{\mu c})$  [ $\text{m}^2/\text{s}/\text{sr}/\text{GV}$ ]

$J(p)$  : GCR rigidity spectrum

$Y(p, x, \theta, p_\mu)$  : No. of muons with  $p_\mu$  produced by a GCR with  $p$  ( Yield function )

$$R(\underbrace{p}_{\text{GCR}}, \underbrace{x, \theta, p_{\mu c}}_{\text{Muon detector}}) = \int_{p_{\mu c}}^{\infty} J(p) \cdot Y(p, x, \theta, p_\mu) dp_\mu$$

$x$  ( atmospheric depth ) : 550, 720, 940, 1030 [ $\text{g}/\text{cm}^2$ ]

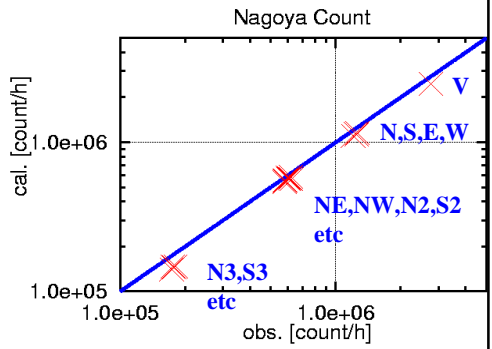
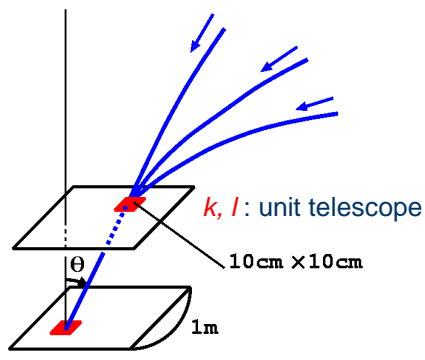
$\theta$  ( zenith angle ) : 0, 16, 32, 48, 64 [ $^\circ$ ]

$p_{\mu c}$  ( muon threshold rigidity ) : 26 values in 0.178 ~ 5620 [GV]

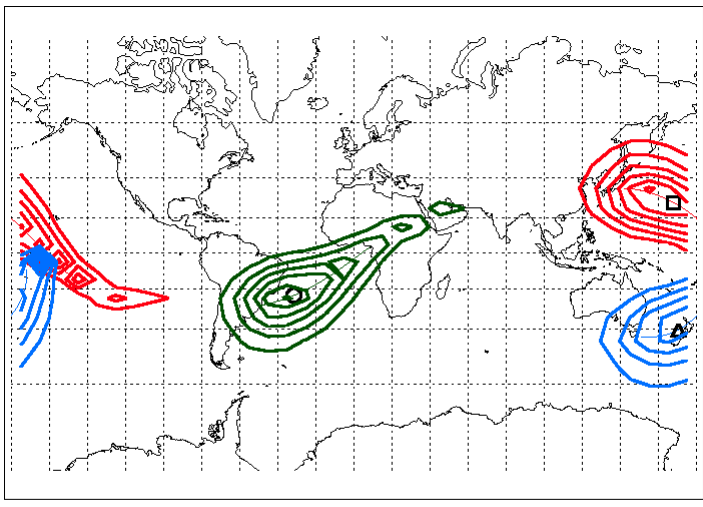


$$I_{i(k,l)}^{cal} = (S\Omega)_{k,l} \int_{P_c}^{\infty} R(p, x, \theta_{k,l}, p_{\mu c}(\theta_{k,l}, \phi_{k,l})) dp$$

$\theta_{k,l}, \phi_{k,l}$  : zenith & azimuth angles  $P_c(\theta_{k,l}, \phi_{k,l})$  : geomag. cut-off rigidity



## 方向計の視野の広がり



- Nagoya muon telescopes
- △ Hobart muon telescopes
- Sao Martinho prototype telescopes

$$\begin{aligned}
D(t) &= \sum_{n=0}^{\infty} \sum_{m=0}^n (A_n^m \cos m\omega t + B_n^m \sin m\omega t) \\
&= A_0^0 c_0^0 + A_1^0 c_1^0 + (c_1^1 x_1^1 + s_1^1 y_1^1) \cos \omega t + (-s_1^1 x_1^1 + c_1^1 y_1^1) \sin \omega t \\
&= A_0^0 c_0^0 + x_1^1 (c_1^1 \cos \omega t - s_1^1 \sin \omega t) + y_1^1 (s_1^1 \cos \omega t + c_1^1 \sin \omega t) + A_1^0 c_1^0
\end{aligned}$$

$$\begin{aligned}
F(\chi) &= \sum_{n=0}^{\infty} \sum_{m=0}^n \eta_n P_n^m(\cos \theta_R) P_n^m(\cos \theta_J) \cos m(\alpha_J - \alpha_R) \\
&= \sum_{n=0}^{\infty} \sum_{m=0}^n \eta_n P_n^m(\cos \theta_R) P_n^m(\cos \theta_J) \cos m\omega(t - t_R) \\
&= \sum_{n=0}^{\infty} \sum_{m=0}^n (x_n^m \cos m\omega t + y_n^m \sin m\omega t)
\end{aligned}$$

$$\begin{pmatrix} A_n^m \\ B_n^m \end{pmatrix} = \begin{pmatrix} c_n^m & s_n^m \\ -s_n^m & c_n^m \end{pmatrix} \begin{pmatrix} x_n^m \\ y_n^m \end{pmatrix}$$

$$\begin{aligned}
c_{ni(k,l)}^m &= \frac{1}{I_{i(k,l)}^{\text{cal}}} (S\Omega)_{k,l} \int_{P_c}^{\infty} R(p, x, \theta_{k,l}, p_{\mu c}(\theta_{k,l}, \phi_{k,l})) P_n^m(\cos \theta_{k,l}^{\text{or}}(p)) \cos m(\psi_{k,l}^{\text{or}}(p) - \psi_i^{\text{st}}) dp \\
s_{ni(k,l)}^m &= \frac{1}{I_{i(k,l)}^{\text{cal}}} (S\Omega)_{k,l} \int_{P_c}^{\infty} R(p, x, \theta_{k,l}, p_{\mu c}(\theta_{k,l}, \phi_{k,l})) P_n^m(\cos \theta_{k,l}^{\text{or}}(p)) \sin m(\psi_{k,l}^{\text{or}}(p) - \psi_i^{\text{st}}) dp
\end{aligned}$$

$$\Delta I_{i(k,l)}^{\text{obs}}(t) = I_{i(k,l)}^{\text{obs}}(t) - \bar{I}_{i(k,l)}(t) \quad \Delta I_{i(k,l)}^{\text{cal}}(t) = I_{i(k,l)}^{\text{cal}}(t) - \bar{I}_{i(k,l)}(t)$$

$$s I_{i(k,l)}^{\text{obs}}(t) = \Delta I_{i(k,l)}^{\text{obs}}(t) / \sigma_{i(k,l)}$$

$$\bar{I}_0(t) = \sum_{t=23}^t I_0(t) / 24$$

$$\bar{\xi}_x^{\text{GEO}}(t) = \sum_{t=23}^t \xi_x^{\text{GEO}}(t) / 24$$

$$f(\theta, P, t) = C_{\text{LC}}(t) f_{\text{LC}}(\theta, P) + C_{\text{EX}}(t) (1 + \cos \theta) / 2$$

$$\bar{\xi}_y^{\text{GEO}}(t) = \sum_{t=23}^t \xi_y^{\text{GEO}}(t) / 24$$

$$\bar{\xi}_z^{\text{GEO}}(t) = \sum_{t=23}^t \xi_z^{\text{GEO}}(t) / 24$$

$$I_{i(k,l)}^{\text{cal}}(t) = I_{i(k,l)}^0(t)$$

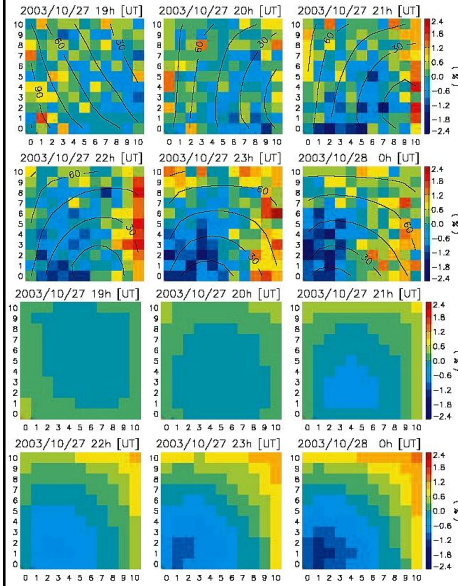
$$+ \xi_x^{\text{GEO}}(t) (c_{1i(k,l)}^1 \cos \omega t_i - s_{1i(k,l)}^1 \sin \omega t_i)$$

$$+ \xi_y^{\text{GEO}}(t) (s_{1i(k,l)}^1 \cos \omega t_i + c_{1i(k,l)}^1 \sin \omega t_i) + \xi_z^{\text{GEO}}(t) c_{1i(k,l)}^0$$

$$+ C_{\text{LC}}(t) \frac{\int_{P_{i(k,l)}^{\text{cut}}}^{\infty} N_{i(k,l)}(P) f_{\text{LC}}(\theta_{i(k,l)}(P), P) dP}{\int_{P_{i(k,l)}^{\text{cut}}}^{\infty} N_{i(k,l)}(P) dP}$$

$$S = \sqrt{\frac{1}{NM} \sum_{m=1}^M \sum_{i,k,l=1}^N \frac{(I_{i(k,l)}^{\text{obs}}(t_m) - I_{i(k,l)}^{\text{cal}}(t_m))^2}{\sigma_{i(k,l)}^2}}$$

# A Loss-cone precursor observed with muon hodoscope on Oct. 28, 2003



- Mt Norikura field of view over a 6-hr period prior to storm sudden commencement.
- TOP: Observations
- BOTTOM: Model
- Blue indicates lower intensity; Red indicates higher intensity
- See Munakata et al., *Geophys. Res. Lett.*, 32, L03S04-1, 2005.

$$f(\theta, P, \tau) = C_0 \left(\frac{P}{30}\right)^{-1} \exp\left(\frac{\tau}{T_0(P/30)\gamma}\right) \exp\left(-\frac{\theta^2}{2\theta_0^2}\right)$$

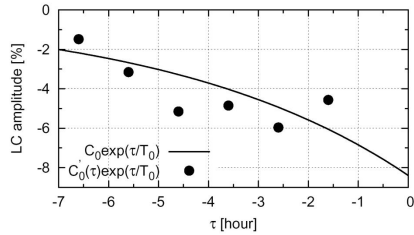
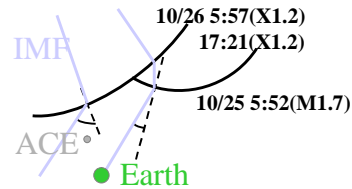
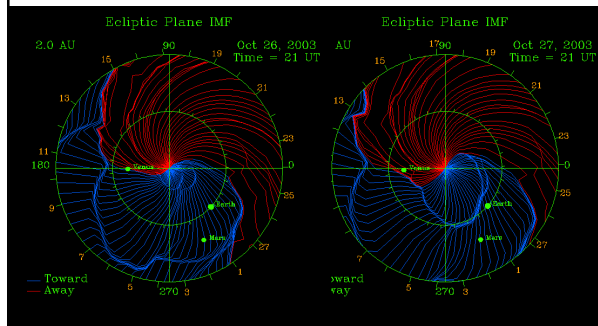
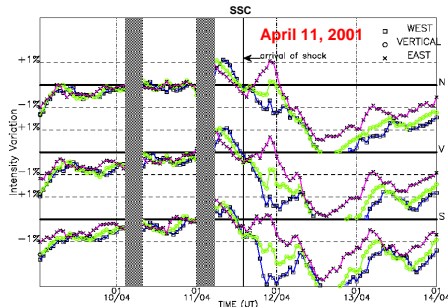


Figure 5. The best-fit LC amplitude at 30 GV as a function of time ( $\tau$ ) measured from the SSC (solid curve). Also plotted are amplitudes derived from the best-fitting on an hourly basis (see text).

$C_0$ [%]	$T_0$ [hour]	$\theta_0$ [°]	$\theta_{HW}$ [°]	$\gamma$	S
-8.397	4.9	55	49.1	0.15	1.147



# Loss-cone precursor with a hodoscopes



## SH2.2-6 Nonaka et al.

- 560m<sup>2</sup> array of PC recording 1.8x10<sup>8</sup> muons/h with ~10° angular resolution (GRAPES3).
- Clearly detected the loss-cone precursor twice, ~24h preceding to a CME-event on April 11, 2001.
- Significant deviation of loss-cone center from sunward IMF is observed half a day preceding the SSC.

## SH2.2-5 Fujimoto et al.

- 25m<sup>2</sup> PC array observed the same precursor.
- Loss-cone is 15° wide

## SH2.2-1-P-214 Petrukhin et al.

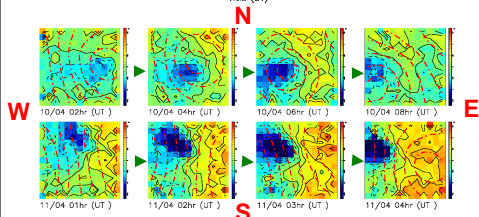
- 9m<sup>2</sup> GMC array with ~7° angular resolution.
- “Tomography” of fluctuation in CME

## SH2.2-7 Szabelski et al.

- 0.65m<sup>2</sup> GM array in operation in Poland.

## SH1.5-1-P-197 Yasue et al.

- New recording system developed for muon telescope using FPGA & VHDL.



## Omni-directional measurement with Neutron Monitors (NM64)



Two main types:

- Proportional counter filled with  $\text{BF}_3$  (NM64):  

$$n + {}^{10}\text{B} \rightarrow \alpha + {}^7\text{Li}$$
- Proportional counter filled with  ${}^3\text{He}$ :  

$$n + {}^3\text{He} \rightarrow p + {}^3\text{H}$$

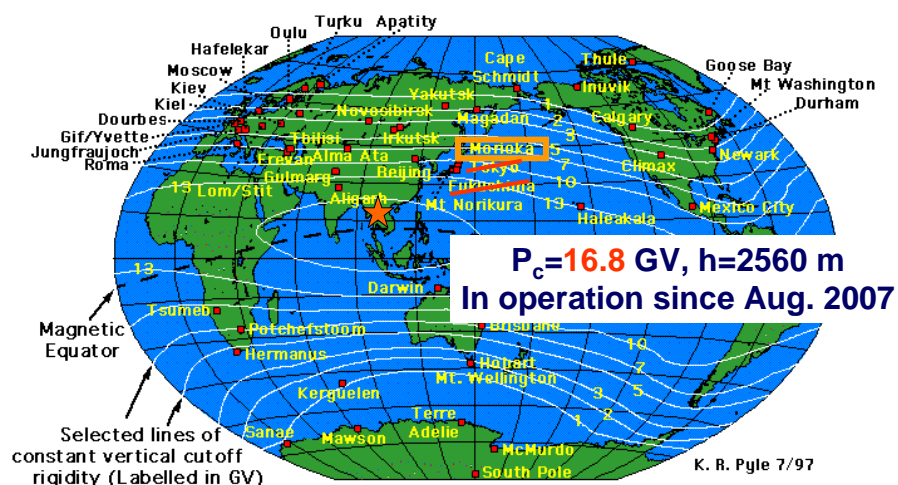
Neutron Monitor in Doi Inthanon, Thailand

- Shipped from Japan in December 2007
- Construction completed in March 2007

## Princess Sirindhorn NM in Thailand

World highest GM cut-off rigidity

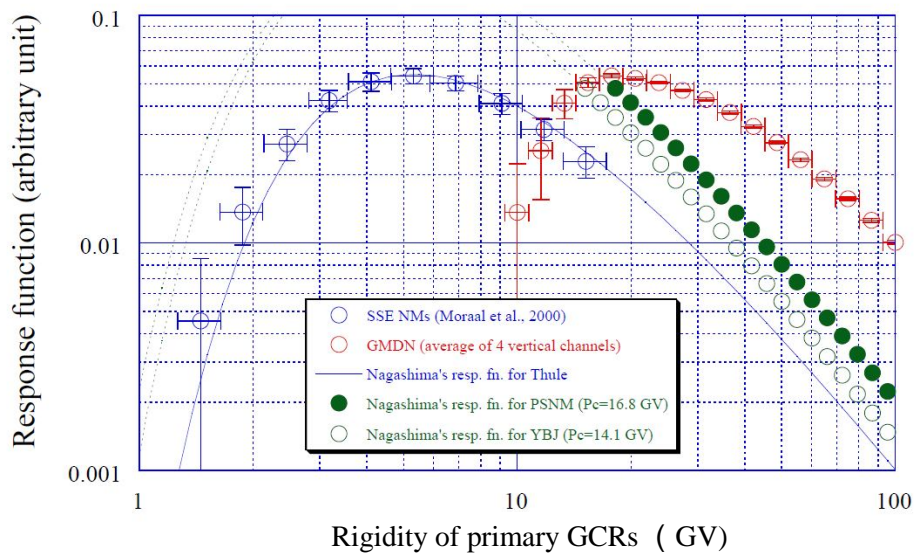
- Better response to high energy CRs
- in between GMDN and SSE

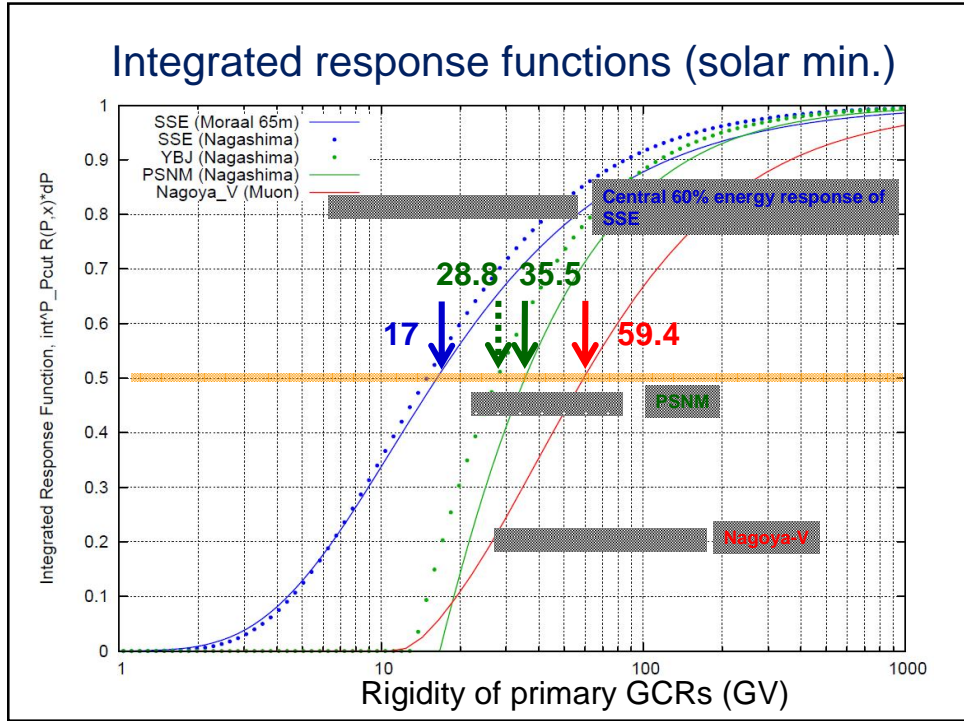


# PSNM opening ceremony (January 21, 2008)



## Differential response functions





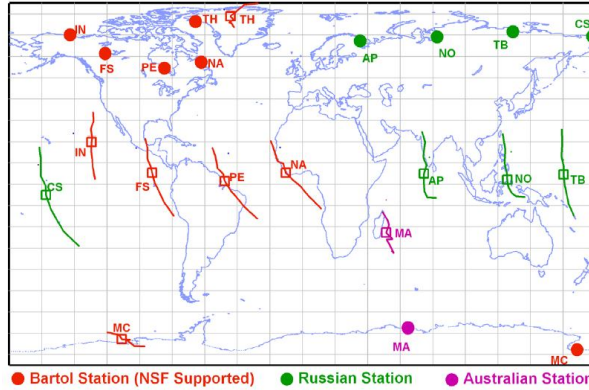
### Characteristics of NM & muon detector

Station name	Type & location	$P_c$ (GV)	$P_m$ (GV)
Tixie Bay (TB) As a representative of SSE	18 NM64s in Russia (71.6N, 128.9E: 0m)	0.53	17 (SSE)
Tibet NM (YBJ)	28 NM64s at Yangbajing, Tibet, China (30.11N, 90.53E: 4300m)	13.7	28.8
Princess Sirindhorn NM (PSNM)	18 NM64s at Doi Inthanon, Thailand (18.59N, 98.49E: 2560m)	16.8	35.5
Nagoya (Nagoya) As a representative of GMDN	Multi-directional muon detector 36 m <sup>2</sup> PS at Nagoya, Japan (35.1N, 137.0E: 77 m)	11.5	59.4 (GMDN)

## SPACESHIP EARTH VIEWING DIRECTIONS

- Optimized for solar cosmic rays
- 9 stations view equatorial plane at 40-degree intervals
- Thule and McMurdo provide crucial 3-dimensional perspective

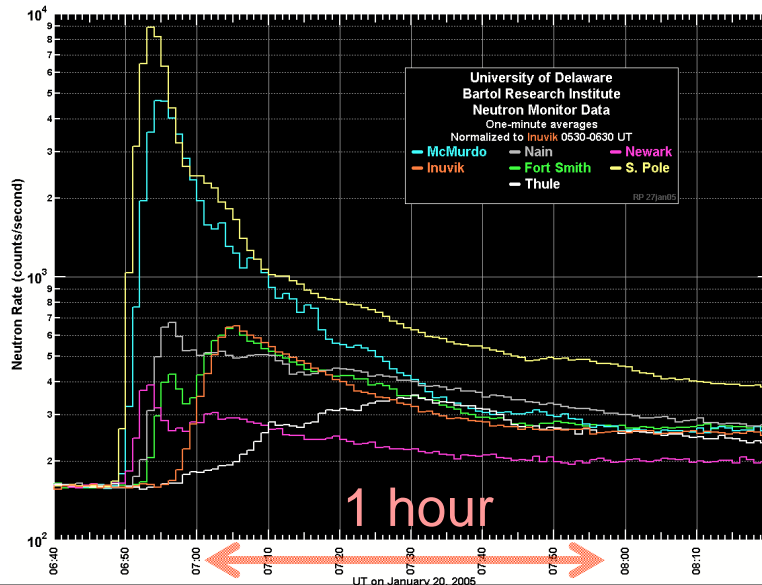
Circles denote station geographical locations. Average viewing directions (squares) and range (lines) are separated from station geographical locations because particles are deflected by Earth's magnetic field.



**STATION CODES**  
 IN: Inuvik, Canada  
 FS: Fort Smith, Canada  
 PE: Peawanuck, Canada  
 NA: Nain, Canada  
 MA: Mawson, Antarctica  
 AP: Apatity, Russia  
 NO: Norilsk, Russia  
 TB: Tixie Bay, Russia  
 CS: Cape Schmidt, Russia  
 TH: Thule, Greenland  
 MC: McMurdo, Antarctica

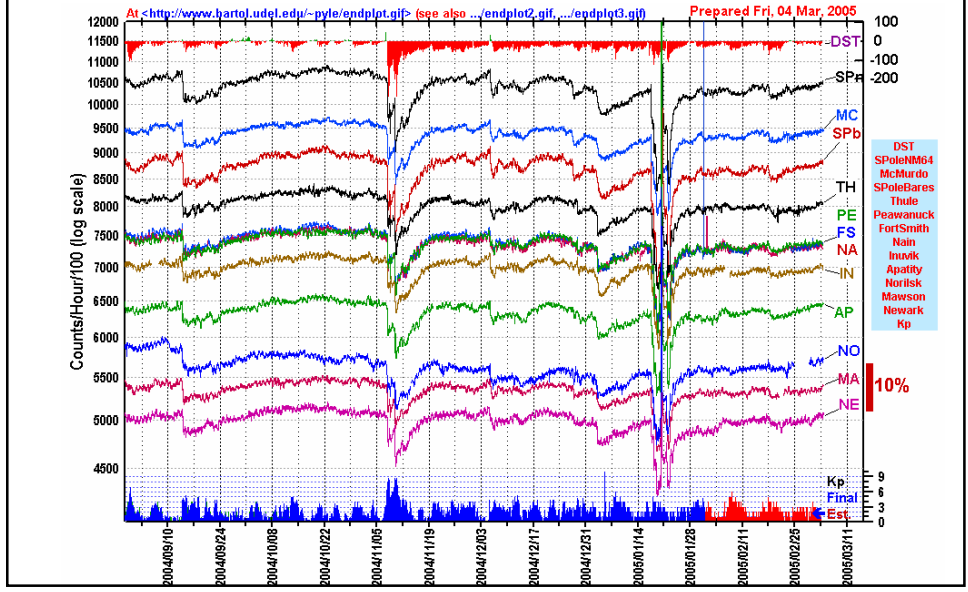
● Bartol Station (NSF Supported) ● Russian Station ● Australian Station

## Ground Level Enhancement (GLE) on January 20, 2005





# Spaceship Earth (11 NMs network by Bartol Res. Inst.)



# Appendix 4

Extreme Space Weather Project, Ottawa

October 17-19, 2011

## **Ground-Based Cosmic Ray Detectors for Space Weather Applications**

John W Bieber

University of Delaware, Bartol Research Institute  
and Department of Physics and Astronomy

Visit our Website: <http://neutronm.bartol.udel.edu/>

To receive e-mail alerts of extreme solar energetic particle events:

<http://www.bartol.udel.edu/~takao/neutronm/glealarm/index.html>

## INTRODUCTION

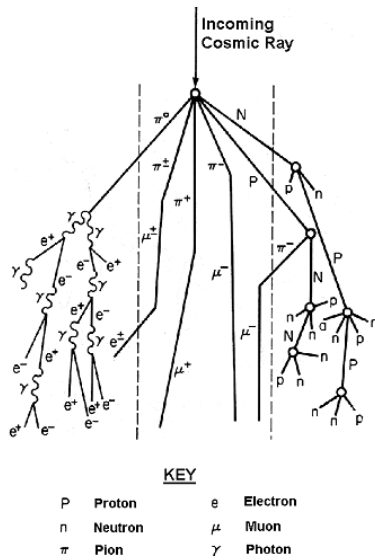
## WHAT IS A NEUTRON MONITOR ?



Neutron Monitor in Nain, Labrador  
Construction completed November 2000

- A large instrument, weighing ~32 tons (standard 18-tube NM64)
- Detects secondary neutrons generated by collision of primary cosmic rays with air molecules
- Detection Method:
  - Older type – proportional counter filled with  $\text{BF}_3$ :  
 $n + {}^{10}\text{B} \rightarrow \alpha + {}^7\text{Li}$
  - Modern type – counter filled with  ${}^3\text{He}$ :  
 $n + {}^3\text{He} \rightarrow p + {}^3\text{H}$

## Neutron Monitors as a Measure of Cosmic Ray Intensity



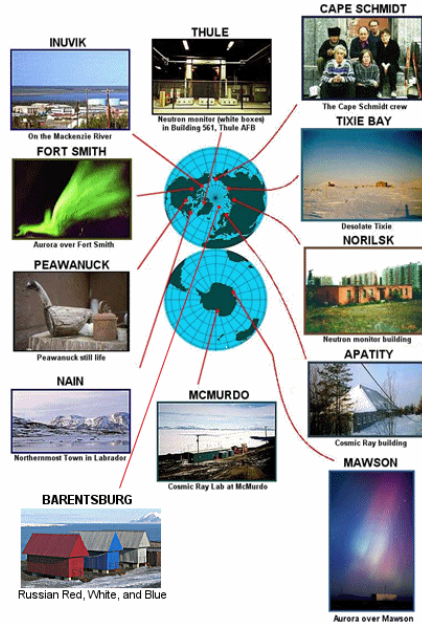
- The neutron monitor directly measures (mostly) secondary neutrons ...
- ... but the primary cosmic ray initiating the cascade is generally a charged particle, usually a proton or helium nucleus
- After adjusting for atmospheric column depth (pressure correction), the neutron monitor count rate provides an accurate measure of the intensity of primary cosmic rays impacting the atmosphere overhead

# Spaceship Earth Neutron Monitor Array

Spaceship Earth is a network of neutron monitors strategically deployed to provide precise, real-time, 3-dimensional measurements of the angular distribution of solar cosmic rays:

- 12 Neutron Monitors on 4 continents
- Multi-national participation:
  - Bartol Research Institute, University of Delaware (U.S.A.)
  - IZMIRAN (Russia)
  - Polar Geophysical Inst. (Russia)
  - Inst. Solar-Terrestrial Physics (Russia)
  - Inst. Cosmophysical Research and Aeronomy (Russia)
  - Inst. Cosmophysical Research and Radio Wave Propagation (Russia)
  - Australian Antarctic Division

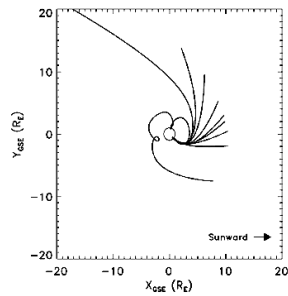
A SHORT TOUR OF SPACESHIP EARTH



## Why are all the stations at high latitude? Prime Reason: Excellent directional sensitivity

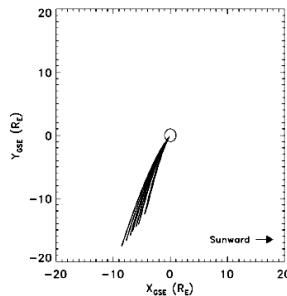
Because of the combined effects of Earth's magnetic field and atmosphere, high latitude sites have superior directional sensitivity, relative to low latitude sites. The cosmic rays are "in focus."

Incoming Protons at Newark



Cosmic rays arriving at low and mid latitude stations (e.g., Newark, Delaware, above) arrive from widely dispersed directions. When the neutron monitor observes something, it can be difficult to determine the source direction.

Incoming Protons at Inuvik



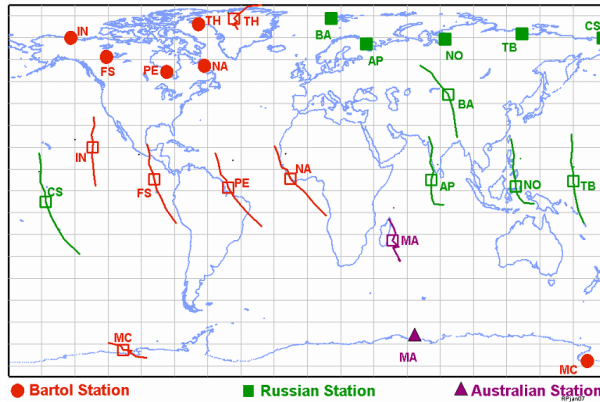
Cosmic rays at high latitude sites (e.g., Inuvik, Canada, above) arrive from a narrow range of directions. The source direction is clear.

Trajectories are shown for vertically incident primaries corresponding to the 10-, 20-, ... 90-percentile rigidities of a typical solar spectrum

## SPACESHIP EARTH VIEWING DIRECTIONS

- Optimized for solar cosmic rays
- 9 stations view equatorial plane at 40-degree intervals
- Thule, McMurdo, Barentsburg provide crucial 3-dimensional perspective

Solid symbols denote station geographical locations. Average viewing directions (open squares) and range (lines) are separated from station geographical locations because particles are deflected by Earth's magnetic field.



### STATION CODES

IN: Inuvik, Canada  
FS: Fort Smith, Canada  
PE: Peawanuck, Canada  
NA: Nain, Canada  
BA: Barentsburg, Norway  
MA: Mawson, Antarctica  
AP: Apatity, Russia  
NO: Norilsk, Russia  
TB: Tixie Bay, Russia  
CS: Cape Schmidt, Russia  
TH: Thule, Greenland  
MC: McMurdo, Antarctica

● Bartol Station

■ Russian Station

▲ Australian Station

## TOPIC 1

### Automated GLE Alert system

## SPACESHIP EARTH STATIONS ARE WELL SITUATED TO ALERT / MONITOR RADIATION HAZARD ON POLAR AIRLINE ROUTES



Line shows Chicago-Beijing great circle route. Squares are *Spaceship Earth* stations. (Two in Antarctica are not shown.)

Friday  
Jul 22, 2005 **AviationToday** NEWSSTAND

- Home
- Subscribe
- Newsstand
- Search
- Regional Aviation
- Special Reports
- Awards
- Aircraft Values
- Safety & Security
- Ask the Experts
- Calendar
- Industry Links
- Career Center
- From the Wires
- Media Kit
- Products
- About the Site
- Helpdesk

**Over The Top: Flying the Polar Routes**

There's another body of water to consider for oceanic flight—the Arctic. Money and flight time can be saved, and the modernization of air traffic services in Russia, Mongolia and China makes transpolar flights even more practical.

*By Capt. Edward R. Hanson Jr. and David Jensen*

It is cold at Elson Air Force Base, near Fairbanks, Alaska. Forty-five degrees below zero cold. It is February 1972, and we are with a KC-135 tanker task force. Our job is to refuel reconnaissance aircraft, including the SR-71 Blackbird, which keeps an eye on the Soviet far east. The cold is hard on the airframe, engines and avionics. Heaters are plugged into the avionics bay, so the boxes don't disintegrate when electrical power is applied.

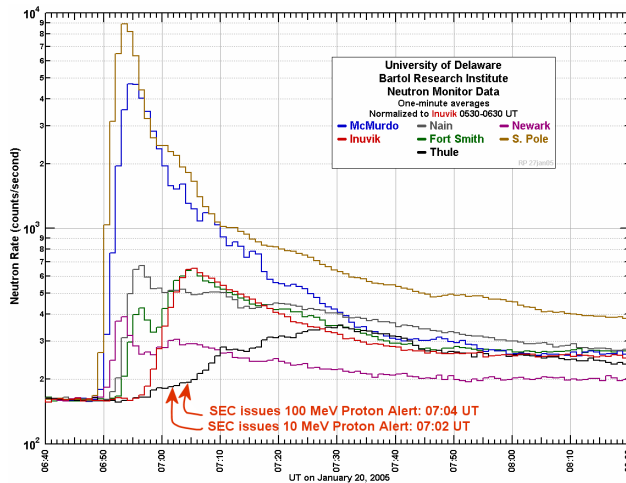
The avionics on the tankers include a single HF radio, two UHF communications radios, a single ADF and dual ILS/VORs. We have a navigator on board who uses pressure patterns, dead reckoning, ground radar mapping and his sextant to keep us legal as we transit the North Pole. It feels great when we hit the rendezvous point and the receiver aircraft is actually where we hoped it would be.

**Then and Now**

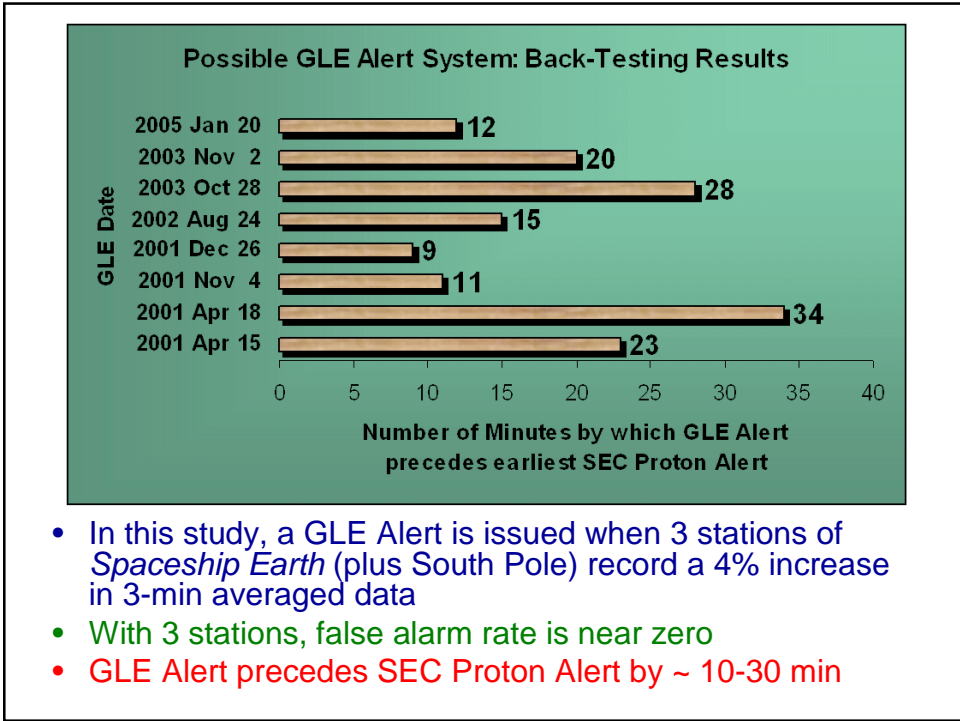
Fast forward to 2002. The North Pole is now the key to cost-efficient air routes between North America and the Far East. Polar weather remains icy cold, but the political climate has thawed since the fall of the Soviet Union in 1991. The United States and Russia are now partners in opening high-value routes to airline operators. In November 1992, the two governments established the Russian/American Coordinating Group for Air Traffic Control (RACGAT—visit [www.racgat.com](http://www.racgat.com)). Among its top priorities have been establishing trans polar routes that link North America with China, Japan and Southeast Asia and modernizing air traffic control (ATC) services



## Neutron Monitors Can Provide the Earliest Alert of a Solar Energetic Particle Event



- In the January 20, 2005 GLE, the earliest neutron monitor onset preceded the earliest Proton Alert issued by the Space Environment Center **by 14 minutes.**



## GLE Alarm Is Now Operating

Criteria of alarm

Num. of stations	Status
0	Quiet
1	Watch
2	Warning
3 or more	Alarm

Current status

Now	Status
Now	Quiet
Past 5-hour	Quiet

Current 1M1 rates (last 24 hours)

GLE Alarm from Bartol Neutron Monitors, List Updated 2010/10/13 00:20UT

1-min Rate (count/hour) and Alarm Increase (%)

Stations: FortSmith, Inuvik, McMurdo, Nain, Newark, Peawanuck, SouthPole, Thule, Peawanuck.

Legend: Watch, Warning, Alert.

Links:  
[Bartol N.M. main page](#)  
[Bartol Spaceship Earth GLE Monitor](#)  
[Sample report of GLE Alarm at past I.C. event](#)

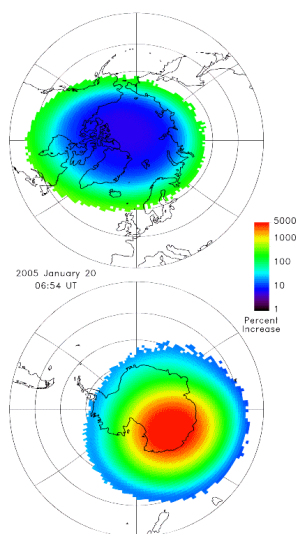
- Developed primarily by Dr Takao Kuwabara
- To receive automated e-mail alerts of possible GLE, send e-mail request to:
  - [jwbieber@bartol.udel.edu](mailto:jwbieber@bartol.udel.edu)
  - ... or visit the Website shown at left: <http://www.bartol.udel.edu/~takao/neutronm/glealarm/Index.html>

## TOPIC 2

### Realtime Mapping of Radiation Intensity in Polar Regions

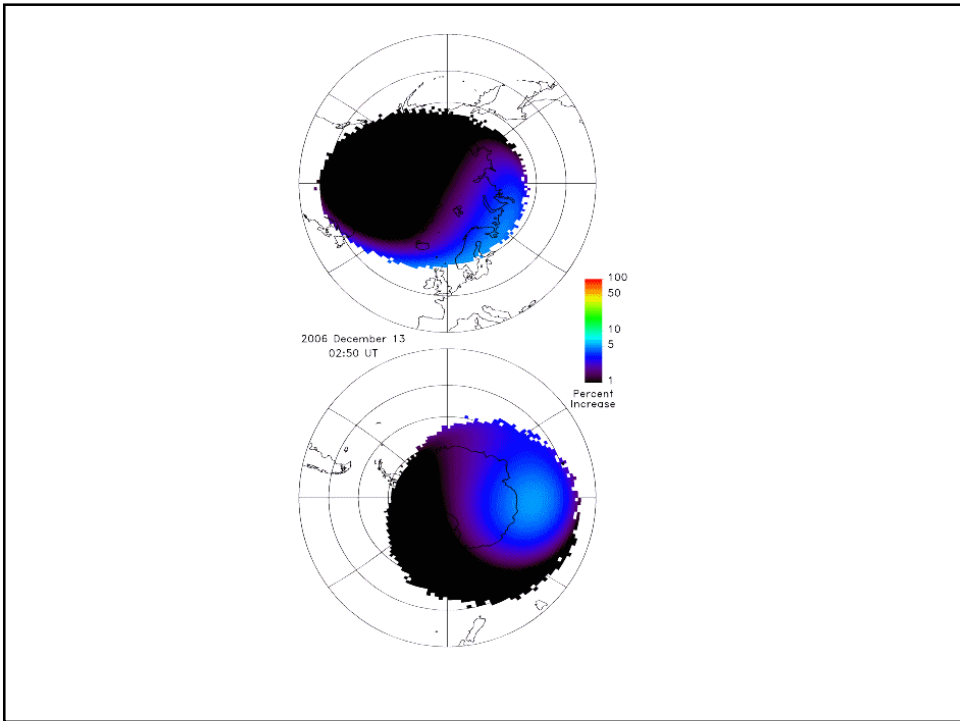
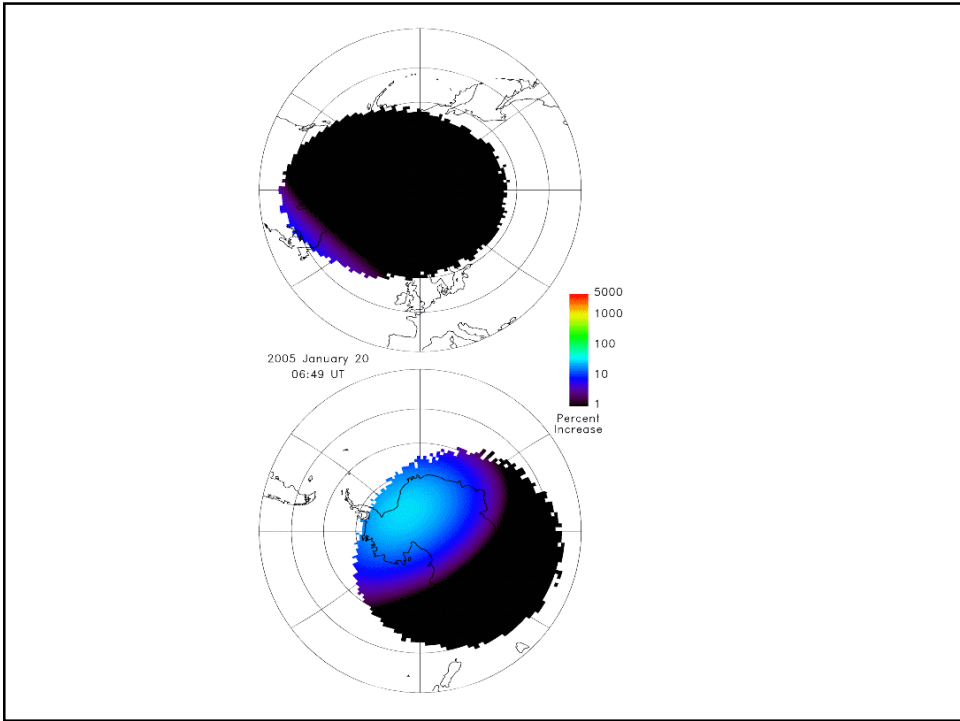
January 20, 2005 GLE and  
December 13, 2006 GLE  
as concrete examples

#### MAPPING RADIATION INTENSITY IN POLAR REGIONS: METHOD



- First, the asymptotic viewing directions of the neutron monitor array are determined, and the cosmic ray pitch angle distribution (here modeled as a constant plus exponential function of pitch angle cosine) is computed in GSE coordinates by least-square fitting
- To form the map, a preliminary computation is done at each grid point to determine if a 1 GV proton is “allowed.” If it is, then that location is considered to have a geomagnetic cutoff below the atmospheric cutoff, and the grid point is included in the map.
- The asymptotic viewing direction at the center of the grid point is then computed in GSE coordinates for a median rigidity particle, permitting the “pitch angle” for the location to be determined.
- From the model pitch angle distribution, the predicted intensity for that grid point is computed and plotted by color code.

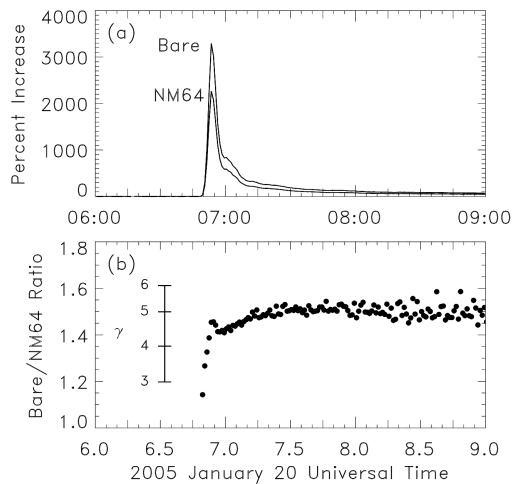




## TOPIC 3

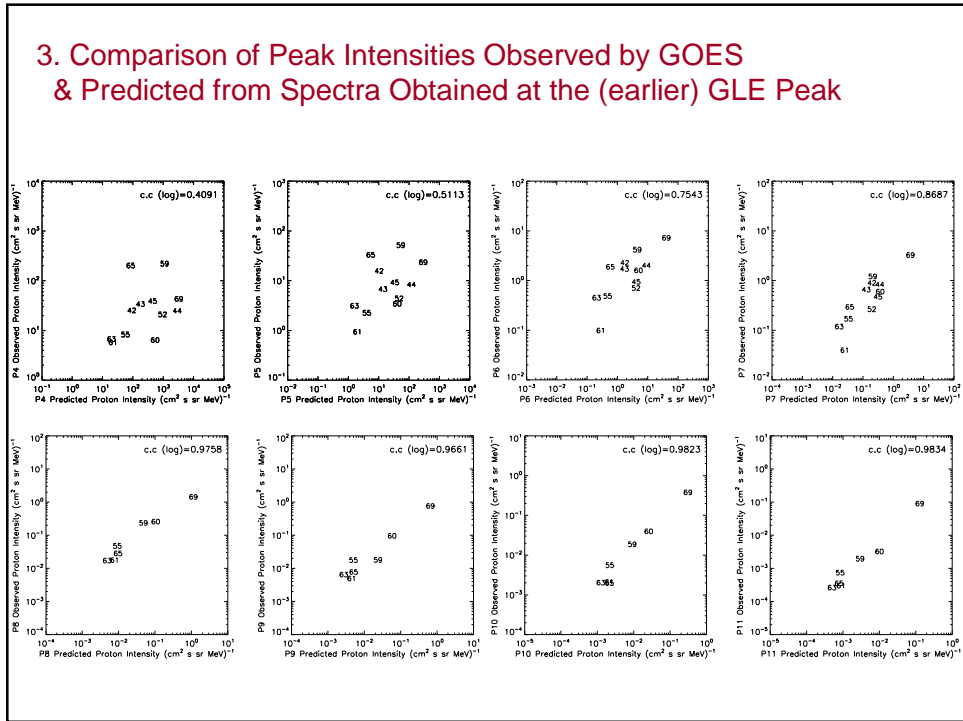
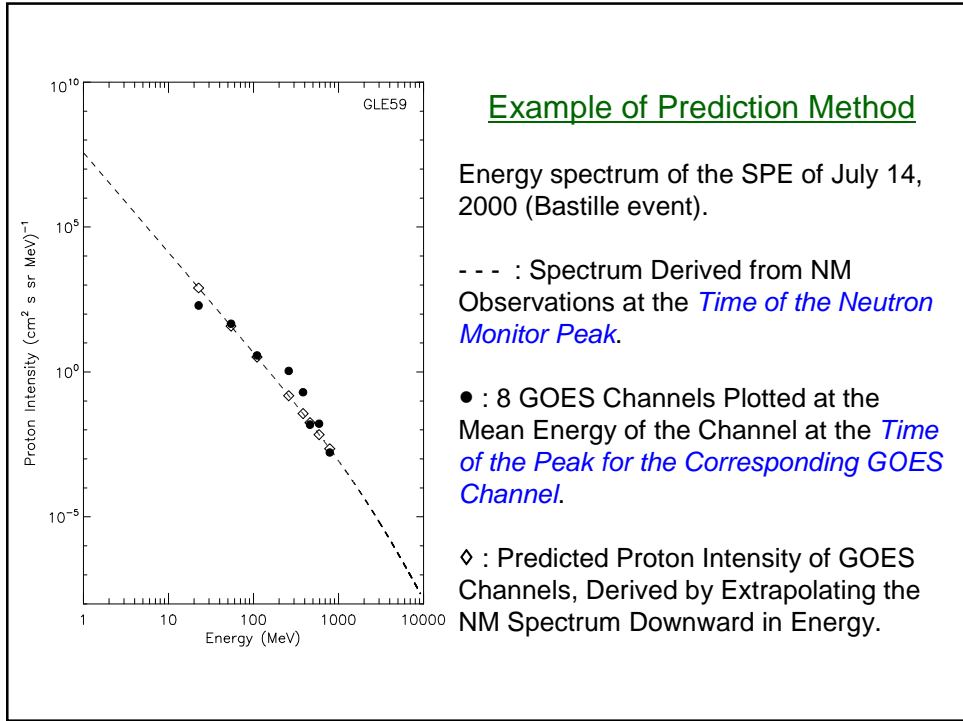
# Neutron Monitor Prediction of Solar Energetic Particle Energy Spectra

### ENERGY SPECTRUM: POLAR BARE METHOD



South Pole station has both a standard neutron monitor (NM64) and a monitor lacking the usual lead shielding (Bare). The Polar Bare responds to lower particle energy on average. Comparison of the Bare to NM64 ratio provides information on the particle spectrum.

- This event displays a beautiful dispersive onset (lower panel), as the faster particles arrive first.
- Later, the rigidity spectrum softens to  $\sim P^{-5}$  (where  $P$  is rigidity), which is fairly typical for GLE<sup>2</sup>.



Proton Channel	Energy Range (MeV)	Peak Intensity	Fluence
		Logarithmic	Logarithmic
P4	15-40	0.4091	0.4093
P5	40-80	0.5113	0.3763
P6	80-165	0.7543	0.5037
P7	165-500	0.8687	0.5888
P8	350-420	0.9758	0.8196
P9	420-510	0.9661	0.8335
P10	510-700	0.9823	0.8665
P11	> 700	0.9834	0.9088

Logarithmic Correlation Coefficients

Between Observed & Predicted Peak Intensity of Proton Channels  
 Between Observed Fluence & Predicted Intensity of Proton Channels

## TOPIC 4

Earth as a  
**Giant Magnetic Spectrometer**  
 A High-Altitude Array Spanning a Range of Cutoffs

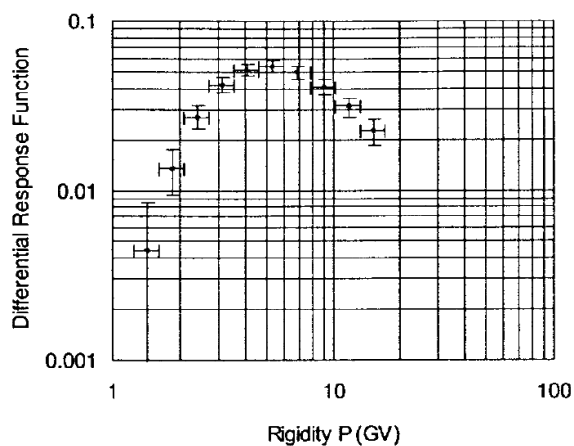
## WHY HIGH-ALTITUDE MONITORS ?

### REASON: ENHANCED SENSITIVITY

Altitude (ft)	Pressure (mm Hg)	Galactic Cosmic Rays Relative Count Rate	Solar Cosmic Rays Relative Count Rate
0	760	1.0	1.0
5,000	632.5	3.6	5.7
10,000	522.7	10.7	25.2
15,000	429.0	27.4	90.2
20,000	349.5	60.6	265.8

A 3-tube neutron monitor at South Pole (510 mm Hg)  
has sensitivity to solar energetic particles equivalent  
to a 90-tube monitor at sea level !

## GALACTIC COSMIC RAY (GCR) SPECTRUM: A NEW MEASUREMENT APPROACH



From Moraal et al. (2000)

- An array of high-altitude monitors at different cutoffs can measure the differential intensity in absolute units, if the monitors are accurately intercalibrated
- Each monitor provides a measure of the differential intensity between its own cutoff and the next higher cutoff in the array

## TWO ANCHORS FOR A HIGH-ALTITUDE GCR ARRAY

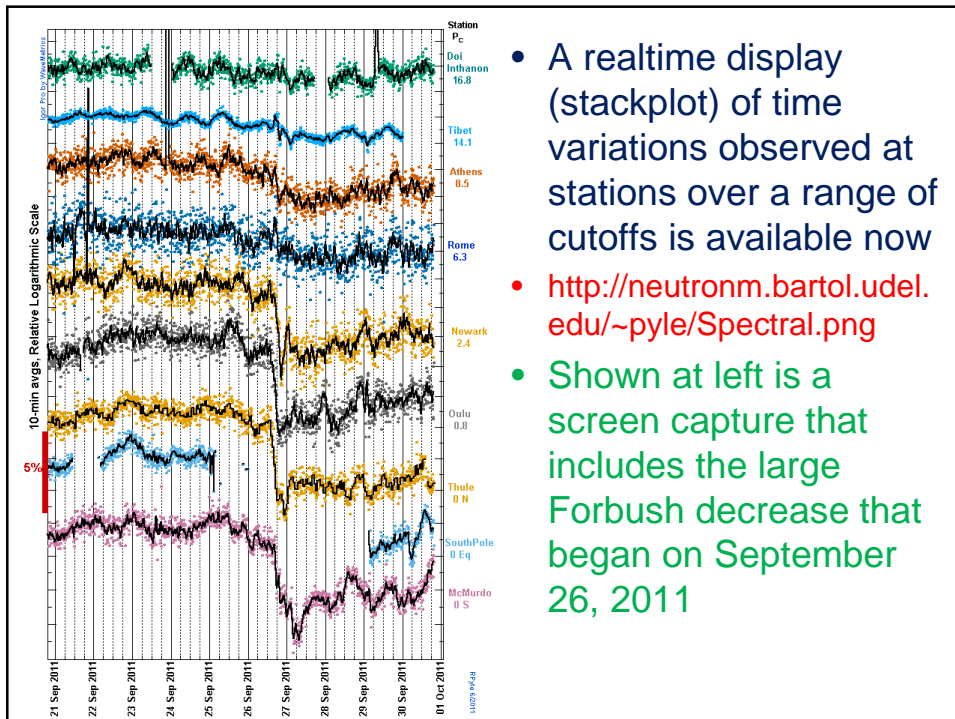
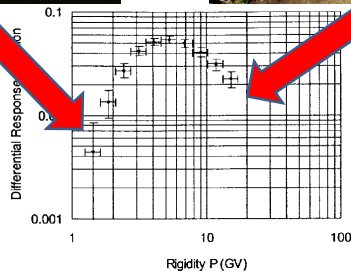
Low-Cutoff (or No Cutoff) Monitor at High Latitude, e.g., Pole or Summit

Below: South Pole Monitor at Sunset, 2002.

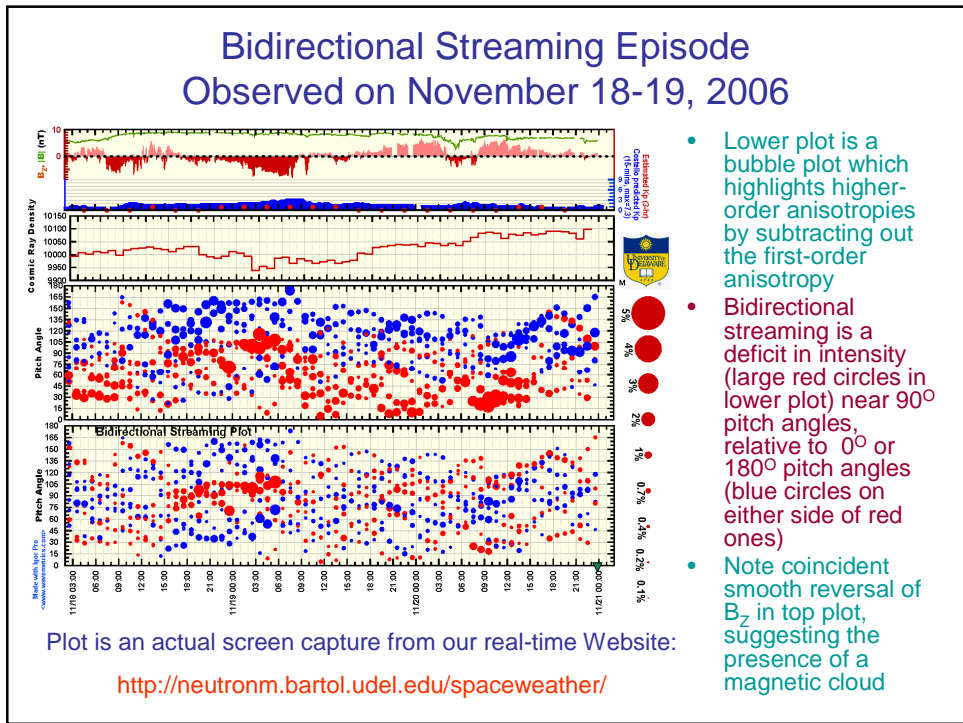
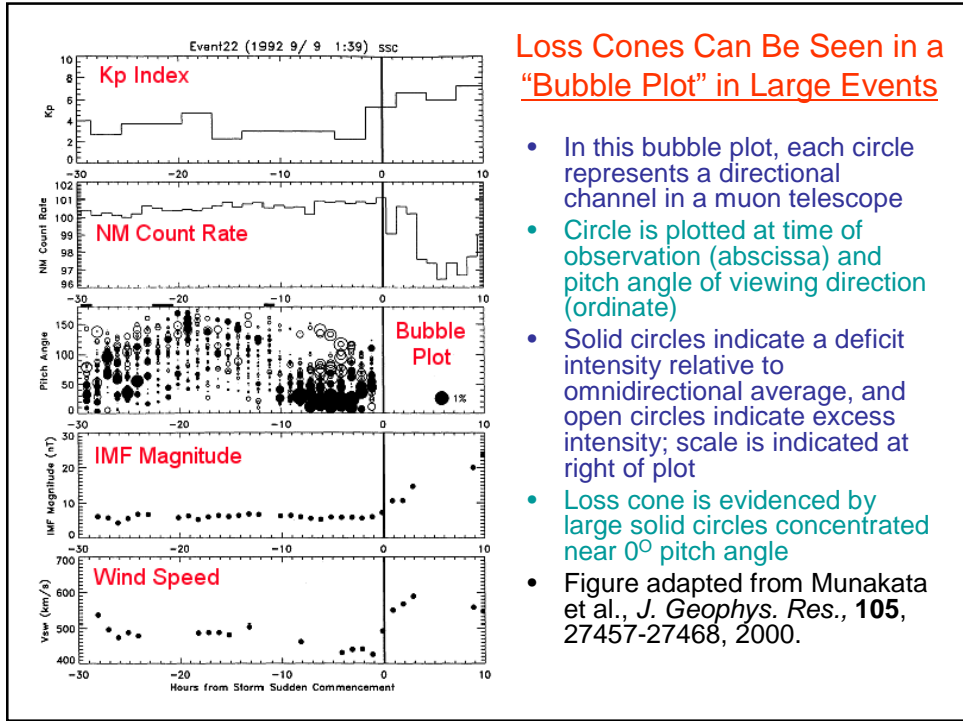


High-Cutoff (17 GV) Monitor in Thailand

Below: Princess Sirindhorn Neutron Monitor. Dedicated January, 2008









University of Delaware / Bartol Research Institute  
Realtime Space Weather Website

Displays bubble plots and many other plots,  
or links to plots

## **SUMMARY**

### **The Role of Neutron Monitor Arrays for Space Weather Forecasting and Specification**

- Automated GLE Alert System: Operational Now!
- Realtime Mapping of Radiation Intensity in Polar Regions
- Prediction of SEP Energy Spectrum (Polar Bare Method)
- Realtime Specification of Galactic Cosmic Ray Spectrum (High-Altitude Array across a Range of Cutoffs)
- Loss Cone Prediction of Approaching ICME
- Diagnostic of ICME Presence from Bidirectional Cosmic Ray Streaming

## Realtime Space Weather Websites Operated by University of Delaware / Bartol Research Institute

- <http://neutronm.bartol.udel.edu/>
  - Home page: Links to all the other sites listed below
- <http://www.bartol.udel.edu/~takao/neutronm/glealarm/index.html>
  - Instructions for subscribing to GLE alert e-mail list
- <http://neutronm.bartol.udel.edu/~pyle/Spectral.png>
  - Stackplot of time variations observed by neutron monitors at different cutoffs
- <http://neutronm.bartol.udel.edu/spaceweather/>
  - Bubble Plots for Loss Cone Identification, Bidirectional Streaming, Many More Plots – Neutron Monitor Data and Muon Detector Data Displayed Side-by-Side
- <http://www.bartol.udel.edu/~takao/icetop/01m/index.html>
  - Summary rates from the IceTop detector at South Pole – Not very user-friendly (yet)

# Appendix 5

## FOREWARN Detector Construction

J. Armitage<sup>1</sup>, J. Botte, K. Boudjemline<sup>2</sup> and A. Robichaud

*Department of Physics, Carleton University, Ottawa, Ontario, Canada*

<sup>1</sup>*armitage@physics.carleton.ca - 613 520 2600 x 4326*

<sup>2</sup>*boudjeml@physics.carleton.ca - 613 520 2600 x 1877*

August 17, 2011

### INTRODUCTION

Muon Forewarn tracking system will use available devices used in the past by a different experiment [1]. The goal is to track cosmic-ray muons by providing the hit position and the angular distributions in two directions. The muon detectors are a single wire drift chambers. Two chambers are available and cover an area of  $40 \times 114 \text{ cm}^2$  each. With a muon flux of  $1 \text{ min}^{-1} \text{ cm}^2$ , the expected number of muons per chamber is then  $4560 \text{ min}^{-1}$ . Two absorber stages will be used to stop non desired low energy particles and will provide a cut on muon momentum.

### DRIFT CHAMBERS

The muon flux will be reduced mainly because of the geometrical acceptance of the system. The distance between both detectors will be chosen accordingly. The disadvantage of having both detectors close to each other will affect the angular resolution. A Monte-Carlo simulation has been performed for the choice of this distance. Another important point is the ambiguity left-right for this type of detector. With a single anode wire, the information that we measure in the direction perpendicular to the wire is the drift time. Since the wire is located in the centre of the chamber, only external trigger can provide the side where the muon traversed the chamber. We will use for that, plastic scintillators.

## TRIGGERS

Many scintillators are available. We are planning to use three planes for the tracking as shown in the figure [1]. Each plane consists of two scintillators to cover separately each side of the anode wire. Three trigger coincidences will be considered. The main will track all type of events and consists of the first three scintillators from the top. The second will consist of the main coincidence combined with the scintillator below the first lead layer to cut low energy particles and the third will give information about the minimum muon momentum.

## ABSORBERS

Two stages of lead will be used to absorb low energy particles like electrons, protons and particles which results from scattering in the roof or from any type of present radioactivity. The thicknesses are from top to bottom, 5 and 10 cm respectively. Each lead layer consists of a many lead pieces of  $5 \times 10 \times 20 \text{ cm}^3$  (~12kg each), and sit on 2.5cm iron slab.

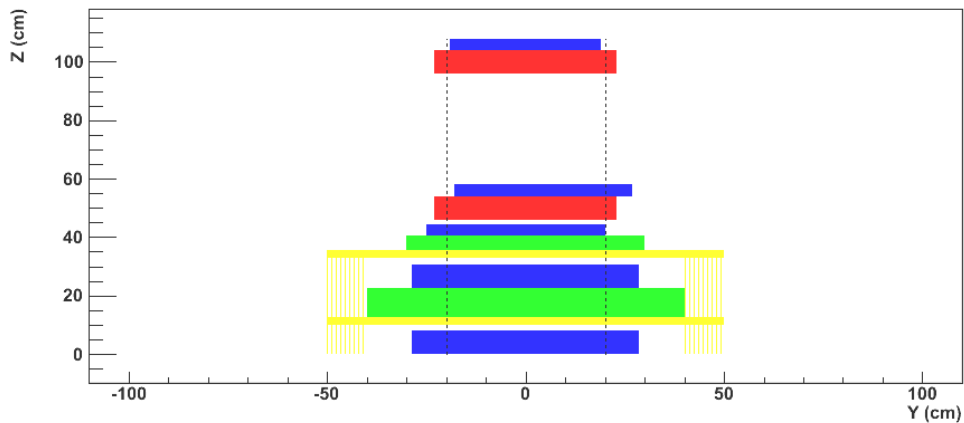
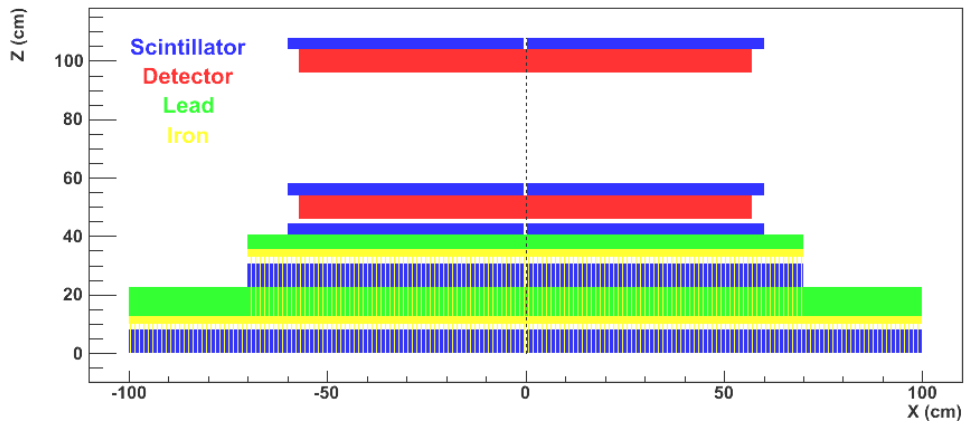


**FIGURE 1.** Scheme of FOREWARN detector. The thickness for each component is the total thickness (active + support + shielding + ...). Example: the scintillators sit on a piece of wood.

## SIMULATION

Two different calculations were done. The first one for setting the vertical position  $Z$  of the drift chambers, the  $X$  and  $Y$  positions of the scintillators and the size of the absorbers. The second is study the absorption of cosmic-ray particle in different lead thicknesses.

The first simulation generates events using  $\cos\theta^2$  distribution. The spatial resolution in the drift chambers used is 3mm in each direction. In the direction perpendicular to the wire  $X$ , the side where the muon traversed the chamber is decided by the scintillator above each chamber. Example: for chamber 1, scintillator 1 corresponds to the left side, and scintillator 2 to the right side. Figure 2 shows an example of a mis-reconstructed event because of this ambiguity.

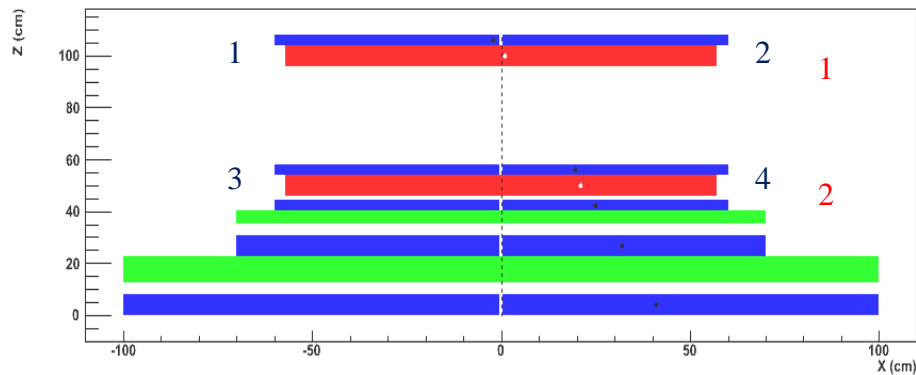


**FIGURE 2.** Example of a mis-reconstructed event due to left-right ambiguity. The event is at the right side of the chamber 1, but the information obtained from the scintillator is left.

For a distance of 50cm between chambers, the fraction of these events is 1.3%. This value decreases when the distance increases. Increasing the distance will reduce the flux within the geometrical acceptance. The angular distribution of the reconstructed tracks has been compared to the true distribution as shown in figure 3. If non regular events occur at large angle, they will be easily distinguished. The main disagreement between both is due to the spatial resolution. Few events due to the left-right ambiguity can be seen at the bottom plot of the same figure.

The spread of the events on the iron support slabs define the size of the lead that we should use (figure 3). Unfortunately, in  $Y$  direction, the available scintillators are not wide enough and cannot cover the desired width. This can be corrected by an angular cut using the muon hit positions at the drift chambers.

To study the absorption of events in the lead, cosmic-ray particles were generated using CRY Software [2] at 0 altitude and 45deg latitude (Ottawa). Only charged particles were selected. Figure 4 shows the total flux as a function of the particle momentum up to 10GeV/c. Only muons, electrons and protons are plotted. The flux of kaons and pions is negligible.

Figure 5 shows the effect of the lead thickness on the flux for each particle. 5cm of lead (first layer) is enough to cut all electrons. 15 cm (both layers) cut muon with momentum below  $\sim 0.25$  GeV/c. The ideal is to use thicker lead layer (figure 6), but unfortunately this amount is not available.

The energy loss used for this calculation was obtained from [3][4][5]. Note that these numbers are an average value. The fluctuation in the energy loss is not taking into account. To study the energy loss in the whole system in details, GEANT4 simulation package will be used [6].

### **GEANT4 SIMULATION (*UNDER CONSTRUCTION*)**

An example of a 0.5GeV/c muon track is shown in figure 7 acknowledgment.

### **DETECTOR CONSTRUCTION**

The FOREWARN tower is under construction (figure 8). The first step is to build the lead layers.

### **ACKNOWLEDGMENTS**

We would like to thank our summer student Mitch Robson for the efforts that he made, especially for lifting lead bricks.

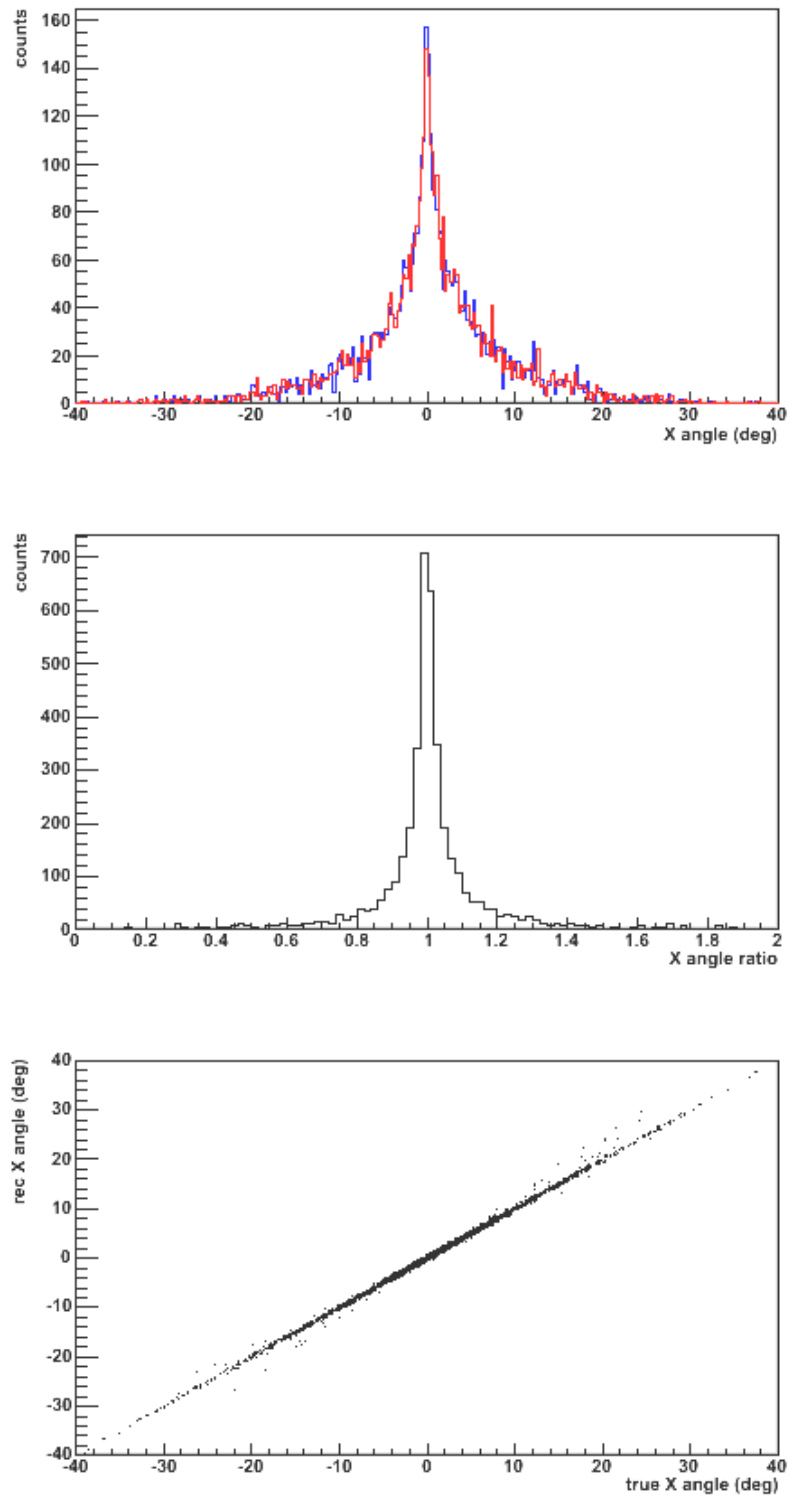


**FIGURE 2.** From top to bottom, true (blue) and reconstructed (red) angular distributions. Ratio between both and one versus the other.

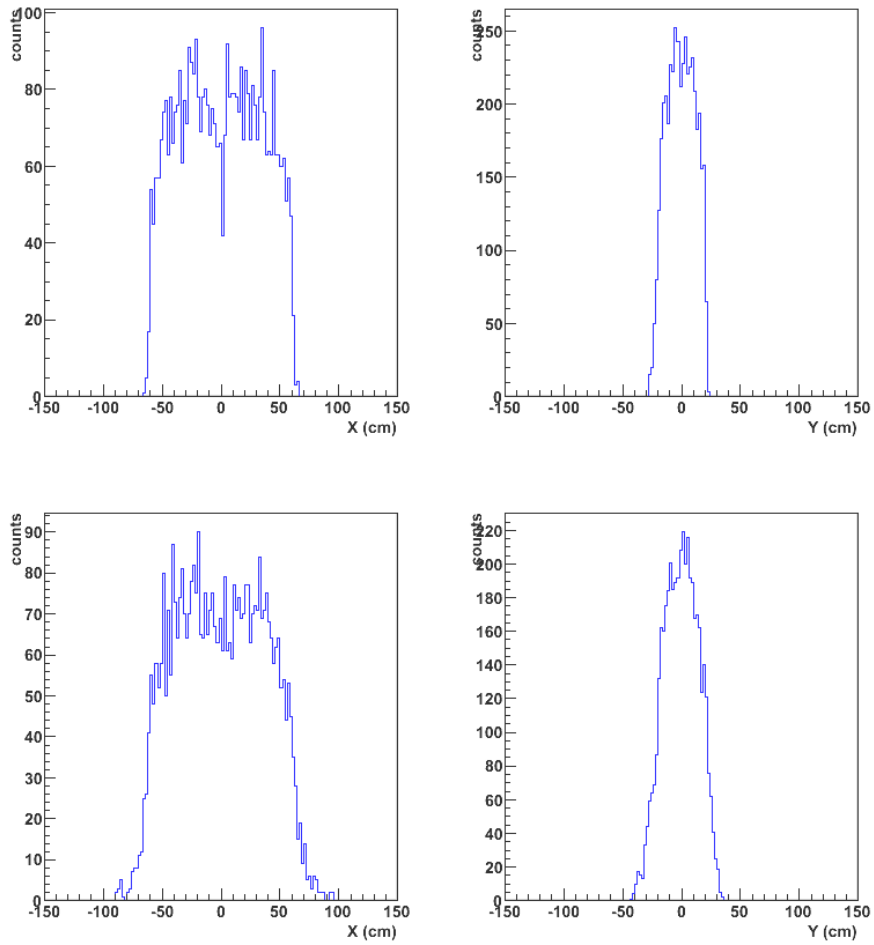


**FIGURE 3.** X and Y distribution on the bottom of the lead layers (top of iron support slabs).

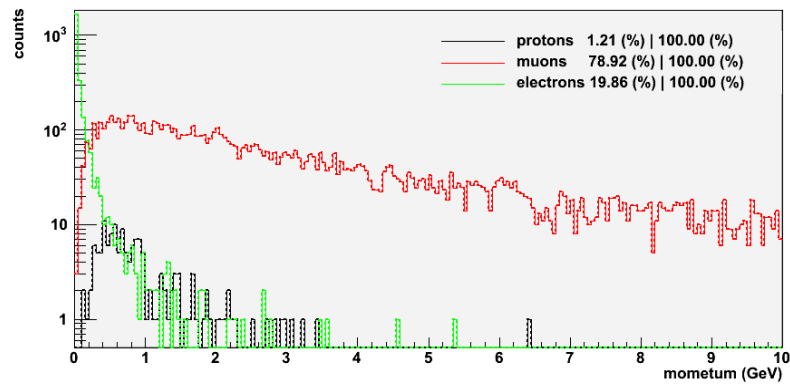


**FIGURE 4.** Cosmic-ray flux obtained with CRY software.



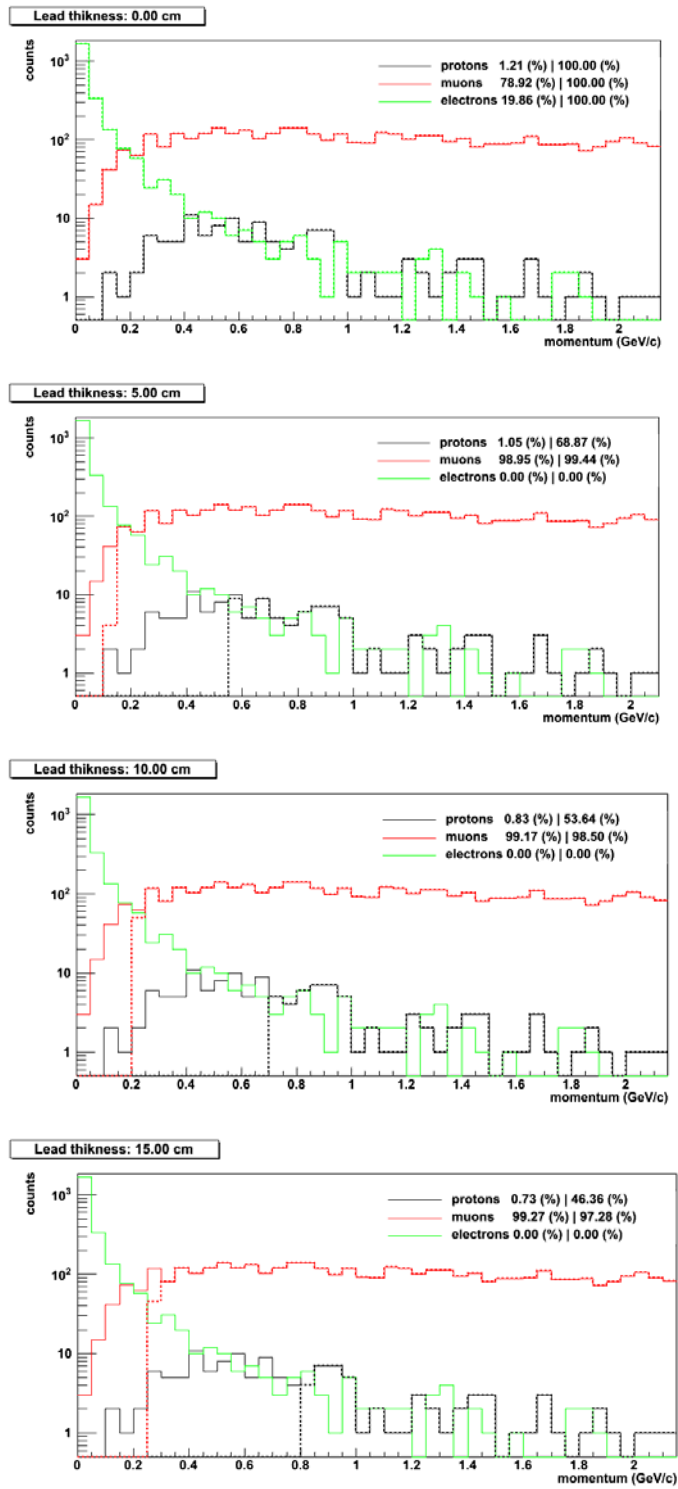
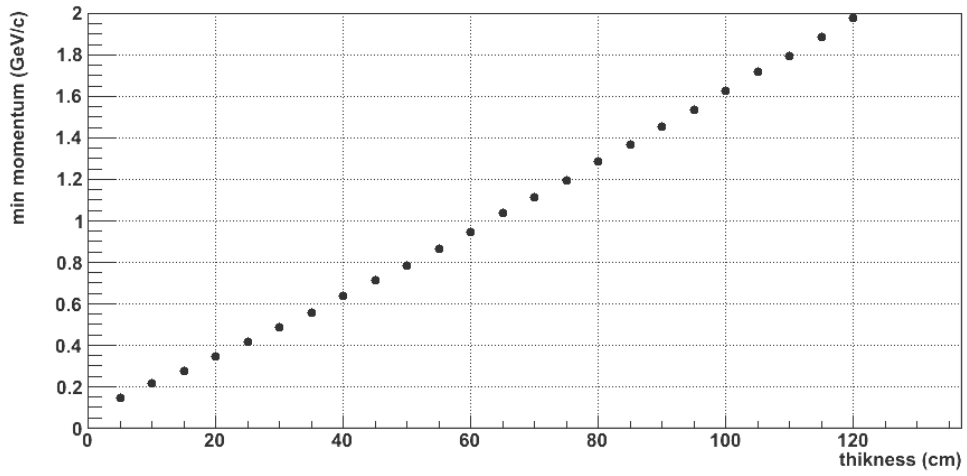
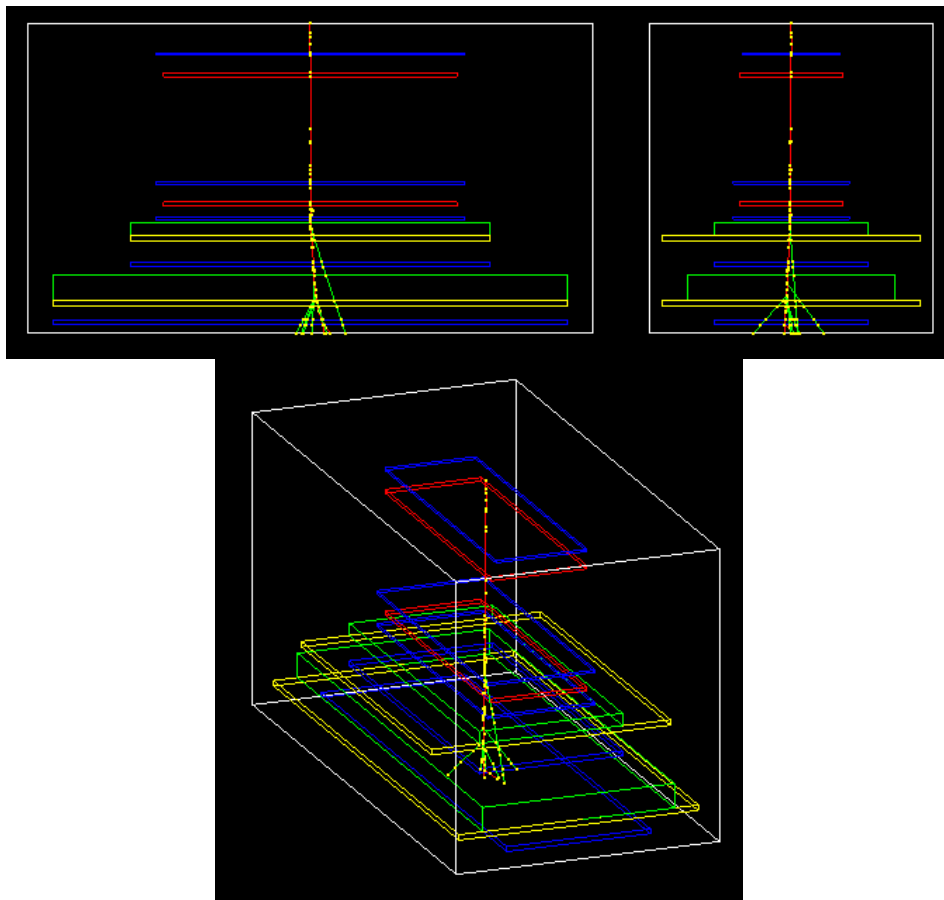


FIGURE 5. Solid lines are the initial fluxes. Dashed lines are events which traverse a given lead thickness.



**FIGURE 6.** Mean minimum muon momentum which traverse a given lead thickness.



**FIGURE 7.** GEANT4 simulation of FOREWARN Detector. An example of a 0.5GeV/c muon is shown.



Area cleared, floor painted, coordinate system laid down.



Lead bricks transported to site (in-kind donation from Carleton University).



Steel plates arrive – start to build a multi-layer cosmic-ray tower.



Lowest level of lead complete.



Second layer of lead in stalled.

**FIGURE 8.** Construction of FOREWARN tower.

## REFERENCES

1. K. Boudjemline et al., *Cosmic ray muon tomography using drift chambers for the detection of special nuclear materials*. IEEE 2010 conference.
2. CRY: <http://nuclear.llnl.gov/simulation/main.html>
3. D. E. Groom et al, Muon stopping power and range tables 10MeV-100TeV, Atomic Data and Nuclear Data Tables **78**, 183–356 (2001).
4. <http://physics.nist.gov/PhysRefData/Star/Text/ESTAR.html>
5. <http://physics.nist.gov/PhysRefData/Star/Text/PSTAR.html>
6. **GEANT4: <http://geant4.cern.ch>, version 9.3.**

# Appendix 6

## GEANT4 Simulation of FOREWARN Detector

K. Boudjemline

*Department of Physics, Carleton University, Ottawa, Ontario, Canada*

*boudjeml@physics.carleton.ca - 613 520 2600 x 1877*

Version 0

August 24, 2011

### INTRODUCTION

The simulation of FOREWARN detector with GEANT4 Simulation Package [1] will inform us about the expected flux of the secondary cosmic-ray within the geometrical acceptance of the trigger systems.

### SIMULATION INGREDIENTS

The main ingredients of GEANT4 simulation are the geometry of the detector, the type of particles involved and the physics used for each particle.

#### 1. GEOMETRY

The geometry of the detector has been shown in the previous report [2]. This document will focus on the parameters used for GEANT4 simulation code. Figure 1 shows the suggested detector plotted with GEANT4. It shows as well different trigger stages. Tables 1 and 2 summarize each material used for the simulation.

	Type	#	Thickness	Material	Formula	Density (g/cm <sup>3</sup> )
Trigger	Plastic scintillator	10	6 x 0.3 cm 4 x 1.5 cm	Polystyrene	C <sub>8</sub> H <sub>8</sub>	1.04
Detector	Drift chamber	2	7.1 cm	See table 2	See table 2	See table 2
Absorber1	Lead	2	10 cm	Lead	Pb	11.35
Absorber2	Iron	2	2.5 cm	Iron	Fe	7.87

Table 1: Materials used for GEANT4 simulation.

	Material	#	Thickness	Density (g/cm <sup>3</sup> )
Active	Argon gas	1	1.5 cm	$1.78 \times 10^{-3}$
Electrodes/ shielding	Copper	4	60 um	8.96
G10 skin	SiO <sub>2</sub>	4	3.1 mm	1.91
Styrofoam	Polystyrene	2	2.5 cm	0.03

Table 2: Drift Chamber materials used for GEANT4 simulation. The numbers shown are for a single drift chamber.

## 2. COSMIC-RAY PARTICLES

The main secondary cosmic ray particles include electrons, muons and protons. The particles have been generated using CRY software [3].

## 3. PHYSICS

The physics used in the simulation is listed in table 3.

Particle	Multiple scattering	Ionization	Bremsstrahlung	Pair production
Proton	x	x		
Electron	x	x	x	
Muon	x	x	x	x

Table 3: Physics used for each particle in GEANT4 simulation.

Figure 2 shows the interaction of each particle with different materials of the detector. Most of muons traverse the whole system. Electrons can make it up to the second stage only. Most of them are trapped in the first and second stage. In the case of protons, some of them are absorbed in the first lead layer and some in the second lead layer. Few of them can make it to the last stage.

## ANALYSIS

Figure 4 summarizes the expected number of events for each trigger stage. From top to bottom: stage 1, 2 and 3. In each plot (each stage), the solid lines are the generated fluxes. The dashed lines are the survived events due to the geometrical acceptance and to the energy loss in different materials. Three columns of fractions are shown. From left to right:

- Fraction of each particle to the total number of events.
- Fraction of each particle to the generated number of events for the same particle type.
- Fraction of each particle to particles survived in stage 1.

The last fraction is the most important. It allows us to compare the detected number of events in each stage. From this figure, the number of muons in the second and in the third stage will be reduced by 5% and 17% respectively compared to the main stage (stage 1). The muon minimum momentum is around 0.2 and 0.4 GeV/c, which is in good agreement with previous calculation [2].

## CONCLUSION

FOREWARN Detector has been simulated using GEANT4 Software. The expected number of muon events for each trigger stage have been estimated. The momentum cut at each lead stage is 0.2 and 0.4 GeV/c which corresponds to a reduction of 5 and 17% compared to the main stage. This simulation can be run again if more realistic cosmic-ray generator software is available.

## REFERENCES

1. **GEANT4:** <http://geant4.cern.ch>, version 9.3.
1. J. Armitage, J. Botte, K. Boudjemline and A. Robichaud, FOREWARN Detector Construction, Internal Report, August 17, 2011.
2. CRY: <http://nuclear.llnl.gov/simulation/main.html>

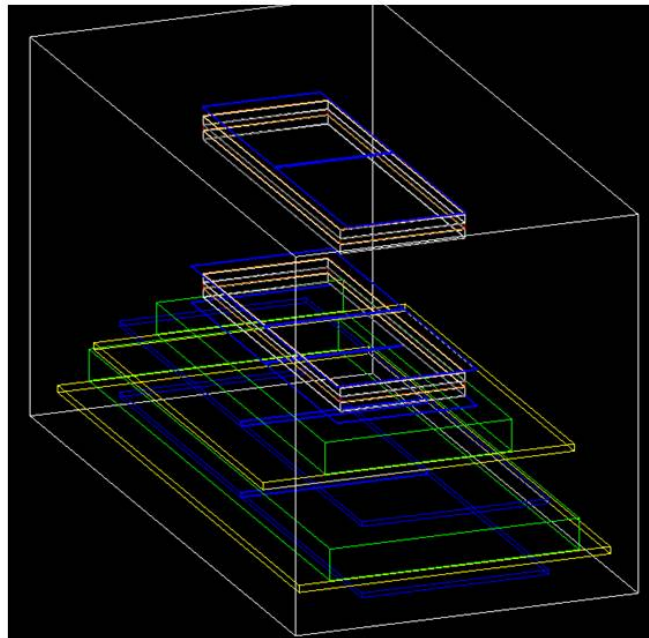
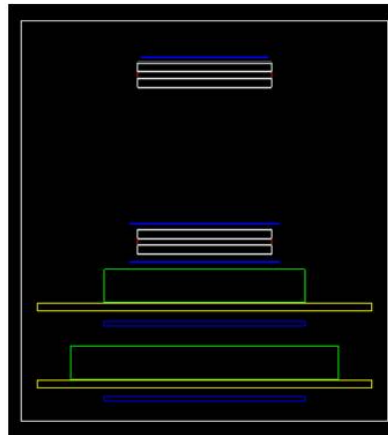
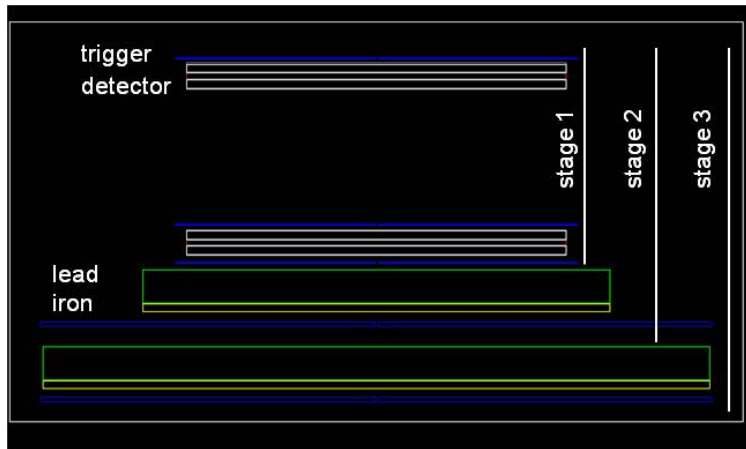


Figure 1: Geometry of Forewarn Detector plotted with GEANT4 simulation.



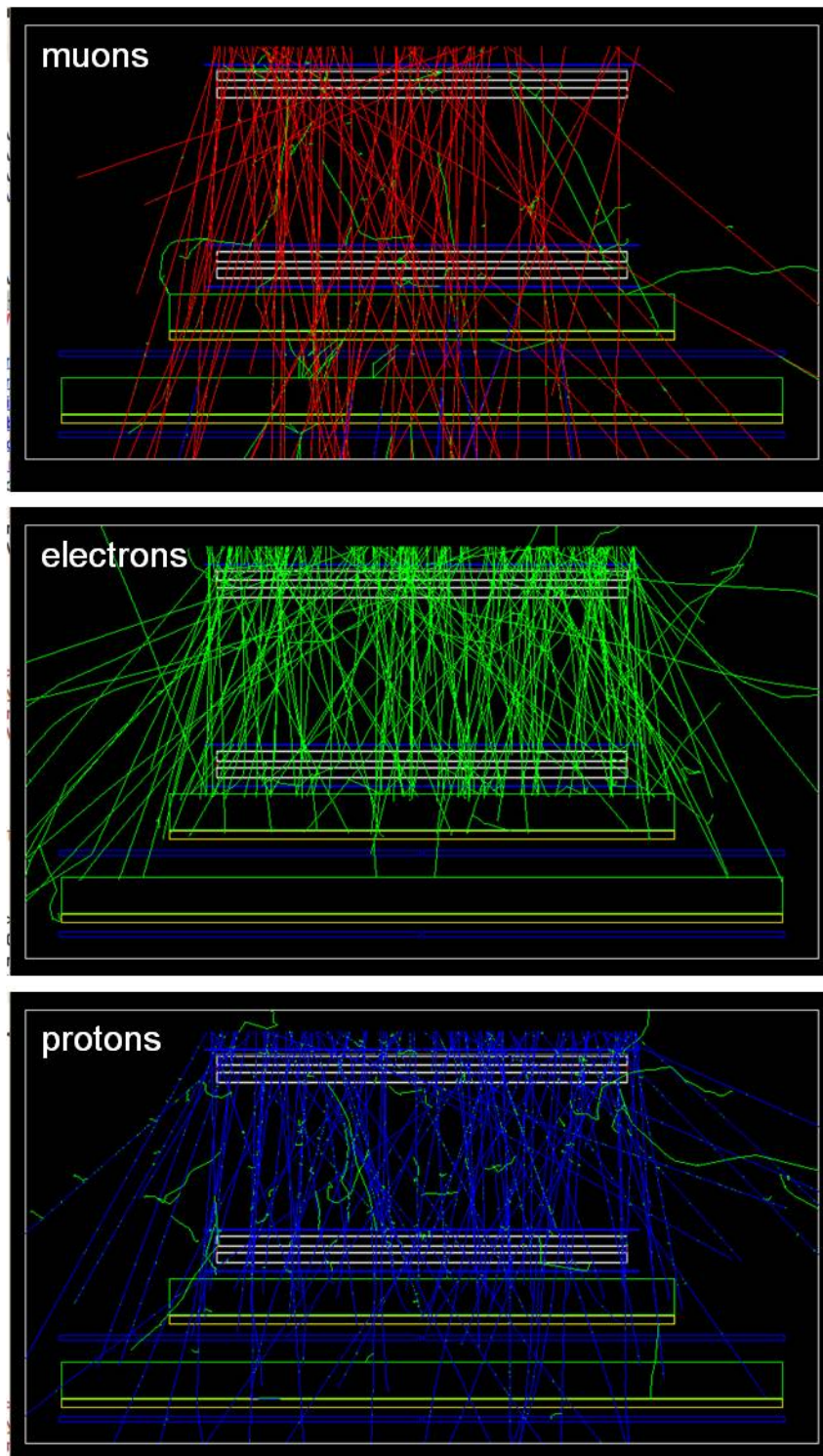


Figure 2: Particle interaction with different materials. Each particle is shown separately. Gammas are not shown for better visual view. Secondary electrons are shown in green in each plot.

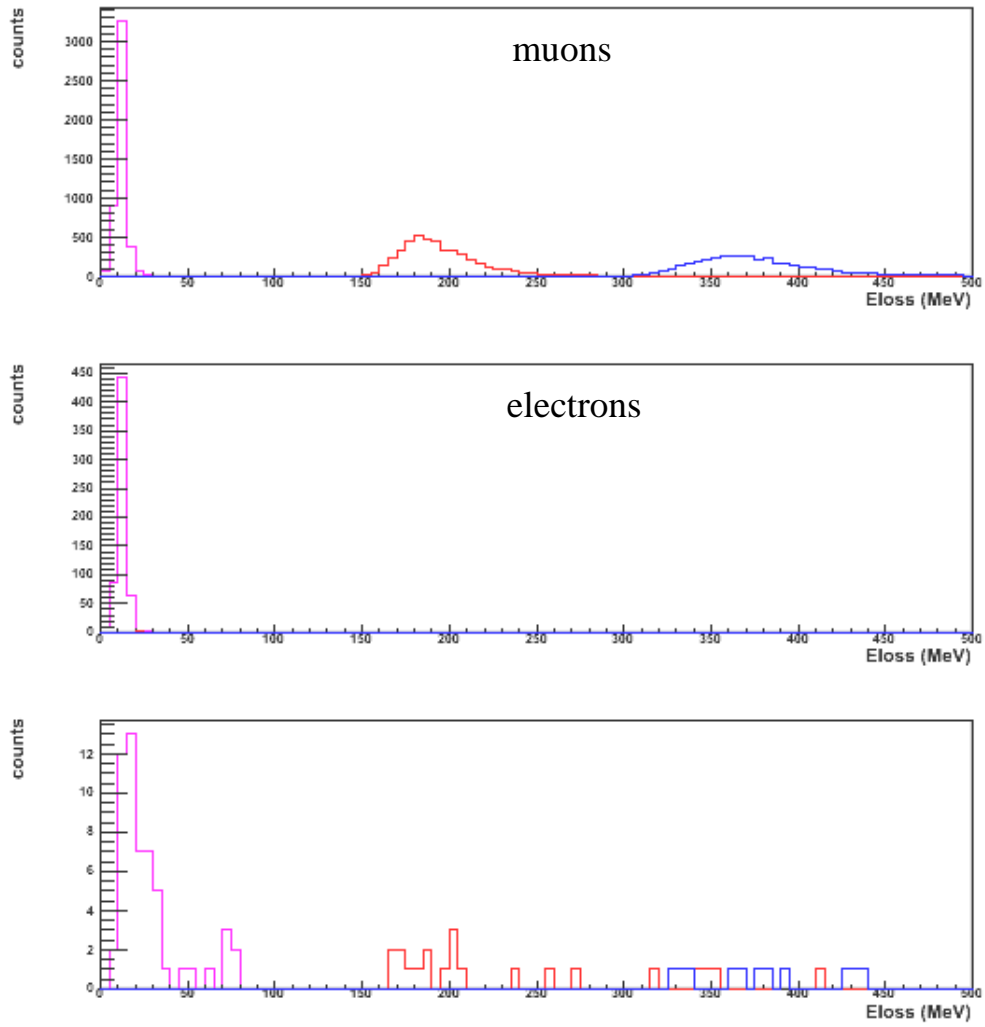


Figure 3: Energy loss for each trigger stage and for each particle.

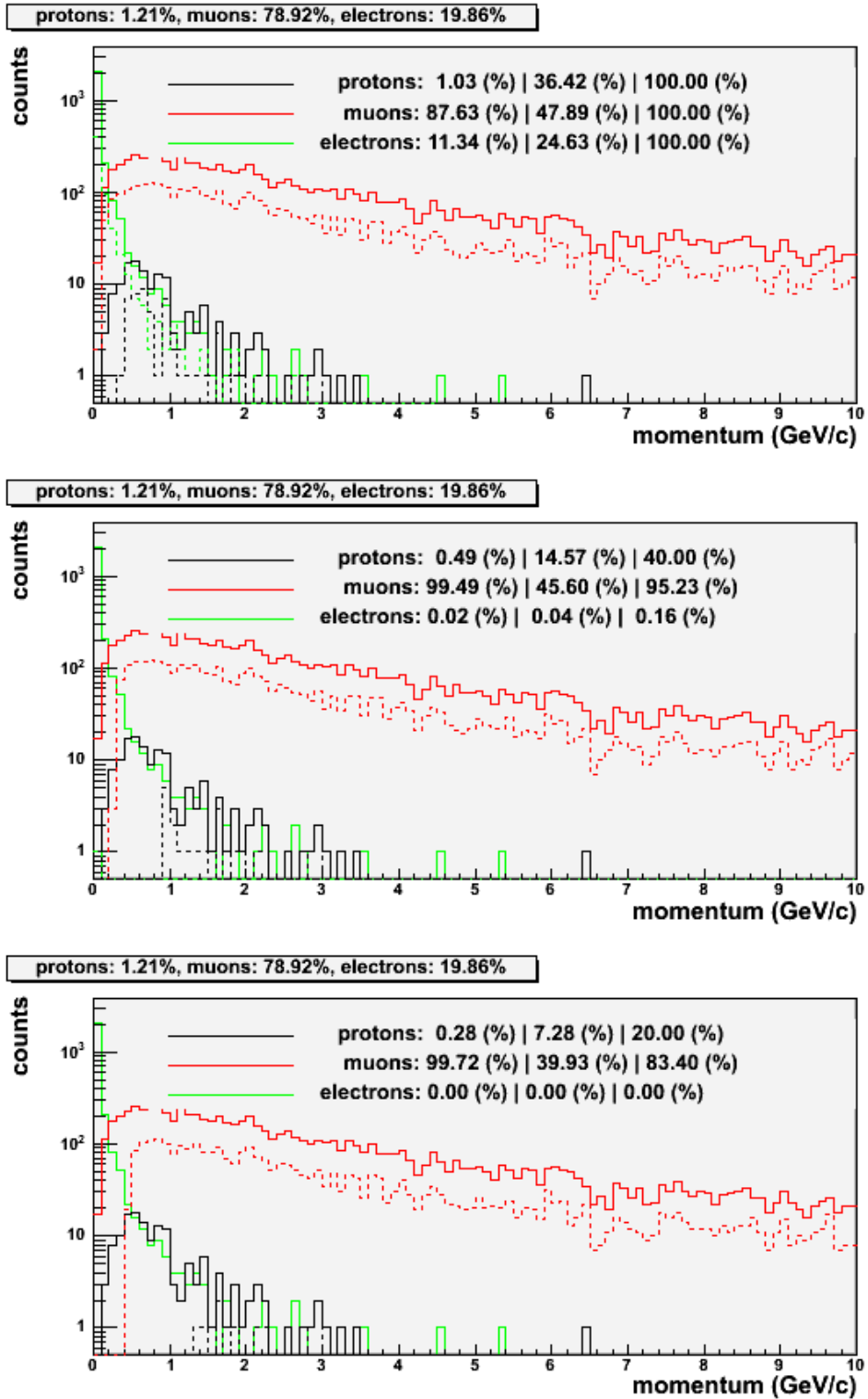
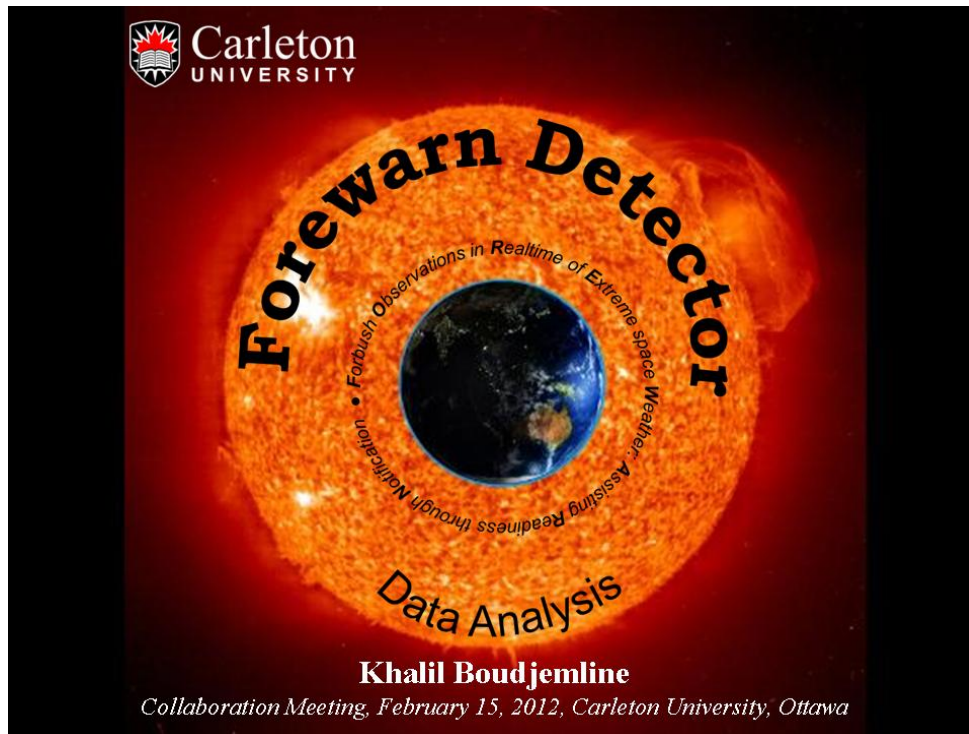


Figure 4: Expected number of events for each trigger stage. The title of each plot shows the initial fraction of each particle.

# Appendix 7



## Outline



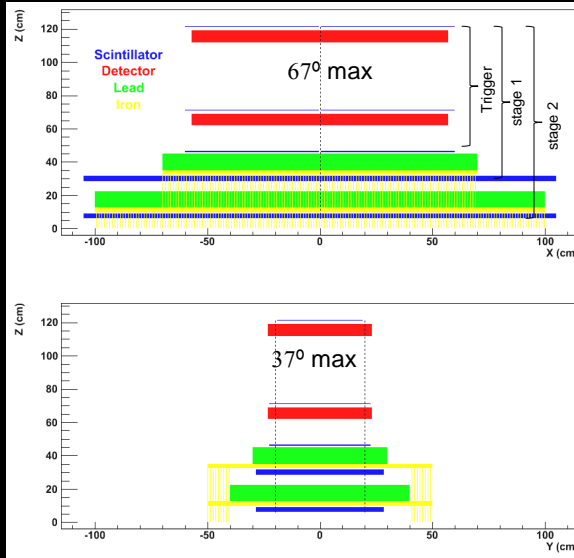
2

1. Forewarn Detector: set-up and expected flux
2. Data Analysis
3. Results / Atmospheric effects and corrections
4. Conclusion

# 1. FOREWARN Detector Set-Up and Expected Flux



3



$\mu$ : 78.9% |  $e^-$ : 19.9% |  $p$ : 1.2%

$\mu$ : 87.5% |  $e^-$ : 11.5% |  $p$ : 1.1%

$\mu$ : 99.5% |  $e^-$ : 0.0% |  $p$ : 0.5%

$\mu$ : 99.7% |  $e^-$ : 0.0% |  $p$ : 0.3%

Muon energy:

- Stage 1:  $> 0.2$  GeV/c

- Stage 2:  $> 0.4$  GeV/c

All events (scintillators):

- Trigger: reference

- Stage 1: 85%

- Stage 2: 76%

Collaboration Meeting, February 15, 2012, Carleton University, Ottawa

Khalil Boudjemline

# 2. Data Analysis Steps



4

1. Scintillators:

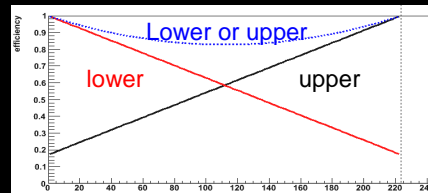
- Good event
  - Correct for the inefficiency of stages (rough correction).
- S1:  $S1(1) + S2(1) | S1(0)$ .

2. Drift chambers:

- Good event: trigger event + pulse in both chambers.
- Event hit positions and angular distributions.
- Correct for the inefficiency of stages (use hit positions + extrapolation + reweight event).

3. Analyzed data: 2 runs

(5 days: Jan 17 – Jan 22, 2012).



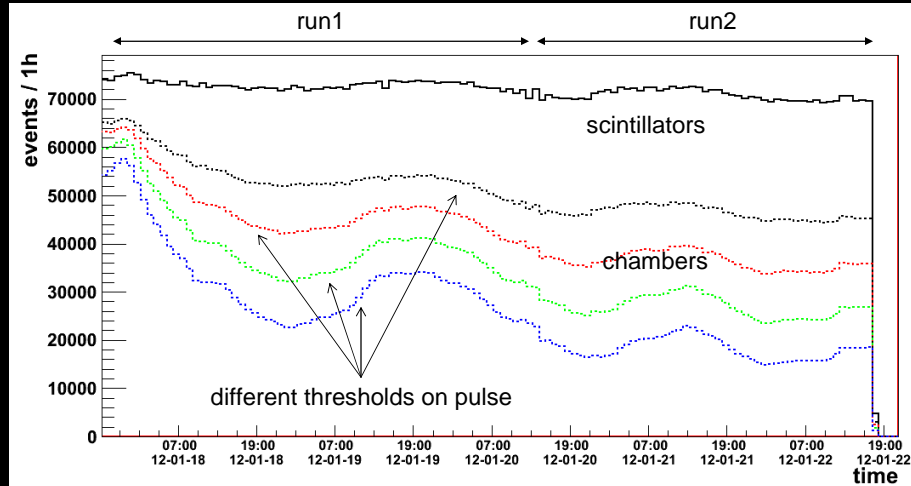
Collaboration Meeting, February 15, 2012, Carleton University, Ottawa

Khalil Boudjemline

### 3. Results (scintillators/chambers) Flux comparison (trigger)



5



Scintillators and chamber fluxes. Four thresholds for chamber flux.

Collaboration Meeting, February 15, 2012, Carleton University, Ottawa

Khalil Boudjemline

### 3. Results (scintillators/chambers) Flux plot shape



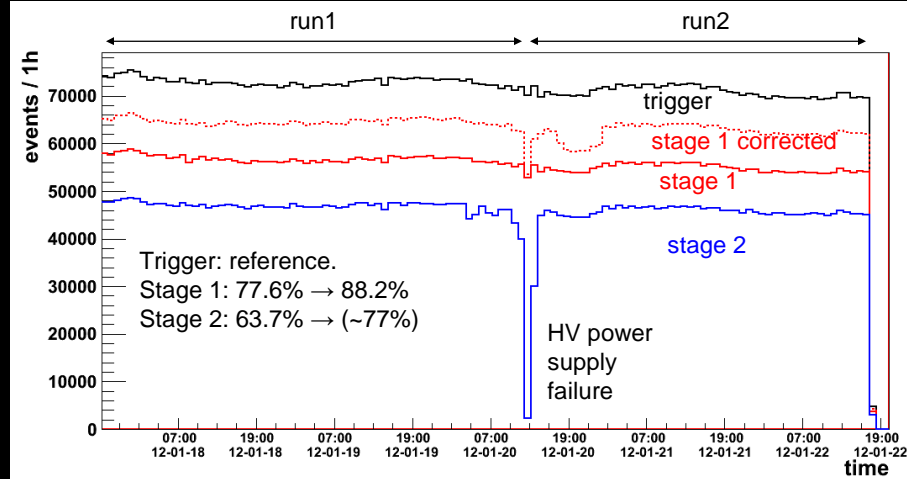
6

1. Scintillators:
  - Atmospheric (pressure, temperature, humidity...)
  - Solar activity
  - Statistics.....
  
2. Drift chambers:
  - All above.
  - Threshold.
  - Primary charge =  $f(P)$ . Increases with P
  - Avalanche gain =  $f(P)$ . Decreases with P
  - Different gain in both chambers.

Collaboration Meeting, February 15, 2012, Carleton University, Ottawa

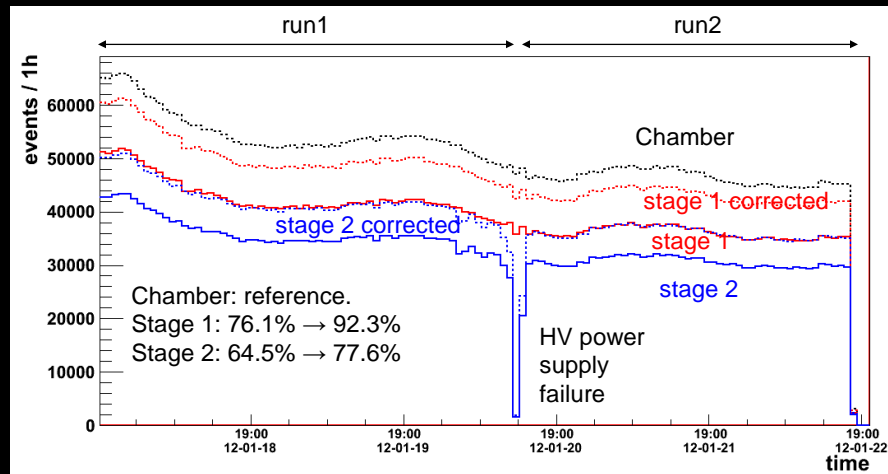
Khalil Boudjemline

### 3. Results (scintillators) Trigger / stages



Trigger and trigger stages. Rough correction of stage 1.

### 3. Results (chambers) Trigger / stages

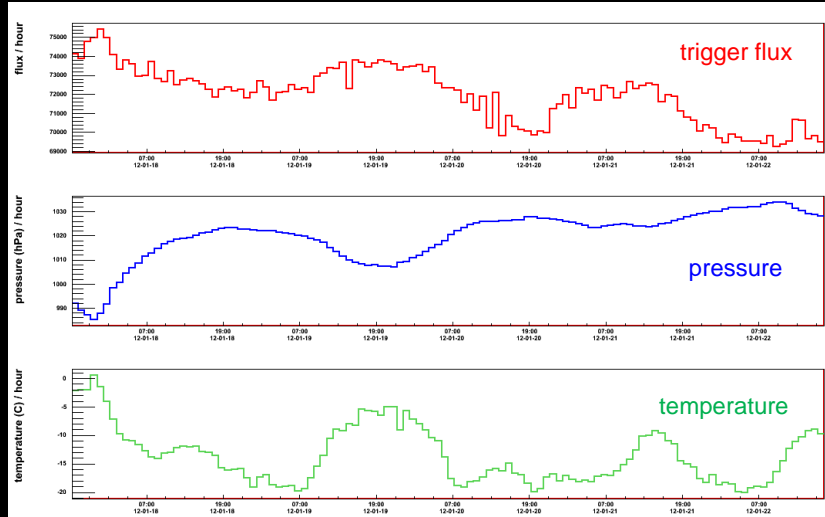


Chamber and chamber stages. Stages corrected according to the event hit position..

### 3. Results (scintillators) Trigger flux / pressure / temperature



9



Trigger flux, pressure and temperature vs time

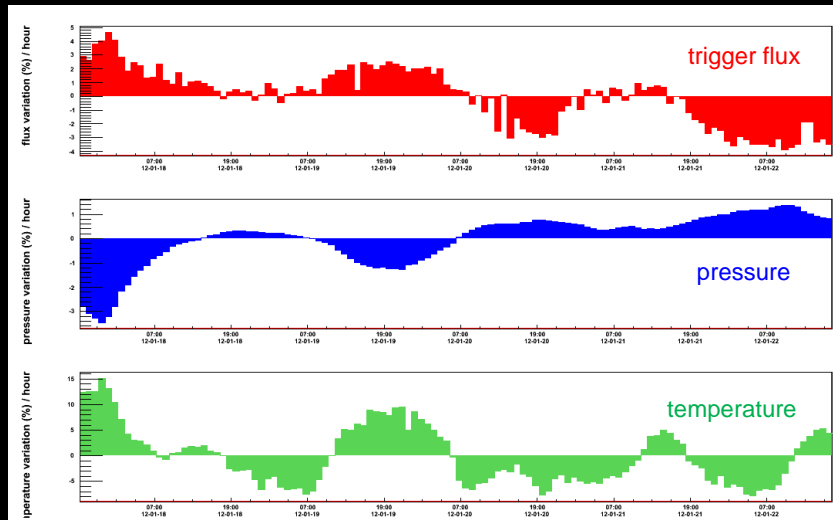
Collaboration Meeting, February 15, 2012, Carleton University, Ottawa

Khalil Boudjemline

### 3. Results (scintillators) Relative variation: $100 \times \text{Log}(X/X_0)$



10



Relative variation: trigger flux, pressure and temperature vs time

Collaboration Meeting, February 15, 2012, Carleton University, Ottawa

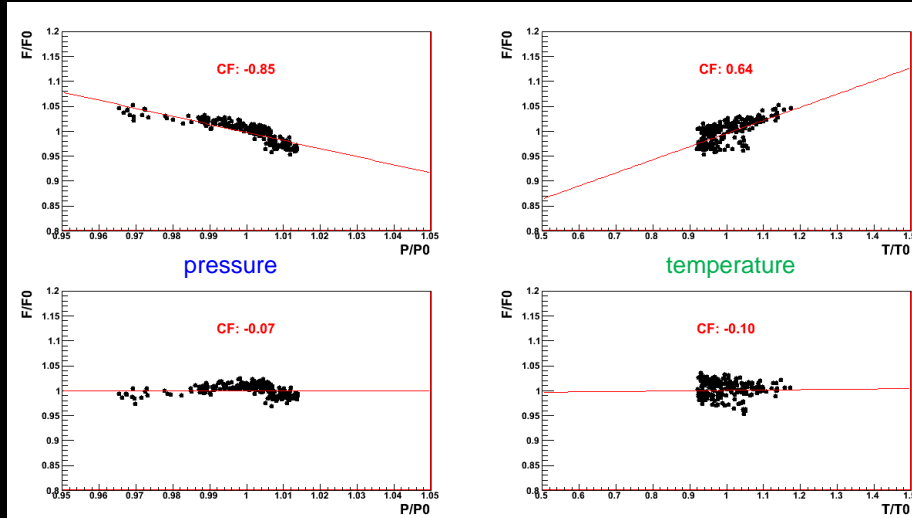
Khalil Boudjemline



### 3. Results (scintillators) Correlation (F/P & F/T)



11



Correlation between trigger flux and pressure/temperature

CF: Correlation Factor

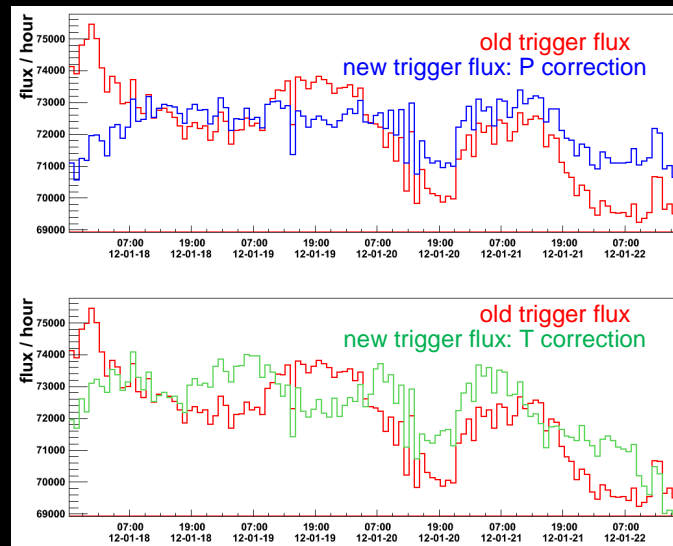
Collaboration Meeting, February 15, 2012, Carleton University, Ottawa

Khalil Boudjemline

### 3. Results (scintillators) Corrected trigger flux



12



Trigger flux before and after correction with pressure and temperature.

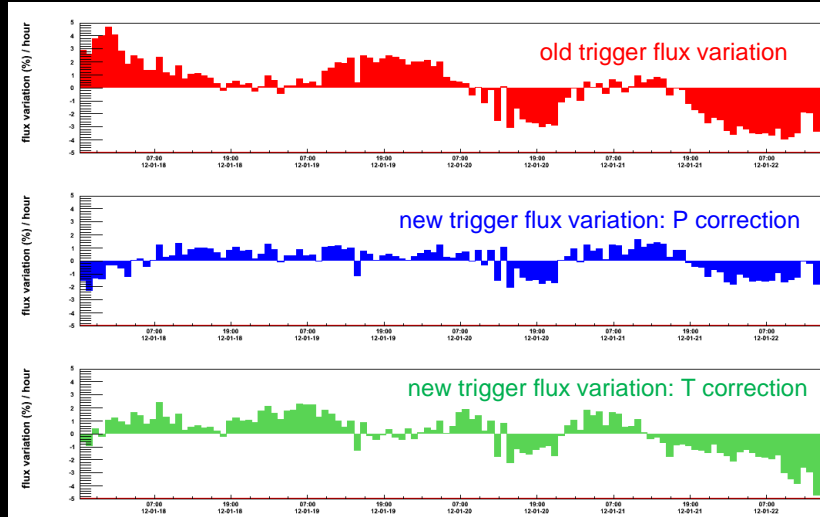
Collaboration Meeting, February 15, 2012, Carleton University, Ottawa

Khalil Boudjemline

### 3. Results (scintillators) Relative variation: $100 \times \text{Log}(X/X_0)$



13



Relative trigger flux before and after correction with pressure and temperature.

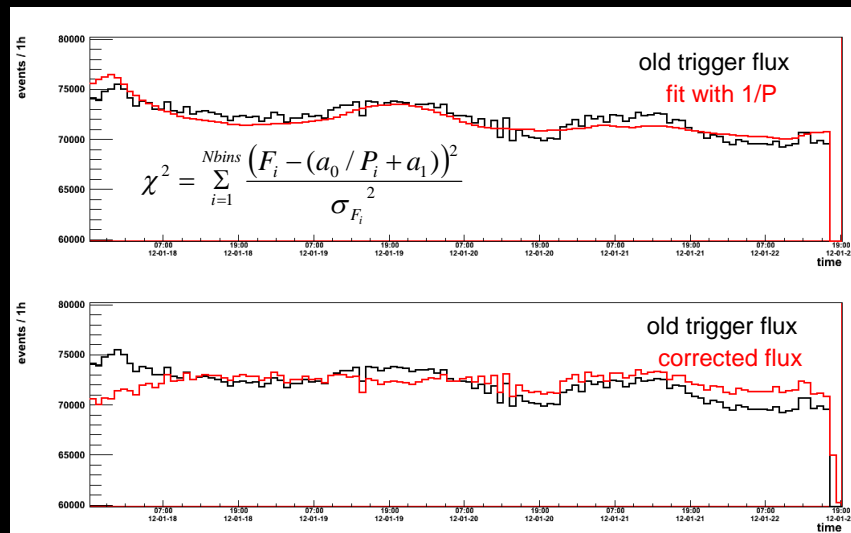
Collaboration Meeting, February 15, 2012, Carleton University, Ottawa

Khalil Boudjemline

### 3. Results (scintillators) $\chi^2$ minimization / Minuit (Root)



14



Trigger flux before and after correction with pressure Using  $\chi^2$  minimization.

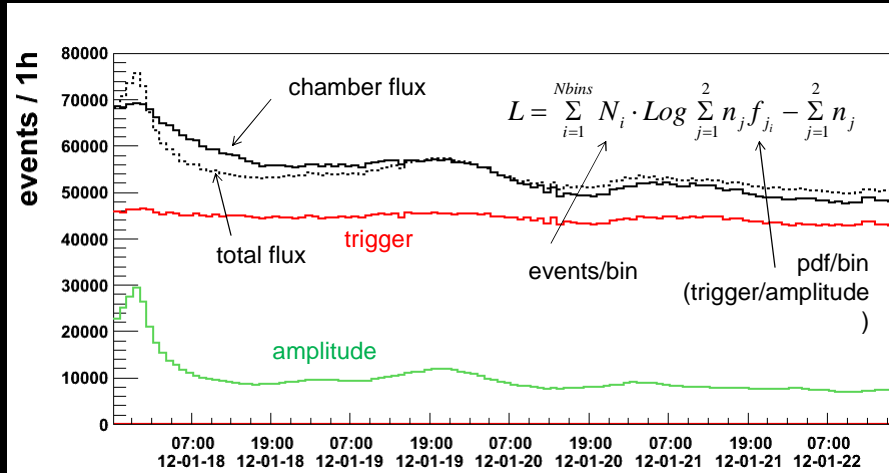
Collaboration Meeting, February 15, 2012, Carleton University, Ottawa

Khalil Boudjemline

### 3. Results (chambers) Understand the flux shape



15

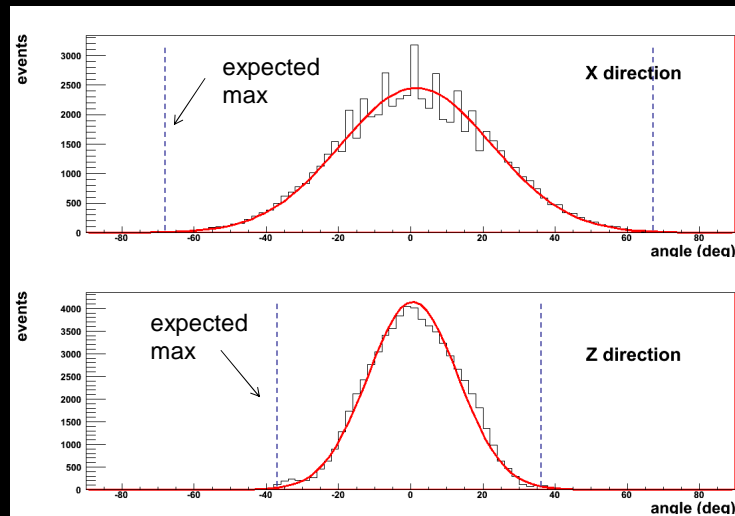


Fit the flux using max log likelihood

### 3. Results (chambers) Angular distributions



16

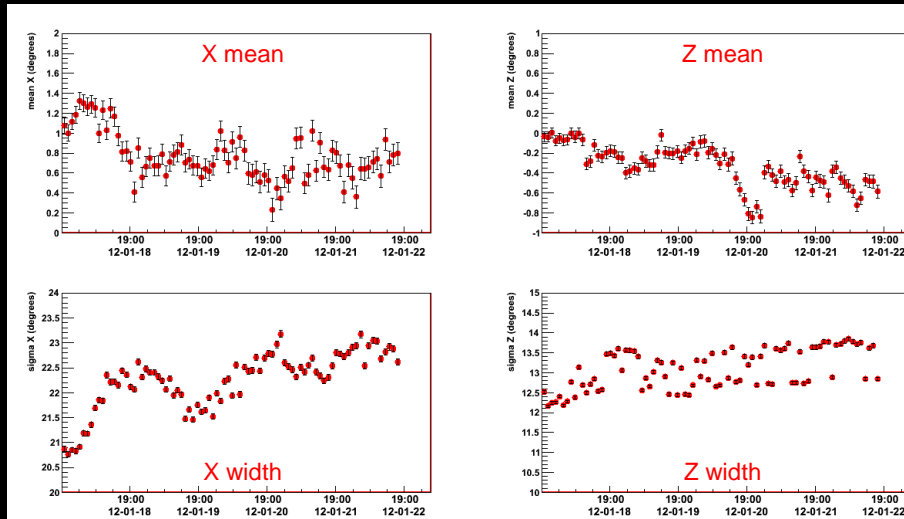


Angular distributions for both directions.

### 3. Results (chambers) Angular parameters (mean/width)



17



Variation of angular parameters vs time.

Collaboration Meeting, February 15, 2012, Carleton University, Ottawa

Khalil Boudjemline

### 4. Conclusion



18

- 1- Small scale muon telescope working as expected.
    - Geometrical acceptance.
    - Relative flux at each stage.
  - 2- Atmospheric effects observed on the flux and corrected for trigger.
    - Similar shape observed on the drift chambers.
- Next:
- Take data with same gain for both chambers.
  - Take data for longer time.
  - Estimate the best mean flux.
  - Understand the variation of the angular parameters vs time.
  - .....

Collaboration Meeting, February 15, 2012, Carleton University, Ottawa

Khalil Boudjemline

# Appendix 8

## Proposal for Future Canadian detector

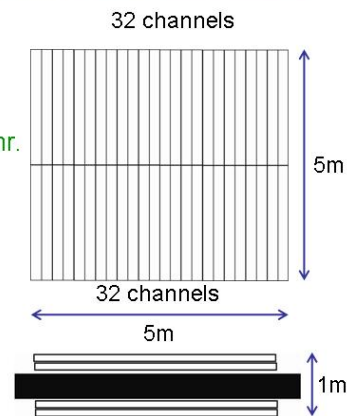
John Armitage  
Carleton University

October 2011

Muon Workshop  
St Emile de Suffolk

### Future detector

- Design criteria
  - $5\text{m} \times 5\text{m} = 25\text{m}^2$   $9 \times 10^6$  counts per hr.
  - Angular resolution  $\sim \pm 10$  degrees  $\sim 175$  mr.
  - Plane separation  $\sim 1.0\text{m}$ .
  - Spatial resolution  $\sim 17$  cm
- Detector dimensions
  - Scintillator strips  $2.5\text{m}$  long,  $16\text{cm}$  wide
  - Angular resolution  $\pm 9$  degrees
  - Angular coverage  $78$  degrees
  - $64$  channels per layer
  - Two x,y layers -  $256$  channels
  - $4 \times 64$  channel PMTs



WLS fibre in machined grooves

October 2011

Muon Workshop.  
St Emile de Suffolk

2

<b>CRIPT Scintillator</b>						
	cross section			vol.m ^3	cost/m	cost/m^3
	0.03	0.017	1	0.0005	\$10	\$19,607.84
<b>New Scintillator</b>						
	cross section	length		vol/bar	cost/bar	No. of bars
	0.16	0.02	2.5	0.008	\$156.86	256
						\$40,157
<b>Fibre cost</b>						
	Number length			Cost/m		
	256	3.5 m		896	\$9.37	\$8,396
<b>PMT cost</b>						
	Number cost					
	4	\$3,208		\$12,832		
<b>CRIPT DAQ</b>						
	No. chan	Cost		Cost/chan		
	1476	\$205,000		\$138.89		
<b>New project</b>						
	No chan	Cost				
	256	\$35,555.56		\$35,555.56		
<b>Lead</b>						
	cross section	height		vol	cost	cost/m^3
	1.3	0.5	1	0.65	\$80,000	\$123,077
<b>New project</b>						
	cross section	height		vol m^3	cost	
	5	5	0.01	0.25	\$30,769	\$30,769

<b>Machining of scintillator frames</b>					
			materials	\$2,000	
1 person	5 weeks	@35 hr/wk	at \$42	machining	\$7,350
<b>Lead and scintillator Support structure</b>					
			materials	\$10,000	
1 person	7 weeks	@ 35hr/wk	at \$42	machining	\$10,290
2 people	3.5 weeks	@35hr/wk	at \$42	assembly	\$10,290
<b>Assembly of scintillator</b>					
2 person	16 weeks	at 35hr/wk	@ \$18/hr		\$20,160
<b>Fibre prep</b>					
	no. fibre	cost per fibre			
	256	\$10			\$2,560
				<b>Total</b>	<b>\$190,359</b>